

# **Jetting of multiple functional materials by Additive Manufacturing**

*Javier Ledesma Fernández, BSc, MSc*

**Doctoral Thesis**

Submitted to the University of Nottingham for the  
degree of Doctor of Philosophy

August 2017







## Abstract

The rise and consolidation of Additive Manufacturing (AM) as a technology has made possible the fabrication of highly customised and complex products in almost every industry. This not only allows the creation of objects that were impossible just a few decades ago but also facilitates the production of small runs of products at a reasonable cost, which reduces the design-prototyping cycles and boosts product innovation. However, to produce truly functional parts it is desirable for these systems to be able to deposit multiple complex materials in a single process to locally embed controllable properties such as electrical conductivity or sensing capabilities into the produced geometries. Consequently, a review of current AM technologies capable of depositing conductive materials is performed in this PhD and discussed to find the most suitable approaches. Similarly, existing multi-material set-ups are studied to find limitations and common practices to create a system that is capable of fulfilling the objectives of this work.

Piezo-activated inkjet printing (PIJ) is identified as an appropriate technology for multi-material applications due to its non-contact nature, high spatial resolution, capability of mixing and digitally grading materials and simple scale-up of the process. Furthermore, in the last decade it has been shown that jetting can be used for the accurate deposition of a wide range of functional materials. However, upon detailed review of this method, the limitations that it imposes on the compositions of the inks are identified as its main drawback. Specifically, the solid content and molecular weight of the fluids that can be jetted are restricted by the viscosity of the final ink, typically under 40 mPa·s. This is problematic in the case of jetting conductive materials, since it forces the solid content to be very low, therefore yielding very thin and often inhomogeneous layers. Additionally, all the organic components on the inks added to facilitate its ejection need to be removed, which typically means longer and more aggressive post-processes before rendering the printed tracks conductive. For this reason, drop-on-demand micro-dispensing valves were chosen as a high viscosity jetting (HVJ) approach in this work, with the intention of assessing their capability as a suitable tool for multi-material AM of functional inks. However, since their resolution and speed are lower than conventional inkjet, a hybrid approach is presented including micro-dispensing valves and inkjet printheads capable of depositing a wide range of viscosities in a single process. A comprehensive description of the hybrid set-up is given, discussing its main elements including the printing heads, the custom design printer assembly, the ultraviolet (UV) and infrared (IR) lamps installed for

in-situ processing, the monitoring system and the set-up to measure the evolution of the electrical resistance in printed tracks in real time during post-processing. Additionally, the printing strategy and process flow is discussed.

The investigated set-up was used to study the printability and performance of several functional materials ranging from UV-curable polymers to conductive formulations such as carbon paint, a silver nanoparticle-based paste and a dispersion of PEDOT:PSS. Each material was thoroughly characterised prior to printing with a special focus on viscosity. Their drop formation and deposition processes were studied at different printing settings using high speed imaging and footprint analysis of the deposited drops. These tests were used to obtain sets of working parameters that allow reliable printing and were used to produce 2D patterns with different resolutions to find the drop spacing that results in flat homogeneous films. Later, these films were post-treated according to the requirements of each material and multilayer structures were produced and analysed with an optical profilometer. The cross-section of these 3D tracks was used together with the measured resistance to obtain the electric conductivity of the materials under the printing conditions used. Finally, the accumulated information during the previous stages of printing was used to produce 3D multi-material demonstrators with incorporated conductive tracks, electric components and electroluminescent elements. These proof-of-concept samples were used to discuss limitations of the approach and showcase future possibilities of the system.

## Acknowledgment

Joining the Centre for Additive Manufacturing of the University of Nottingham has been a truly transformative experience and without a doubt the most crucial step in my academic career. Here I have had the opportunity of using state-of-the-art equipment for my research and learning from a group of very talented professionals, which allowed me to improve every day during four wonderful years. More importantly, they made all the time and effort spent on this project worthwhile and helped me to enjoy it even in the most stressful moments. For this, I am and always will be thankful to every person involved in this group.

Special thanks to my supervisors, Prof. Richard Hague and Prof. Christopher Tuck for all the support and patience over the years. Without their technical advice and management this thesis would not have reached its full potential, which would have resulted in leaving out the most interesting sections. However, their guidance often went beyond the purely technical aspects and covered areas as diverse as presentation and writing skills, professional development, team working and more. Thus, it is clear to me that without their input I would not have transitioned from a hesitant student to a self-sufficient researcher.

Similarly, this work would not have been possible without the assistance of Mr. Mark East, Mr. Mark Hardy and Mr. Joseph White, the super-human technicians of the Centre for Additive Manufacturing. They were often my first stop of the day, at the beginning for various technical issues, but soon for their company and energy. They never accepted anything as impossible, rising the standards of everyone around them.

I am grateful for the support of the whole group and listing their individual contribution to my day to day activities would require a document almost as long as the present thesis. Still, I would like to thank the outstanding contributions of Dr. Ehab Saleh, Dr. Bochuan Liu, Dr. Yinfeng He, Dr. Jayasheelan Vaithilingam, Dr. Aleksandra Foerster and Ms. Hagit Gilon for their initial training on the commercial printer (LP50) and insightful discussions about piezoelectric jetting; Dr. Fan Zhang and Dr. Belén Begines for synthesising the TPGDA and helping my deal with the chemistry-related parts of the project; Dr. Richard Leach, Mr. Adam Thompson and Mr. Lewis Newton from the Metrology Group for performing the 3D profilometry of the printed tracks; Dr. Ajit Panesar for his custom 3D slicing-code (Matlab) and general advice on part design; and to

Ms. Mirela Axinte for helping me with the endless paperwork, often more overwhelming than the experiments themselves. Also, thanks to Michele, Adam, Amir, Craig, Zhengkai, Amanda, Luke, Meisam and the rest of doctors and professors of tomorrow that shared the PhD journey with me in Nottingham. If there is something that makes me prouder than having successfully finished this project is knowing that I can count most of the above people as my friends.

Finally, thanks to Alba Soria, my wife-to-be, who not only helped with the overall design and layout of the present document but also read and listened to most of its contents, providing always key feedback with a smile in her face. Experiments failed and instruments broke but no matter how long or bad a day was, she was always there for me, keeping me levelled and focused. She believed in me even when I doubted, so it is safe to say that this thesis was completed because of her.

# Contents

Abstract.....	v
Acknowledgment .....	vii
Contents.....	ix
Nomenclature: List of Symbols .....	xiii
Nomenclature: List of Acronyms.....	xiv
1. Introduction.....	1
1.1 Additive Manufacturing (AM) .....	2
1.2 Manufacturing electronics .....	4
1.3 Contribution of the present work .....	6
1.3.1 Motivation of thesis .....	6
1.3.2 Novelty of Research .....	7
1.3.3 Aim and objectives.....	7
1.3.4 Thesis structure .....	8
2. Literature Review .....	9
2.1 Conductive Materials compatible with AM.....	9
2.1.1 Metals .....	9
2.1.2 Organic conductive materials .....	21
2.1.3 Electrically conductive composites and hybrid materials .....	23
2.2 Multi-material and Hybrid AM systems .....	24
2.2.1 Laser-based powdered systems .....	24
2.2.2 Stereolithography (SLA).....	25
2.2.3 Cold Extrusion .....	26
2.2.4 Fused Filament Fabrication (FFF) .....	28
2.2.5 Jetting .....	30
2.3 Inkjet Printing Review.....	33
2.3.1 Classification of inkjet systems .....	33
2.3.2 High viscosity non-contact selective deposition .....	37
2.4 Theory of inkjet and dispensing .....	39
2.4.1 Fundaments of rheology .....	39
2.4.2 Theory of piezoelectric inkjet (PIJ) .....	51
2.5 Conclusions from reviewed literature and plan for this work .....	62
3. Platform development and understanding.....	65
3.1 Printing elements .....	66
3.1.1 Description of high viscosity jetting (HVJ) valve .....	66
3.1.2 Description of low viscosity jetting system.....	69
3.2 Printing platform.....	71
3.2.1 LP50 original system.....	73

---

3.2.2	Hybrid system.....	77
4.	Experimental Methods and Materials.....	97
4.1	Statistical analysis.....	97
4.2	Chosen materials.....	98
4.2.1	Carbon Paint dispensed by HVJ.....	98
4.2.2	Photo-curable resin dispensed by HVJ.....	99
4.2.3	Photo-curable low viscosity ink (TPGDA) dispensed by PIJ.....	99
4.2.4	Conductive polymer (PEDOT:PSS) dispensed by HVJ.....	99
4.2.5	Hybrid silver paste dispensed by HVJ.....	100
4.2.6	Substrates.....	101
4.3	Materials characterization.....	102
4.3.1	Density.....	102
4.3.2	Particle size and size distribution.....	102
4.3.3	Thermogravimetric Analysis (TGA).....	103
4.3.4	Surface Tension.....	104
4.3.5	Viscosity.....	105
4.4	Printing characterization.....	110
4.4.1	Drop formation and deposition.....	110
4.5	3D geometric analysis.....	118
4.6	Electrical conductivity and resistivity.....	118
4.6.1	Brief magnitudes description.....	118
4.6.2	Measuring method.....	120
5.	Results and discussion: Material characterisation.....	123
5.1	Density.....	123
5.2	Particle Size and size distribution.....	124
5.3	Solid content and thermal stability.....	125
5.4	Surface tension.....	131
5.5	Viscosity.....	132
5.5.1	Shear viscosity.....	132
5.5.2	Viscoelasticity.....	139
5.6	Conclusions from characterisation.....	141
6.	Results and discussion: Drop formation and deposition.....	143
6.1	Jettability study of low viscosity TPGDA.....	143
6.2	High Speed video analysis.....	144
6.2.1	Matrix Experiment.....	145
6.2.2	Representative drops impacting on glass substrate.....	156
6.3	Drop footprint investigation with optical microscopy.....	159
6.3.1	Footprints experiment summary and conclusions.....	168
6.4	Drop mass and volume.....	170
6.5	Discussion and printability calculations.....	175

6.5.1	Experiments performed: evaluation and potential improvements.....	175
6.5.2	Printing parameters.....	177
6.5.3	Printability map .....	181
7.	Results and discussion: 2D & 3D deposition of functional materials.....	185
7.1	2D-tests: Resolution and post-processing conditions.....	185
7.1.1	UV-curing.....	188
7.1.2	Solvent Evaporation .....	190
7.1.3	Sintering.....	196
7.1.4	Conclusions of the 2-dimensional tests .....	202
7.2	3D-tests: Layer thickness and resistivity .....	206
7.2.1	Layer thickness .....	207
7.2.2	Electrical performance .....	210
7.2.3	Conclusions of the 3-dimensional and functional tests .....	216
7.3	Multi-material proof-of-concept functional structures.....	220
7.3.1	Multi-material interaction matrix .....	220
7.3.2	Complex multi-material designs with locally designed properties .....	222
7.3.3	Functional circuits in 2D.....	224
7.3.4	Flat multi-layered devices.....	226
7.3.5	3D demonstrators .....	229
7.3.6	Embedded components and capacitive sensors.....	235
7.3.7	Printed electroluminescent devices .....	237
8.	Conclusions and future work.....	243
8.1	Identification of required features for a multi-material AM system.....	244
8.2	Platform design and development .....	244
8.3	Choice and characterisation of materials .....	246
8.4	Printability studies and processing window of the system.....	247
8.5	Post-processing studies.....	249
8.6	Fabrication of 3D multi-material functional structures.....	250
9.	Appendices.....	253
A1.	Fundamental code for the printing platform .....	253
A2.	UV-resin and carbon paint early post-treatment and 3D-tests .....	261
A3.	Electroluminescent initial tests and material formulation.....	264
10.	References.....	269



## Nomenclature: List of Symbols

$A$	Area [m <sup>3</sup> ]	$r_{eq}$	Equivalent Radius [m]
$a$	Radius [m]	$SE$	Standard Error
$B$	Shape parameter of drop (DSA)	$T$	Temperature [°C]
$Bo$	Bond Number	$t$	Time [s]
$Ca$	Capillary number	$T_{5\%}$	5% Mass Loss Temperature [°C]
$De$	Deborah Number	$t_c$	Closing Time (valve) [s]
$d_N$	Nozzle diameter [m]	$t_{cyc}$	Cycle Time [s]
$e$	Charge of the Electron [C]	$t_o$	Opening Time (valve) [s]
$E$	Electric Field [N C <sup>-1</sup> ]	$t_p$	Pulse Time [s]
$Ec$	Elastocapillary number	$t_{rx}$	Relaxation Time [s]
$f_{circ}$	Circularity	$u$	Velocity (also $v$ ) [m s <sup>-1</sup> ]
$FitE$	Profile Fit Error (DSA)	$V$	Voltage [V]
$g$	Gravitational acceleration [m s <sup>-2</sup> ]	$We$	Weber number
$G^*$	Complex Modulus [Pa]	$\bar{x}$	Mean of N observations ( $x_i$ )
$G'$	Elastic / Storage Modulus [Pa]	$\gamma$	Shear Deformation
$G''$	Viscous / Loss Modulus [Pa]	$\dot{\gamma}$	Shear Rate [s <sup>-1</sup> ]
$I$	Current [A]	$\delta$	Phase Angle [rad]
$j_c$	Current Density [A m <sup>-2</sup> ]	$\Delta m_T$	Mass Loss at T (°C) [kg]
$L$	Length [m]	$\delta x$	Uncertainty of magnitude $x$
$l_c$	Characteristic Length [m]	$\varepsilon$	Extensional deformation
$l_e$	Entry Length [m]	$\dot{\varepsilon}$	Extension Strain Rate [s <sup>-1</sup> ]
$N$	Number of observations	$\eta$	Shear Viscosity [Pa s]
$n_c$	Number of Charge Carriers	$\eta_0$	Zero Shear Viscosity [Pa s]
$n_x$	Refractive Index of material $x$	$\eta_\infty$	$\eta$ at Infinite Shear Rate [Pa s]
$O\%$	Percentage of Overlap	$\eta_e$	Extensional Viscosity [Pa s]
$Oh$	Ohnesorge number	$\mu_c$	Charge mobility [m V <sup>-1</sup> s <sup>-1</sup> ]
$P$	Pressure [Pa]	$\rho$	Density [kg m <sup>-3</sup> ]
$pD$	Drop Pitch [m]	$\rho_r$	Electric Resistivity [ $\Omega$ m]
$P_L$	Perimeter [m]	$\sigma$	Shear Stress [Pa]
$Q$	Volumetric Flow Rate [m <sup>3</sup> s <sup>-1</sup> ]	$\sigma_0$	Apparent Yield Stress [Pa]
$R$	Electric Resistance [ $\Omega$ ]	$\sigma_c$	Electric Conductivity [S m <sup>-1</sup> ]
$R^2$	Adjusted square of the Correlation Coefficient	$\sigma_e$	Extensional Stress [Pa]
$R_{DPI}$	Resolution [DPI]	$\sigma_{ST}$	Surface Tension [N m <sup>-1</sup> ]
$Re$	Reynolds Number	$\omega$	Angular Frequency [rad s <sup>-1</sup> ]

## Nomenclature: List of Acronyms

<i>2D</i>	2-dimensional	<i>LED</i>	Light Emitting Diode
<i>3D</i>	3-dimensional	<i>I/O</i>	Electronic Input / Output
<i>ABS</i>	Acrylonitrile Butadiene Styrene	<i>IR</i>	Infrared (Radiation)
<i>ADA</i>	Advanced Drop Analysis	<i>LM</i>	Laser Melting
<i>AFM</i>	Atomic Force Microscope	<i>LS</i>	Laser Sintering
<i>AM</i>	Additive Manufacturing	<i>LVER</i>	Linear Viscoelastic Region
<i>ATR</i>	Attenuated Total Reflection	<i>MOD</i>	Metal-Organic Decomposition
<i>BMP</i>	Bitmap (file)	<i>NIR</i>	Near infrared radiation
<i>C#</i>	C-sharp (programming)	<i>PC</i>	Personal computer
<i>CAD</i>	Computer Assisted Design	<i>PCB</i>	Printed Circuit Board
<i>CCD</i>	Charged-Coupled Device	<i>PDMS</i>	Polydimethylsiloxane
<i>CIJ</i>	Continuous Inkjet	<i>PEDOT</i>	Poly(3,4-ethylenedioxythiophene)
<i>CNTs</i>	Carbon Nanotubes	<i>PIJ</i>	Piezoelectric Inkjet
<i>DCON</i>	Digital Controller	<i>PL</i>	Photoluminescence
<i>DIY</i>	Do It Yourself	<i>PLA</i>	Polylactic Acid
<i>DoD</i>	Drop-on-Demand	<i>PSS</i>	Polystyrene sulfonate
<i>DPI</i>	Drops Per Inch	<i>PVP</i>	Polyvinylpyrrolidone
<i>DSA</i>	Drop Shape Analyser	<i>PWM</i>	Pulse-Width Modulation
<i>DTG</i>	Derivative Thermogravimetric	<i>RFID</i>	Radio Frequency Identification
<i>EL</i>	Electroluminescence	<i>ROI</i>	Region Of Interest
<i>FDM</i>	Fused Deposition Modelling	<i>SEM</i>	Scanning Electron Microscope
<i>FFF</i>	Fused Filament Fabrication	<i>SLA</i>	Stereolithography
<i>FOV</i>	Field Of View	<i>STL</i>	Stereolithography (file)
<i>FPS</i>	Frames Per Second	<i>TGA</i>	Thermogravimetric Analysis
<i>FTIR</i>	Fourier Transform Infrared Spectroscopy	<i>ToF</i>	Time of Flight
<i>GUI</i>	Graphics User Interface	<i>TPGDA</i>	Tripropylene Glycol Diacrylate
<i>HMI</i>	Human Machine Interface	<i>USB</i>	Universal Serial Bus
<i>HPB</i>	Head Personality Board	<i>UV</i>	Ultraviolet (Radiation)
<i>HVJ</i>	High Viscosity Jetting	<i>XML</i>	Extensible Markup Language

# 1. Introduction

Rapid Prototyping was conceived in the 1980s with clear advantages over traditional fabrication methods such as individual product customization, increased complexity of parts at no extra cost and reduction of wasted material. Still, until recently, the actual performance of the additive technologies has not always matched the expectations of industry and consumers, relegating their application to the creation of prototypes and low value products. However, as it is common with digital technologies, the growth has been exponential in the last decades, leading to a situation where the technology is not a speculative approach anymore, which is reflected in its most recent designation, Additive Manufacturing (AM). To get to this point, new methodologies have been developed and older techniques have been improved thanks to a deeper understanding of the fundamental mechanisms behind them. This, together with a reduction in the cost of the systems and easier interfaces, has caused the rapid spreading of these machines in countless fields. Yet, being capable of manufacturing intricate parts in a variety of scales with a single material is not enough for many applications, since some complexity is inevitably restricted by the embedding and assembling of external components. Therefore, the next step for Additive Manufacturing on its way to harnessing its full potential must be the creation of multi-material parts with designed functionality. Particularly interesting is the case of electrical conductivity as a function to introduce into fabricated parts, since successful conductivity between different elements is the base of any circuit, making it crucial to control this property before moving to more sophisticated functionalities and active components. Printed tracks into 3D structures would not only enable the creation of more compact and efficient devices but could also allow the introduction of sensors in many objects, increasing the amount of feedback (i.e. Internet of Things) that we get from them. More importantly, the creation of 3D parts with incorporated functionality will provide more freedom to designers and engineers to create innovative products that are impossible with traditional fabrication.

## 1.1 Additive Manufacturing (AM)

A definition of Additive Manufacturing can be found on the standard provided by the F42 committee of the American Society for Testing and Materials (ASTM) (ASTM International 2012). In this document, Additive Manufacturing (AM) is defined as “a process of joining materials to make objects from 3D model data, usually layer upon layer, as opposed to subtractive manufacturing methodologies.”

Nevertheless, due to the broadness of this definition, many different approaches are possible to follow the common process chain that result in a 3D object, which makes AM a category of technologies instead of a specific process itself. This ambiguity, together with the newness of the mentioned standard, allowed the spreading during decades of alternative terminology such as Layer Manufacturing (ASTM International 2012), Freeform Fabrication (ASTM International 2012), Rapid Prototyping (Chua et al. 2010), Direct Digital Manufacturing (Gibson et al. 2009) and, more recently, 3D Printing, despite all these having slightly different implications.

In this work, Additive Manufacturing will be the preferred term, and the different technology families contained within AM will be referred, according with the ASTM standard, as follows:

- **Binder Jetting:** Droplets of a liquid bonding agent are selectively deposited to agglomerate powder materials.
- **Directed Energy Deposition:** An energy source (typically a laser or an electron beam) is focused to fuse materials by melting as they are deposited.
- **Material Extrusion:** Fluid material is dispensed through a nozzle to form the desired patterns.
- **Material Jetting:** Discrete droplets of build material are deposited and solidified to create 3D parts.
- **Powder Bed Fusion:** Regions of a powder bed of material are selectively fused by the application of thermal energy.
- **Sheet Lamination:** Sheets of material are cut and bonded together to form a 3D object.
- **Vat Photo-polymerization:** A liquid photopolymer is cured by light-activated polymerization to induce a phase change and build an object layer-by-layer.

While the different systems comprised under the AM banner are dissimilar from a technical point of view, they all follow the idea of layered fabrication and usually share a similar process chain that can be simplified in eight key steps (Gibson et al. 2009).

- **Design stage:** The concept of the part to be fabricated need to be transferred to a Computer Aided Designed (CAD) file. This can be done by direct input of the user or by reverse engineering techniques such as 3D scanning and the corresponding “point cloud” treatment (Tuck et al. 2008).
- **Conversion to .STL:** The .STL file format (derived from STereoLithography, the first commercially available AM system from 3D Systems (Gibson et al. 2009)) is one of the most common file extensions used by AM and is essentially a simpler triangle-based version of the geometry contained in the CAD file. The conversion from CAD to STL is automatic in most 3D CAD software packages, but some discontinuity errors may occur that need to be addressed by external STL repair programs.
- **Manipulation of .STL file and transference to AM system:** Once the .STL file is ready and the part has been checked with a visualization tool, it is time to perform final manipulations such as scaling, rotation and positioning on the virtual building volume of the additive system to allow different objects to be created at once.
- **Machine set-up:** The .STL file does not contain machine-specific commands; therefore, one final file conversion is required to set parameters such as layer width or building trajectories. These decisions heavily affect the quality of the generated part.
- **Object building:** After completing the previous semi-automated steps the system is ready to build the part without further human input.
- **Part clean-up:** This stage varies greatly from one AM technique to another but in all cases it aims to take the part from the building area and remove any support structures that the system needed to generate in order to complete successfully the geometry of the object. This step may involve manual manipulation and can affect deeply the quality of the product.
- **Post-processing:** It depends both on the particular AM technique used and intended application of the part. As the previous step, it usually involves manual manipulation.
- **Application:** The part is ready to be used. It is noteworthy that even though some materials used in conventional manufacturing can be also used in AM, their behaviour may differ.

Apart from the common approach and process flow, it is possible to identify some shared characteristics that help to understand the relevance of AM. For instance, since the use of moulds or additional tooling is not needed in these processes, AM allows the creation of more complex structures with fewer limitations imposed by the fabrication method itself, which leads to greater design freedom and plays a decisive role in the product development cycle (Hague et al. 2003). Furthermore, these additive systems allow easy customization of individual pieces at no extra cost, which remove the need of fabricating a large number of items in order to amortise production costs (Tuck et al. 2008) and enables the production of different components simultaneously in the same facility (Ruffo & Hague 2007), which eventually may lead to alternative business models to develop. In addition, the local aspect of this approach presents other advantages over traditional manufacturing such as reduced transport costs and the possibility of implementing virtual storage of products instead of using physical warehouses (Wohlers 2008).

Additive Manufacturing systems are not exempt of limitations and, although there has been noticeable progress in recent years, these technologies generally need to improve aspects such as process speed, surface finish, repeatability and dimensional accuracy to broaden their applications in industry. Also, the spectrum of available materials is still narrow compared with the possibilities that other manufacturing methods offer and their properties are not always comparable in terms of performance. Besides, most of the current AM systems are only capable of dealing with one material at a time, which restricts the final functionality of the fabricated piece and forces the use of additional steps and fabrication methods. It is precisely this last limitation which is addressed in the present work through the study of conductive materials compatible with AM and the creation of a hybrid approach capable of dealing with different ranges of viscosity.

## **1.2 Manufacturing electronics**

Electronic devices based on semi-conductors are ubiquitous in our society and current trends indicate that they will keep spreading to many more aspects of our lives. The progressive improvement of their performance, reduction of their cost and miniaturization of their size have allowed the integration of millions of

transistors per square millimetre, enabling as many calculations per second, which permit the resolution of complex mathematical problems. In order to achieve such precision and volume of fabrication many multi-step methodologies have been used in the electronics industry, typically involving stages like deposition, removal, patterning, and modification of electronic materials (Parekh et al. 2015), extensive reviews of these technologies can be found in the literature (Madou 2011). Figure 1 describes the process of photolithography, one of the most extended techniques in industry. Despite the effectiveness and high resolution of this method it has some disadvantages such as the intrinsic 2-dimensionality of the process, the limited availability of substrates, the requirement of specific masks for each design and elevated cost.

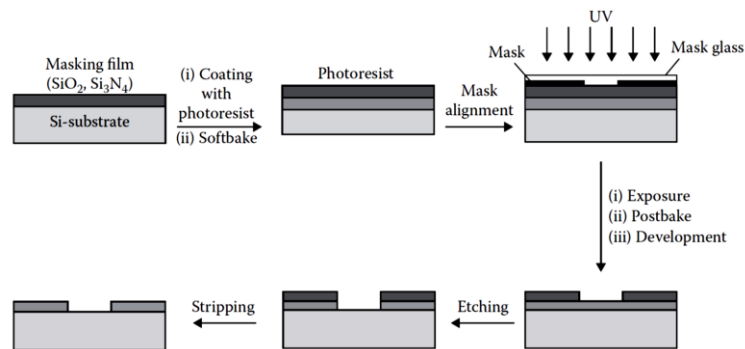


**Figure 1:** Schematic process of photolithography showing the different manufacturing stages required to create a flat deposition of metal or semiconductor materials. Figure from (Parekh et al. 2015).

The cost of traditional manufacturing techniques and the limitations that silicon wafers impose to the mechanical and optical properties of the final chip motivated the exploration and use of alternative fabrication methods. One of these efforts consists on the adaptation of existing technologies, mainly from the printing industry, to deposit low-cost conductive materials in rigid and flexible substrates, which is nowadays referred as Printed Electronics and has become an area of active research (Suganuma 2014). Techniques such as screen printing (Shin et al. 2009) and reel-to-reel flexographic printing (Deganello et al. 2010) have been successfully used to produce electronic tracks and devices on industrial scales, but their non-digital nature limits the variation of each design in production runs, requiring specific screens or plates for every variation, as it was the case of the masks in traditional photolithography. Therefore, if a unique solution is desired that is capable of depositing accurately conductive materials on a variety of substrates, cost-effectively and allowing freedom of fabrication, a digital technology is required.

Moreover, if the designs being printed are complex and include different layers of conductive and non-conductive materials stacked on top of each other, AM would allow the reimagination of many flat circuits, potentially increasing their efficiency and packing factor. Furthermore, AM would reduce the waste generated, which in this area are normally precious materials. Also, it can create cost-efficient unique parts, speeding up the design-testing cycle. However, not every AM technology is suitable for the deposition of conductive materials and, more importantly, not all the approaches that do allow the deposition of conductors can also fabricate with multiple materials in a single process. Therefore, a thorough review of current AM techniques and conductive materials was required to find the most appropriate combination to successfully create functional 3D structures.

### **1.3 Contribution of the present work**

#### ***1.3.1 Motivation of thesis***

Following the previous reasoning it seems that the application of AM to the fabrication of electronic components is the next logical step in the evolution of both areas. Thus, this work will study the digital deposition of highly loaded conductive materials with an additive approach to create 3-dimensional and heterogeneous structures. Piezoelectric Inkjet (PIJ) is the manufacturing methodology selected due to its capability of voxel by voxel fabrication, but the viscosity limitations of the jettable inks reduce drastically the properties and functionality of the printed tracks. Therefore, a high viscosity approach would allow the deposition of a wider variety of materials, increasing the potential of inkjet as a fabrication tool. In the present work, high viscosity jetting (HVJ) is explored using commercial micro-dispensing valves that combine mechanical and pneumatic actuation. However, since the size of the deposited drops by these valves is bigger than in PIJ and they are single nozzle devices, a hybrid system capable of using both dispensing types was developed. This resulted in a system able to deposit and process a wide range of materials without abandoning some of the characteristics that make jetting a technique so powerful, such as the ability of mixing materials or the possibility of printing on a variety of substrates without contact. The development and exploration of this system, along with the characterisation of multiple functional materials, allowed the extraction of valuable general conclusions that can help to push this approach further in the future.

### **1.3.2 Novelty of Research**

From the literature review, it can be concluded that there is no system to date that presents all the following features in a single process:

- **Multiple dispensing elements** to deposit functional and structural materials in 3D. A **voxel by voxel** approach with resolution in the micro-range is required to harness the full potential of digital fabrication.
- Capability of using **different types of printheads** to allow for the deposition of a wider range of materials, especially regarding viscosity.
- Capable of **reading digital files**, **slice** them into individual layers and find a suitable and **optimised path** to deposit the drops in the minimum possible time.
- **Integrated post-processing capabilities** for different materials such as UV-curable polymers, solvent-based fluids and metallic nanoparticles that require sintering.
- **Integrated vision system** to calibrate the printheads, align the printing patterns and inspect the results.

Consequently, the design and implementation of such a system is by itself a novel achievement, since it would allow the creation of complex 3D multi-material structures on a voxel by voxel basis mixing materials with very different rheological properties. The novelty of this PhD concerns the ability and understanding to co-print high and low viscosity functional materials using HVJ and PIJ in a unified AM tool. In addition to the development of the apparatus the performance of the system has been studied and quantified in relation to printability windows and functional applications.

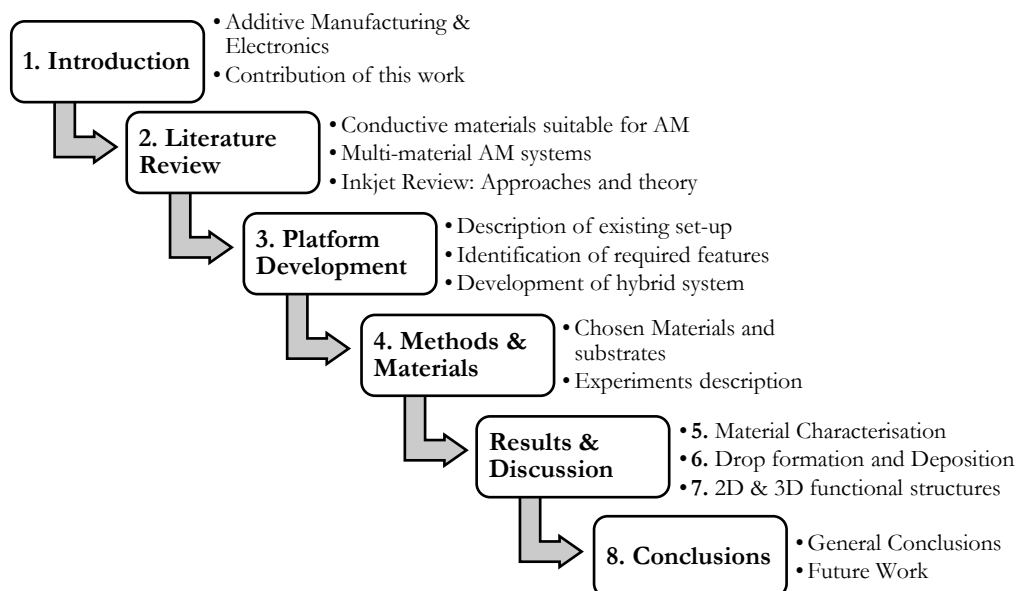
### **1.3.3 Aim and objectives**

The aim of this project is to fabricate functional 3D multi-material samples in a single additive process. The approach selected is the digital co-deposition of materials with different functions and physical characteristics. To achieve this, the following technical objectives need to be met:

- Identify **desirable** and **critical features** for a multi-material system capable of dispensing materials with different properties. A digital fabrication approach is preferred to allow the creation of complex patterns. This review needs to include the post-processing required for certain functional materials to activate their properties.

- **Design, develop and calibrate** a manufacturing system fulfilling the requirements previously recognised. This includes the definition and implementation of a clear **printing strategy** capable of dispensing and processing the materials in an efficient way.
- Characterise the **physical and electrical properties** of the fluids involved in the process that can affect their printability and functional performance. These properties include but are not limited to: density, shear viscosity, surface tension, particle size and electric resistivity.
- Test and optimise the **printability** of the selected materials on the developed system. The discussion of their behaviour should be performed in terms of **dimensionless numbers** and **processing windows** to facilitate the comparison of the results with established technologies such as piezoelectric inkjet printing (PIJ).
- Study different **post-processing** treatments to polymerise, dry and sinter the printed materials within the same apparatus. Parameters such as the geometry or electrical resistance of the deposited films can be used to assess the applied post-treatments in terms of the functionality of the produced samples. Furthermore, since the present work is based on a layer-by-layer approach, the speed of the post-processing of each layer should be considered to reduce the length of the overall process.
- Use the knowledge about the selected materials and the developed system to build **proof-of-concept parts** displaying high manufacturing freedom and internal electronic tracks.

### 1.3.4 Thesis structure



## 2. Literature Review

The first step to achieve the objectives was to perform a literature review to identify the state-of-the-art in the areas of **conductive materials** compatible with Additive Manufacturing and the most promising **multi-material** approaches tested to date. Later, piezo-actuated **inkjet (PIJ)** printing is identified as a suitable manufacturing technique for multi-material parts and is consequently reviewed, emphasizing on the alternative set-ups capable of depositing high viscosity fluids with the intention of improving the performance of the printed parts. The main scientific fundamentals behind the jetting mechanism and its different stages are covered in the last section.

### 2.1 Conductive Materials compatible with AM

The following section presents a review of the most promising conductive materials for AM. The classification is made based on their properties and divided into three categories: metals, organic compounds and composites, as it is shown in Figure 2.

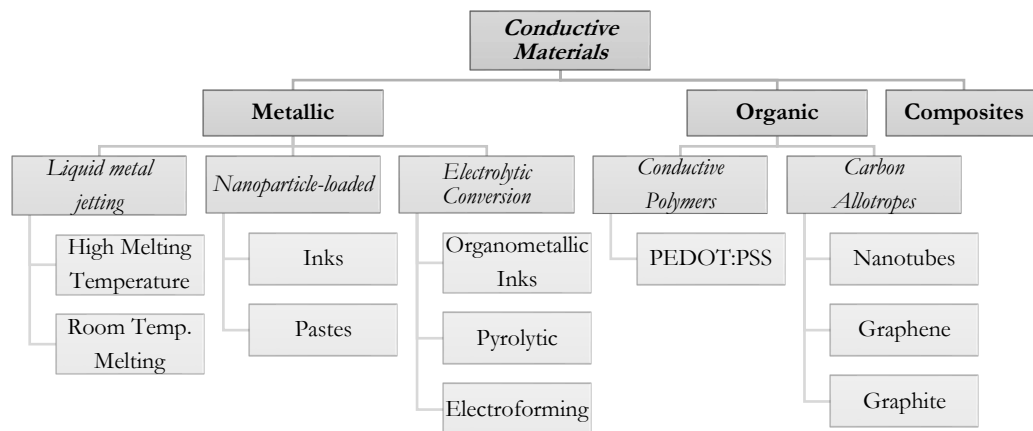


**Figure 2:** Classification of conductive materials compatible with Additive Manufacturing covered in this chapter.

#### 2.1.1 Metals

Metals are the most obvious choice when electrical conductivity is required due to the known capacity of their valence electrons to become conduction electrons, which can move freely around the whole structure with small resistance (Kittel 2004). It is also common for metals to display good thermal conductivity and appealing mechanical properties. Consequently, the use of metal has evolved along history, leading to several established production processes such as forging, moulding or machining. However, with the emergence of AM, new possibilities have opened up and much interest has been

attracted back to this field, which is leading to a strong presence of these methods on the fabrication of prototypes and parts (Wohlers 2008). Most of these established methods rely on the selective agglomeration or sintering of metallic powder on a moving stage using varied active elements such as a high power laser (Das et al. 1998), a focused electron beam (Ackelid & Wallgren 2010) or a jetting head dispensing a polymeric binder (Emanuel M. Sachs, John S. Haggerty, Michael J. Cima 1993). However, the interest for this work is to find a way to selectively deposit only small amounts of conductive material along with other non-conductive materials in a voxel by voxel approach. Therefore, direct deposition techniques such as extrusion or inkjet are preferred.

### 2.1.1.1 Liquid metal jetting

#### Pure metals

Most of the systems based on the ejection of liquid metal rely on a crucible to melt the raw material at high temperatures before it is forced to flow through a nozzle by different actuation methods such as piezoelectric, hydraulic or magnetohydrodynamic. This is possible mainly because most metals display relatively low viscosities when they are in their liquid form, and therefore can be jetted (Priest et al. 1997).

**Piezoelectric** printheads are one of the oldest and most extended approaches for metal jetting (Priest et al. 1997). Its working principle is based on the forced break-up of a column of fluid emerging from the nozzle. This set-up has been widely used with low melting point metals such as solders (Priest et al. 1997), however, thanks to the improvement on the thermal resistance of the piezoelectric elements it has also been applied on the ejection of aluminium alloy (AA2024) at processing temperatures near 800 °C to achieve solid parts (Orme et al. 2000), as is shown in Figure 3. Analysis showed that both the composition and the specific gravity of the printed metal were consistent with the bulk material. However, there is still room for improvement in terms of surface finish, deposition accuracy and overall resolution.

Another actuation mechanism that can be used to generate droplets of molten metal is the one known as the **StarJet method** (Tropmann et al. 2011). In this case, a pneumatic system is used in combination with a silicon star-shaped nozzle accurately constructed via MEMS fabrication to create stable droplets, as is shown in Figure 3. In this case, both continuous inkjet and drop-on-demand can be achieved, with droplet sizes as small as 60 µm (Lass et al. 2013).

The third alternative method to control the droplet generation relies on a **magnetohydrodynamic (MHD) valve** (Figure 3) and, in essence, it forces the charges on the molten metal to move on the influence of a magnetic field, which creates an ejection force (Lorenz force) on the transversal direction of the printhead (Suter et al. 2012). Despite the attractive simplicity of this system, it needs to improve its droplet deposition mechanism and its range of working temperatures (it was tested with tin at an effective temperature of 300 °C) to find further applications in AM.

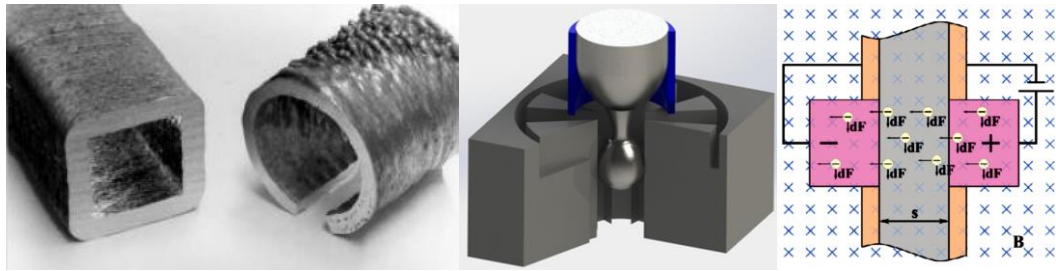


**Figure 3:** **Left)** Preliminary components fabricated with Precision Droplet-based net-form Manufacturing (PDM) (Orme et al. 2000). The pieces were longer than 10 cm and display geometric defects due to the inhomogeneous heat flow on the pieces. **Middle)** Schematic structure of a MEMS-fabricated nozzle chip typical from the StarJet method (Lass et al. 2013). A gas flow can be set through the star shaped channels to inhibit oxidation and control droplet break-up. **Right)** Schematic structure of a MHD pump (Suter et al. 2012), where  $B$  is the magnetic field perpendicular to the page and  $s$  is the distance between the electrodes that maintain the electric field. The charges are accelerated and the fluid is jetted in the direction of the nozzle due to the Lorenz force.

In theory, these approaches provide high density parts with no organic residue and do not require a sintering step within the process flow, which improves their speed and mechanical properties. However, they present some common limitations such as the oxidation of the metals, which affects both their electrical conductivity and wetting behaviour, leading to a loss of repeatability and nozzle clogging (Suter et al. 2012). This can be partially solved by placing the jetting head into an inert atmosphere or vacuum (Suter et al. 2012) but complicates the set-up. Furthermore, the high temperature needed to melt the metals and the requirement for the deposited droplets to re-melt a thin film of the previous layer to ensure proper adhesion and homogeneous properties (Michaelis et al. 2007) (Orme et al. 2000) strongly limit the materials that can be involved in the process. This thermal limitation discards the possibility of using most polymers, which collides with the multi-material objectives of this work.

### Low melting point alloys

In case that the mechanical properties are not the main concern, metals or alloys with lower melting points such as Gallium, Indium or Tin can be used. For instance, a binary eutectic alloy of gallium and indium (EGaIn, 75 wt% Ga 25 wt%) with melting point of 15.5 °C was deposited with a syringe needle without further heating to produce

self-standing conductive structures (Ladd et al. 2013). This was possible due to the passivation nanometric skin that the alloy formed due to oxidation upon exposure to air. Complex structures such as vertical wires, arches and cubes were achieved by controlling the gauge pressure and the translation speed of the needle, as can be seen in Figure 4. The same eutectic alloy was also used following a micro-contact approach to create parts with a resistivity of  $3 \cdot 10^{-7} \Omega \cdot \text{m}$  (Tabatabai et al. 2013). Nevertheless, due to its liquid form, additional actions need to be taken to deposit these alloys accurately on substrates to form 3D patterns. The most common approach to this problem is to encapsulate the liquid alloy in micro-channels that provide the required structure (Dickey et al. 2008), but this limits the freedom of fabrication due to the introduction of an additional process step and the requirement of connectivity between channels. Therefore, other approaches such as tuning the viscosity and surface tension by controlling the oxidation of the metals during a stirring process have been successfully demonstrated (Gao et al. 2012).

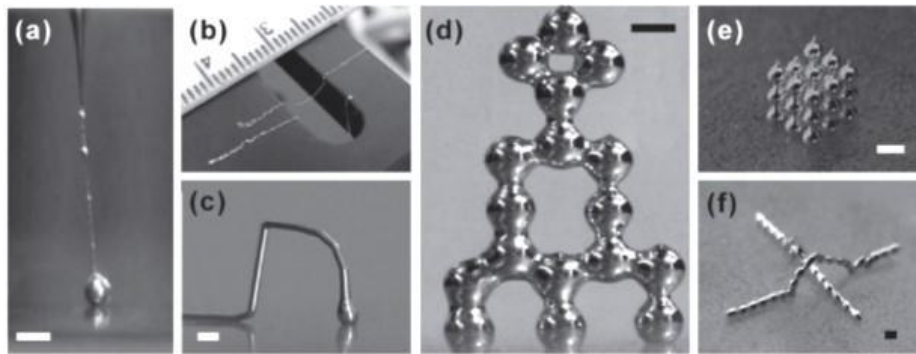


**Figure 4:** Structures created at room temperature following a Direct Write approach and using a eutectic alloy of gallium and indium. All scale bars are 500  $\mu\text{m}$ . **a)** Thin wire produced by fast metal ejection. **b)** Fibres suspended over a gap. **c)** Free-standing metal arch. **d)** Tower formed by several droplets. **e)** Cubic array. **f)** Wire and arch showing the 3D capabilities of the system. Image from (Ladd et al. 2013).

To improve the mechanical integrity of the materials and prevent liquid leaks it is possible to modify the composition of the alloys to increase their melting point out of the room temperature region and allow their solidification after being jetted in their liquid form, which is a typical approach for low-temperature solders (Mei et al. 1996). This modification of the composition can be performed changing the proportion of the alloy components to move away from the eutectic point or by adding new species to the mixture. This last option can potentially be exploited to also decrease the overall resistivity if the chosen dopants are also good conductors, as it is the case of the Ag-Ga (Baren 1990) and Au-Ga (Elliott & Shunk 1981) systems.

There are a few aspects that may discourage the use of low melting temperature alloys on nozzle-based systems. Firstly, gallium-based alloys have generally shown values of surface tension on the order of 0.5 N/m (Morley et al. 2008), which is high compared with conventional inkjet inks and can cause processing problems with this approach (Zheng et al. 2014). Also, the fast oxidation can create jetting issues in the printhead while the material is idle in the nozzle, which is expected to lead to low process repeatability and blockages.

### **2.1.1.2 Nanoparticle-loaded inks and pastes**

One way to selectively deposit metal without melting it beforehand is using jetting systems with inks based on metallic nanoparticles. This does not eliminate the need of melting or sinter them together to achieve conductive tracks, but allow their processing at much lower temperatures than conventional jetting liquid metal. For instance, following this approach it has been shown that silver nanoparticles have been sintered at temperatures as low as 80 °C when the melt-temperature of the bulk material is 960°C (Perelaer et al. 2008). This advantage is based on the depression of the melting point that most materials display when they are in nano-scale form, which is attributed to their high surface-to-volume ratio (Borel 1981) (Moon et al. 2005), where superficial atoms are less bounded to the body than the internal ones. However, this suggests that the main parameter is the curvature and not specifically the size, which explains why these reduction in the melting point is less relevant on flat nanoparticles (Perelaer 2012).

Although it is possible to print with nanoparticles of almost any material, silver and copper are the most common choice when electrical conductivity is desired. The former not only is one of the less resistive non-manufactured materials ( $1.617 \cdot 10^{-8} \Omega \cdot \text{m}$  at 25 °C) (David R. Lide 2005), but its oxide is also conductive (Sutter 2012). However, due to the high cost of silver, it has been substituted in some situations by copper (B. K. Park et al. 2007), which shows also low resistivity ( $1.712 \cdot 10^{-8} \Omega \cdot \text{m}$  at 25 °C) (David R. Lide 2005), but oxidizes rapidly in contact with air and reduces its conductivity. However, the properties of the printed tracks have not yet reached the same values as bulk metals due to pores, imperfections and impurities (Sridhar 2010). Among the impurities it is necessary to include all the additives that are added to improve process-related properties such as flowability, adhesion or shelf-life. Some of these organic components are eliminated during a thermal treatment but residues are often left behind.

Furthermore, specific processes impose additional restrictions on the materials that can be deposited. Inkjet printing is a good example of this, since it can only effectively eject fluids with viscosities typically below  $40 \text{ mPa}\cdot\text{s}$  (Magdassi 2010). The reason for this will be discussed in future sections but the consequence is that the solid loading tends to be very low in comparison with the whole volume of the ink. Conversely, for dispensing processes with more flexibility in terms of viscosity, such as screen printing, direct writing or robocasting, higher solid content materials can be found. These concentrated versions of the previously described inks are commonly known as **nano-pastes** and can reach particle loadings higher than 80 wt% (Ahn et al. 2009). Apart from the reduced volumetric shrinkage that they experience, another immediate consequence of the high solid content of these dispersions is the drastic change in their flow properties. Specifically, the overall viscosity increases, which requires higher pressures to deposit these materials through a micro-nozzle but also improves the stability of the dispersion, reducing and delaying sedimentation and phase separation. As the material is sheared on the internal walls of the system and ultimately in the nozzle, their viscosity tends to decrease proportionally in a non-Newtonian behaviour known as shear thinning (Barnes et al. 1989), which facilitates deposition. Once the stress is removed, the fluids recover their microstructures, experiencing again an increase in viscosity which, depending on the formulation of the paste, can eventually become the dominating force and stop capillary spreading, leading to mechanically stable threads of fluid that can be stacked on top of each other even before all the solvent has been evaporated. In fact, as the solvent evaporates the threads become more mechanically stable, which can be used in combination of a controlled printing speed to create self-supporting structures directly in 3D without following the layer-by-layer approach (Ahn et al. 2009) (Guo et al. 2013). This property was used to create 3D structures with minimum widths of  $2 \mu\text{m}$  depositing a silver-loaded nano-paste by direct writing which displayed a resistivity of  $5.2\cdot 10^{-7} \Omega\cdot\text{m}$  after 30 minutes at  $250 \text{ }^\circ\text{C}$  (Ahn et al. 2009), as can be seen in Figure 5.

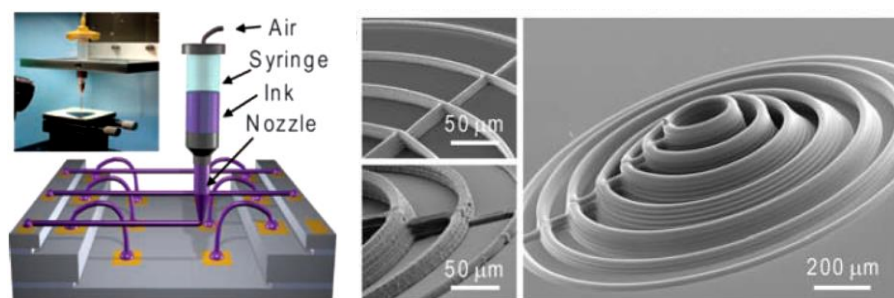


**Figure 5: Left)** Diagram of the omnidirectional set-up used to deposit silver nanopaste by Direct Writing. **Right)** SEM images of multilayer structures created with different nozzle sizes. Images adapted from (Ahn et al. 2009).

**Table 1:** Common post-treatment alternatives to the thermal process

<b>Process</b>	<b>Description</b>	<b>References</b>
<i>LASER sintering</i>	This selective technique is based on the scanning of a laser beam across the areas to be sintered. The great amount of energy deposited in a short time allows rapid heating in very precisely controlled spots.	(Ko et al. 2007) (Bieri et al. 2004)
<i>Flash-lamp sintering</i>	A flash-lamp with high intensity and a broad spectrum is flashed in intervals of approximately 1 ms to induce the photothermal heating of a particular area.	(Yung et al. 2010) (Kim et al. 2009)
<i>Microwave sintering</i>	A train of microwaves is irradiated over a selected area to induce heating due to dipole polarization. The required exposure can be reduced up to 1s.	(Perelaer et al. 2009) (Perelaer et al. 2006)
<i>Electric sintering</i>	A constant voltage is applied through a track with some previous conductivity to induce heat based on the Joule effect. The final resistance of the sintered structure can be controlled regulating the applied current. Both area sintering and selective sintering can be performed if a probe is used to administrate the electric field.	(Allen et al. 2008)
<i>Chemical sintering</i>	In this case, the non-sintered track is put into contact with another substance that has the capability of removing the polymeric stabilizers that cover the particles. This exposes the bare metal and allows the room temperature coalescence of the grains.	(Wakuda & Suganuma 2009) (Tang et al. 2012) (Magdassi et al. 2010)
<i>Solvent evaporation sintering</i>	If only a very small proportion of coating agent is present on the surface of the nanoparticles that are dispersed in a specific solvent, when said solvent evaporates the particles come into contact and can initiate coalescence.	(Wakuda et al. 2008) (Wakuda et al. 2010)

Despite their different concentrations, both inks and pastes have limitations that affect the produced patterns. Some of them are the weak adhesion that most silver inks display on many substrates (Kolbe et al. 2007), the clogging of the printing nozzle when the solvent evaporates too fast (Kamyshny & Magdassi 2012), the discontinuities and cracks that appear after the sintering process (Sutter 2012) or the volumetric shrinkage associated with the evaporation of the solvent (Ahn et al. 2009)(Kolbe et al. 2007). Furthermore, due to the need to remove the organic materials present in the ink to unlock its conductive properties, the thermal post-processing stage is often extended. This can be alleviated by ink formulations with minimal presence of additives and avoiding strong

adsorbing species, as it was shown by Perelaer *et al.* (Perelaer *et al.* 2008), who achieved sintering effects at 80 °C. Another route to solve the same problem was shown by Jung *et al.* (Jung *et al.* 2013) based on the pre-treatment of the nanoparticles to exchange and remove part of the surface ligands covering the nanoparticles. This approach lead to conductive tracks of electrical resistivity lower than  $10^{-7} \Omega \cdot \text{m}$  for processes either at 250 °C during 5 minutes or 100 °C for 1h.

Although thermal treatments based on high temperature furnaces are the most common post-process to induce conductivity in a printed track, there are alternative processes capable of achieving similar results, the most common ones are summarised in Table 1. Most of these processes consist on alternative ways of energy application to the nanoparticles to induce sintering, except the last two, which are based on a different coalescence mechanism that can happen at room temperature. In essence, when the external layer of organic stabilizers is removed, the exposed nanoparticles are left to aggregate, creating multiple surface-surface contacts. Under the right circumstances, an spontaneous Ostwald ripening processes can occur, promoting the coalescence of the small particles into greater volumes, reducing the total energy of the system (Finsky 2004). The removing of the organic coating can be performed by dipping the silver samples, mainly coated with dodecylamine, in methanol at 40 °C for several minutes to achieve a resistivity of  $7.0 - 8.9 \times 10^{-7} \Omega \cdot \text{m}$  (Wakuda & Suganuma 2009). Also, if the coating is predominantly formed by poly(vinyl pyrrolidone) (PVP), a solution rich in chloride ions can be used for 70 min (Tang *et al.* 2012) to obtain a resistivity as low as  $9.91 \times 10^{-8} \Omega \cdot \text{m}$ , as it is shown in Figure 6. Moreover, a solution of polycations (PDAC, 1 wt %) can also be used to induce room temperature sintering, in this case applied over the printed silver samples also by inkjet printing (Magdassi *et al.* 2010).

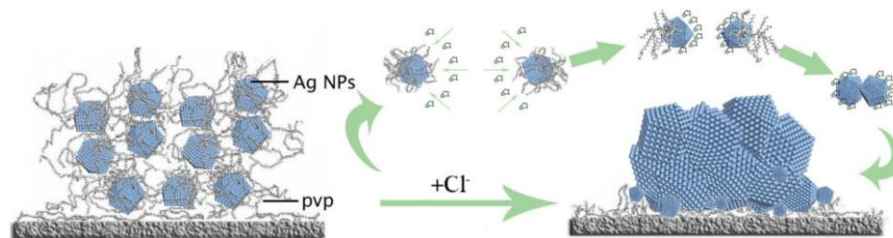


**Figure 6:** Schematic illustration of the chemical sintering process caused by PVP removal by chloride ions at room temperature. Image from (Tang *et al.* 2012)

Some of the alternative methods for sintering show promising results but they require high-power consumption, costly and bulky equipment that would be challenging to implement in a multi-material system that includes other deposition devices for the non-conductive materials. Others, require the use of probes to apply a current (electric

sintering), which is something that can be difficult if a 3-dimensional object is to be built, especially if the conductive elements are embedded and are not in the plane of deposition of the set-up. Finally, chemical and solvent-based approaches can induce acceptable conductivity on the film but there is little information on where and how the organic materials left behind are arranged. More importantly, these processes are not likely to induce sintering between successive stacked layers, which ultimately complicate or prevent completely the transfer of current in the direction perpendicular to the substrate.

In general, nano-particulated inks are a good fit for multi-material printing due to the process freedom that inkjet provides. However, the main drawback of this approach is their low metal content compared with the amount of solvent and additives, which normally result in noticeable volumetric shrinkage after post-treatment, limits the speed of the process and, because more layers are required for a given thickness, subjects the other materials to prolonged heat treatments. A high proportion of these additives are added precisely to reduce the overall viscosity and surface tension of the ink, but these same elements are the ones that need to be removed either by evaporation or decomposition. Therefore, it is expected that removing the viscosity limitations of the deposition system would result in functional improvements. For instance, a reduced presence of surface ligands on the nanoparticles can lead to shorter times and lower temperatures for post-processing (Jung et al. 2013), while a reduction of solvent will limit the volumetric shrinkage (Ahn et al. 2009).

### **2.1.1.3 Electrolytic conversion**

Apart from the direct deposition of liquid metal and nanoparticles, there are alternative systems that use metallic precursor materials that can be converted into metal after or during deposition. This normally presents some processing advantages but limits the achievable solid content.

#### **Metal-organic decomposition (MOD)**

This approach essentially relies on the deposition of an organometallic precursor based on a metallic salt dissolved on a volatile solvent in order to synthesise the desired nanoparticles in-situ instead of creating them prior to printing (Smith et al. 2006). The post-process normally involves temperatures in the order of 150 °C (Smith et al. 2006) to break the organic bonds containing the metallic ions, synthesise the nanoparticles in-situ

and induce their sintering. This approach has yielded track resistivity values lower than 3 times that of bulk silver (Mei et al. 2005) (Smith et al. 2006).

This approach presents some advantages such as the absence of surfactants, low viscosity, negligible nozzle clogging and a potentially high level of chemical stability. Also, even though most groups focus on gold (Molesa et al. 2003), silver (Smith et al. 2006) (Mei et al. 2005) or copper (Cuk et al. 2000) due to their low electric resistance, it can in theory be performed with most metals. However, the fraction of metal that can be deposited with this technique rarely exceeding 20 wt% of the ink (Kamyshny et al. 2011) (Magdassi 2010), this leads to long processing times for thick samples and high energy consumption due to the need of processing more layers of material. Additionally, since the concentration of synthesized nanoparticles is low, they are easily carried by internal flows in the solvent, which can cause inhomogeneous deposition.

It is noteworthy that recent work has demonstrated the creation of crystalline silver from organometallic inks in a sinter-free process that does not create intermediate nanoparticles (Black et al. 2016). The formulation consists on a mixture of organometallic salts and alcohol as a catalytic reducing agent, which results in very thin films of silver at processing temperatures of 120 °C with electric resistivity of 39.2 % that of bulk silver. This novel approach eliminates some of the drawbacks associated with this type of inks and allows a viable way of printing functional electronic tracks at relatively low temperatures, however, for the moment it has only been demonstrated with silver and it is unclear if the method can be extended to other functional materials.

### **Pyrolytic conversion**

Another way of depositing metal without having to melt it beforehand is the so called **Pyrolytic Printing** (Oosterhuis & Feenstra 2008). Droplets of a solution of a precursor salt (Silver Nitrate ( $\text{AgNO}_3$ ) in this case) are ejected by a piezoelectric printhead into an inert gas stream surrounded by an in-flight furnace (Figure 7). The furnace heats the droplets up to 450 °C, which induces the evaporation of the solvent and the pyrolytic conversion of the salt into molten silver. An accuracy of deposition better than 5  $\mu\text{m}$  can be achieved thanks to the aerodynamic focusing system -together with a free-standing column of 2 mm height and 20  $\mu\text{m}$  in diameter (Oosterhuis & Feenstra 2008).

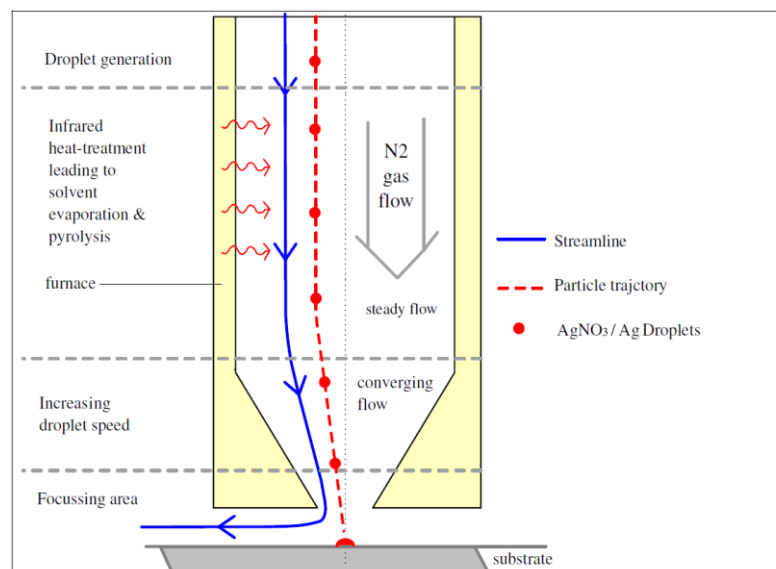


**Figure 7:** Overview of a pyrolytic system that jets droplets of metal precursor into a focusing stream surrounded by an infrared furnace. The droplets are converted into metal in-flight, melted and deposited on a substrate. Image adapted from (Oosterhuis & Feenstra 2008).

Pyrolytic jetting of metals shows promising characteristics in terms of depositing molten highly conductive metals avoiding most of the problems caused by the required high temperatures. However, the heat transfer needs to be performed in-flight, which forces to increase the time-of-flight of the material, reducing its deposition accuracy or transferring a great amount of energy in very short times, which to date it has not been achieved. This incapability of transferring enough energy can also affect the purity of the deposited metal, since the organic components of the metallic salt need to be completely removed to allow good contact between deposited droplets. Also, the system requires a stream of high pressurized air and an in-flight furnace, which make it very difficult to adapt to work together with other technologies to achieve multi-functional parts.

### **Electroforming**

Electroforming is based on the electrolytic deposition of metallic ions from a solution of a salt of said metal over a conductive surface which acts as the cathode of the system when a current is applied. If the size and position of the electrode is controlled, it is possible to create structures by the selective thickening of the deposited layers, which may lead to highly reproducible models without size limitations (Hernández et al. 2013). One way of addressing this objective is by combining a real time modelling application with a device able to rotate and orient the model inside the electrolytic cell (Hernández et al. 2013). However, even though that this system represented an improvement on the uniformity of thickness distribution, it is still in an early stage of development. Alternatively, more direct approaches to three-dimensional electroforming are possible

and have been reported in the last two decades. Li *et al.* (Li et al. 2001) showed that the meniscus formed under the tip of an atomic force microscope (AFM) could be used as a nano-electrochemical cell to selectively deposit platinum on a silicon wafer. Following a similar method in a larger scale, Hu & Yu (Hu & Yu 2010) showed that a micropipette could also be used to create a meniscus of an electrolyte on a conductive substrate in order to deposit different metals, as it is presented in Figure 8. Besides, if the translation of the pipette is synchronized with the electro-deposition rate, self-standing structures of several millimetres can be fabricated. Wires of platinum and copper were fabricated with this method, where the latter displayed overall resistance of  $\sim 3\Omega$  which is barely double the expected value for a Cu connector of the same geometry (Hu & Yu 2010).

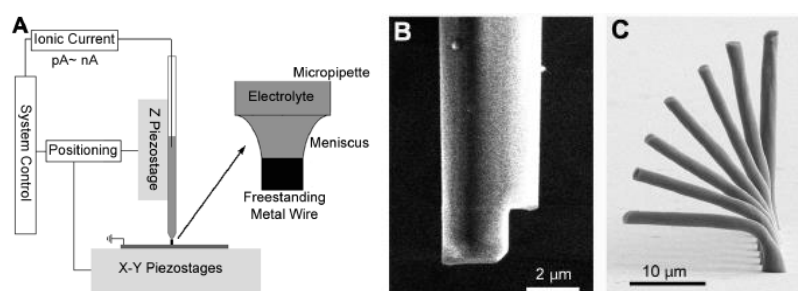


**Figure 8:** **A)** Schematic of the set-up for meniscus-confined electrodeposition. **B)** Nozzle modified by Focused Ion Beam (FIB) to achieve better control of the meniscus. **C)** Electrodeposited self-standing copper wires. Image from (Hu & Yu 2010)

Another micro-fabrication technique based on a similar electrochemical approach consists in the use of micro-channelled atomic force microscopy (AFM) cantilevers with an aperture at the tip that dispenses the metal salt solution on demand (Gabi et al. 2009). Localized electroplating is possible when the cantilever is immersed in a 3-electrode electrochemical cell, since under sufficient cathodic potential the electroplating would only happen under the tip as it is explained in Figure 9. Combining this dispensing system with an appropriate 3D stage it is possible to produce metallic structures in a layer-by-layer approach, controlling their growth in-situ by the monitorisation of the cantilever deflection (Hirt et al. 2016). Although electroforming could lead to highly dense and conductive materials without post-process, it is still in a very early stage of development. Furthermore, the requirement of the stage to be conductive to allow the correct application of the electric field to the electrolytic solution it is likely to affect the complexity of the fabricated structures once insulator materials are introduced.

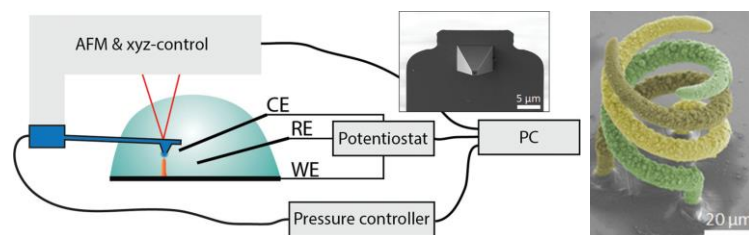


**Figure 9:** **Left)** Schematic of the AFM-based 3D electroforming set-up. The hollow AFM cantilever dispenses the metal ions in a liquid environment under pressure while the structure growth is controlled by the potentiostat, which polarises the substrate to allow the reduction of the metal ions. **Right)** Coloured SEM image of a triple helix structure fabricated with the 3D electrodeposition system. Both images were adapted from (Hirt et al. 2016).

## 2.1.2 Organic conductive materials

### 2.1.2.1 Conductive Polymers

Their working principle is based on the particular hybridization ( $sp^2p_z$ ) of their orbitals (Heeger et al. 1988), which lead to the formation of  $\sigma$ -bonds and  $\pi$ -bonds. The former play mainly a structural role, but the overlapping of the adjacent delocalized  $\pi$ -bonds creates a configuration of energy bands that provide semiconductor properties to these so called conjugated polymers. However, apart from conjugation, charge carriers are needed in order to render the polymers conductive, which is achieved by controlled oxidation with halogens (Heeger et al. 2000). Since their discovery, great development has been done and nowadays there are many available polymers that fulfil the explained structure. Especially widespread use has been reported in the case of polyaniline (PANI) (Jang et al. 2007) and polyethylene dioxythiophene (PEDOT) (Heywang & Jonas 1992) (Yoshioka et al. 2005), both normally found in combination with Polystyrene sulfonate (PSS). Reviews of the field of polymers with electric properties can be found (Heeger 2010) (Weng et al. 2010).

These materials are normally used when the flexibility or transparency of the device is as important as its conductivity, since the achievable resistivity is rarely lower than the metal-based approaches (Perelaer et al. 2010), mainly due to the reduced electron mobility on these polymers compared to pure metals. Specifically, one of the most conductive and widely used polymeric materials is PEDOT:PSS, which presents values of electric resistivity in the order of  $10^{-5}$  -  $10^{-4} \Omega \cdot m$  (Weng et al. 2010) (Löffelmann et al. 2012), which is 3 or 4 orders of magnitude higher than the value for bulk silver. Also, since these materials are normally insoluble (Lee et al. 2000), their processability is considered a drawback for their implementation in AM. However, the possibility of creating dispersions of polymeric nanoparticles in a solvent has helped to overcome the dispensing problem (Jang et al. 2007). In fact, thanks to these adjustments conductive polymers can now be

applied by a variety of methods such as screen printing (Withnall et al. 2011) (Olberding et al. 2014), gravure printing (Kopola et al. 2009), aerosol jetting (Paulsen et al. 2012) or inkjet (Jang et al. 2007) (Weng et al. 2010) (Yoshioka et al. 2005). Still, the solid content in this type of polymeric dispersions is generally low, which can cause noticeable volumetric shrinkage and may result in very thin layers, which ultimately would lead to long processing times if a multi-layer structure is to be fabricated.

### 2.1.2.2 Carbon allotropes

**Graphene** is a promising material that can display high conductivity, transparency and flexibility, which makes it an ideal choice for flexible displays (Bae et al. 2010) and circuits (L. Huang et al. 2011) (Chen et al. 2007). However, in order to reach its full potential and find more applications it requires improvements on processability, stabilization in solution and material purity upon fabrication (Hirsch 2010). Deposition methods need to be improved to allow the in-situ fabrication of single monolayer sheets of graphene instead of placing many micro-flakes, since the contact resistance among plates is expected to cause a decrease in the overall properties. Alternatively, **carbon nanotubes (CNTs)** have been subject of research for longer than graphene, which may explain why more examples of their applications can be found on the creation of conductive tracks and circuits (Kordás et al. 2006) (Small & in het Panhuis 2007) (Denneulin et al. 2009). CNTs have unique properties such as length-to-diameter ratios higher than  $10^8:1$  (Zhang et al. 2013), which facilitates their percolation in combined formulations (Sangermano et al. 2013), and their ability to change their electronic behaviour according with their geometry (Lu & Chen 2005). Formulations based on CNTs do not generally need post-processing because sintering is not required. Also, CNTs can be potentially deposited without many additives but their high tendency of self-aggregation suggest the functionalization of their surface (Islam et al. 2003) (Small & in het Panhuis 2007), which affects the maximum concentration of conductive material into the ink. Moreover, the adhesion of a dispersion of CNTs to typical substrates such as glass is generally not satisfactory without further polymeric additives, which is another reason why the focus on this field has shifted to the investigation of composites of CNTs in a polymeric matrix (Small & in het Panhuis 2007) (Denneulin et al. 2009)(C. Yang et al. 2013) instead of CNTs solutions.

### 2.1.3 Electrically conductive composites and hybrid materials

Several conductive materials have been discussed so far, but there is also the possibility of combining some of them to obtain different characteristics. For instance, the flexibility and adhesion of the formulations can be improved if the solid conductive elements are embedded in a polymeric matrix. Thus, to obtain relevant conductivity with a high presence of organic material the concentration of the filler particles have to be higher than the percolation threshold (C. Yang et al. 2013), which is to say that the particles need to be close enough to interact with each other. The shape of the particles is also decisive, since it has been observed that high shape factors reduce the percolation threshold notably (Sangermano et al. 2013). This has been explored for different high aspect ratio structures such as silver nanowires (Zhang et al. 2011) or carbon nanotubes (Sandler et al. 1999). Alternatively, part or the whole polymeric matrix can be composed by a conductive polymer to enhance the electric conductivity of the composite. For instance, jettable inks formed by PEDOT:PSS/CNTs with sheet resistance of 0,23 – 10,54 k $\Omega$ /sq (Denneulin et al. 2009) and transparent formulations of PMAS/CNTs with 40 k $\Omega$ /sq (4 layers) (Small & in het Panhuis 2007) were reported. An excellent review of composites mixing silver and conductive polymers can be found in Stejskal (Stejskal 2013).

Other properties normally associated with polymeric formulations can also be incorporated to metallic compositions, as it is the case of UV-curing, which is attractive from a processing point of view since it involves lower temperatures than thermal sintering. To achieve this, monomers, oligomers and photoinitiators are added to the functional elements along with other process required additives (Magdassi 2010). Sangermano *et al.* (Sangermano et al. 2013) achieved a resistivity around 5·10  $\Omega$ ·m with a UV-curable ink based on silver nanoparticles (24 wt%) on poly(ethylene glycol) diacrylate (PEGDA).

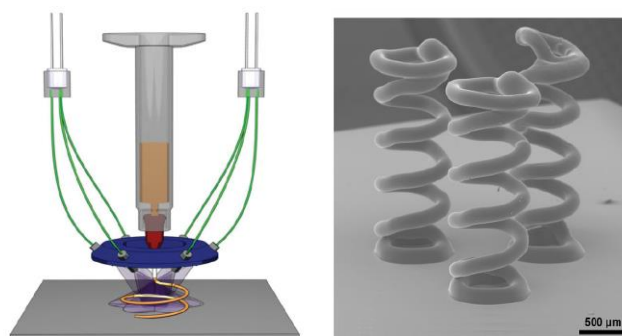


**Figure 10: Left)** Schematic representation of the Direct Writing (DW) tool. **Right)** Conductive microcoils fabricated by UV-DW. Adapted from (Lebel et al. 2010).

The UV-curing approach can also be used with higher viscosity materials, as it was shown by Lebel *et al.* (Lebel et al. 2010). They presented a set-up that combined Direct Writing of a polyurethane/CNTs/silica composite with UV-curing as it is shown in Figure 10. Arrays of micro-coils with a total height of 2 mm and a resistivity of  $\sim 10^4 \Omega \cdot \text{m}$  were created, which is expected to improve with a higher load of CNTs.

## 2.2 Multi-material and Hybrid AM systems

In this section, several AM techniques capable of multi-material deposition are reviewed to understand their possibilities, requirements and limitations. Some of these systems are unaltered AM methods such as extrusion printing or jetting, natively capable of depositing numerous materials. Other set-ups, such as Stereolithography (SLA) or Laser Sintering (LS), required adjustments to enable multiple building materials. Many of the examples are hybrid systems that combine the approaches of different AM techniques to achieve what they cannot do on their own.

### 2.2.1 Laser-based powdered systems

*Laser sintering* and *laser melting* are Powder bed fusion AM processes that require a closed and controlled environment, a container of a polymeric or metallic powder, a system for spreading such powder every layer and a laser to sinter or melt locally the powder. This powder-based nature limits the use of multiple materials and until recently the only relevant examples of multi-material in this area came from parts with controlled porosity that were infiltrated with different coloured dyes after the fabrication by LS was finished (Ming & Gibson 1999). One way to overcome the material variety limitation in this method is to include a vacuum device that removes the powder excess before re-coating the printing surface with a different material (Laappo et al. 2003). Similarly, the powder coating mechanism can be redesigned to dispense different powders in consecutive layers (Ott & Zaeh 2010). However, despite the significance of this modification of a well-established system, this approach would struggle to process many materials that cannot readily be found in powder form. Also, due to the high temperatures attained in the parts and the closed chamber, it would be challenging to embed electronic components to fabricate complex devices. Therefore, this methodology is not suitable for the objectives of this thesis.

### 2.2.2 Stereolithography (SLA)

Stereolithography is a system that falls into the AM category of Vat Photopolymerization and is intrinsically mono-material due to its single reservoir that contains the photo-resins. However, **multi-material stereolithography (MMSL)** based on a rotating carousel holding multiple vats has been reported (Choi et al. 2011), as can be seen in Figure 11. Possible issues with this approach include material contamination due to the successive switching of vats, laser shadowing (previously printed part blocks the laser), surface tension problems and trapped volumes.

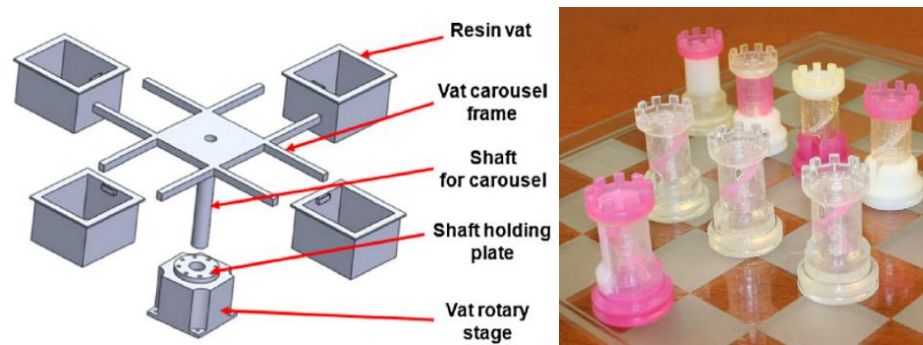


**Figure 11: Left)** Description of the rotating vat carousel that made multi-material SLA possible. **Right)** Examples of multi-material 3D structures produced by this method. Figures modified and combined from (Choi et al. 2011)

A hybrid approach combining **stereolithography and direct printing** of nanoparticle-based silver paste by a micro-dispensing pump was used to create 3D parts with embedded components and electronic tracks (Navarrete et al. 2007)(Lopes et al. 2012), as can be seen in Figure 12. The process required several start and stops and manual manipulation to clean the parts and insert the components but had the pneumatic system integrated in the same rig. Such pneumatic micro-dispensing pump (nScript Inc., USA) can deposit materials with viscosities up to 1000 Pa·s with volumes below the nanolitre. This is possible thanks to the high resolution which the pump can control the pressure of the system, which can provide negative pressure at the end of a pattern before moving. Finally, the SL laser is used to scan over the conductive materials to process them enough for the procedure to continue, but either requires several passes to achieve maximum conductivity or a thermal post-process of the whole part after the fabrication stage is completed.

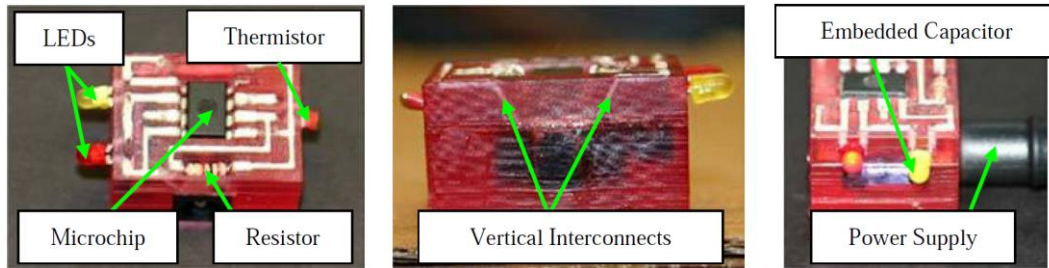


**Figure 12:** **Left)** Printed 3D 555-timer circuit with embedded microchip. **Middle)** Side view showing vertical interconnects. **Right)** Working circuit (note the activated yellow LED). Figure from (Lopes et al. 2012).

This approach is attractive for its capability of depositing conductive materials with high viscosity along with photo-polymers in a controlled way. Also, the possibility of applying a heat treatment within the same system is crucial for a complete manufacturing solution. However, its main limitation comes from the stereolithography process, which requires intermediate baths to eliminate uncured resin, slowing down the process. Also, the micro-dispensing system based solely on pneumatic pressure needs contact with the surface to finish the deposition, which requires either flat surfaces or precise knowledge of their geometry.

### 2.2.3 Cold Extrusion

This category refers to the AM systems that are based on the extrusion of fluid material through a small nozzle by the application of pneumatic or mechanical pressure. The source material is normally a high viscosity paste or slurry but not a solid that must undergo a phase change, as is the case of FFF. Nonetheless, these materials can be heated to modify their flow properties but the temperatures are normally lower than 100 °C. This approach has been intentionally separated from FFF in this review due to the different materials that they can use and the applications where are normally present.

Since extrusion-based systems are technically simple and reasonably low-cost, they are one of the most commonly used forms of AM. Among their numerous and varied applications are the creation of 3D objects with embedded electronics based on the combination of a 2-part silicone and a 1-part silver-filled silicone with an electrical resistivity in the order of  $10^{-6} \Omega \cdot \text{m}$  (Periard et al. 2007). Thanks to the elastomeric nature of the materials the 3D structures with embedded tracks were fabricated and fully cured before placing the electric components by piercing the outer layer of the objects, as it is shown in Figure 13. Following a similar approach, other functional demonstrators such as a LED-based torch with an all-printed push-button and stretchable figures with embedded LEDs were fabricated. Several limitations were identified such as low resolution, volumetric shrinkage, poor electrical contact between cured and uncured silver-filled silicone and relatively high resistivity.

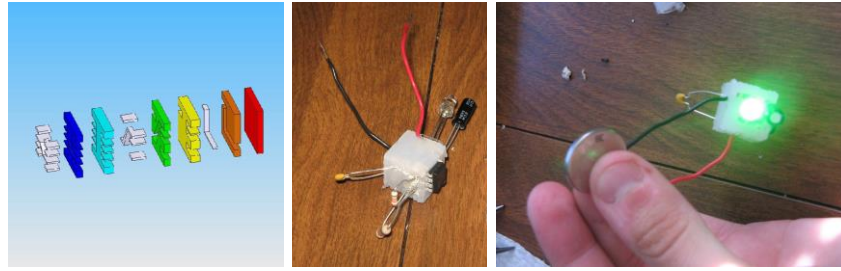


**Figure 13:** Left) Layers required to fabricate a 555-timer circuit. Fabrication was carried out from right to left. The conductive material is shown in white. Middle) Finished part with inserted components. Right) The circuit shows functionality when powered by a 3V battery. Figures from (Periard et al. 2007).

The ability of controllably depositing multiple materials such as hydrogels without the need of heating is the main reason why this technique is widely spread in bio-engineering (Shim et al. 2012) (Billiet et al. 2012). These materials tend to have weak mechanical properties and do not retain their shapes unless cross-linked, which limits the designs and sizes that can be printed with cold extrusion only. This can be partially overcome combining **cold extrusion and Fused Filament Fabrication** (J. W. Jung et al. 2016), where hard frames are printed with an FFF system with bio-compatible and biodegradable materials such as poly ( $\epsilon$ -caprolactone) (PCL), poly (lactic-co-glycolic acid) (PLA), and poly (lactic-co-glycolic acid) (PLGA), as it is described in Figure 14. This mixture of cell-laden hydrogels and thermoplastics was used to fabricate heterogeneous structures of the outer ear, kidney and tooth.

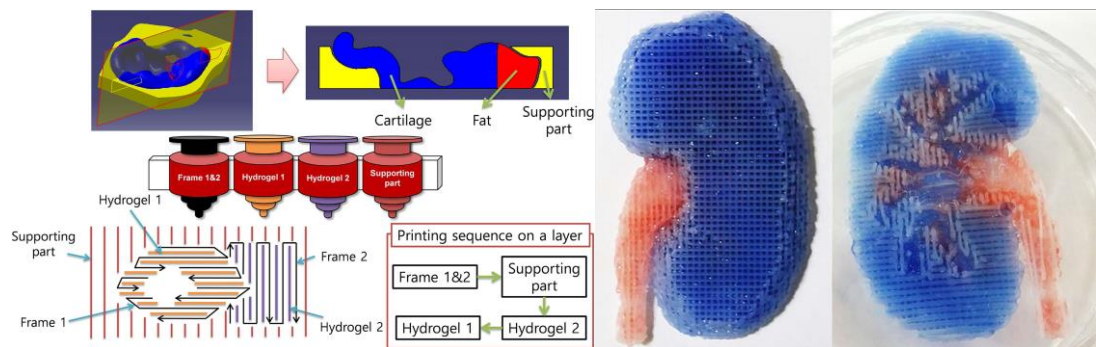


**Figure 14:** Left) Print strategy to fabricate multi-material constructs using 2 tissue parts and support parts required to mimic the native structure. Right) Structure of kidney composed of heterogeneous tissue parts. Figures from (J. W. Jung et al. 2016).

The same ease of scalability of extrusion processes that allow the addition of multiple fluids can be used to create **graded samples** out of a single material. For instance, a system accommodating several dispensing syringes loaded with different concentrations of a chitosan solution was used to create parts with localised functionality (Duro-Royo et al. 2015). To achieve this, a fabrication approach referred as Flow-based fabrication was followed. This consists on a database of tested material properties coupled with a custom algorithm to create a fabrication tool capable of depositing different thickness and

concentrations in different areas of the design, choosing automatically printing parameters such as nozzle size, print speed and pressure. This was used to create several bio-inspired structures displaying designed properties such as flexibility and transparency, as can be seen in Figure 15.

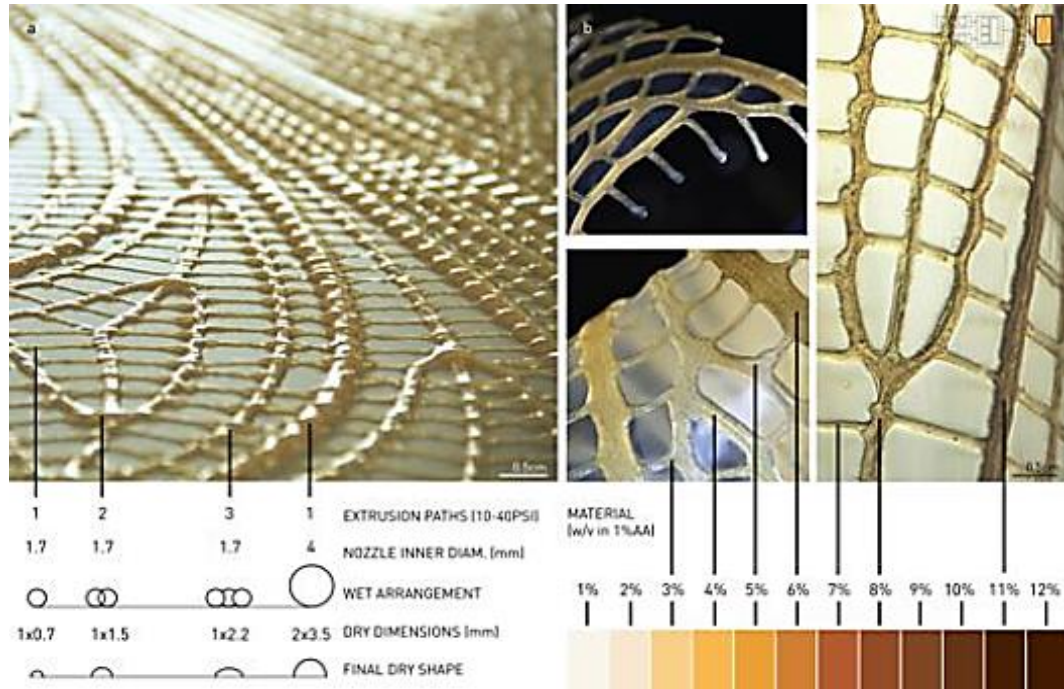


**Figure 15: A)** Example of deposition showing different geometrical features depending on the print strategy. **B)** Different concentrations of a chitosan-based hydrogel in acidic solutions was used to create graded properties. Figure from (Duro-Royo et al. 2015).

## 2.2.4 Fused Filament Fabrication (FFF)

Fused Filament Fabrication (FFF) is another AM technique contained in the category of material extrusion, but in this case the source material is fed in solid form to the heated extruder, which liquefies it and pushes through a small nozzle. Combination of several materials by dedicating an extruder for each of them is common practice. Furthermore, the extruders can be redesigned to accept multiple polymeric filaments and combine them during the process (Taubert 2012) (Corbett 2012), which allows local variation of the properties of the printed parts (Figure 16).

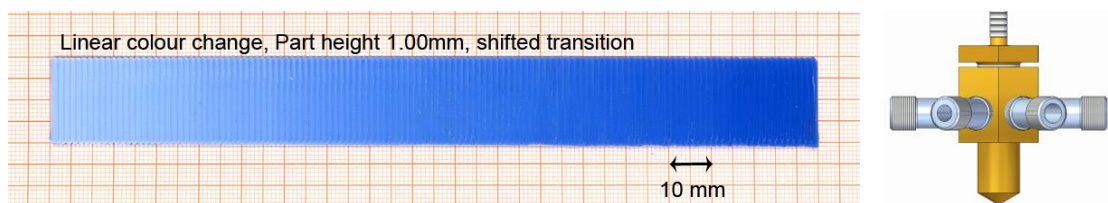


**Figure 16: Left)** Sample displaying a colour gradient obtained by the mixing and deposition of a white and a blue PVA filament using a custom multi-material extruder. **Right)** FDM extruder capable of accepting 4 different filaments and create a mixed output. Figures from (Taubert 2012).

Some of the main characteristics of FFF systems are their low cost and easy customization, since most of them use hardware and firmware based on the Open Source project RepRap (Bowyer 2004) (Jones et al. 2011). The open architecture of these systems allows their combination with many other deposition methodologies. An interesting approach was demonstrated where an FFF system with two extruders was used in combination with an **airbrush** to incorporate conductive tracks to 3D parts, even on non-planar surfaces (Sarik et al. 2012). The main structures were printed in ABS while a soluble mask for the electronic tracks was printed with PLA, then the airbrush is used on top of such mask. The conductive material used was an electric paint based on silver flakes that dried at room temperature.

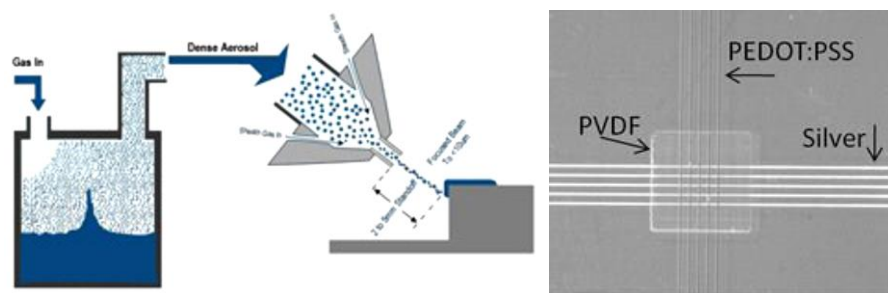


**Figure 17: Left)** Schematic diagram of Aerosol Jet dispensing. The fluids are atomized to create a dense aerosol cloud of 2-5 micron diameter droplets. A carrier gas is later used to transfer the aerosol to the printhead, where a co-flowing sheath gas focuses the drops on the substrate. **Right)** Crossover of 20 micron tracks of PEDOT:PSS and silver isolated by a layer of PVDF dielectric. Figure from (Paulsen et al. 2012).

A similar approach was used by Paulsen et al. (Paulsen et al. 2012) with the notable difference of changing the airbrush for an **Aerosol Jet dispenser** (Optomec Inc., USA), where the material is also atomised but the deposition is under much more control, as it is summarised in Figure 17. The aerosolized material is ejected at approximately 80 m/s onto the surface of the parts without the requirement of contact. This system can deal with viscosities up to 1 Pa·s, which in the case of the discussed study were a dielectric material (Polyvinylidene fluoride) and two conductive materials, namely a high viscosity PEDOT:PSS dispersion and a nanoparticle-based silver paste. The three materials were printed on top of the thermoplastic structures fabricated by FFF to create different circuits (Figure 17) and later treated during 30 min at temperatures as high as 180 °C, enough to dry and sinter the deposited materials but not the thermoplastic structure. However, the cost, complexity and size of these dispensers complicates the adoption of this approach as a multi-material tool.

Another popular process combination is **FFF with one or many cold extruders**, which provides the mechanical integrity of melted thermoplastics and the functionality of custom-designed slurries. Malone *et al.* (Malone et al. 2004) demonstrated the fabrication

of a zinc-air battery with the structure described in Figure 18. This variety of battery is based on the conversion of chemical potential energy between the anode and cathode materials into electrical energy by means of redox reactions (reduction at the cathode, and oxidation at the anode). The printed battery was able to power a small DC brush motor, which consumes about 30 mW (unloaded), for at least 2 seconds. The authors later improved the design and material formulation and produced other batch of batteries, reaching in this case a 10% of the energy density of commercial Zn-air batteries (Malone et al. 2008). However, in this case they only used cold extrusion, changing the ABS for an RTV silicone as a material for the case, which provided flexibility to the design. To explore this property, the authors also created an elongated version of the battery which also worked successfully (Figure 18).



**Figure 18:** **Left)** CAD model of cylindrical Zn-air battery showing its components. **Middle)** Complete printed cylindrical battery. **Right)** Deformable two-cell zinc-air battery printed by cold extrusion. Figures from (Malone et al. 2008).

### 2.2.5 Jetting

Nowadays we generally understand jetting in the context of AM as “material jetting”, the technique that deposits small amounts of material selectively on a substrate, post-process the fluid to solidify it and then continue the fabrication process jetting the next layer. However, until not too long ago the most popular jetting-based AM method was the so called binder jetting or, as it was originally coined, 3D Printing (Emanuel M. Sachs, John S. Haggerty, Michael J. Cima 1993). In that case, the jetting part of the process was essentially the same but the substrate where the liquid was deposited on was a bed of powder (polymeric, metallic or ceramic) that absorbed the fluids, agglomerating and normally changing colour due to the dyes contained on the inks. Alternatively, the part can be later post-processed to sinter the powder to increase its mechanical properties. This could be considered multi-material printing but the local properties of the powder, apart from the colour, are normally the same, which limits the use of this application for truly multi-functional parts.

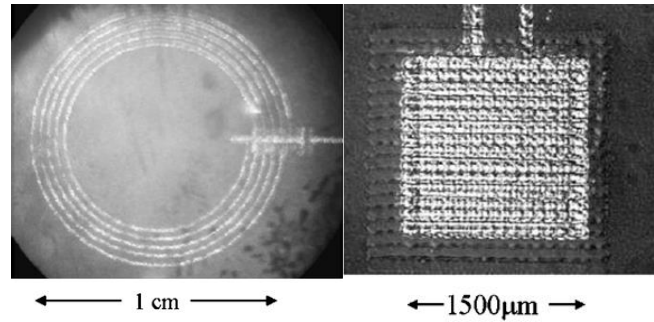


**Figure 19: Left)** A 350-nH inductor showing contact to centre coil thanks to the crossover process including polyimide as an insulator. **Right)** Printed parallel plate capacitor with an average capacitance of 42 pF. Figure from (Redinger et al. 2004).

Material jetting has been used to deposit materials such as polymers (de Gans et al. 2004) (Tekin et al. 2008), metal-based inks (Kamyshny et al. 2011) (Tekin et al. 2008) and ceramic suspensions (Reis & Derby 2000). However, often these studies involve individual materials and only in the last decade multi-material approaches have emerged. For instance, conductive crossovers of silver have been printed with a UV-curable insulator between them (Sanchez-Romaguera et al. 2008). The silver ink had a solid content of 20 wt% and had to be sintered at 150 °C for 10 minutes before displaying a resistivity of  $2.5 - 5.6 \times 10^{-7} \Omega \text{ m}$ . The multi-layered structures were printed with a commercial material printer (Dimatix DMP-2800, Fujifilm Dimatix Inc., USA) with the capability of dispensing a single material, so the cartridge had to be sequentially switched. Additionally, the thermal and UV-treatment were applied externally. Similarly, Redinger *et al.* (Redinger et al. 2004) created several printed multi-layer components for Radio-Frequency Identification (RFID) applications. They used a custom printer based on single nozzle printheads (Microfab Technologies, USA) to deposit gold nanoparticles as conductor and polyimide as insulator to create spiral inductors, vertical interconnects and parallel capacitors, as the ones shown in Figure 19. Both the temperature of the platform and the drop spacing were studied to obtain the most homogeneous films without pinholes. A more recent and complete approach was presented by researchers at MIT with a modular system capable of depositing several different materials simultaneously in a single printer that also features a UV-curing module and a 3D scanner to allow surface characterization and accurate alignment of external objects to be manually inserted on the parts (Sitthi-Amorn et al. 2015). Using this bespoke system together with their own software (Chen et al. 2013) they produced a variety of demonstrators such as microlens arrays, graded materials, multi-coloured objects, fabric-like patterns and proof-of-concept meta-materials, some of them are shown in Figure 20. This system is very promising but it has not yet been tested with conductive materials nor it has a heater module to sinter or cure them. Also, even though it makes the most out of the jetting printheads it cannot avoid their viscosity limitations, which reduce the material catalogue.



**Figure 20:** **Left)** Graded material resulting from the mixing of 2 different inks. **Centre)** Multi-coloured 3D object. **Right)** Proof-of-concept meta-material. Figure adapted from (Sitthi-Amorn et al. 2015).

Most of the jetting systems discussed were custom made or heavily modified, which allowed the researchers to investigate the limitations of the method. However, commercial jetting systems capable of depositing multiple low viscosity photopolymers are available nowadays. Bartlett *et al.* (Bartlett et al. 2015) used a commercial system (Connex500, Stratasys) to create different versions of a combustion actuated-robot to investigate the effect that certain soft parts have on its mechanical performance. Using jetting allowed them to create graded materials with seamlessly transitions between rigid and soft materials. The final design features a rigid core and a soft skirt that allow the robot to jump and land without breaking, as can be seen in Figure 21.

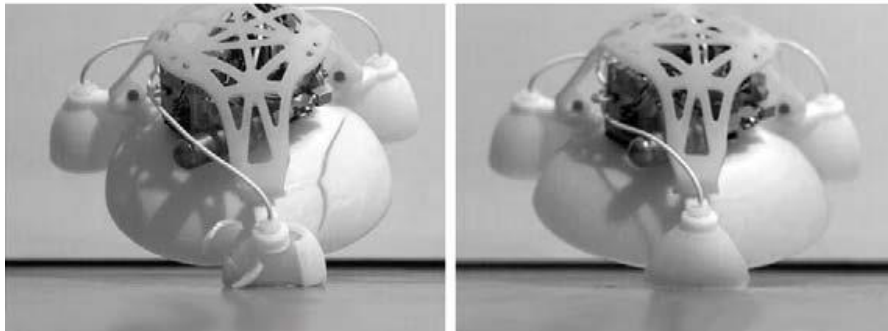


**Figure 21:** Static frames of the landing tests performed under identical conditions for a jumping robot printed fully with rigid material (**left**) and another version of the robot using a graded transition from rigid to flexible (**right**). Figure from (Bartlett et al. 2015).

Another example of complexity achieved by a commercial jetting printer (Connex500, Stratasys) is the research of Bader *et al.* (Bader et al. 2016), where the authors presented a 3D printed fluidic wearable inspired by organic structures with a continuous internal network of biocompatible fluidic channels (Figure 22). The aim is to incorporate microbial communities in these channels to impart biological functionality to the designs. A design environment for geometrically complex parts is outlined as well as a custom slicer algorithm to create the bitmap files fed to the printer.

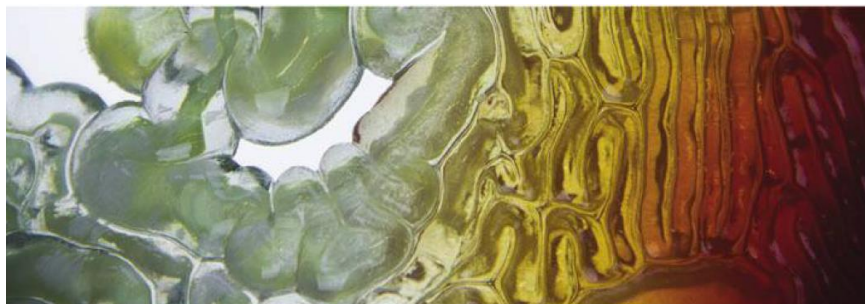


**Figure 22:** Part of an all-printed bio-inspired wearable showing gradients on its optical transparency. This property was later explored as a mechanism to selectively cultivate phototrophs micro-organisms in the clear areas of the inner channels contained along the piece. Figure from (Bader et al. 2016).

All the previous examples show that inkjet printing is already a mature technology capable of accurately deposit a wide range of materials and even combine and grade them to produce truly complex patterns. Also, its non-contact approach allows it to adapt to non-flat surfaces and facilitates its hybridization with other systems. Moreover, its multi-nozzle nature and the modularity of its design means that scalability is relatively easy without complicating the set-up, which means that speeding the process up or adding more materials is generally a matter of adding more dispensing heads. However, its inks are strongly limited by the viscosity that the head is capable of dispense, reducing the solid-content and molecular weight of the materials. Therefore, it seems appropriate to consider a hybrid system that combines the above mentioned positive features of inkjet with a dispensing device capable of depositing high viscosity materials. Consequently, the following sections will provide a deeper investigation at inkjet printing as a technology and will discuss suitable high viscosity solutions to palliate its viscosity limitations.

## 2.3 Inkjet Printing Review

**Inkjet printing** is chosen as the main dispensing system for this work and consequently its various configurations and fundamental mechanisms are reviewed in the following section.

### 2.3.1 *Classification of inkjet systems*

The basic idea behind inkjet printing is the generation and deposition of small droplets onto a substrate to create a specific pattern. This can be achieved by different approaches that strongly influence the characteristics of the final set-up. Particularly relevant is the difference between systems which produce a continuous stream of droplets (Continuous Inkjet) and therefore rely on droplet selection systems to control the deposition and the set-ups that can create droplets only when these are required (Drop-on-Demand). A classification tree of the main inkjet technologies is shown in Figure 23.

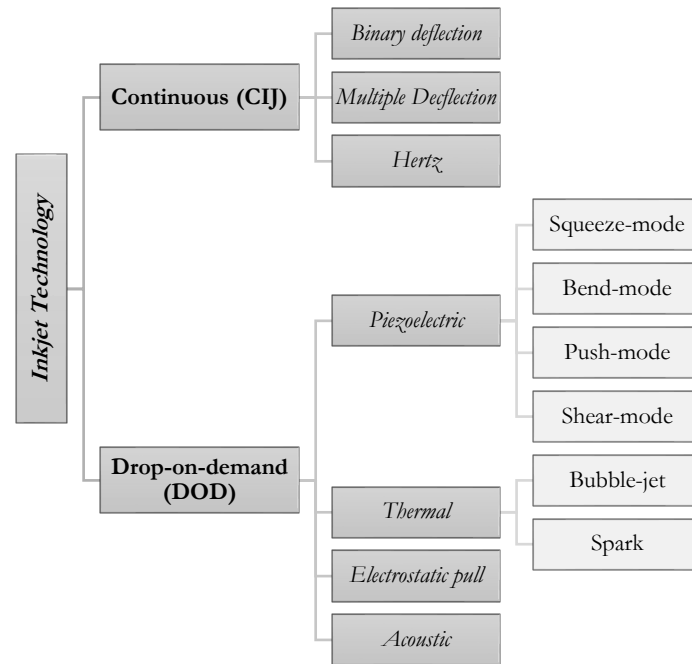


**Figure 23:** Overview of relevant inkjet technologies with different drop generation mechanisms. Adapted from (Le 1998)

In **Continuous Inkjet (CIJ) systems** the material is generally pressurized to push a column of liquid through a nozzle of micrometric diameter. According with the Rayleigh instability (Strutt & Rayleigh 1879) this jet will naturally break up at a certain wavelength defined by its diameter due to the fact that the surface energy of a spherical droplet is lower than the energy of a cylinder of the same volume. However, if a regular disturbance of known frequency is created (generally by a piezoelectric element in CIJ), the break-up phenomena can be tuned to achieve droplets at a particular rate (Martin et al. 2008). Once the train of droplets is started, a method to control their position on the substrate as well as a system to select only specific droplets from the stream are required to achieve complicated patterns. A common way of control these factors is to induce a charge on the droplets right after their creation and then deflect them on flight with an electric field, as is illustrated in Figure 24.

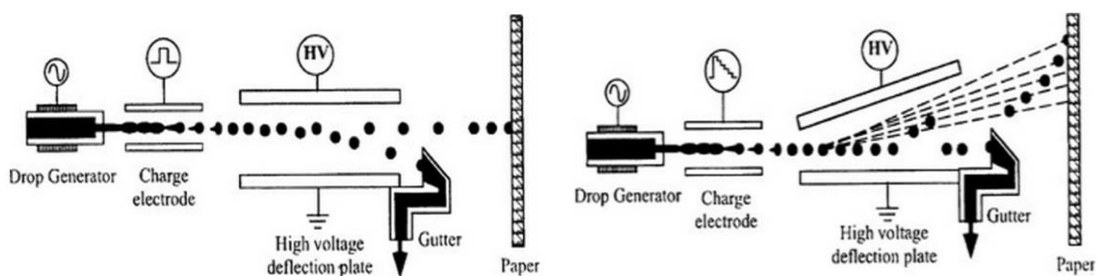


**Figure 24:** Main configurations of Continuous Inkjet. **Left)** Binary-deflection system with constant pulse amplitude. **Right)** Multiple-deflection system with variable pulse amplitude. Images from (Le 1998).

Although, the use of electric fields as a deflecting system is widely used, it has some limitations. For instance, in highly charged streams of droplets the equal sign of their charge may cause electrostatic repulsion between them, which affects the accuracy of deposition. This effect does not typically constitute a problem in conventional CIJ due to the relatively small deflections required and the correspondent low charge imparted to the droplets (Liu et al. 2000) but it has shown to cause printing errors in processes involving highly charged metallic droplets (Liu et al. 2000). Another limitation of the electrostatic deflecting method is that the conductive and dielectric properties of the ink need to be accurately controlled. This imposes some restrictions to the printable materials in CIJ but it can be partially overcome changing the formulation of the ink by adding conductivity salts appropriately selected for the used solvent (Magdassi 2010).

**Drop-on-demand (DOD) systems** are characterized by their drop generation method and do not require additional instrumentation to select individual droplets. One of the most common actuation components is a **piezoelectric element** placed inside or next to the material chamber. Depending on its position and expansion-contraction cycle when a voltage signal is applied, the system is designed as squeeze-mode (Zoltan 1972), bend-mode (Edmond L. Kyser 1976), pushing-mode (Howkins 1984) and shear-mode (Kenneth H. Fischbeck 1986). The schematics of each head type are shown in Figure 25.

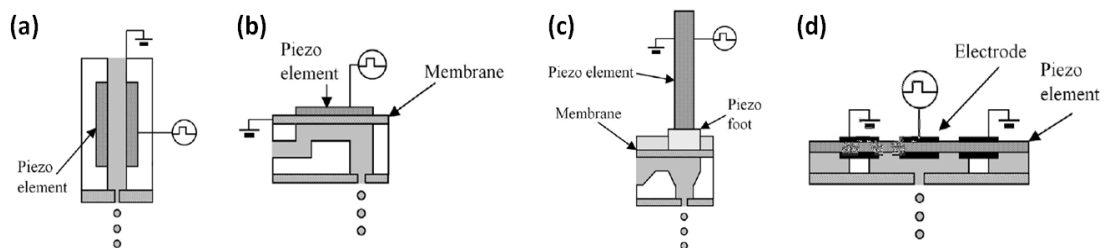


**Figure 25:** Schematic illustration of the most common models of piezoelectric DOD printhead. **a)** Squeeze-mode. **b)** Bend-mode. **c)** Push-mode. **d)** Shear-mode. Adapted from (Houben 2012).

Their working principle is based on a fast signal forcing the piezo-element to modify its shape, which creates a pressure wave that propagates inside the chamber. This wave is reflected on the nozzle and interferes with the original pressure pulse generated by the piezoelectric. The original and reflected signals interfere constructively if the printing pulse is optimised for the specific geometry of the nozzle chamber (Wijshoff 2010) (Bogy & Talke 1984), which results in an amplified wave that helps to overcome the surface tension of the fluid, resulting in the break-up of the jet (Sridhar 2010). This system, since it does not rely on the heating of the ink, has the advantage of allowing a wider range of solvents avoiding degradation issues or explosion hazards.

An alternative way of triggering the ejection is to create a vapour bubble inside the chamber that will create a shockwave when it collapses. In order to create this perturbation there are two main methods, the **bubble-jet** (Hara et al. 1981) and **thermal spark** (Brescia et al. 1985). The former relies on a resistor to heat the ink up to its boiling point while the latter uses a high current to induce vaporization. These approaches have limitations (Morita 2012) such as internal failures due to heat stress, residual gas bubbles inside the material channel, adhesion of debris on the heater or electrode and ink degradation due to excessive heat.

Conversely, **electrohydrodynamic** or **electrostatic pull inkjet** (Winston 1962) presents a different approach which relies on the application of electric fields to achieve higher resolutions without using smaller nozzles and higher pressure (Jang-Ung & Rogers 2012). This set-up uses a metallic capillary nozzle that acts as one of the electrodes of the system, while the substrate is placed on a conductive plate which is normally grounded and situated barely 100  $\mu\text{m}$  away from the nozzle. The material is partially forced out of the nozzle with a pneumatic system under the effect of an electric field. This induces the mobile charges of the ink to repulse each other and accumulate on the droplet surface, which transforms the semi-spherical meniscus into a more instable Taylor cone and allow the generation of droplets smaller than the nozzle to travel towards the substrate (Choi et al. 2008), as it is shown in Figure 26.

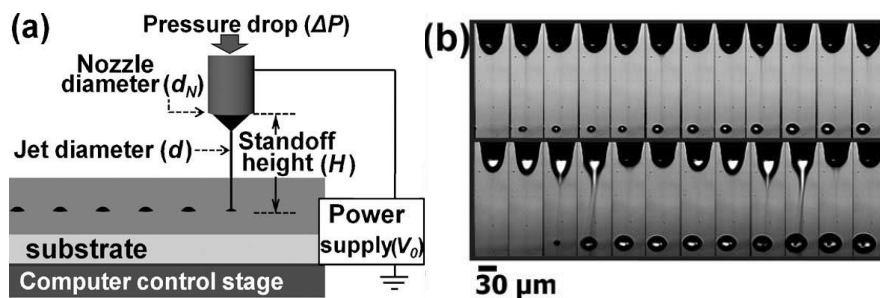


**Figure 26:** (a) Schematic illustration of an electrohydrodynamic set-up. (b) High-speed camera images from 2 different jetting events at  $\Delta P = 0$  (top) and  $\Delta P = 3.45 \text{ kPa}$  (bottom). Images from (Choi et al. 2008).

The resolution achieved by this method is several orders of magnitude higher than other conventional inkjet systems and has been reported to be able to produce discrete dots of 100 nm in diameter when using an aqueous suspension of DNA (Park et al. 2008). An additional advantage of this method is that the material characteristics required for a material to be jetted are not very restrictive and, as Jayasinghe *et al.* (Jayasinghe & Edirisinghe 2004) summarised from recent research on the field, they can be used as long as their electrical conductivity is between  $10^{-13}$  and  $10^{-3} \text{ S/m}$  and their viscosity remains

lower than 150 mPa·s. This versatility allow the jetting of a variety of functional materials both organic (Park et al. 2008) (Sekitani et al. 2008) and inorganic (J.-U. Park et al. 2007). However, this approach has the disadvantage of slow printing output and the fact that the producing droplets are noticeably charged, which can interact between them or with the substrate in an unwanted fashion (J.-U. Park et al. 2007).

A further actuation mechanism is the one behind **acoustic inkjet printing**, which still uses a piezoelectric element to create and control the mechanical perturbations but bases its functioning in a slight different principle than the previously explained. The generated ultrasounds are focused by an “acoustic lens”, which results in the deposit of energy on the free surface of the ink. In the case that this focused energy is higher than the “threshold energy” (heavily influenced by the surface energy) a droplet is generated (Elrod et al. 1989). This droplet generation method does not rely on fluid flowing through a nozzle and is therefore more independent from the viscosity of the ink. However, the accurate control of the fluid level during the jetting process is the main disadvantage of this method (Meacham et al. 2004).

### ***2.3.2 High viscosity non-contact selective deposition***

For conventional piezoelectric inkjet (PIJ), the fluid viscosity needs to be typically below 40 mPa·s to avoid high dissipation of the pressure wave and, thus, be jettable (de Gans et al. 2004). This limitation is also strongly related with the nozzle size and the range of pressures required to force the fluid through it in a stable way and therefore it is not possible to overcome it without changing the working principle involved in the generation and ejection of droplets. Therefore, several techniques capable of depositing discrete amounts of fluids in a non-contact manner with potential to be hybridised with standard jetting are here discussed.

The first technical problem in high viscosity jetting (HVJ) is that, even if a stable jet is ejected through the nozzle, it may not break into droplets following the Rayleigh principle (Strutt & Rayleigh 1879), which calls for an alternative break-up method. This can be addressed by the mechanical segmentation of the jet, as it occurs in the **jet cutter** approach, where a rotating tool cuts a stream of highly viscous fluid in equally sized cylinders that coalesce in flight into drops due to the effect of surface tension (Prüße et al. 2002). This mechanism, however, has drawbacks such as the lack of an integrated drop selection system, the limited deposition accuracy or the loss of material due to the impact of the cutting wires (Prüße et al. 2002). Another way of avoiding issues with the break-up

of a liquid column is precisely avoiding the break-up step and creating directly a stream of droplets via fluid atomization. This approach, usually known as **Aerosol Jet system** (Optomec Inc., USA) (Renn 2006), has as a central element a pressurized chamber that contains the source fluid and permits its atomization by applying compressed air or nitrogen. This creates an aerosol composed of droplets which volume is limited by their own weight, leading to diameters of a few microns (Hedges & Marin 2012). The aerosol is then pushed from the atomization chamber to the deposition head, where a sheath gas focusses it on a substrate that can be from 1 to 5 mm from the nozzle, as it was shown in Figure 17 when it was briefly mentioned in the multi-material section. Besides, the combination of a mechanical shutter on the nozzle and the capability of moving the head in a non-planar way allow the creation of complex 3D patterns. This system can function with a wide range of materials with viscosities up to 2.5 Pa·s (King & Renn n.d.) and is potentially able to produce high resolution features. However, even though a multi-nozzle version of the system is technically possible (King 2014), each different material would require its own dispenser and atomiser unit, which not only increases the cost and complexity of the system but it also reaches a considerable size that makes it very difficult to hybridise with other systems.

Despite the possibilities of aerosol deposition, for some applications the traditional approach involving a stream of individual droplets is desired. One route to achieve this is to opt for an **acoustic printing** device as the ones previously explained, but this is not the only option. Instead, it is possible to use a **micro-dispensing valve** to deposit selectively small amounts of viscous materials using a combination of pneumatic and mechanical actuation to create the required pressure. One version of this approach is proposed and widely explained by Houben (Houben 2012). In summary, this CIJ set-up bases its droplet generation on the focusing of the actuator vibration very close to the nozzle (Houben 2004), which results in the break-up of columns even for high viscosity fluids. To achieve this, the main approach considers a piezoelectric element as the obvious option due to its high performance and flexibility of waveform, which can be used either as the actuator itself or to induce vibration in a flexible nozzle plate in combination with a fixed focus element (Rijfers et al. 2009), as it is displayed in Figure 27. However, due to the relative fragility of the piezoelectric elements, alternative set-ups based on mechanical rotation are also considered in his work. The device is completed by a material vessel externally and constantly pressurized (Houben 2008) and a drop selection system based on electrostatic deflection.

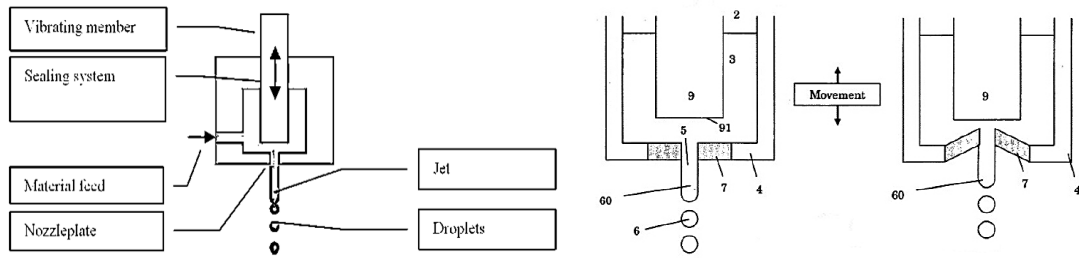


**Figure 27: Left)** Set-up of a microdispensing valve with a moving actuator. **Right)** Schematic illustration of an alternative designed based in a flexible nozzle plate that vibrates in the presence of a static focusing member. Both images are from (Houben 2012).

Alternatively, if a DOD system is required, a different design of valve needs to be used, where the mechanical movement is not restricted to oscillate to create pressure fluctuations but it is also able to physically open and close the nozzle. This is normally possible thanks to the piezo-electric actuation of an internal rod ended in a spherical element with the exact geometry of the inner part of the nozzle plate, sealing the nozzle. This type of valve is the most versatile in terms of the materials that it can deposit, since it does not have special requirements for the fluids. Furthermore, there are reliable and their printing parameters can be adjusted to selectively deposit very small volumes of fluid. Consequently, DOD micro-dispensing valves are selected for the work presented in this thesis and will be described in detail in a future section.

## 2.4 Theory of inkjet and dispensing

The limitation in terms of viscosity that PIJ imposes on the inks and the possibility of using alternative set-ups such as micro-dispensing valves to cover that region of the viscosity spectrum is one of the main concepts behind this PhD. Therefore, the basics of inkjet and micro-dispensing will be covered in this chapter along with some useful parameters that will be used in following sections to evaluate the results obtained experimentally. To complement such a review of the science behind the deposition stage, an introduction to rheology is given, explaining terms such as Newtonian and non-Newtonian fluids, shear and extensional flows and viscoelasticity.

### 2.4.1 Fundamentals of rheology

Rheology is the study of **flow** in matter, such that “flow” is simply defined as the non-recoverable deformation of an infinitely small element within the fluid and the relative movement of its adjacent points (Barnes 2000). Two main types of flow are normally defined in relation with the relative movement of adjacent elements depending whether it happens between hypothetical layers of fluid or in line with the deformation, known as **shear** and **extensional flows** respectively (Figure 28). Then, the dynamic viscosity

(referred to as viscosity from now on) can be initially defined as the resistance to flow or the internal friction of the elements of the fluid, which result in the shear and extensional viscosities that are going to be further discussed. An example of shear flow is the movement of a fluid through a pipe or nozzle, while the break-up of a droplet's tail can be seen as a mechanism governed by extensional viscosity. Nevertheless, in real applications it is common that both effects are present and inter-related.

The approach where the deformation of the material is non-recoverable and can be explained solely based on its flow properties implicitly assumes that such a material is a perfect fluid with no elastic contributions. This is a good approximation in many real applications but there are fluids that display strong elastic effects apart from their viscous behaviour, which introduces the concept of **viscoelasticity**.

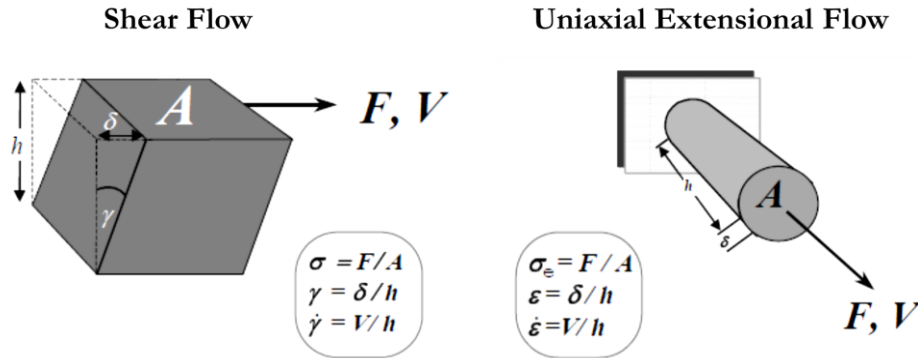


**Figure 28:** Schematics of shear (**left**) and extensional (**right**) flows, showing the direction of the applied force ( $F$ ) over a known area ( $A$ ) and the produced deformation ( $\delta$ ). Adapted from (Barnes 2000)

#### 2.4.1.1 Shear flows

Shear flows can be described in terms of their **shear deformation** ( $\gamma$ ) and **shear stress** ( $\sigma$ ), as it is shown in Figure 28. Particularly, the shear stress is defined as the force per unit area required to deform the material and impart a velocity ( $v$ ) to the elements of the fluid. However, such velocity is typically dependent on the distance perpendicular to the flow ( $h$ ) and, in the case of laminar flow, it leads to a layered structure where the velocity increases as the distance from the stationary wall increases. It is common to refer to the variation of the velocity in the perpendicular direction to the flow as **shear rate**:

$$\dot{\gamma} = \frac{dv}{dh} = \frac{dv}{dh} \quad (1)$$

It was previously introduced that the resistance to shear flow is known as the **shear viscosity**, which can be defined as the ratio between the shear stress and the shear rate

and has units of Pa·s. This should not be confused with the kinematic viscosity, which is essentially the shear viscosity divided by its density and has the centi-Stoke (cS) as its pre-SI unit (Barnes 2000). Notice that if the viscosity is constant across different shear rates the fluid is known as **Newtonian**. Alternatively, if the relation between the shear rate and the shear stress is more complex the fluids are referred as **non-Newtonian**.

### **Newtonian fluids**

Newtonian fluids display a shear viscosity ( $\eta$ ) value independent from shear rate:

$$\sigma = \eta\dot{\gamma} \quad (2)$$

It is noteworthy that, since a particular experiment can only monitor the viscosity response in a certain range of shear rates, it is not correct to classify fluids as uniquely Newtonian but rather as fluids with a Newtonian behaviour in the measured range. In fact, the Newtonian model represents an ideal fluid and it is expected that all fluids show non-Newtonianess at a sufficiently high shear rate (Barnes 2000). It is also relevant that this definition assumes a constant viscosity in terms of shear rate and time, but it is not incompatible with viscous variations at different temperatures and pressures. Particularly, viscosity tends to decrease with **temperature** ( $T$ ) due to the increase of the Brownian motion of the fluid's molecules, which opposes the attraction mechanisms that originate the viscosity in the first place (Barnes 2000). Moreover, this reduction in viscosity at increased temperatures is more noticeable for higher viscosities (Cameron 1966). This dependency can be explained by the Arrhenius (or sometimes referred as Andrade) (Barnes 2000) relationship, where  $A$  and  $b$  are constants of the fluid,  $b$  being related to the activation energy of the material:

$$\eta = Ae^{\frac{b}{T}} \quad (3)$$

The **pressure** ( $P$ ) dependence of the viscosity of liquids is related with their compressibility, since a significant pressure would reduce the volume of the fluid and move closer its constituent molecules, increasing their interaction. However, in order to generate a noticeable change in the viscosity, a pressure in the order of MPa is required (Barnes 2000), which is far greater than the generated pressure during jetting. With this in mind and the assumption of fluid incompressibility for this study, the effect of pressure variation on the shear viscosity will not be taken into account any further.

A practical example of a Newtonian liquid flowing through a straight pipe of known length ( $L$ ) and radius ( $a$ ) is explained in order to clarify some of the situations that are normally encountered in jetting and micro-fluidic devices. Thus, using the Navier-Stokes equations with the assumptions of Newtonian incompressible fluid under laminar and steady flow with no wall-slip, the well-known **Hagen–Poiseuille equation** is derived (Munson et al. 2009), which relates the pressure drop in the pipe ( $\Delta P$ ), with the volumetric flow rate ( $Q$ ) and the shear viscosity ( $\eta$ ) as follows:

$$\Delta P = \frac{8Q\eta L}{\pi a^4} \quad (4)$$

An expression for the **average fluid velocity** ( $u_a$ ) in the stream can be defined in terms of the volumetric flow rate as:

$$u_a = \frac{Q}{\pi a^2} = \frac{\Delta P a^2}{8\eta L} \quad (5)$$

However, from the Poiseuille approach a more precise equation for the **velocity of the fluid** ( $u$ ) at different radial distances from the centre ( $r$ ) can also be obtained:

$$u(r) = \frac{\Delta P}{4\eta L} (a^2 - r^2) \quad (6)$$

Making use of the previous expression, the definition of shear rate shown in Equation (1) and the relation between shear rate and shear stress on a Newtonian fluid displayed in Equation (2), it is possible to obtain the **shear rate** ( $\dot{\gamma}_w$ ) and **shear stress** ( $\sigma_w$ ) **at the wall** of the pipe:

$$\dot{\gamma}_w = \frac{\Delta P a}{2\eta L} \quad (7)$$

$$\sigma_w = \frac{\Delta P a}{2L} \quad (8)$$

These expressions reveal a parabolic velocity profile with zero displacement on the wall and a maximum velocity ( $u_{max}$ ) in the middle of the pipe ( $r = 0$ ), where both the shear rate and stress are zero. Moreover, the previous equations can be rearranged to provide an expression for the shear rate at the wall of the pipe in terms of the average ( $u_a$ ) or maximum ( $u_{max}$ ) fluid velocities as follows:

$$\dot{\gamma}_w = \frac{\Delta Pa}{2\eta L} = \frac{4Q}{\pi a^3} = \frac{4u_a}{a} = \frac{2u_{max}}{a} \quad (9)$$

It has been assumed that the flow is laminar and steady, which is a reasonable approach used in many practical applications, however, these need to be evaluated for the previously shown equations to be valid. Therefore, since the relationship between inertial and viscous forces needs to be assessed, the dimensionless Reynolds number ( $Re$ ) is an appropriate indicator (Munson et al. 2009) that compares the dynamic viscosity ( $\eta$ ) with the density ( $\rho$ ), velocity ( $u$ ) and the characteristic length of the system ( $l_c$ ):

$$Re = \frac{\rho u l_c}{\eta} \quad (10)$$

For the present example,  $Re$  can be written in terms of the flow rate using the average fluid velocity ( $u_a$ ) and the diameter of the pipe ( $2a$ ) as the characteristic length:

$$Re_a = \frac{\rho u_a (2a)}{\eta} = \frac{2\rho Q}{\eta \pi a} \quad (11)$$

This number can be used to assess the nature of the flow, since there is a threshold value that marks the moment when the viscous forces can no longer damp the inertial-driven instabilities of the fluid, resulting in a turbulent regime. This critical value depends on the geometry of the fluid container but for circular pipes it is generally accepted that flows with  $Re < 2100$  are in a laminar regime (Munson et al. 2009).

The assumption of **steady-state** is based in the fact that the distance that a laminar flow needs to travel in a pipe before stabilising and reaching its time independent velocity profile is proportional to the characteristic length and fluid velocity (Barnes 2000). Therefore, for long and narrow pipes under relatively low fluid velocity, the entry length is small compared with the other dimensions in the system and can be considered in a laminar regime. An approximate expression for such distance, known as entry length ( $l_e$ ), can be written as follows (Barnes 2000):

$$\frac{l_e}{a} = 0.5 + \frac{0.225 Q \rho}{a \pi \eta} = 0.5 + 0.113 Re_a \quad (12)$$

It is noteworthy that the entry length is also inversely proportional to the viscosity, which means that for sufficiently viscous fluids the previous expression can be simplified to  $L_e = a/2$ .

### Non-Newtonian fluids

Since many flows present in real applications cannot be described by the previously ideal model, it is important to consider the behaviour of the non-Newtonian fluids. In this case their viscosity is dependent on the shear rate, but this deviation from Newtonian flow can happen in different ways, as can be observed in Figure 29. These simplified descriptions, however, are not exclusive and it is common to find fluids with hybrid behaviour.

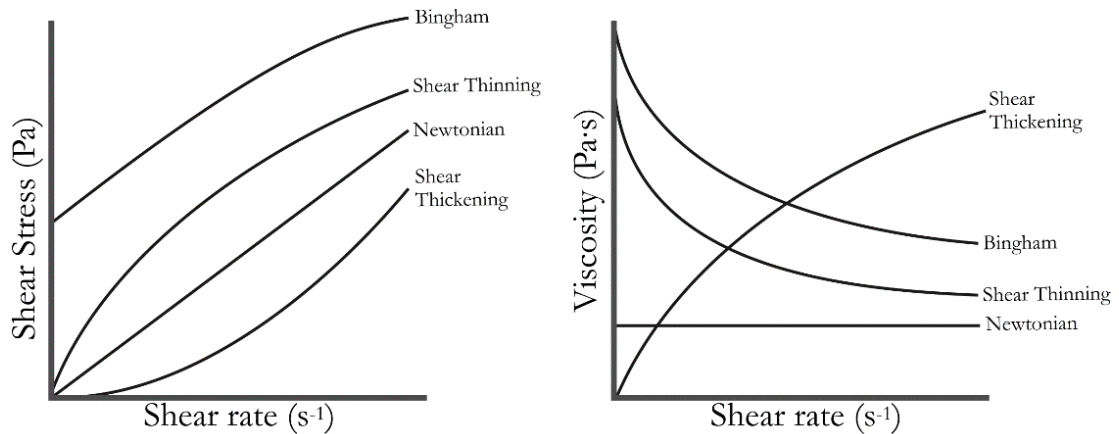


**Figure 29:** Characteristic behaviour of Newtonian and non-Newtonian fluids showing the dependency of their viscosity (**left**) and shear stress (**right**) under a wide range of shear rates.

As it was previously mentioned, the viscosity can be understood as an interaction between the components of the fluid such as molecules or suspended particles. Thus, the initially high viscosity of some of these materials can be explained by the presence of an internal micro-structure in the fluid based on inter-particle attraction or polymer chain entanglement (Lewis 2006) (Barnes 2000). Then, once the shear rate is incremented, the original arrangement is disrupted, causing variations in the internal interactions and consequently the displayed viscosity. For instance, it is common for materials with such internal structure to experience a reduction in viscosity as the shear rate increases, which results in the molecules aligning with the flow and any potential flocs to be broken. This behaviour is described as **shear thinning** or **pseudoplastic** and is the most common form of non-Newtonian fluid. Pseudoplastics are especially useful in applications where a fluid needs to be extruded through a small pipe from a bigger reservoir, since the viscosity is lower at higher shear rates, which lowers the required pressure, but display good stability to sedimentation during storage thanks to its higher viscosity. The opposite scenario, i.e. a fluid that increases its viscosity as the shear rate is also incremented, is possible and known as **shear thickening** or **dilatant**. However, rather than a type of fluid on its own, dilatants are normally shear thinning fluids that experience thickening after a critical shear rate. The

microscopic explanation in this case comes from the possibility of new aggregates forming in the transversal directions to the flow at the critical shear rate, i.e. a transition from 2D to 3D flow, which breaks down again the flow-induced order achieved up to that point (H. a. Barnes 1999). This however is typical from highly loaded suspensions of relatively big particles at high shear rates and it is not expected to affect the present work.

Another defining feature that a non-Newtonian fluid may display is the so called **apparent yield stress**, which is typically defined as the minimum stress that need to be applied to a fluid to initiate the flow. This, however, implies that the viscosity of the fluid below that critical stress is infinite, which many rheologists argue is incorrect and instead is proposed that even if such viscosity is large, it can be measured with an experiment long enough (H. A. Barnes 1999). This update in the interpretation of the yield stress shines some light in the internal mechanisms of slow flows, but does not forbid the use of the concept to describe certain applications. However, it is important to accept that the yield stress is a product of extrapolation of conclusions beyond the experimental data, which is something that should be performed with caution. An example of a historic non-Newtonian flow typically described by its apparent yield stress is the **Bingham plastic**.

All the previously mentioned flows are assumed to be time independent, however another look to the microscopic interpretation of the viscosity and its evolution with shear rate may complicate this assumption. This is because most of the internal interactions that lead to the initial high viscosity are reversible and therefore the microstructure can be reformed over time. This effect is known as **thixotropy** and it is behind the concept of **shear history** (or shear memory), since the material will react differently to the same perturbation depending on its previous condition. This is something that needs to be carefully managed during the characterisation of fluids, especially in rotary rheometers, but it is less relevant in applications where the fluid is not re-circulated after the highest shear is applied, as it is the case in jetting.

To characterise mathematically the flow curve of the previous flows, several models are available, normally adapted to the type of material under study and the range of shear rates employed in the test. The most general description of time-independent shear-thinning fluids is the **Cross model** (Cross 1965), which relies on two constants ( $K'$ ,  $m$ ) and the asymptotic values of the viscosity at very low ( $\eta_0$ ) and very high ( $\eta_\infty$ ) shear rates:

$$\frac{\eta_0 - \eta}{\eta - \eta_\infty} = (K'\dot{\gamma})^m \quad (13)$$

This model would be ideal if the full flow curve of a material can be obtained, however this situation is rarely the case, since limitations of the equipment normally allow for only part of the curve to be measured, missing one or both extreme viscosities. Consequently, for a viscosity range that does not fall into any of the extreme cases one can assume  $\eta \ll \eta_0$  and  $\eta \gg \eta_\infty$  to obtain the well-known **power-law model** (or Ostwald-de Waele model) from Equation (13) after a simple redefinition of parameters (Barnes et al. 1989), where  $K$  is the consistency and  $n$  the power-law index :

$$\eta = \frac{\eta_0}{(K'\dot{\gamma})^m} = K\dot{\gamma}^{n-1} \quad (14)$$

Alternatively, assuming only  $\eta \ll \eta_0$  it is possible to obtain the **Sisko model** (Sisko 1958) from the Cross model (Barnes et al. 1989), which shares the definition of constants with the power-law:

$$\eta = \eta_\infty + K\dot{\gamma}^{n-1} \quad (15)$$

The Sisko model is especially suited when the initial zero shear viscosity ( $\eta_0$ ) is outside of the measuring range of the rheometer. Interestingly, in the case of  $n = 0$ , this model is reduced to the **Bingham model** (Barnes et al. 1989), which is typically written in terms of shear stress instead of shear rate and displays an apparent yield stress ( $\sigma_0$ ) as previously described and a constant plastic viscosity ( $\eta_p$ ).

In the following, the example of a non-Newtonian liquid flowing through a cylindrical pipe of constant radius ( $a$ ) and known length ( $L$ ) is discussed, assuming first than its flow can be explained by the power-law equation. Thus, the equations describing the pressure drop ( $\Delta P$ ), radial velocity profile ( $u(r)$ ) and shear rate at the wall ( $\dot{\gamma}_w$ ) are (Barnes 2000):

$$\Delta P = \frac{2KL}{a} \left[ Q \frac{3 + \frac{1}{n}}{\pi a^3} \right]^n \quad (16)$$

$$u(r) = \frac{n}{n+1} \left( \frac{\Delta P}{2LK} \right)^{1/n} a^{n+\frac{1}{n}} \left( 1 - \left( \frac{r}{a} \right)^{n+\frac{1}{n}} \right) \quad (17)$$

$$\dot{\gamma}_w = \frac{4Q}{\pi a^3} \left( \frac{3}{4} + \frac{1}{4n} \right) = \frac{Q}{\pi a^3} \left( 3 + \frac{1}{n} \right) \quad (18)$$

Note that the bracketed term in the last equation is the so called **Rabinowitsch correction** for a power-law fluid (Barnes et al. 1989), which has a  $d(\ln Q)/d(\ln \sigma_w)$  instead of  $1/n$  in its general form. Alternatively, if the fluid is better described by the Sisko model shown in Equation (15), its pressure drop ( $\Delta P$ ) is given by (Barnes et al. 1989):

$$\Delta P = 2 \frac{L}{a} \left[ K \left( \frac{v(3n + 4s + 1)}{a(n + s)} \right)^n + \frac{v \eta_\infty (3n + 4s + 1)}{a(n + s)} \right] \quad (19)$$

$$s = \frac{\eta_\infty}{K \left( 4 \frac{v}{a} \right)^{n-1}}$$

#### 2.4.1.2 Extensional flows

In extensional flows the deformation of the fluid is typically elongational and there is no shear. In the case of a uniaxial extension, the mechanism is characterised by the deformation ( $\mathcal{E}$ ), the extension strain rate ( $\dot{\mathcal{E}}$ ), the extensional stress or tension ( $\sigma_e$ ) and the extensional viscosity ( $\eta_e$ ) as can be observed in Figure 28. The fundamental relation between extensional stress and strain rate is as follows, similar to the one given for shear flows:

$$\sigma_e = \eta_e \dot{\mathcal{E}} \quad (20)$$

In this case, the velocity gradient in the fluid is parallel to the flow, contrasting with the situation for shear flows, where the gradient is perpendicular to the direction of motion. Nevertheless, the elongational viscosity is still the opposition of the fluid to such external deformation as it was the case with the shear viscosity. However, although the extensional viscosity can be understood as a fluid's internal friction, it has a major elastic contribution that arises mainly from the resistance of internal components such as polymer chains to be stretched or compressed. Consequently, in a situation where fibre-like structures are suspended in a fluid under an applied pressure it is expected that such fibres align with the flow, decreasing the shear viscosity as they break their original random orientation but increasing the extensional viscosity of the fluid as the fibres stretch. This example shows how both shear and extensional viscosity react to the same stimulus in very different ways even though the physical changes in the fluid are the same. Furthermore, in shear flows there is a radial gradient of speeds that tends to impose rotation in the fluid elements,

which ultimately deforms less such elements that equivalent elongational stresses (Barnes 2000). This is the reason why in some texts shear flows are referred as weak flows while extensional regimes are called strong flows.

A widely extended way of assessing a fluids elasticity and comparing its shear and elongational responses is the **Trouton ratio**, originally defined as the relation of the extensional viscosity to the shear viscosity. However, this led to some ambiguities in terms of the equivalence of deformation rates, so it was redefined as follows (Barnes et al. 1989):

$$T_R = \frac{\eta_e(\dot{\epsilon})}{\eta(\sqrt{3}\dot{\epsilon})} \quad (21)$$

It has been shown that if the fluid is incompressible and inelastic the Trouton ratio has a value of 3 across all shear rates (Petrie 2006)(Barnes 2000). However, any elastic components would induce a deformation rate dependant variation of the extensional viscosity, resulting in Trouton ratios multiple orders of magnitude above the inelastic scenario. This ratio, however, eventually plateaus, leading to a constant  $T_R$  at high strain rates, which is the result of the shear and extensional viscosity curves being parallel to each other once the internal elements are totally aligned with the flow (Barnes et al. 1989) (Petrie 2006) (Rózanska et al. 2014).

Although there are several suggested methods to measure extensional viscosity, doing so at high deformation rates in a steady state has been historically problematic (Barnes 2000)(Petrie 2006). Two of the most promising methodologies are the Capillary Breakup Extensional Rheometer (Rodd et al. 2005) and the hyperbolic contraction microfluidic device (Ober et al. 2013). The former consists of two separating plates that precisely stretch a liquid bridge in front of a high-speed camera and produces situations similar to the jetting process, while the microfluidic option bases its operation in the monitoring of the pressure drop along a micro-channel with a hyperbolic contraction designed to apply a constant stress. However, this complex characterisation is outside of the scope of the present work.

### 2.4.1.3 Viscoelasticity

Some fluids have an internal microstructure that rule their flow properties, especially at low shear rates. This can be understood as a natural rest condition that represents a minimum-energy state and explain the thermodynamic forces that oppose any

deformation in order to restore such equilibrium (Barnes 2000). Yet, this elastic behaviour seems to contradict the very own concept of flow previously introduced, which is dissipative in nature. It seems appropriate that to fully describe a fluid both elastic and viscous contributions are considered, which introduces the **viscoelasticity** concept. This, however, is not as contradictory as initially seems, since it provides a more flexible term that can accommodate not only the behaviour of non-Newtonian fluids, but also the flow of ideal Newtonian liquids and even elastic solids, understanding that their ultimate performance under deformation would be a matter of the magnitude of the perturbation and the time of the process. In fact, one of the simplest yet illustrative interpretations for viscoelastic fluids is based on a mechanical analogy that combines ideal springs and dashpots to account for both the elastic and viscous behaviours (Barnes 2000). In these examples the spring follow Hooke's law, i.e. the strain is proportional to the applied stress with the elastic modulus acting as the elastic constant and its reaction is instantaneous. Alternatively, the dashpot's plunger moving through a viscous Newtonian fluid represents the non-recoverable deformations of the system, where the stress and the deformation rate are proportional.

A common characterisation technique for the influence of the elastic and viscous components is the **oscillatory test**, which basically consist of the perturbation of the fluid with a sinusoidal wave of small amplitude with the intention of assessing its response without breaking the internal structure. The response of the material is monitored in real time and compared with the input wave using their phase ( $\delta$ ). In the case of a perfect solid, the applied stress and measured strain would be in phase ( $\delta = 0^\circ$ ), while for an ideal liquid they would be completely out of phase ( $\delta = 90^\circ$ ). It should be no surprise that these extreme situations are rarely encountered and instead the measured behaviour is a combination of both situations. However, since it is still very useful to consider the contribution of the elastic and viscous components separately, the measured complex modulus ( $G^*$ ) is defined as the combination of the **elastic (or storage) modulus** ( $G'$ ) and the **viscous (or loss) modulus** ( $G''$ ), as follows:

$$G^* = G' + i G'' \quad (22)$$

$$G' = G^* \cos \delta \quad (23)$$

$$G'' = G^* \sin \delta \quad (24)$$

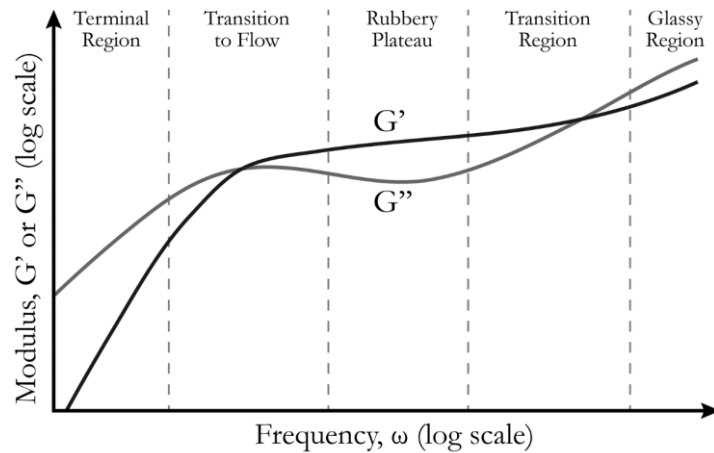


**Figure 30:** General curve showing the alternation of the dominant moduli for the different viscoelastic regions. Adapted from (Barnes 2000).

The relative value of these moduli at different time scales is a good indicator of which forces are governing the fluid's response. Thus, a general moduli vs frequency curve can be constructed as the one shown in Figure 30, where the most common viscoelastic regions are defined (Barnes 2000), namely the terminal (or viscous) region, the transition flow, the rubbery (or plateau) section, the higher (or leathery) transition and the glassy region. This type of master curve was originally defined for polymer melts but it has also been shown to be descriptive of the viscoelasticity of nanocomposites (Mangal et al. 2015).

The characteristic viscoelastic curve is complex and would require an intricate model to describe it completely in a single equation. However, providing an analytical description of these curves is outside the scope of this work. Instead, it is important to understand what these transitions mean for the fluids. First, in the terminal region, the loss module ( $G''$ ) dominates over the storage module ( $G'$ ), which translates as a viscous-dominated regime where the material behaves as a liquid. There, in the case of polymers, the chains have enough time to free themselves from their entanglement and are able to slip past each other by a mechanism known as reptation (Duffy 2015). Then, at the crossover frequency ( $G' = G''$ ) the plateau region begins, where the solid-like behaviour dominates the situation. In the polymer example, the molecules do not have time to free themselves from entanglements, which results in tension on the chain segments between coupling points, which explains the overall elastic behaviour of the material. The length of the plateau is typically related with the concentration of polymer and molecular weight, since it depends on the polymer chain length and branching (Duffy 2015). Furthermore, the crossover frequency can be taken as the inverse of the longest **relaxation time** of the fluid, which corresponds with the time for approximately 63% of the stored elastic energy to be converted to viscous energy and dissipated (Barnes 2000). Alternatively, we can

understand the longest relaxation time as a measure of how long it takes to the molecules to disentangle. This relaxation time is key to determine if a viscoelastic fluid is behaving as a liquid or solid, since it is common practise to compare it with the characteristic timescale of the process under examination. A way of doing this is by calculating the **Deborah number** ( $De$ ) (Barnes et al. 1989) as the ratio of the longest relaxation time ( $t_{rx}$ ) of the material and a relevant timescale ( $t$ ):

$$De = \frac{t_{rx}}{t} \quad (25)$$

Then, if  $De < 1$  it is accepted that the material behaves fluid-like, since the internal structure has enough time to relax within the characteristic time. However, when such characteristic timescale is lower than relaxation time,  $De > 1$  and then the material is dominated by its elastic behaviour. Back to the master viscoelastic curve, there is a higher crossover transition that initiates the glassy region, which describes a situation at very short timescales where the internal structure of the fluid cannot move translationally but rotational and vibrational modes are present (Duffy 2015).

#### ***2.4.2 Theory of piezoelectric inkjet (PIJ)***

In this section, the main mechanisms behind the jetting process are described along with its distinctive **printing stages**, namely jet formation, jet break-up, impact on the substrate and solidification. During the explanation of said stages several **dimensionless numbers** and printing parameters are introduced to facilitate the comprehension and later analysis of each effect. These are the product of dimensional analysis and highlight the balance of involved forces. For an in depth review on these parameters see McKinley (McKinley 2005). Additionally, some of these printing indicators are used to define **processing guidelines** (also known as printability windows) to allow for fine control of the system's output.

##### **2.4.2.1 Printing stages**

###### **Jet formation**

From an energetic point of view, the perturbation required to initiate a jet of fluid through a narrow nozzle needs to overcome two main barriers, the **losses** arising from a conversion of kinetic energy into thermal energy due to the viscosity of the fluid within the nozzle and the energy required to form the **free surface of the fluid column** (McKinley 2005). Furthermore, since the jet is required to travel at a certain speed towards

the substrate, additional kinetic energy is necessary. Hence, the energy balance can be summarised as follows (Rosen et al. 2008):

$$E_{imparted} = E_{loss} + E_{surface} + E_{kinetic} \quad (26)$$

In a piezoelectric system, the energy imparted to the fluid is determined mainly by the printing pulse applied to the piezo-actuators. The amplitude of such pulse is directly related with the magnitude of the generated pressure wave and therefore is the main factor in the actuation system. However, the shape of the pulse is as important as the amplitude if efficient jetting is pursued. This is because once the pressure pulse is generated within the nozzle chamber two waves travelling in opposite directions are formed. These two waves interfere constructively for certain pulse shapes, depending on the fluid properties and the channel geometry, resulting in optimum ejection and minimising energy losses during the process (Bogy & Talke 1984) (Wijshoff 2010). With these fundamentals in mind, more complex pulses can be generated to further tune the energy imparted to the generated droplets. The modulation of the pulse can also lead to a significant reduction of droplet volume (Chen & Basaran 2002), which in turn would increase the resolution of the process.

However, as it was introduced in the previous energy consideration (Equation 26), the successful ejection of a fluid jet is not only dependent on its speed ( $v$ ) but also in other factors such as fluid density ( $\rho$ ), viscosity ( $\eta$ ) and surface tension ( $\sigma_{ST}$ ). Therefore, to study the relation of these factors a series of dimensionless numbers have been historically defined. The **Reynolds number** ( $Re$ ) is the ratio of inertial factors and viscosity and it was previously introduced (Equation 10). Similarly, the **Weber number** ( $We$ ) is the comparison between inertial and capillary effects and can be defined as follows, where the nozzle diameter ( $d_N$ ) is typically used as characteristic length of the system ( $l_c$ ):

$$We = \frac{v^2 \rho l_c}{\sigma_{ST}} \quad (27)$$

Since both the Reynolds and Weber numbers depend on the velocity of the drop and in some situations a control parameter independent of inertial effects is desired, the **Ohnesorge number** ( $Oh$ ) is defined:

$$Oh = \frac{\sqrt{We}}{Re} = \frac{\eta}{\sqrt{\sigma_{ST} \rho l_c}} \quad (28)$$

Additionally, to evaluate the relevance of the gravitational force in the system under study, the **Bond number** ( $Bo$ ) (also known as Eötvös number) is typically calculated,

where  $g$  is the acceleration of gravity. In jetting processes, it is generally true that  $Bo \ll 1$  and consequently the effect of gravity is neglected (Derby 2010).

$$Bo = \frac{\rho g l_c^2}{\sigma_{ST}} \quad (29)$$

These dimensionless numbers are widely used to create simple printability guidelines for jetting processes. For instance, the **minimum speed** ( $v_{min}$ ) that a jet requires to overcome the surface tension of the fluid at the nozzle (Duineveld et al. 2002) can be reduced to the condition  $We > 4$  (Derby 2010). Although this relation is useful to understand the ejection of fluids and can help to establish the minimum kinetic energy required in the process, it is based on estimations regarding the minimum required pressure and the inertia of the jetted drops and so it should be refined if a precise  $v_{min}$  is required.

### Jet Break-up

The fluid jet leaves the nozzle at a certain speed due to the imparted energy and it stretches towards the substrate until it breaks, creating a main body of fluid that continues travelling in the same direction and a receding volume of fluid that travels back to the nozzle. Surface tension then drives the detached fluid into one or many (satellite) spherical droplets that would eventually land on the substrate (Martin et al. 2008). Therefore, the break-up process is a competition of several mechanisms such as viscoelastic forces, surface tension and inertial effects, and the balance among them determines the moment and position of the jet break-up. For an inelastic fluid travelling away from the nozzle at sufficient speed to overcome the surface tension barrier, the break-up time ( $t_{break}$ ) can be estimated according with the Rayleigh-Weber mechanism as a combination of the inertial (or Rayleigh) timescale ( $t_i$ ) and the viscous timescale ( $t_v$ ) (Bazilevskii et al. 2005), where the characteristic length ( $l_c$ ) is typically the diameter of the jet:

$$t_{break} \sim t_i + t_v \quad (30)$$

$$t_i \sim \sqrt{\frac{\rho l_c^3}{\sigma_{ST}}} \quad (31)$$

$$t_v \sim \frac{\eta l_c}{\sigma_{ST}} \quad (32)$$

From the previous equations, surface tension is one of the main drivers of break-up, and an increase in this magnitude would decrease the overall break-up time of the jet.

Alternatively, high viscosity fluids would present longer break-up times, since the viscous forces are dissipative in nature and stabilise the jet. However, if the ejected material presents also elastic properties, the situation gets more complicated and this magnitude needs to be considered for both jet break-up and satellite formation. Bazilevskii et al. (Bazilevskii et al. 2005) showed that there are **different break-up scenarios** depending on the concentration and molecular weight of aqueous-glycerin solutions of polyacrylamide, which translates as a variation in the viscoelastic properties of the fluids (Figure 31). They observed that for low or non-existent concentrations of polymer (cases 0, 1 and 2 in Figure 31) long tails that eventually collapse into multiple drops are formed. The disintegration of the main jet is delayed by an increased concentration of polymeric additive. This behaviour is explained by the fact that in this regime the elastic mode is shorter than the timescale of the process and therefore its contribution is small, leading to a neck thinning mechanism predominantly driven by viscous forces. Alternatively, when the polymeric concentration and/or the molecular weight is high, the elastic stresses relax slower and their contribution rules over the viscous component. This increased elasticity slows down the droplet and, above a certain threshold, it results in a situation where the fluid filament is never broken and drops are not formed (case 4 in Figure 31). This case is analogous to the situation previously described where the drop does not have enough kinetic energy to overcome the energy barriers imposed by surface tension and viscoelasticity. An appropriate indicator for the ratio between the polymer's relaxation time and the timescale of the experiment is the Deborah number ( $De$ ), previously introduced (equation 25). Furthermore, if the fluids are highly viscous the dynamics of the break-up is mainly driven by elastic and viscous components, which can be compared with the **Elastocapillary number ( $Ec$ )** (McKinley 2005), where  $t_{poly}$  and  $t_v$  are the elastic and viscous timescales,  $t_{rx}$  is the relaxation time of the polymer,  $\sigma_{ST}$  the surface tension,  $\eta$  the shear viscosity and  $l_c$  the characteristic length.

$$Ec = \frac{De}{Oh} = \frac{t_{poly}}{t_v} = \frac{t_{rx}\sigma_{ST}}{\eta l_c} \quad (33)$$

Lastly, if the polymer concentration is high but below the critical threshold, jets are formed with short tails and no satellite drops (case 3 in Figure 31). Instead, the leading part of the drop and the fluid accumulated at the end of its tail form dumbbell-like structures, i.e. two quasi-spherical drops connected by a fluid bridge. These structures are unstable and can only result in the merger of both drops or an in-flight break-up leading to the formation of a satellite drop. The end result for the microjet is determined by the

competition between two mechanisms: the elastic contraction of the filament and its thinning behaviour governed by capillary forces, which push liquid from the filament to the end drops (Bazilevskii & Rozhkov 2015).

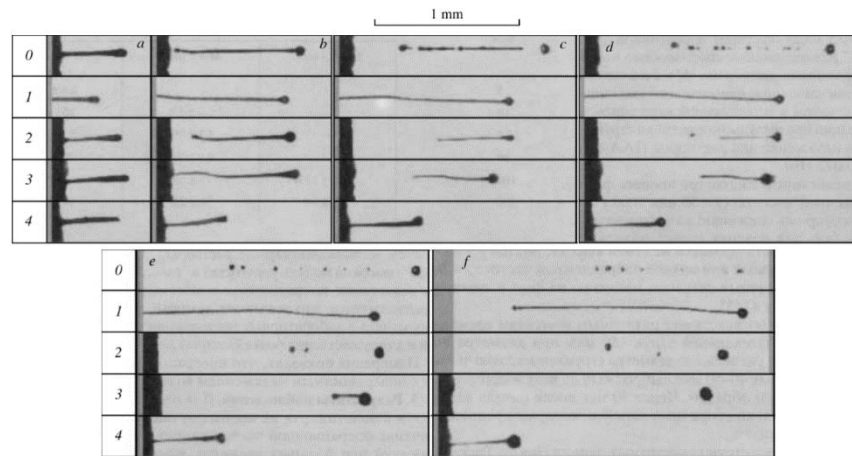


**Figure 31:** Different scenarios of drop formation and ejection depending on the molecular weight and concentration ( $M_w$  in MDa \ concentration in wt ppm) of a water-glycerin solution of polyacrylamide. 0 corresponds to a water-glycerin (50/50) mixture, 1 to 0.5\25, 2 to 2\25, 3 to 2\50, and 4 to 2\200. The flight times (a – f) are 40, 100, 140, 160, 200 and 260  $\mu$ s respectively. This figure was adapted from (Bazilevskii et al. 2005).

In the previous study based mainly on the viscoelasticity of the fluids, Bazilevskii *et al.* were also able to formulate and successfully test two different break-up models based on the internal stresses of the fluid column and the relaxation mechanisms of the polymeric chains during neck thinning. However, as de Gans *et al.* (de Gans et al. 2004) pointed out, this approach neglected the role of the extensional viscosity and therefore it was not a complete model for complex fluids. A key scenario that exemplifies the relevance of this magnitude is the so-called beads-on-a-string structure, which is a jet with several drops joined by a fluid filament, as can be seen in Figure 32. This effect has been widely reported for viscoelastic fluids and was linked with elastic effects since the early observations (Goldin et al. 1969) (Goldin et al. 1972) (Mun et al. 1998) but a criterion for its formation was not found until Christanti *et al.* (Christanti & Walker 2001) published their findings regarding the extensional viscosity of non-shear-thinning viscoelastic fluids. They used a stroboscopic set-up to study the fluid filament in the beads-on-a-string structure appearing in fluids with high molecular weight additives ( $M_w > 300\,000$  in their experiment) and showed that it is possible to obtain the elongation rate from this thinning mechanism. These results are compatible with previously measured elongation rates for the same fluids using an opposed-nozzle rheometer (Mun et al. 1998) and confirm that the key factor behind this mechanism is the critical elongation rate at which the extensional viscosity becomes strain hardening.



**Figure 32:** Example of a beads-on-a-string jet caused by the high extensional viscosity of the polymeric additives of the ink (50/50 water-glycerol + 0.05 % 1 MDa poly(ethylene oxide)). Image from (Christanti & Walker 2002).

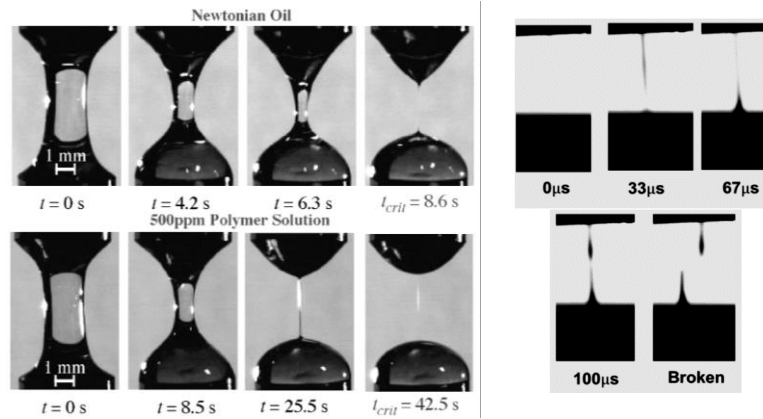


**Figure 33:** **Left**) Liquid bridge break-up of a Newtonian and a viscoelastic fluid. Images adapted from (Cambridge Polymer Group 2004). **Right**) Images from the deposition of a highly viscoelastic fluid with a micro-dispensing valve. It shows a liquid bridge where the neck is broken only after translational movement of the head. A spike-like structure is retained after break-up due to the high apparent yield stress of the material. Image adapted from (H. Yang et al. 2013).

The increased stability of the jets due to viscoelastic effects can lead to a situation where the expected break-up length is longer than the stand-off distance of the printing system, resulting in a **liquid bridge** connecting the nozzle plate and the substrate. This scenario is different from that previously described because once the fluid filament is formed and the inertia of the fluid is dissipated by the viscous forces, the actual break-up of the liquid bridge is described purely by the properties of the material (Cambridge Polymer Group 2004) (McKinley & Sridhar 2002). Despite the lack of inertial components, the behaviour of the liquid bridge is similar to the previously described and presents mainly 2 breakage regimes: capillary and the elastic. The former happens at low extension strain rates and results in short-lived necks that thin exponentially and display a ductile failure. Conversely, elastic threads tend to transition towards a neck of constant radius along its length that eventually collapses into smaller drops (Christanti & Walker 2001). An example of both types of break-up is shown in Figure 33. In this situation a long break-up time can lead to process complications if it is significantly longer than the time that the printhead stays on top of the landing site of the jet, since the lateral movement of the nozzle can cause a lateral collapse of the liquid bridge that results in elongated depositions (Hoath et al. 2009). Furthermore, if the break-up is longer than the thixotropic re-building time of a fluid with a high apparent yield stress, the material does not fall to the substrate and coalesce into a semi-spherical drop but instead can retain its spike-like structure (Figure 33), as it was observed by Yang *et al.* (H. Yang et al. 2013).

### Drop impact and spreading

Once the jet is finally broken, the main body of fluid travels towards the substrate and impacts at a certain speed. The elapsed time from the initiation of the jet to the landing moment is known as the **time of flight (ToF)** of the drop. This is an important parameter in inkjet because the printing system need to adjust its movement accordingly to allow each drop to be placed in the right place according with the printing pattern. Specifically, in a unidirectional approach the offset resulting from an inaccurate ToF is constant and can be corrected by simple calibration but in a bidirectional situation these alternating positional shifts can result in unwanted zig-zag edges on the printed features.

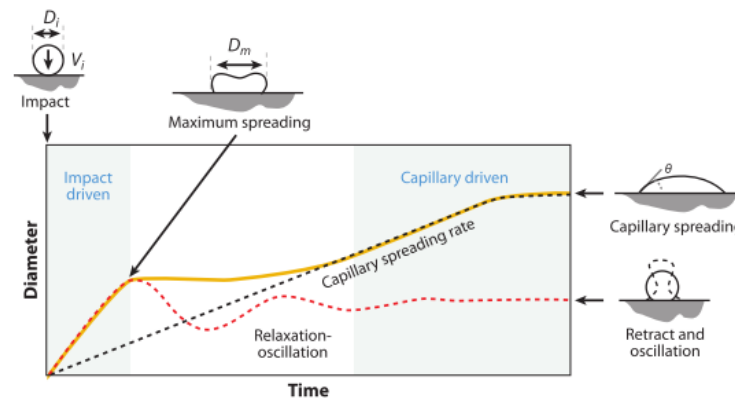


**Figure 34:** Schematic illustration of the main routes of spreading of a droplet. Initially, the droplet reaches the substrate with a velocity  $V_i$  and a diameter  $D_i$  but due to the impact its diameter changes up to a maximum  $D_m$ . Initial deformation is followed by a series of oscillations before the capillary-driven regime takes control. The capillary spreading is typically monitored by the analysis of the droplet contact angle ( $\theta$ ). Figure retrieved as it is in (Derby 2010).

The drop deposition itself can be split into specific stages where the different involved mechanisms alternate its relative effect on the displacement of fluid. These stages are depicted in Figure 34 and classified as (Rioboo et al. 2002): the kinematic phase (or impact), the spreading phase, the relaxation phase and the wetting/equilibrium phase. In the **kinematic stage** the drop contacts the substrate for the first time and a shock wave is formed that travels radially outwards. This is the step most affected by impact speed and less relying on other fluid properties. Then, the drop **spreads** quickly and forms a growing thin disc, also known as lamella, that typically accumulates an increased volume of fluid at its edge. This process is a direct competition of capillary and inertial effects that eventually leads to the drop to its maximum diameter before initiating the receding stage. However, if the rim of the disc has enough energy, this momentary balance of forces is not reached and splashing can occur, which in many ways is another version of the break-up mechanism described in the previous section, where a crown-like structure is often formed and satellite drops can be ejected (Rozhkov 2005). Stow & Hadfield (Stow & Hadfield 1981) showed that the critical impact speed for splash is dependent on the roughness of

the substrate, where smooth surfaces lead to higher critical speeds and therefore reduce splashing. Their original expression for the splash threshold was later expanded and rewritten in terms of dimensionless parameters (Cossali et al. 1997), where  $K_L$  is a function of the nondimensional roughness ( $R_{ND}$ ) (based on the surface roughness of the substrate ( $Ra$ ) and the radius of the drop on flight ( $r\theta$ )) and the fluid film depth on the substrate previous impact ( $\delta$ ), which is 0 for a dry surface:

$$Oh^{-0.37}We = K_L(\delta, R_{ND}) \quad (34)$$

$$K_L(0, R_{ND}) = 649 + \frac{3.76}{R_{ND}^{0.63}}; \quad R_{ND} = \frac{Ra}{2r_0} \quad (35)$$

This splash criterion is compatible with the results presented by many authors (Stow & Hadfield 1981) (Mundo et al. 1995) (Crooks & Boger 2000) but is also descriptive in the specific case of Newtonian fluids. Consequently, Crooks & Boger (Crooks & Boger 2000) realised a similar experiment involving not only Newtonian fluids but also formulations with distinct extensional viscosity. They found that the addition of polymeric additives, while keeping the rest fluid properties constant, raised the splash threshold, requiring higher speeds to induce radial break-up. Furthermore, they observed that their results could be shifted in a consistent manner to collapse them into a single master curve equivalent to the initial Newtonian fluid without polymeric modifiers. The shift factor ( $a$ ) was then compared with the relaxation time ( $t_{rx}$ ) of the polymers, yielding a 99 % correlation. The relation between the splash function for the reference Newtonian fluid ( $K_{Ln}$ ) and the elastic material ( $K_{Le}$ ) can be written as follows:

$$K_{Ln} = (1 - a)K_{Le} \quad (36)$$

$$a = 1.04t_{rx}^{0.22} \quad (37)$$

These results show an increase of required kinetic energy to produce splash as the relaxation time of the polymers grow, which would result in a solid-like response of the molecules, denoted by high Deborah numbers.

After the spreading stage and reaching of the maximum diameter, the **relaxation phase** is initiated, where the surface tension forces the fluid to recede. Depending on the balance of the involved forces the drop may retract, oscillate a few times or even bounce away from the substrate. The mobility of the drop during the relaxation stage is greatly

reduced if polymeric agents are introduced (Bergeron et al. 2000). In particular, incrementing the viscosity and elastic components of the dispensed materials contributes to dampen the oscillations and reduce the receding speed, which limits the energy available for further movement. Eventually, the fluid dissipates its impact energy and adopts an equilibrium shape that for low Bond numbers typically resembles a spherical cap. The previously described stages have a different relevance depending on the properties of the fluid and the conditions of the ejection. For Newtonian fluids, Schiaffino & Sonin (Schiaffino & Sonin 1997) formulated a process map (Figure 35) based on the Weber and Ohnesorge numbers, since they consider them good descriptions of the spreading and the resisting driving forces respectively. However, this diagram does not contain the effect of the contact angle between the drops and the substrate, which is typically considered to be a relevant factor during the post-impact stages.

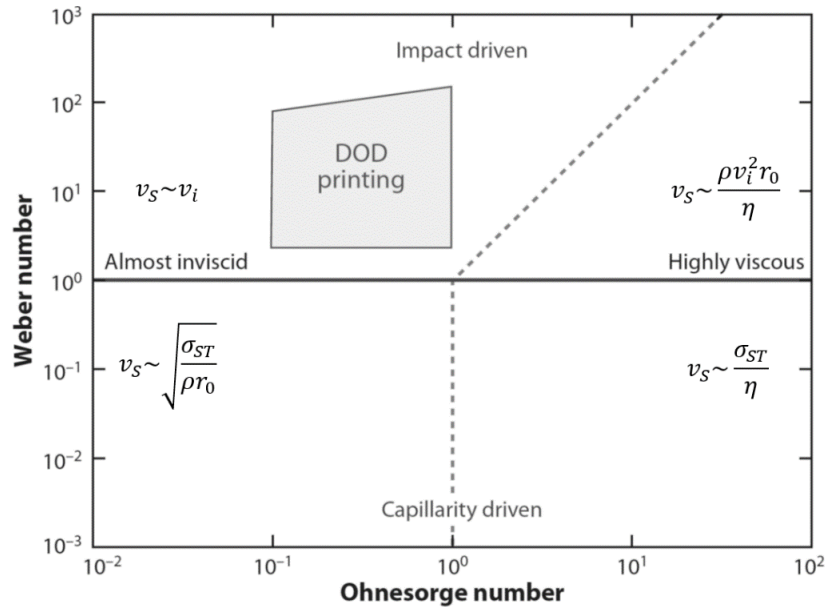


**Figure 35:** Parameter space defined by the Ohnesorge and Weber numbers showing the main spreading driving forces. An estimation for the spreading velocity ( $v_s$ ) arising from order of magnitude analysis of the radial component of the Navier-Stokes equation is overlaid in each region, where  $r_0$  is the drop radius pre-impact,  $v_i$  the impact velocity,  $\rho$  is the density,  $\eta$  is the shear viscosity and  $\sigma_{ST}$  is the surface tension of the fluid. The conditions for conventional drop-on-demand inkjet are represented by the shaded box. The figure was adapted from (Derby 2010) according with the original study of (Schiaffino & Sonin 1997).

Non-Newtonian spreading mechanisms can no longer be described in terms of viscosity and surface tension anymore. Furthermore, the presence of an apparent yield stress, arising from the viscoelastic properties, introduces a flow threshold that should be considered. Luu & Forterre (Luu & Forterre 2009) analysed the impact and spreading dynamics of several fluids displaying an apparent yield stress and classified their behaviour in terms of kinetic and viscoelastic components alone. Thixotropic effects were neglected but it was acknowledged that they would play a role in the spreading of the fluid as the

viscosity increases over time. They presented an alternative parameter space for drop spreading (Figure 36) based on the Deborah number ( $De$ ) (equation 25), the critical strain ( $\gamma_c$ ) and the elastic Mach number ( $M_e$ ), where  $\sigma_0$  is the apparent yield stress and  $G'$  is the elastic shear modulus:

$$\gamma_c = \frac{\sigma_0}{G'} \quad (38)$$

$$M_e = \frac{v_i}{\sqrt{G'/\rho}} \quad (39)$$

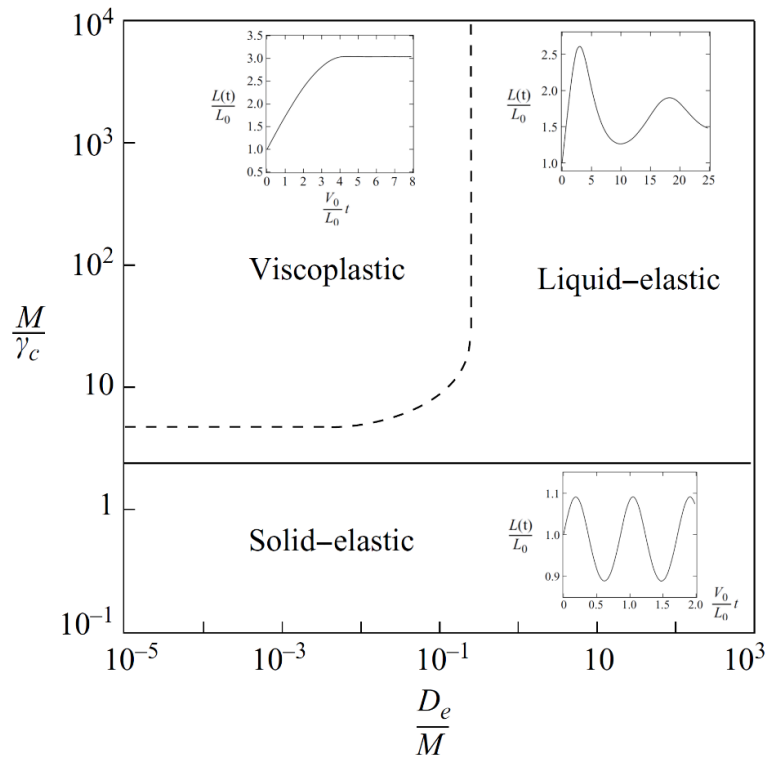


**Figure 36:** Parameter space defined by kinetic and viscoelastic factors for non-Newtonian fluids. Three regimes of impact are identified: viscoplastic, liquid-elastic and solid-elastic. The insets in each region represent the time evolution of the normalized drop diameter, where  $L_0$  is the initial diameter before impact. Modified from (Luu & Forterre 2009).

In this representation, the magnitude  $De/M_e$  does not depend on the impact speed and can be interpreted as a ratio between the viscous relaxation time and the elastic mode of drop vibration. Thus, this coefficient is an elastic analogue to the Ohnesorge number, which compares the viscous damping and the capillary timescales. This ratio is the main control parameter in the transition between purely viscoplastic behaviour, where the drop spreads without apparent oscillations, and the liquid-elastic regime, where deformations are reversible due to the elastic component of the fluid and oscillations are present. In both regimes droplets with a spike in their centre are observed for certain formulations even after the spreading phase has finished. This is attributed to the uneven distribution of shear

stresses, higher on the edge than in the middle, which can lead to an un-deformed body of fluid in the centre of the lamella (German & Bertola 2009). Alternatively, the factor  $Me/\gamma_c$  does include kinetic effects and therefore accounts for the flow threshold imposed by the apparent yield stress. This axis of the diagram shows the condition for solid-elastic impact, where the fluid does not flow and all the response is elastic, leading to substantial drop bounce for hydrophobic substrates.

### **Drop solidification**

Most inkjet applications require that the deposited fluids transition to a solid to fix the printed patterns to the substrate. This is particularly important in a 3D approach, where the next layer needs to be deposited on a stable surface to grow in the z-direction without mixing the fluids of both layers. This transition is normally accompanied by an overall reduction in volume, which is known as **volumetric shrinkage**. The magnitude of this effect, however, depends on the solidification mechanism.

Solvent evaporation is one of the most common processes of solidification, as it is typically fast for small drops and it can be greatly tuned via ink formulation and environment control. However, in this type of process it is common that the solid particles dispersed in the solvent (normally known as pigments) migrate towards the initial contact line as the solvent is removed, resulting in a characteristic inhomogeneous deposition pattern known as coffee stain (Derby 2010) (Magdassi 2010) (Deegan et al. 1997). This phenomenon was explained by Deegan *et al.* (Deegan et al. 1997) as a result of the faster evaporation rate of the fluid near the contact line and the subsequent replenishing flow from the middle to the edge, which consistently transport more solids to the perimeter of the drop as the solvent is evaporated. Therefore, it follows that any situation that reduces the internal flows in the drop will automatically palliate the coffee stain effect as well. Examples of reduced flow as a consequence of increased viscoelastic properties have been extensively produced in the previous sections, which would result in more homogeneous deposition than low viscosity inks. Additionally, a phase change can be induced to stop the flows completely, as is the case of molten wax inkjet printing (Seerden et al. 2001) or photocurable fluids that solidify under UV radiation (Sangermano et al. 2013). Alternatively, the coffee stain effect can also be reduced by increasing the vapour pressure of the surrounding environment or by combining solvents with different boiling points on the ink formulation, which can create a counter-flow due to a gradient of surface tension that compensates the evaporation-driven flow (Magdassi 2010).

## 2.5 Conclusions from reviewed literature and plan for this work

Several conductive materials have been identified as potentially useful in multi-material Additive Manufacturing. Melting metal seems to be technically difficult, especially when it comes to the protection of other materials being co-deposited (such as polymers) from such high temperatures. However, **nanoparticle-based inks and pastes** have demonstrated the ability to produce acceptable conductive tracks requiring only a fraction of the heat to sinter. **Silver** is selected as the preferred material based on its lower resistivity compared with other metals and the fact that silver oxide is also a good conductor. **Conductive polymers** are expected to have a conductivity orders of magnitude lower than metals, but their flexibility and transparency makes them very appealing. Therefore, an aqueous solution of **PEDOT:PSS** nanoparticles is selected as another testing material for this work. Combining conductive materials and polymers have resulted in many interesting **composites** that were able to produce low resistivity while retaining the flexibility and adhesion of the polymeric matrix. Nonetheless, most of the discussed approaches required in house formulation and synthesis, which is out of the scope of this work, so a commercial **carbon paint** based on natural polymers will be used instead as a proof-of-concept for other composites. Furthermore, it was seen during the review that higher viscosity can be beneficial for the process itself, providing higher stability against sedimentation, reducing drop spreading, limiting volumetric shrinkage and increasing the conductivity. Therefore, highly loaded versions of these conductive materials are chosen.

The AM **multi-material processes** review revealed a few common trends in the combination of manufacturing techniques. For instance, most systems used an established and reliable method such as SLA, extrusion or jetting to create the structural parts while using a slower approach with more processing flexibility, such as cold extrusion or aerosol, to deposit the functional materials. Additionally, in most cases the involved systems were conceptually similar, combining the same type of dispensing agents or slight variations of them, as it is the case for the cold and melted extrusion systems. Furthermore, **drop-on-demand jetting** was identified as the most suitable technology for multi-material manufacturing based on its scalability, non-contact nature, multi-nozzle and high control of local material properties. However, it was observed that the inks that can be jetted by this approach are greatly constrained due to the maximum viscosity that the inkjet systems can dispense, which translates to low solid-loadings and low molecular weights. This not only severely limits the material catalogue, but it restricts the achievable functionality of

the parts. Thus, upon closer analysis of the types of jetting devices, **micro-dispensing valves** based on a combination of pneumatic and mechanical actuation were selected as the most suitable complementary technology to extend the range of jettable viscosity in a hybrid drop-on-demand multi-material AM approach. Nevertheless, since a system of these characteristics had not been developed at the time of starting this research, designing and implementing such innovative process became the first objective of the present project. To do it, a list of desirable features was compiled based on the literature review of existing multi-material approaches that became the route-map for the next part of the work (Chapter 3). This list included capabilities such as the deposition of at least 2 high viscosity materials in the same process following a drop-on-demand approach, resolution and control over the local composition in the micro-range, integrated post-processing capable of inducing polymerization and sintering, alongside a built-in vision system.

A review of the fundamental mechanisms behind the different stages of jetting clarified the origin of the viscous limitations. Specifically, the energy imparted by the actuation mechanism to the fluid is shared between the creation of the new surface, the jet kinetic energy and the losses coming from internal friction. As a result, the higher the viscosity, the more energy is required to reach the ejection threshold. Furthermore, from the examples involving a fluid on a cylindrical pipe, it follows that smaller nozzles would require higher applied pressures to sustain flow. Thus, processes such as piezoelectric inkjet cannot provide enough energy to create viscous jets through micrometric nozzles, but a micro-dispensing valve can, thanks to the combination of mechanical and pneumatic actuation. Surface tension also plays a role in the initiation and break-up of the jets but its contribution is not as profound as the viscosity, since the range of this magnitude is typically smaller than the viscous one, which can span across several orders of magnitude. However, despite the processing limitations that this fluid property imposes on the jettability of the inks, the literature also reveals several advantages of the dispensing of materials of considerable viscosity. For instance, viscous flows are typically more stable and less prone to splashing when they impact a flat surface. Also, since the excess of energy is damped faster than in a lower viscosity fluid, oscillations in flight or after impact are less common. Furthermore, the spreading of viscous fluids is typically slow, especially for materials with an apparent yield stress of a fast recovery of their microstructure, which result in smaller footprints and a higher independency from the printing substrate. The drying of the solvents contained on the fluids happens with reduced internal flows, which limits particles' transport and increases the homogeneity of the dry output. Moreover, since

the proportion of volatile volume is smaller than in low viscosity formulations, the volumetric shrinkage is reduced and the deposited films are thicker. All these features are potentially beneficial for a fluid-based AM process like the one developed in this thesis and are studied during the following sections.

In summary, the literature review revealed a gap in the knowledge on the combined use of different types of dispensing printheads despite the advantages that it can provide to multi-material Additive Manufacturing in the form of an extended material catalogue. Thus, in the present thesis such a system is developed and tested with several functional fluids. Dispensing stages such as drop formation, jet break-up, drop impact and solidification are also discussed with the final goal of producing 3D functional multi-material samples displaying properties like optical translucency, flexibility, electrical conductivity and electroluminescence.

### **3. Platform development and understanding**

Viscous materials such as highly loaded pastes and hydrogels would be a very interesting addition to the jetting material catalogue but their viscosity impedes the use of PIJ heads to deposit them. Nevertheless, micro-dispensing valves that combine mechanical and pneumatic actuation were identified as potentially suitable systems to deliver highly viscous materials in a drop-on-demand approach. Therefore, to test these valves as the main component in an AM environment it is first required that such a system is built, since at the time of writing there is no commercial alternative capable of planning tool paths, depositing different materials, post-processing them and continue the layer-by-layer process using this type of valves. Moreover, the review of current literature revealed that a hybrid system combining different dispensing heads would be more attractive in the long term than a purely micro-dispensing approach, which could combine the high viscosity material capability of the dispensing valves with the higher speed, accuracy and material throughput of conventional inkjet.

The development of such system could be tackled in several ways, the simplest of them being the use of a 3-axis linear stage capable of controlling the position and ejection of the printheads. This, was explored for a single valve with acceptable preliminary results but doing the same for the multi-nozzle inkjet heads proved to be a much more complex process and computational challenge, since each nozzle needs to be driven individually, fast and accurately enough to allow the creation of reliable patterns. Consequently, a different approach was selected where a commercial inkjet printer already capable of printing with two printheads was adapted to accommodate and operate two additional micro-dispensing valves in the same way. This required the modification of both software and hardware, since the existing elements were not designed to operate with such valves. A representative example of the designing process is the printing assembly that had to be redesigned to accommodate the 4 heads with their respective fluid reservoirs and external UV-lamp.

## 3.1 Printing elements

### 3.1.1 Description of high viscosity jetting (HVJ) valve

The micro-dispensing valves used in this work are the PICO xMOD (Nordson EFD, USA), which base their operation on the combination of pneumatic and mechanical actuation to dispense discrete volumes of viscous fluids on demand. They resemble in some aspects traditional and well established dispensing systems such as time-pressure or positive-displacement valves (Nguon & Jouaneh 2004) and can dispense the same type of highly viscous materials. Nonetheless, since they can apply higher pressures in short periods of time, these valves can be used to eject streams of fluid towards the substrate in a non-contact approach, which removes problems typically associated with contact needle-based systems such as: collisions with other deposited elements; positional inaccuracies due to needle bending; inhomogeneous wetting and the dependency of dispensed volume with the surface tension of the fluid during fluid break up (Quoc Hung Nguyen et al. 2008). Additionally, contact systems require that the distance between the nozzle and the substrate is kept constant, which requires accurate knowledge of the substrate geometry and repeated motion in the z-axis, which complicates the set-up and slows down the process. Another processing advantage of this approach comes from the actuation mechanism being based on piezoelectric stacks, which are faster and can provide more complex actuation than pressure and screw-based systems. However, the strain that piezostacks are capable of providing in this configuration is normally less than 100  $\mu\text{m}$ , which is insufficient for most dispensing applications (Q H Nguyen et al. 2008). Therefore, most jetting valves of this type use a **magnification mechanism** to increase the displacement of the ball-needle, which can be hydraulic (Q H Nguyen et al. 2008) or mechanical (Wang et al. 2013) (Jeon et al. 2015) (Q.-H. Nguyen et al. 2008). The valves used in this work rely on a lever-type displacement amplifier operated with two piezostacks in anti-symmetric fashion to actuate the ball-needle plunger. The use of an intermediate system also provides additional protection for the piezostacks against elevated temperatures.

The **general working principle** of the dispensing valve requires both mechanical and pneumatic actuation to operate. Specifically, the fluid is pressurized up to 0.6 MPa and injected on the jetting chamber along a fluid path that can be heated up to 100 °C. There, the piezo-electrically driven needle ended with a ceramic sealing ball is oscillated according to the printing signal (up to 500 Hz), opening and closing the nozzle as a consequence.

When the needle is in its upper position the pressurised fluid can flow through the nozzle (50  $\mu\text{m}$  in diameter) for as long as it stays open. Alternatively, when the ball-needle system rapidly moves to its lower position it closes the valve and provides enough kinetic energy to the fluid stream to allow it to break from the nozzle plate and travel towards the substrate, where it would form a dot. The **driving pulses** are mainly described by its pulse time ( $t_p$ ) and cycle time ( $t_{cyc}$ ), which are set on the digital controller, and the opening ( $t_o$ ) and closing times ( $t_c$ ), which is not under user control but can be selected from a limited amount of pre-sets (120  $\mu\text{s}$ , 200  $\mu\text{s}$ , 300  $\mu\text{s}$ , 400  $\mu\text{s}$ , 600  $\mu\text{s}$ , 1300  $\mu\text{s}$ ). The digital controller is designed to operate the valve in a continuous way at the selected frequency but this can be overridden if such controller is externally triggered, which results in drop-on-demand ejection. This system allows the ejection of materials up to 200.000 mPa·s even if they display strong non-Newtonian behaviour (Nordson EFD 2013b). A schematic illustration of this system is shown in Figure 37 along with a description of the printing pulses.

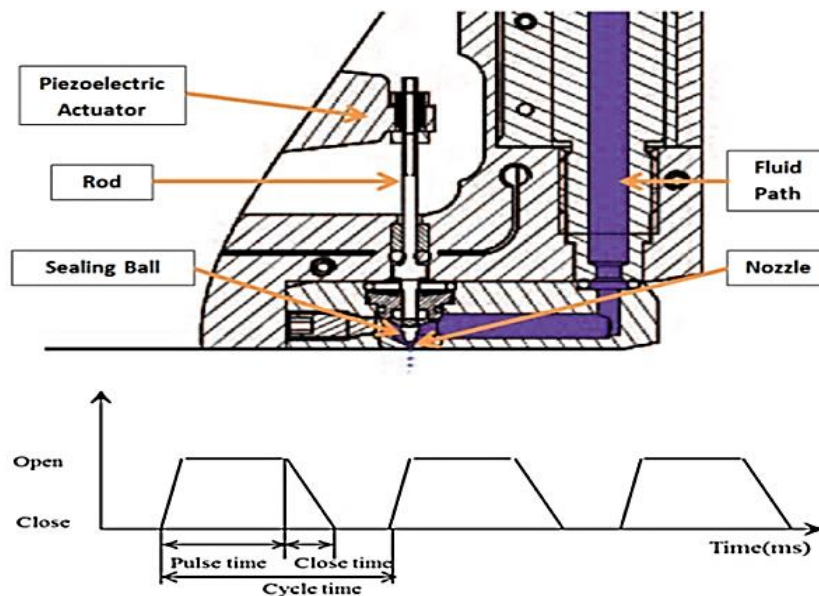


**Figure 37: Top)** Schematic illustration of the micro-dispensing valve with a description of its most relevant parts. Modified from valve user manual (Nordson EFD 2013b). **Bottom)** Description of the relevant parts of the driving pulse and its effect on the nozzle state.

The **pneumatic pressure** is supplied by a compressor with a maximum pressure of 0.6 MPa, it is later filtered and further controlled and stabilised with an analogic regulator. The compressed air is distributed with connecting tubes throughout the system until it reaches the 3 ml plastic syringe full of dispensing fluid connected via Luer lock to the upper part of the fluid channel of the valve. A plastic piston is introduced between the fluid and the compressed air to avoid contamination and homogenise the pressure, since air displays higher compressibility than most fluids and it would act as a shock absorber if left below the piston, affecting the response time of the system.

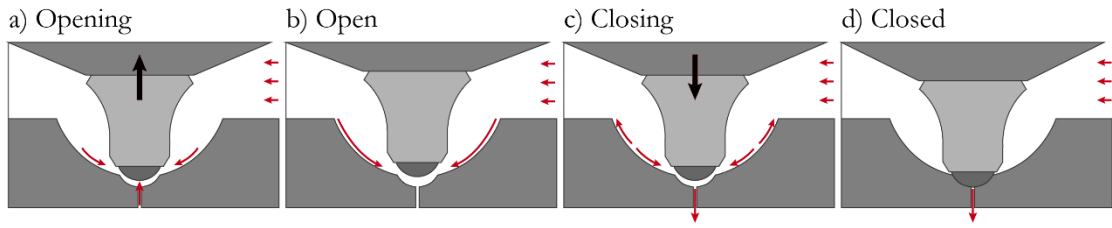


**Figure 38:** **a)** Valve opening (chamber re-fill). **b)** Valve open (pneumatic flow if pneumatic actuation is above the critical pressure). **c)** Valve closing (mechanical ejection starts). **d)** Valve closed (final transfer of momentum and stream break-up). The black lines represent the movement of the plunger while the red ones mark the flows.

Figure 38a shows the **opening of the valve**, which causes a local negative pressure in the area below the ceramic ball that, combined with the positive pressure applied to the fluid in the feed channel, fills the nozzle chamber with the dispensing liquid. It is noteworthy that if the pressure inside the chamber is too low, air from the outside can be suctioned creating entrapped microbubbles, which would affect the dispensing dynamics and eventually migrate to the deposited dots in the substrate. This can be problematic since air expands more than the printed fluids during the post-treatment cycle causing mechanical instabilities and adhesion problems. Furthermore, some materials are sensitive to air or moisture, so a trapped microbubble in the nozzle chamber can induce changes on the material properties. This effect, however, is not expected to be of great importance in the current set-up due to the big difference in diameter between the nozzle and the fluid channel that leads to the chamber and the high viscosity of the fluids dispensed. Moreover, although minimising the pneumatic pressure is one of the actions that will be discussed in later sections as an improvement to the deposited volume, such pressure is never reduced below 0.1 MPa to reduce the probability of air entrapment.

Figure 38b depicts the **valve after the opening time**, which marks the beginning of the purely pneumatic influenced flow. This can start during the opening but it depends on the balance of pressure previously described. In this regime, it is expected that longer pulse times result in bigger deposited volumes and increased pressure in faster jet speeds. However, it is possible that the applied pneumatic pressure is not enough to extrude the material through the nozzle in which case the pulse time is irrelevant after the moment when the nozzle chamber is completely full.

In Figure 38c the **closing of the valve** is represented, where the pressure on the nozzle plate is suddenly increased due to the actuation of the ball-needle system. The outcome of this dispensing stage is greatly influenced by the previous one, since this pressure increase would either initiate the fluid stream or contribute to its conclusion depending on whether the pneumatic pressure was insufficient or sufficient to push

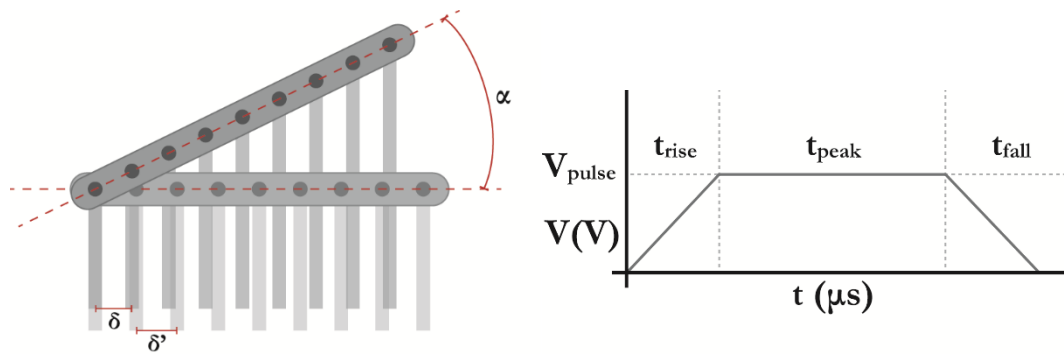
material through the nozzle respectively. In both situations, it is significant that the pressure increase caused by the downward movement of the plunger displaces fluid inside the chamber in two different directions, the nozzle and back to the nozzle chamber. The relation between the dispensed volume through the nozzle and the backflow is expected to be dependent on the viscosity and density of the material, the geometry of the nozzle, the actuation speed of the valve and the pressure balance between the pneumatic and atmospheric pressures (Wang et al. 2013).

Figure 38d finally shows the micro-dispensing valve in its **closed position**, where the sealing ball fits perfectly the spherical nozzle plate bowl. The stroke of the valve is fixed at 160  $\mu\text{m}$  but the closing time can be selected from a list of pre-sets to obtain average closing speeds from 0.12 to 1.33 m/s. The closing speed directly affects the speed and length of the tail of the jet, which in turn control the deposited volume and the repeatability of ejection via break up mechanism. The maximum speed of the fluid is obtained at the moment of impact of the sealing ball with the nozzle plate, where an inelastic collision is assumed and by conservation of momentum the jet is imparted with additional kinetic energy. However, depending on the speed of the plunger and the viscosity of the surrounding fluid, this transition can be more complicated and it has been shown that the plunger may bounce on the nozzle plate, creating discontinuities in the dispensing flow and originating satellite drops (Quoc Hung Nguyen et al. 2008). Nevertheless, this effect was observed to be proportional to the stroke and its influence at needle displacements smaller than 500  $\mu\text{m}$  was negligible. Independently of the actuation speed of the valve, being capable of fully closing the nozzle at idle times is very useful from a processing perspective, since this prevents evaporation and blocks external radiation that can interact with the dispensing fluids, which ultimately increases the stability of the heads.

### ***3.1.2 Description of low viscosity jetting system***

The principle of operation of piezoelectric inkjet printing (PIJ) has been discussed during the literature review in Chapter 2. Here, the piezo-actuated printheads used for low viscosity deposition are described together with their main operation parameters. Specifically, the devices used in this work are Spectra SE-128 (Dimatix, Fujifilm, Japan), which are widely available and used in many industrial systems. Their attractiveness compared with other similar printheads are their small nozzle diameter (35  $\mu\text{m}$ ), high rate of operation (up to 40 kHz) and compact design. The last feature is illustrated by its 128 addressable channels packed in a linear head of 102 x 5 x 104 mm and 25 g, resulting in a

nozzle separation of 0.508 mm that leads to a native resolution of 50 DPI. This resolution can be incremented by different approaches such as combining several printheads with a small offset, printing in multiple swaths with a lateral movement in between passes or by rotating the head by an known angle ( $\alpha$ ) so the effective distance between adjacent nozzles is reduced, as shown in Figure 39.



**Figure 39: Left)** Description of the saber angle ( $\alpha$ ) used to modify the distance between drops ( $\delta$ ,  $\delta'$ ), and consequently the resolution of the printed patterns. **Right)** Trapezoidal printing pulse applied to the piezo-actuators showing the rise ( $t_{rise}$ ), peak ( $t_{peak}$ ) and falling ( $t_{fall}$ ) times and the amplitude of the applied voltage ( $V_{pulse}$ ).

These printheads are capable of ejecting drops with an adjustable volume of 25 to 30 pL with a travel speed between 6 and 18 m/s. However, their precise performance is dependent on three main parameters under user control, namely the temperature of the fluid on the head, the applied pressure and the printing pulse applied to the ceramic piezo-actuators. The **temperature** is controlled with an embedded thermistor and an integrated heated ink bar. The temperature range goes from room temperature to 80 °C with no cooling capabilities unless externally implemented. The possibility of heating the fluid channel has processing advantages due to the local reduction in viscosity that it creates but it can also induce unwanted curing and evaporation, which leads to instabilities and clogging. Furthermore, the fact that the liquid reservoir is not heated requires that the viscosity of the fluid at room temperature is low enough so it can flow through the pipes that lead to the printhead under the action of gravity and pneumatic applied pressure, otherwise the material cannot reach the piezo-actuators and therefore being jetted. The role of **pressure** in this case is different than for the micro-dispensing valves, since most of the time it is not exerting a positive force on the fluid to facilitate its ejection but the opposite. Specifically, the pressure in the head is normally negative to avoid fluid leakage and nozzle plate flooding. This negative pressure is also referred as meniscus pressure and can be used to compensate the hydrostatic pressure variation due to the change of the ink level on the reservoir. A positive pressure is used only for maintenance reasons when the nozzles need to be flushed to clean potential impurities settled on them. There is a very

interesting possibility of using this positive pressure as an aid for printing (for instance to break long elastic droplet tails), however the mechanical actuation of the solenoid valve controlling the pressure is not fast enough to keep up with the printing frequency delivered by the piezoelectric elements and therefore this was not investigated further.

The **printing pulse** is the most complex factor under user control and the one with more flexibility for droplet optimization (Figure 39). In essence, the variation in voltage forces the piezoelements to deform and create differences in the local pressure, which imparts energy to the fluid. This pulse can adopt different shapes but one of the most common is trapezoidal, with 2 regions of fast voltage change (rise and falling times) and a longer constant plateau (peak time). The adequate determination of these parameters is based on the optimization of applied energy, which in turn depends on the geometry of the nozzle chamber, since the optimum printing settings are those that result in constructive interference between the applied and reflected pressure waves within the channel. This optimised pulse is typically achieved by finding the pulse that results in the fastest stable drop, since that means that as much energy as possible is being used to overcome the jetting barriers arising from surface tension and imparting kinetic energy to the drop, instead of producing secondary vibrations or heating the fluid. More details about this optimization cycle based on linear acoustics can be found in the detailed work of Bogy *et al.* (Bogy & Talke 1984) and the more recent and extensive Wijshoff (Wijshoff 2010).

For all the above explained, these printheads are very versatile and powerful fabrication tools but limited in terms of viscosity. This can be understood in terms of the maximum kinetic energy delivered by the piezo-actuators, which can be insufficient to push the material through the internal pipes and nozzle of the system. Moreover, even if the material reaches the outside of the nozzle, a successful droplet would need a minimum amount of energy to detach from the column of fluid in a consistent and repeatable way, which is increasingly difficult as the viscosity of the material rises. These ejection mechanisms were discussed in detail in section 2.4. For the present printhead the working range for the viscosity is given as 8 – 20 mPa.s, while the surface tension is restricted to 24 to 36 mN/m. These values are compatible with the limits proposed by other sources (Magdassi 2010) (Derby 2010) (Wallace 2012).

### 3.2 Printing platform

An inkjet system requires deposition devices like those described in the previous section but it would not be able to form patterns if it lacks other basic capabilities such as

head movement and inspection sub-systems. Furthermore, since the present work is focused on an Additive Manufacturing process, this movement must be in 3D and a post-process step is required to consolidate each material layer before depositing the next one. Based on the literature review presented in Chapter 2 and the accumulated experience of the author with other AM systems the following features are considered necessary for the hybrid system to be developed:

- Capability of housing and powering at least **2 dispensing elements** and their fluid reservoirs to deposit a *functional* and a *structural material*. These heads are required to function in a drop-on-demand approach with minimal electronic delay. A higher number of heads would introduce the possibility of depositing more materials in a single process, which would increase the complexity of the parts.
- Capability of using **different types of printheads** to allow for a wider range of materials. For the present study, this means that the system need to be able to operate in an equivalent manner for PIJ printheads and micro-dispensing valves.
- **Modular design** that allows for a quick change of the heads, either to switch to other viscosity range or to perform maintenance. Modular design also allows for continuous improvement of the system.
- **Minimum lateral movement** of printing assembly that contain the dispensing elements to limit the distortions arising from inertial factors and vibrations. This can be achieved with a movable substrate, which would reduce the required translation of the heads.
- The system needs to be able to **read digital files, slice** them into individual layers and find a suitable and **optimised path** to deposit the drops in the minimum possible time. Parameters such as *print speed, frequency* and *resolution* should be under total user control and they need to be specific for each printhead and material.
- **Substrate clamping system** to avoid the samples to move during the jetting process. It needs to be a reversible and repeatable system that permits quick exchange of substrates.
- **Hybrid pressure system** capable of suppling adjustable negative pressure to the low viscosity printheads and a high constant pressure to the micro-dispensing valves. This system needs to be as compact and flexible as possible to not interfere with the movement of the printing assembly.
- **Post-processing capabilities** for different materials such as UV-curable polymers, solvent-based fluids and metallic nanoparticles that require sintering. These sub-systems need to be as independent as possible to switch them when they are required. Safety measures should be in place to account for the risks that these elements bring, such as UV-radiation and elevated temperatures.

- The system need to be enclosed within a **solid case** with extraction capabilities to protect the user from additional risks such as mechanical movement, UV, heat and chemical exposure. Additionally, a case around the printing area reduces the influence of air currents and other environmental fluctuations. The case, however, needs to be transparent to allow for continuous monitoring of the printing process and should be easy and quick to open to allow for a fast workflow.
- An **automated cleaning station** is necessary to ensure the good performance of the printheads. This is crucial for materials than can react quick to environmental factors such as radiation, humidity or temperature, since failing to clean the nozzle plate on time would lead to the formation of a thin film on the nozzle plate and the process would need to be stopped to perform maintenance. Such sub-system need to be automatic to limit the exposure of the heads to the environment, otherwise the solid case needs to be removed often to manually clean the heads.
- **Top camera** is required to calibrate the printheads, select printing origin and align substrates. Since numerous configurations and materials are going to be tested in the set-up it would be beneficial if the system could automatically record images at selected locations during the printing process.

Since some of these features can already be found in material printers available on the market, the approach of this work was to build upon an existing system (Pixdro LP50, Roth & Rau B.V., Netherlands), adding the required upgrades to meet the requirements of the present work. Consequently, a description of the unmodified material printer and the sub-systems added during this work are described in the following sections.

### ***3.2.1 LP50 original system***

The LP50 is a high precision R&D printer equipped with **5 motion axes** and an overall system accuracy and repeatability of 5  $\mu\text{m}$ . The general structure of the system and function of each axis is shown in Figure 40. All the axis except Y are driven by stepper motors and use either optical (X, Y) or magnetic (Z, P, S) encoders. Since movement from the substrate is generally preferred over the displacement of the print assembly, the Y-axis is typically considered the main printing axis and it concentrates most of the movement during the process. This axis is directly driven by an ironless linear motor and can reach speeds up to 400 mm/s, double the speed of the X-axis. This combination of motors allows for a printing envelope of 310 x 210 x 25 mm, with P rotating over 94° and S moving 1° in each direction. The system has a metallic **stage platform** capable of acting as a vacuum clamp to hold flat samples, which is further equipped with a thermistor and an integrated heater, allowing for temperature control up to  $90 \pm 1$  °C.

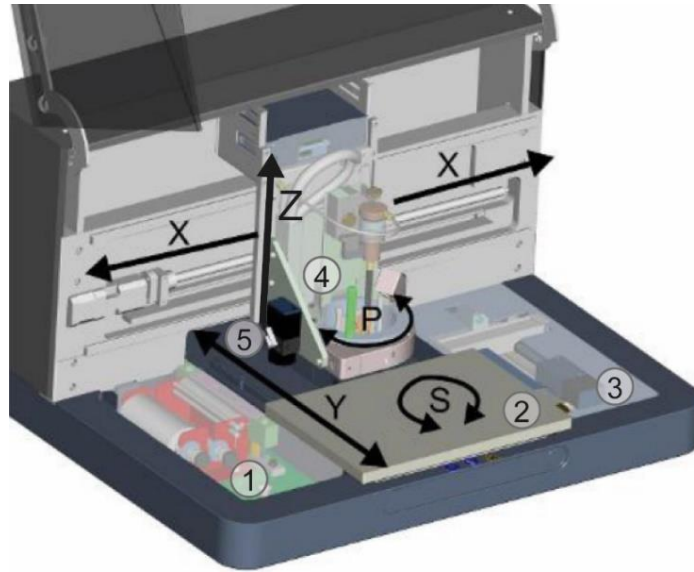


**Figure 40:** Schematic of the LP50 motion system showing the main printing axes (X, Y and Z), the rotation capability of the print assembly (P) and the aligning motor of the substrate (S). In the diagram the transparent protective enclosing is lifted. Other relevant parts such as the cleaning station (1), the printbed (2), the drop-viewer camera (3), the printing assembly (4) and the print-view camera (5) are also shown. The image has been modified from (PiXDRO B.V. 2011).

The printer has **2 integrated monochrome CCD cameras** (Manta, Allied Vision Technologies GmbH) designed to monitor the drop formation (dropview) and the deposited patterns on the substrate (printview). The printview camera has a pixel area of 656 x 492 px, which spans over a field of view (FOV) of 1.99 x 1.74 mm. The FOV is illuminated by a diffused ring light and a coaxial light, both coming from red LEDs. This vision system is mainly used to calibrate the printheads, deciding the print origin and align pre-existing substrate features with the printed patterns. The dropview camera has an area of 656 x 492 px, with a FOV of 1.1 x 0.7 mm. The light source is a stroboscopic red LED synchronised with the printing signal, which provides an average image of the many drops being ejected each second (the actual number depends on the fire frequency). These images allow for real time monitoring of the effect of modifying printing parameters such as temperature, printing pulse or pressure. Since the image is calibrated according the real dimensions of the printhead and the system is capable of 3D movement, this inspection is possible for all nozzles. To automate the optimization of the print parameters the operator can use the so called Advanced Drop Analysis (ADA), a software feature that automatically modifies the printing parameters within a specified range and records the images for later analysis, providing information such as drop volume and speed.

The **software** side of the system is divided in three main aspects: the graphics user interface (GUI), the scripts and the generation of printing paths. The GUI allows the user to interact with the machine, select the active head, set the relevant printing parameters and launch the printing jobs, also known in this context as “recipes”. The scripts are

written in C# and the parameter handling is managed with Visual Basic .NET (VB.NET), which combined with the fact that most of the internal routines of the system are open, allows for user modification and endless customisation. Some of the standard scripts include the general print of a pattern, the movement during calibration and maintenance functions such as wiping or purging. A typical recipe includes several nested sub-scripts, which allows for simpler and cleaner programming. Additionally, the user has access to some auxiliary inputs and outputs (I/O) that can be configured to exchange signals with external devices, but these are severely limited in number and function, which does not allow for the addition of multiple co-existent sub-systems. Alternatively, the algorithms in charge of calculating the printing paths from the digital files (only 2D file formats such as bitmaps are accepted) are not part of the recipes but an external software that must be called before or during each layer of material is printed. These algorithms are not modifiable but can perform several tasks depending on the input given. The main application is the generation of the synchronised print signal and machine movement so the material is deposited in the right place in the minimum number of passes. Moreover, the algorithm can exclude individual nozzles if the user considers that they are underperforming, recalculating the output accordingly. This allows to keep printing at high quality even when the printhead is not in perfect condition, which saves time and extends the effective life of the heads notably. The output of the generation algorithms can be pre-viewed within the GUI before launching a recipe, which allows for virtual experimentation and reduces the generated waste that typically comes with initial testing.

In the present work, Spectra SE-128 printheads are used based on their compact geometry and 128 nozzles. These are available in single and dual configuration, the former shown in Figure 41 for its simplicity. The **assembly** has one ink reservoir of 15 ml per printhead, which is under negative pressure (-3 to 0 kPa) during printing and can reach up to 25 kPa of positive pressure during purging cycles. Each reservoir has a solenoid valve opening and closing the channel to prevent leakages at idle times. The ink travels from the reservoir to the heater through chemically resistant tubing and is later feed into the printhead fluid chamber. The thermal elements can heat the inks up to 80 °C to modify its rheological properties and facilitate its ejection. The printing assembly is fixed on the main system with a magnetic mounting ring, which provides accurate positioning and prevents the heads from taking too much pressure in case that they encounter an obstruction in the Z-axis, which would cause the assembly to be disengaged. The dual assembly has essentially the same elements but duplicated and requires that each printhead is accurately calibrated with respect to each other, since they are treated geometrically as one element in the

system. This is the main source for misalignment, since the software is not able to compensate for any physical deviation. Once the heads are calibrated they can be operated in two different modes, namely sequential and parallel. The first prints with one head at a time, which is slower but allows for simpler printing paths, while the second method uses both heads at the same time. This is ideal in terms of process speed but it can lead to complex moving patterns that can result in longer times or unexpected results.

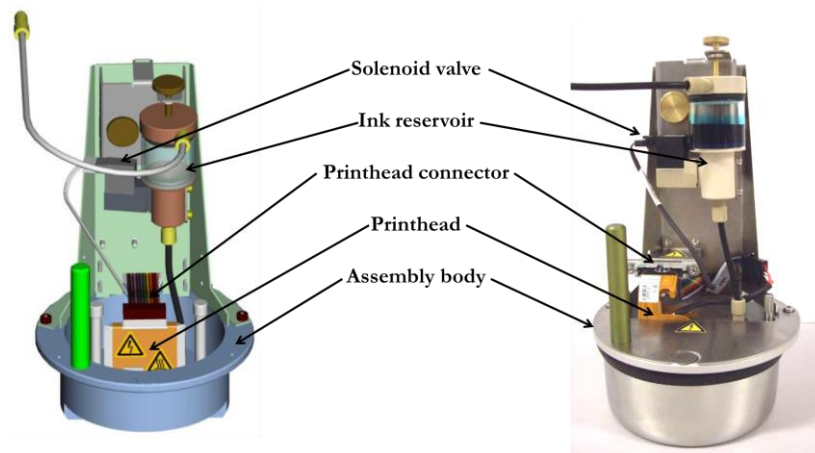


**Figure 41:** Schematic (left) and picture (right) of a single Spectra assembly for the Pixdro LP50. Both show key parts of the print assembly such as the printheads (including the heater), the solenoid valve controlling the flow of liquid and the ink reservoir under negative pressure. Figure adapted from (PiXDRO B.V. 2011).

From above it is clear that the LP50 is a system that can fulfil many of the requirements identified for the present work but it still needs additions to satisfy all of them. Limitations and required modifications include:

- Current configuration is capable of holding **two Spectra printheads** for multi-material deposition; however, increasing the number of deposition elements is physically impossible without modifying the assembly completely.
- It can operate different types of inkjet printheads, including hot-melt configurations, but not micro-dispensing valves for high viscosity deposition. Moreover, it **cannot combine dissimilar heads**.
- Present **modular design** although switching heads is not particularly quick.
- The **stage is movable**, which limits the assembly need for displacement. More problematic is the fact that the movement in the Z-direction is exclusively contemplated to adapt for the substrate thickness. This is understandable keeping in mind that the system is essentially a 2D printer, but this limitation should be resolved for the system to become an effective Additive Manufacturing tool.
- It can read **bitmaps for 2D deposition** but it does not have the capability of reading or slicing 3D files such as .STL. It does however, create optimised printing paths with a wide range of possibilities.

- **Vacuum clamping** is possible for flat surfaces. Also, the substrate is heated for ink spreading and evaporation control.
- It can provide both negative and positive **pressures**, but the magnitude of the positive is very low (25 kPa) considering what it is generally required for micro-dispensing valves (100 – 600 kPa).
- The LP50 basic system **has not post-processing capabilities** and the I/O are very limited.
- The set-up is **fully enclosed** with a solid and transparent case.
- The system has a cleaning station and several cleaning routines that can be implemented on the printing process but the **cloth roller is not automated**, which still requires frequent user input.
- There are two **integrated vision systems** that allow fine calibration of the heads and accurate selection of printing origin. There are not recipes that allow for the automation of image capture and substrate scan but they can be implemented.

### ***3.2.2 Hybrid system***

In the following sections, each upgrade to the original research printer is explained and a description of the final set-up is given. The incorporation of the micro-dispensing valves to the system require the modification of the hardware to allow physical placement, the creation of a synchronising circuit to translate the printing signal to something that can trigger the new heads and the re-design of the printing strategy to account for the differences of the added sub-systems.

#### **3.2.2.1 Redesign of the printing assembly**

##### **Computer Assisted Design (CAD) of required parts**

The main objective of the design of a new assembly was originally to be able to place at least one PIJ head and a HVJ valve along with a UV-lamp to cure the structural material and allow 3D fabrication. However, very early in the prototyping stage the UV-lamp was moved outside the main body of the printing assembly, since its rotation was not relevant for the outcome of the process if the printing direction was kept constant, in this case printing along the Y-axis. This allowed placing 2 printheads of each type to reach a total of 4 available materials during a single process. This, however, tightened even further the restrictions on the design, since each dispensing element requires not only space for themselves but for their electrical connections, pressure systems and fluid reservoirs too. The main design requirements and related taken actions are summarised as follows:

- The system is fully **modular** and each printhead has its own holder that fits in the main body of the printing assembly. This means that the current configuration is designed for a combination of 2 PIJ heads and 2 HVJ valves, but other combinations of these or other elements would be possible in the future. This modular design allows for easy replacement and upgrading of individual elements. Figure 42 shows a rendered image of the designed modules together with some examples of produced parts.
- The printing assembly **physical dimensions** must allow it to be placed on the designated carrier of the printer and should be able to rotate freely to accommodate to different printing angles. This was achieved by removing the external metallic ring to use more efficiently the available space and a redesign of the main body of the assembly. Furthermore, axial symmetry was pursued to facilitate the rotation of the assembly. However, the symmetry should not lead to a part that could be inserted at any angle, since that would create problems defining a reference position, so a zero-position was defined and enforced by design. The geometry of the assembly was designed so it does not collide with static elements such as the wiper cloth roller or the dropview camera. The final design for the assembly and how it fits on the printing platform can be seen in Figure 43.
- The **placement mechanism** needs to be stable to prevent vibrations but allow for a quick release of the assembly and protect the nozzle plates of the heads from over-pressure in case that an obstacle is encountered in the z-direction. Consequently, the original kinematic mount was emulated with 4 neodymium disc magnets (N701-RB, Eclipse Magnetics Ltd, UK) and positioning elements.
- Initial attempts were performed where the **centre of mass** of the heaviest elements (mainly the printheads and the heaters) was situated in a lower position to provide additional stability against vibrations but it resulted in a longer assembly than the original. This is not on its own a problem since the reference positions can be modified to accommodate for this variation but it reduced further the available travel of the assembly in the z-direction, which ultimately reduces the printing envelope. Therefore, the nozzle plates were moved to a position above the original height of the inkjet heads and tighter dimensions were used in the main receptacle of the assembly, which prevented vibrations during operation and allowed for repeatable positions of the different elements.
- The **ink reservoirs** were the most challenging elements to place, since not only take most of the space in the upper part of the assembly but also are the most sensitive to mechanical manipulation. In other words, the reservoir needed to be clamped in place with little room for movement or the air pressure build inside of them would be disrupted and the printheads would be underfed. At the same time these elements needed to be of the most accessible elements of the assembly for re-filling and cleaning purposes. In the end, a solid hood was added and fixed on top of the main body of the assembly with a pair of columns and a lid holding the reservoirs in their position and applying enough pressure to keep them closed. The top lid is easily detachable by removing 2 screws, which facilitates re-filling of the reservoirs even without removing them from the system.

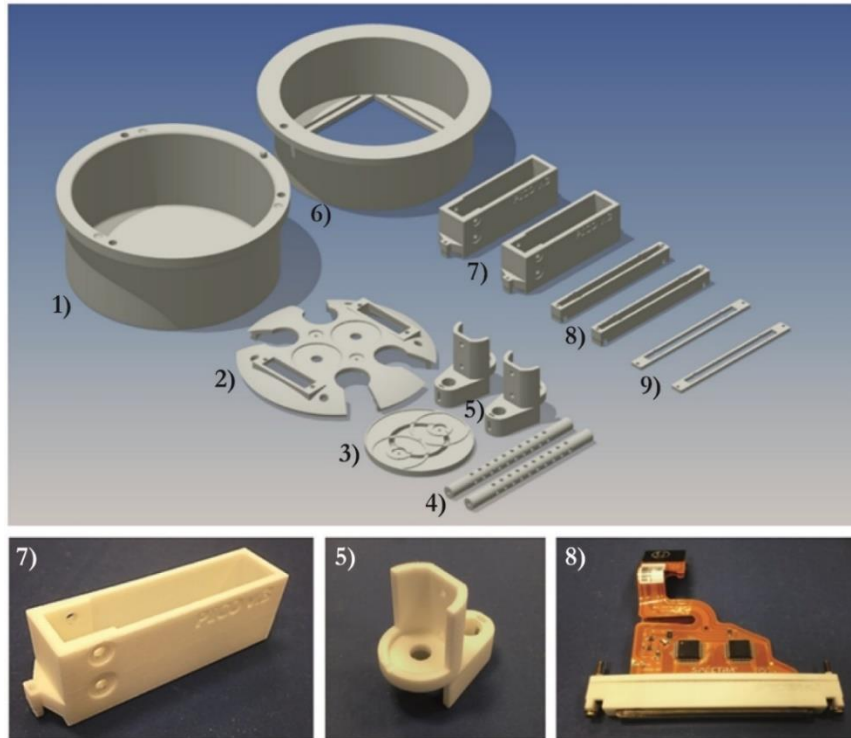


**Figure 42: Top)** Rendered image displaying the main modules of the printing assembly: assembly protective case (1), hood (2), lid of the columnar system (3), columns that maintain the reservoir in place (4), ink reservoir holders (5), main body of the assembly (6), 2 holders for the micro-dispensing valves (7), inkjet holders (8) and their top covers (9). The images on the **bottom** show real pictures of some of these elements fabricated in nylon via Laser Sintering (LS).

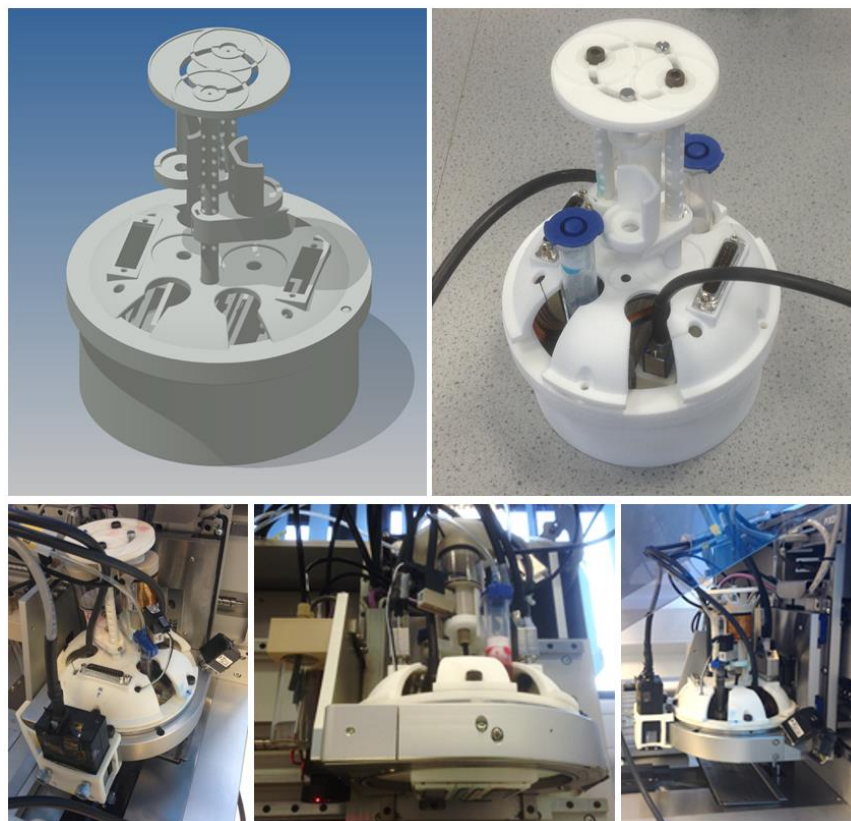


**Figure 43: Top)** Comparison between a rendered image of the designed assembly (left) and the printed part (right). **Bottom)** Fit of the assembly within the printing platform. In the central image the nozzle plates of the 4 dispensing heads can be seen, with the inkjet printheads in the middle and one micro-dispensing valve at each side. The images on the left and right show the position of the UV-lamp and its holder, directly attached to the body of the assembly.

The fast-iterative design and prototyping cycles that the hybrid assembly required were possible thanks to the availability of Additive Manufacturing systems such as LS and advanced CAD software like Inventor 2015 (Autodesk, USA), which was the main designing tool for this section. The combination of these tools allowed not only the creation of an assembly that fulfilled the requirements but also permitted complex parts like the dome that covers the assembly or the hollow columns, which helped to reduce the total weight of the part. For the laser sintering a P-100 Formiga (EOS GmbH Electro Optical Systems, Germany) loaded with Nylon PA12 was used. The mechanical properties of this material are suitable for the present application as long as the temperature stays below approximately 150 °C, since its melting temperature is 172 – 180 °C and the softening temperature B/50 is 163 °C according with the material data sheet. Neither the assembly nor the individual components have shown geometric variations during this project but a further study would be required at higher temperatures to ensure the repeatability of the process. The printed parts were cleaned with a brush and later grit blasted before rinsing them with water and allow them to dry at 40 °C in an oven for 2 hours.

#### **Printing signal synchronisation circuit**

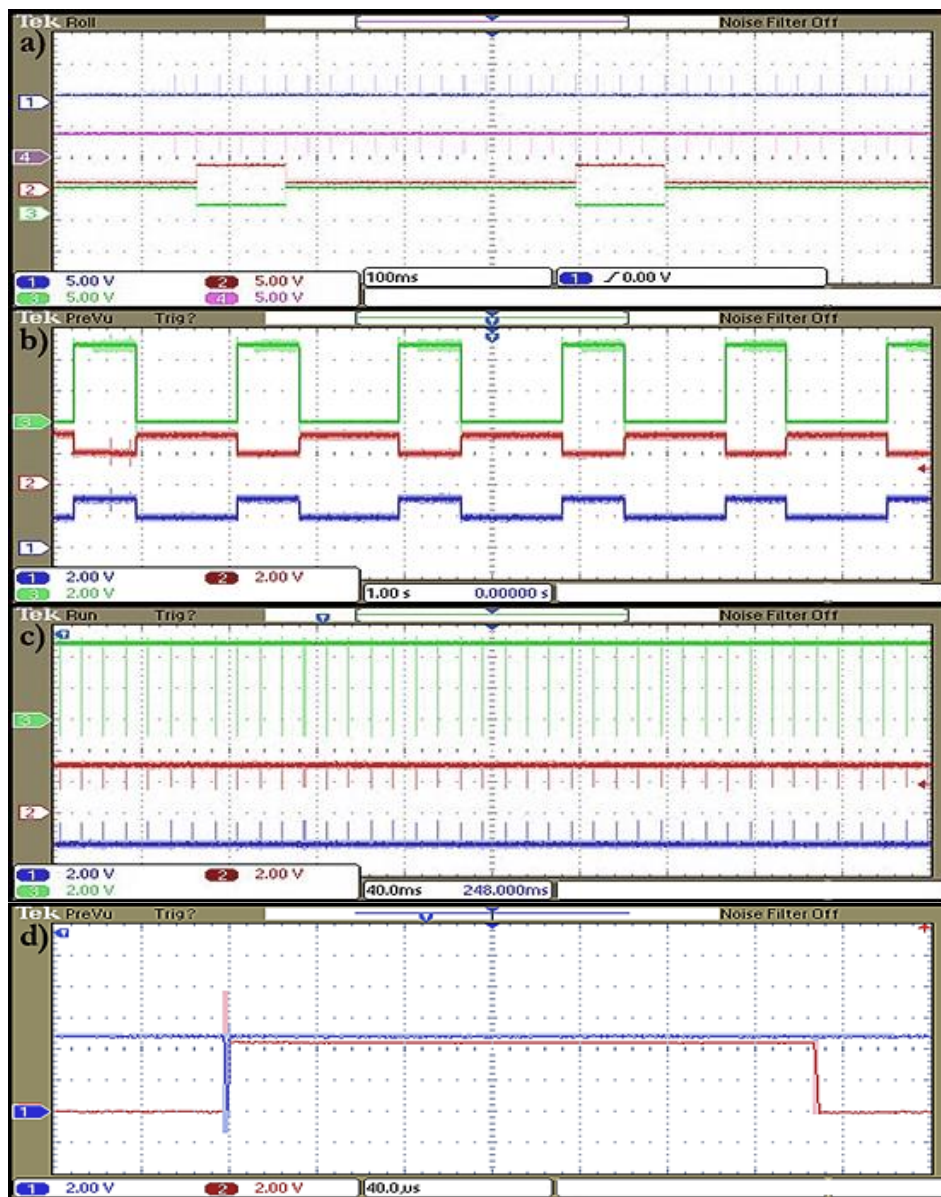
The printing platform can send the fire signal to the auxiliary port (AUX) instead of the printhead connectors, which is the base for the incorporation of the dispensing valves into the system. However, the output signal does not have the required characteristics to trigger the digital controller (DCON) that drives the PICO valves (Table 2), so a synchronization circuit was developed to translate the printing signal. Particularly, the output signal has a maximum amplitude of 5 V and a pulse width of 400 ns, which render the signal undetectable for the DCON.

**Table 2:** Required signal characteristics to externally trigger the micro-dispensing valve controller (EFD 2013)

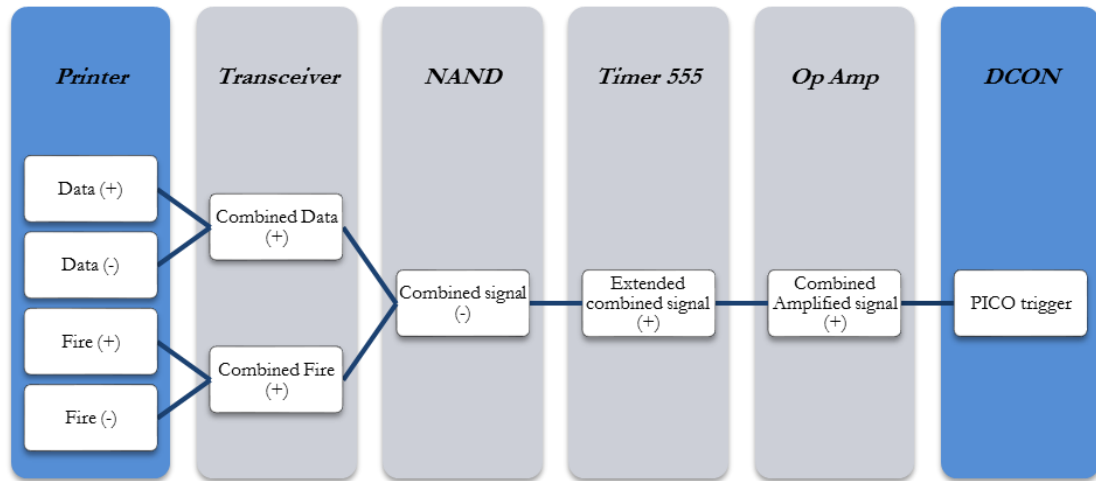
<b>Min pulse width</b>	<b>Max Load</b>	<b>Valve Closed</b>	<b>Valve Opened</b>
0.12 ms	50 mA	0 – 5 V	15 – 24 V

Figure 44a shows the 4 original output signals from the printing platform, namely Fire (or clock), Inverted Fire, Data and Inverted Data. It is worth noting that the Fire signals are constant at all times while the Data depend on the pattern being printed. These signals follow the technical standard RS-422 (PiXDRO B.V. 2011) and therefore they require appropriate **transceivers** (MAX485, Maxim, USA) to combine each pair of inverted and non-inverted signals into 2 stable signals of 5 V which will be positive or negative depending on how are connected to the transceiver (Figure 44b and c). The new

Fire and Data signals were combined using **NAND logic gates** (SN7400, Texas Instruments, USA) into a printing signal that will produce a negative pulse when both signals are active at the same time. The printing signal at this point already had the shape that was required to trigger the DCON in a drop-on-demand fashion but the voltage and length of the pulses were still not suitable to trigger the DCON. Consequently, a **Precision Timer** (Timer555, Texas Instruments, USA) was added to the circuit to increase the length of the incoming pulses from 600 ns to 260  $\mu$ s (Figure 44d). Finally, the voltage was raised from 5 V to 24 V using an **Operational Amplifier** (LM7372, Texas Instruments, USA). The process is summarised in Figure 45.



**Figure 44:** a) From top to bottom the signals displayed on the image are: Fire, Inverted Fire, Data and Inverted Data. This set of signals corresponds to two lines of 5 pixels each. The frequency of printing is set to 40 Hz. b) From top to bottom: Combined Data with positive configuration, Inverted Data and Data. c) From top to bottom: Combined Fire with negative configuration, Inverted Fire and Fire. d) From top to bottom the signals displayed on the image are: printing signal before the effect of the Precision Timer, Printing Signal after the effect of the Precision Timer.



**Figure 45:** Flow diagram of the evolution of the output signal from the printing platform to the digital controller (DCON) of the micro-dispensing valves. The intermediate blocks represent the different electronic elements included in the synchronisation circuit.

Initial testing was performed with a breadboard, prototyping jumper leads, 15-pins terminal block adaptors, connectors of different sizes and various electronic components. The signals were monitored with a Digital Phosphor Oscilloscope (DPO 2014, Tektronix, USA). The final set-up was wired in a circuit prototyping board (Perma-Proto, Adafruit, USA), soldered for reliability and robustness and enclosed in an insulating plastic box. Removable connectors were used for portability and to preserve the modularity of the system.

### 3.2.2.2 I/O increase and other sub-systems

Since more sub-systems need to be added to the set-up than there are free inputs and outputs available in the original printing system, it was decided to ignore these pre-configured I/O in favour of additional data acquisition devices. A script was written in C# capable of communicating via serial port with external micro-controllers that in turn control the different sub-systems. In the present work, the micro-controller is an Arduino UNO board (Arduino, Italy) based on an ATmega328P chip and counting with 14 digital I/O, 6 analogue inputs, USB connection and a clock speed of 16 MHz. The board was programmed to read continuously the serial port, ignore superfluous signals and react to specific commands sent by the main system using a simple *switch* function. This has the implication that each sub-system needs to be used sequentially instead of simultaneously, but this is not an issue since the external elements are not required to work in parallel at any time. In the current configuration of the system there is only one micro-controller in charge of the different external devices, but there is nothing preventing multiple controllers to work together for more complex computation. In fact, as it will be further explained in

the methodology section (Chapter 4), a second micro-controller can be added to the system to develop specific tasks without interfering with the main board. Some examples of the secondary micro-controller's uses are the measurement of temperatures during thermal treatment using a thermocouple or the measurements in real time of the resistance of a printed track.

#### **PICO switching via relay**

The transformation of the printing signal from the printer to trigger the micro-dispensing valves have been previously explained. However, if two valves are used within the same configuration there is an additional limitation that should be considered, and that is the fact that there is only one printing signal. This signal could be routed simultaneously to both heads if the objective was to print the same pattern twice with an offset. However, in the present work the aim is to use both heads to deposit different materials sequentially, so a mechanical relay was added to physically switch the signal from one head to the other. Therefore, the serial port can be used to switch where the printing signal is sent to select the active head.

#### **Cleaning station**

The existing cleaning system of the material printer, consisting originally on a rolling cloth that require manual manipulation, was automated to reduce the amount of time that the printer case had to remain open and limit the materials' exposure to external factors such as UV-radiation. To do this, a **continuous rotation servo motor** (900-00008 Parallax, USA), held in place by a custom designed part printed by Fused Deposition Modelling (K8200, Velleman) and an adaptor fabricated by Laser Sintering was added to the existing cleaning station.

#### **UV-lamp**

To cure photo-sensitive polymers a UV-lamp (FireFly 25x10, Phoseon Technology, USA) was installed on the outside of the print assembly, as can be seen in Figure 46 and previously in Figure 43. This position, 12 cm away from the centre of the assembly permits to cure the deposited patterns without allowing a significant amount of the emitted radiation to reach the nozzle plates due to reflexion on the substrate, which would cause severe nozzle clogging. The unit has its own power source and a trigger mechanism that can be used to switch on and off the lamp from the micro-controller.

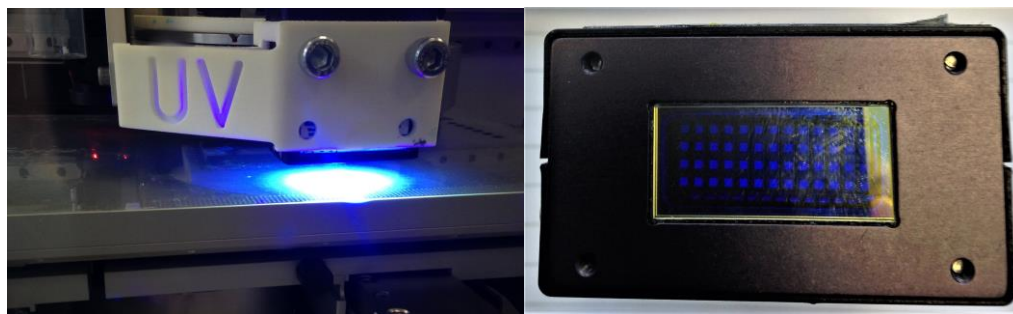


**Figure 46: Left)** The UV-lamp was secured by a bespoke printed holder. From the variation in brightness it can be assessed that the middle region under the lamp was exposed to a higher intensity than the outer area. **Right)** Front image of the lamp emitter window (20 x 10 mm) displaying the integrated array of 52 high power UV-LEDs.

The lamp itself has a peak irradiance of  $4 \text{ W/cm}^2$  and an emission peak at 395 nm, with a spread of 380 – 420 nm (Phoseon Technology 2013), corresponding with the near UV or UV-A region (Ryer 1997). The emission window is 20 by 10 mm and is composed of an array of 52 high power UV-LEDs. The semiconductor nature of the radiant element grants a narrow spectral emission, low power operation, moderated working temperatures and fast on/off cycles (50 ms in this case), which ultimately allows for intensity regulation by pulse width modulation (PWM). For the present work, however, a reduction of the intensity was not required. Furthermore, to protect the material from external radiation and the user from the UV-light emitted inside, the transparent case of the printer was covered in clear UV-protective film (Clear UV, The Window Film Company, UK).

### NIR-lamp

Thermal treatments are one of the most common form of post-process in industry, they are capable of accelerating solvent evaporation, initiate chemical reactions, melt substances and sinter granulated materials. Infrared radiation is one of many available heat transfer methods but its core characteristics made it a suitable option for the present application. Specifically, radiant heat does not require an intermediate medium since it is based on the absorption of electromagnetic radiation. Similarly, the waves can be directed towards the target by focusing and reflection mechanisms, which limit the exposure of other parts of the system and reduces energy losses. Moreover, since different materials absorb different wavelengths, it is possible to design processes that affect a particular element without significantly interacting with others. This is especially useful to heat printed materials without degrading sensitive substrates such as paper or polymer films, which typically have working temperatures below  $100 \text{ }^\circ\text{C}$  (Wünscher et al. 2014). Photonic sintering has also been demonstrated to be an effective way of creating conductive tracks from metallic nanoparticle-based inks (Cherrington et al. 2011) (Wünscher et al. 2014) (Tobjörk et al. 2012) (Sowade et al. 2015).

For the present work, a 600 W twin tube near infrared (NIR) lamp (Heraeus Noblelight Ltd., UK) was selected for its relatively narrow emission spectrum (Figure 47) centered around  $1.3\ \mu\text{m}$  and its high maximum irradiance ( $20\ \text{W}/\text{cm}^2$ ). The small dimensions of the device ( $23\ \times\ 11\ \text{mm}$ ) allowed for a non-intrusive implementation in the system in the form of a custom bridge mount fabricated with laser sintered nylon (PA12) parts and metal frames, as can be seen in Figure 47. The height and lateral positions of the lamp holder are manually adjustable and have location markers for consistent placement. The structure is electrically grounded to avoid charge build up and shocks.

The lamp requires 110 V and 600 W to operate at full power, but a way of regulating the emitted intensity is highly advantageous. One option would be to switch the emitter on and off, but this would produce a high inrush current for a small period of time due to induction, which destabilises the output and can damage the equipment. Instead, a phase control dimmer (Pro-dim 10 master, Anytronics Ltd., UK) powered at 110 V via transformer (110 V portable transformer, Carroll and Meynell Transformers, UK) is used. This external unit has a dual 0 – 10 V analogue input, which connected to the output of the Arduino board allows fine and fast control over the intensity of the lamp at all times. The output signal of the Arduino is 5 V, which only covers half the range of the dimmer's input scale and therefore limits the available power to approximately half the maximum. This was intentional and preferred over using an amplified 10 V signal since it serves as a safeguard for overheating the system and provides more resolution over the available range. Furthermore, since the relationship between the input voltage and the emitted radiation is not necessarily linear, from this point onwards the input voltages will be referred in terms of the percentage of input voltage applied, where 100 % relates with a 10 V signal that would produce the maximum output of the lamp.

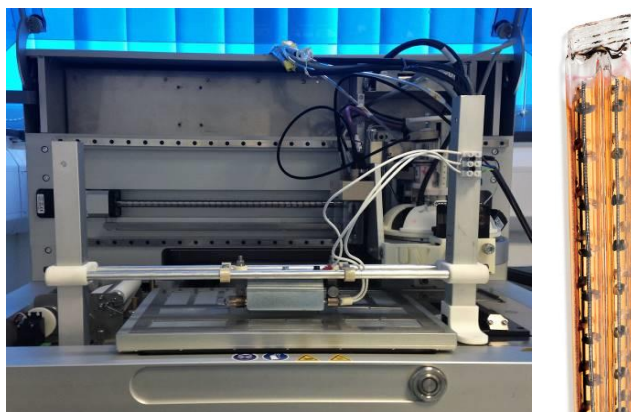


**Figure 47:** Left) IR-lamp custom-made holder with manual adjustable positions in Z and X. Right) Real image of the twin tube emitter with its gold back reflector (Heraeus Noblelight Ltd., UK). The peak emission is reached at  $1.3\ \mu\text{m}$ .

The heating capabilities of the system at different input voltage values were tested using a digital thermometer (TENMA, 72-7712, TENMA, USA) equipped with a K-probe and a USB interface that allows for data collection with 0.1 °C resolution at a frequency of 1 Hz. The thermocouple end was fixed to a glass slide of 1 mm thickness with high temperature resistant polyimide tape and covered evenly with non-silicone heat transfer paste (HTC10S, Electrolube, UK) to ensure homogeneous thermal distribution. The distance between the thermocouple and the lamp was set to 10 mm and the exposure time fixed at 60 s. Then, using a power supply, a voltage between 0 and 10 V was administered to the analogue input of the dimmer, which in turn switched on the lamp at the correspondent power. The emitted radiation heated the thermocouple and thermal paste, incrementing the detected temperature. The heat is diffused through the glass slide towards the metallic substrate, since the thermal conductivity of both materials are higher than air. To provide a common start temperature, the system was cooled down before each measurement using air extraction and an air blower until the monitored temperature is  $25 \pm 5$  °C, each setting was measured 3 times and then averaged. Precisely because of the high dependency of the heat transfer mechanisms on the thermal conductivity and thickness of the involved materials, the results of these experiments cannot be directly transferred to other situations. The conclusions extracted however, are useful for the understanding of the system and present good agreement with expectations, since higher power settings result in higher temperatures, as can be seen in Figure 48. All the profiles experience a rapid temperature increase when the light is switched on, reaching over 80 % of their maximum temperature within 15 s. The initial rise is followed by a linear region of positive slope as the overall temperature is augmented. The slope of these regions is small and a certain equilibrium is reached for power settings below 60 % but above that it seems to keep increasing without finding a plateau. The switch off behaviour is similar to the rise trend, with approximately 70 % of temperature reduction in 20 s. Nevertheless, the rapid reaction of the lamp does not prevent the higher power settings to require longer cooling times to reach the original temperature. It is also noteworthy that temperatures above 200 °C are achieved for input voltages below 50 %, which is the domain of the Arduino board (0 to 5 V). This, together with the fact that input voltages below 20 % have no noticeably impact on the temperature of the sample contribute to select the region between 2 and 5 V as the working range that the Arduino board will use to control the power of the lamp. Using the calibration curve shown in Figure 48 it is possible to interpolate the expected temperatures for any given input voltage using a parabolic model.

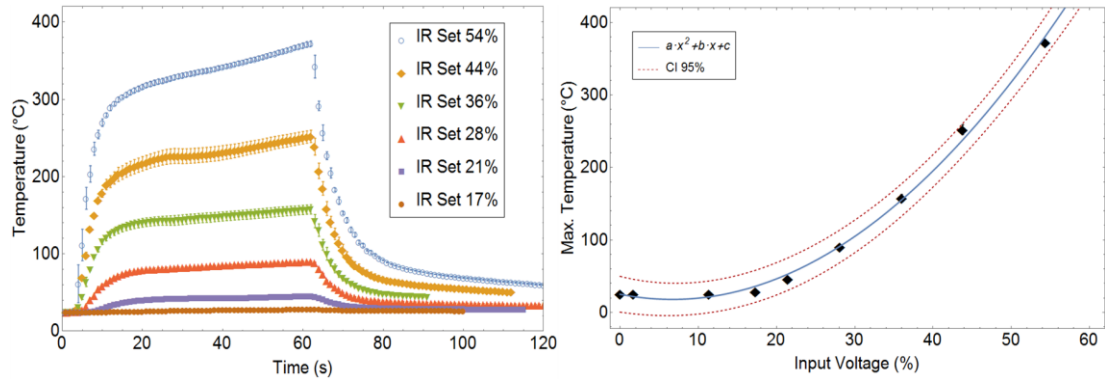


**Figure 48:** Temperature response of a thermocouple embedded in thermal paste and placed on a glass slide at 10 mm of the NIR lamp. Each exposition was 60 s and the power was equivalent to the dimmer's input voltage (0 – 10 V). The left graph shows the thermal behaviour over time while the right figure displays the maximum temperatures achieved compared with the input voltage. A parabolic model was fitted to the experimental data to serve as a calibration curve, the results of the fit were  $a = 0.160 \pm 0.010 \text{ } ^\circ\text{C}^{-1}$ ,  $b = -2.1 \pm 0.5$ ,  $c = 25 \pm 6 \text{ } ^\circ\text{C}$  with an adjusted  $r^2$  of 0.998.

To study the influence of distance between the sample and the lamp another experiment was performed. This time the slide containing the thermocouple was placed in an incrementing stack of glass slides and the temperature monitored in every step at a constant power setting of 60 % and an active time of 60 s. The cooling between samples was performed in the same way than before and each height is measured 3 times, the results can be seen in Figure 49. The maximum temperature after one minute of exposition decreases linearly with the increment of the distance, which is probably due to the close position of the sensor and the extensive nature of the dual tube lamp. It is noteworthy that a variation of only 50 °C is observed for a range of 8 mm, which is 3 times the maximum sample height printed with the current configuration. This gives additional support to the decision of keeping the power level constant during the whole fabrication process, even though it is acknowledged that the sample's height will gradually increase. Nevertheless, as previously mentioned, since the materials involved in the experiment, i.e. the metal probe, the thermal paste and the glass slides, have different thermal conductivities than the materials that are going to be processed in the system, these results can only be taken as orientative. Considering that the thermal conductivity of glass is relatively high it is expected that the temperatures observed for the printed materials are lower. Regardless of their magnitude, higher temperatures result in longer required cooling times, as can also be seen in the comparison between 3 and 9 mm of distance during a longer time (Figure 49). During the recording of the presented data no manual cooling was performed and therefore all the energy loss can be attributed to heat diffusion to the environment.

As it will be shown in future sections, the lack of cooling introduces uncontrollability on the temperature of the sample, that instead of reaching an equilibrium tend to increment overtime. Furthermore, the excess radiation can heat its surroundings

which is potentially problematic for the nozzles, which can block due to increased solvent evaporation rates. This could be addressed by adding a cooling system based on circulating liquid around the lamp or a fan directed to a heat sink on the cover. The main issue of the fan approach is that it would introduce air currents that can affect the printing repeatability, which is the reason why it was originally not implemented. Nevertheless, the current configuration places the heat source as far from the the printing head as possible, which combined with the gold plate reflector of the lamp and its close distance with the sample reduces greatly the radiation that reaches the print assembly. Additionally, since the substrate and the main body of the instrument are made of metal and represent the dominating mass of the system it acts as a heat sink that further limits the heating of the printing chamber. Finally, both the substrate and the printheads have internal thermistors that control the temperature, which were used to monitor the system at all times. Using these control mechanisms, the observed temperature on the printheads did not increase more than 5 °C even after hours of operation, causing no problems to either their performance or the properties of the printed parts.

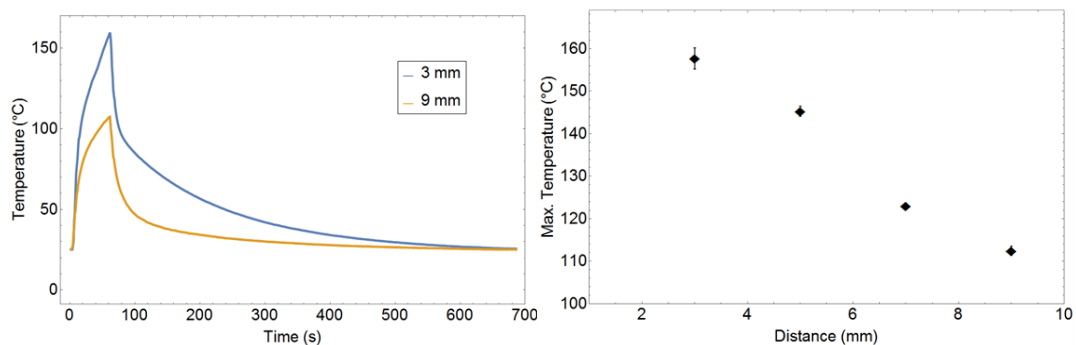


**Figure 49:** Thermal curves at different distances between the sample and the NIR lamp. The top figure shows the behaviour of the sample at 3 and 9 mm during almost 12 minutes. On the bottom, the maximum temperatures achieved during 1 minute of exposition for 4 different distances are shown.

### 3.2.2.3 Modified printing cycle

The redesign and addition of numerous sub-systems would not be complete without a revision of the process and an appropriate modification of the control software. This is especially important since some of the changes made affect core elements of the original system such as the number and nature of printheads and the evolution from 2D to 3D fabrication. Figure 50 shows the basic process flow of the developed system and how it compares it to the unmodified method to highlight the differences. The specific changes affecting calibration, design, file creation, printing, curing and inspection will be covered in the following sections, but first is key to explain the overall change of approach. In the original **process for the dual assembly** the user must prepare the so-called *recipe*,

which consisted in a printing file per head and a collection of parameters such pattern size, print speed, resolution and maintenance actions. Then, the active head is selected and relevant settings like temperature, printing pulse and usable nozzles are introduced. Finally, the user launches the print job, which combines the information regarding the dispensing heads, the file and the printing parameters to create the machine instructions that would lead to a compatible set of movements and a print signal that eventually prints the desired pattern on the substrate. This process can easily be modified to automatically change the printing file and print layer upon layer but its main limitations are the independence of the head selection with the recipe and the fact that most of the printing parameters are fixed on said recipe, forcing them through all the process.

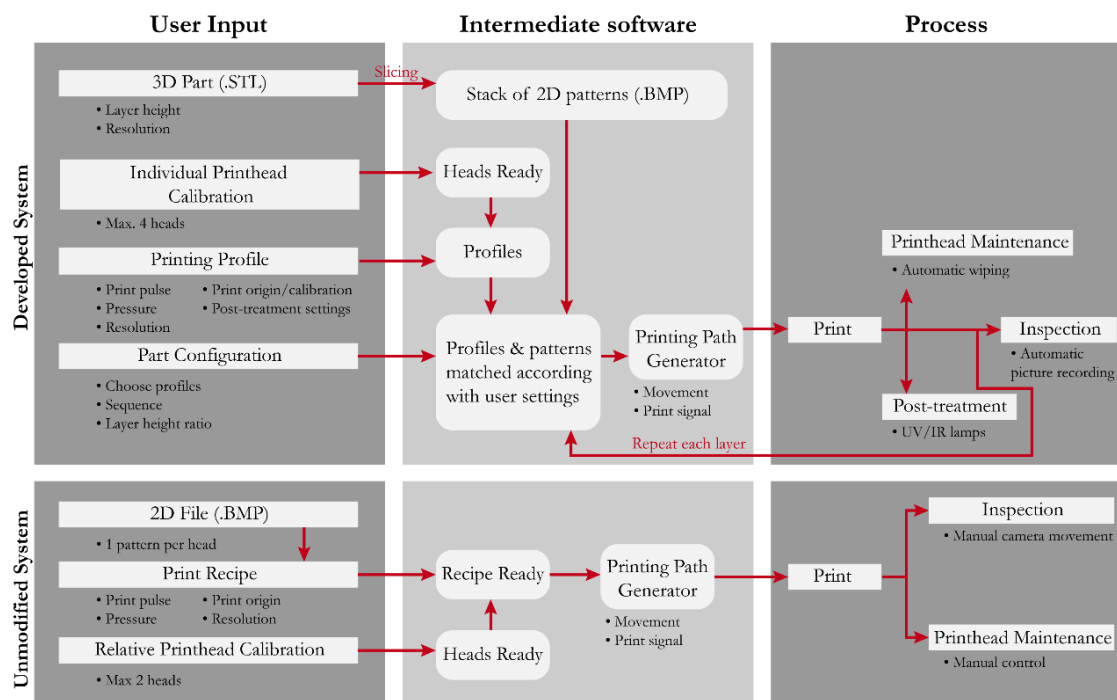


**Figure 50:** Flow diagram of both the printing process of an unaltered dual system (LP50) and the here developed hybrid approach.

The **modified process** for the hybrid assembly is structured differently, splitting the function of the *recipes* into two separate structures, namely *printing profiles* and the *part configurator* (the main code for these two structures is shown in Appendix A1). The *printing profiles* in this case are very similar to the *recipes* with the main difference that they do not contain any printing file but are always linked to a physical dispensing head. These profiles also contain information about the maintenance and post-process stages and is consequently capable of communicating with the required sub-systems. The *printing profiles* are not limited to the number of heads, so it is entirely possible to create two profiles that use the same physical head but behave differently during printing. Alternatively, the *part*

*configurator* structure act as a moderator between the different printing profiles and the printing files. These files are the result of slicing a 3D CAD design into individual bitmaps. Thus, once the user introduces the sequence of print profiles, the part configurator makes sure that each head is correctly paired with their respective files and executed in the right order. From this point onwards, the process again resembles its original counterpart with the addition of calls to the external sub-systems to perform advanced maintenance and post-process routines. Finally, the camera of the system is used to scan over the printed structure at certain intervals to image its evolution.

### **Calibration**

The calibration of an individual printhead is central for accurate performance, but it becomes crucial for a multi-material system. Specifically, an acceptable calibration will ensure that the relative positioning of the different patterns from the different printheads involved in each layer are correct. This is even more relevant for conductive tracks, since a misplacement of just a few microns can cause discontinuities resulting in interrupted tracks or short circuits. The calibration of every head in this work was performed with the typical approach of printing specific patterns such as a solid square or a straight line and study their shape and relative position with the print origin to introduce corrections in the software to achieve consistent and predictable results. This was performed using the integrated vision system that allows the monitoring of the substrate. Fiducial and edge alignment are both possible and natively implemented on the printing platform. This process also allows for the identification of underperforming nozzles, that can be excluded.

The relevant aspect of this calibration stage in the present work is the deviation from the original procedure before the upgrades were introduced. Specifically, the Dual Spectra assembly had to undergo a complicated manual adjustment to align both heads before performing the camera-based calibration previously described. However, this approach is demanding on the assembly tolerances, where a small deviation can cause noticeable defects. Consequently, each printhead of the hybrid assembly here developed was calibrated individually with respect to the same point, creating a common reference system. This approach was tested numerous times with the 4 printheads with results indistinguishable from the original dual assembly. Figure 51 shows square calibration patterns of individual drops produced with the inkjet printheads mounted on the hybrid assembly and two different calibration inks. Apart from the high circularity and repeatability of the drops, it can be observed that in the drop-on-drop experiment the maximum deviations are below 5  $\mu\text{m}$ , represented in the images by the areas of only red or blue colour. This is consistent with the accuracy of the original system and therefore from here onwards the hybrid assembly is considered equivalent to the un-modified one.

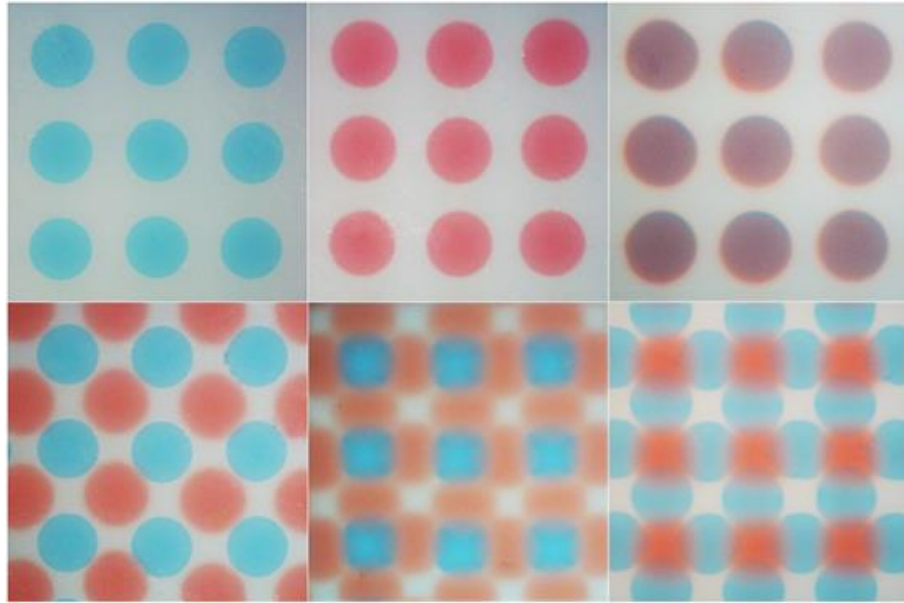


**Figure 51:** In the top row, individual drops of blue and red ink are displayed along with a drop-on-drop test that show colour mixing. From the last image a maximum deviation in deposition accuracy below 6% is obtained. In the bottom row, there are different drop patterns that further show the reliability of the system. The diameter of the blue and red drops is in average 83 and 88  $\mu\text{m}$  respectively and the substrate is photographic paper.

The successful calibration of the 4 heads in the system allowed the creation of multi material patterns without positioning issues, precise local mixing of deposited materials and the creation of complex patterns such as gradients. Examples of these features are shown in Figure 52.

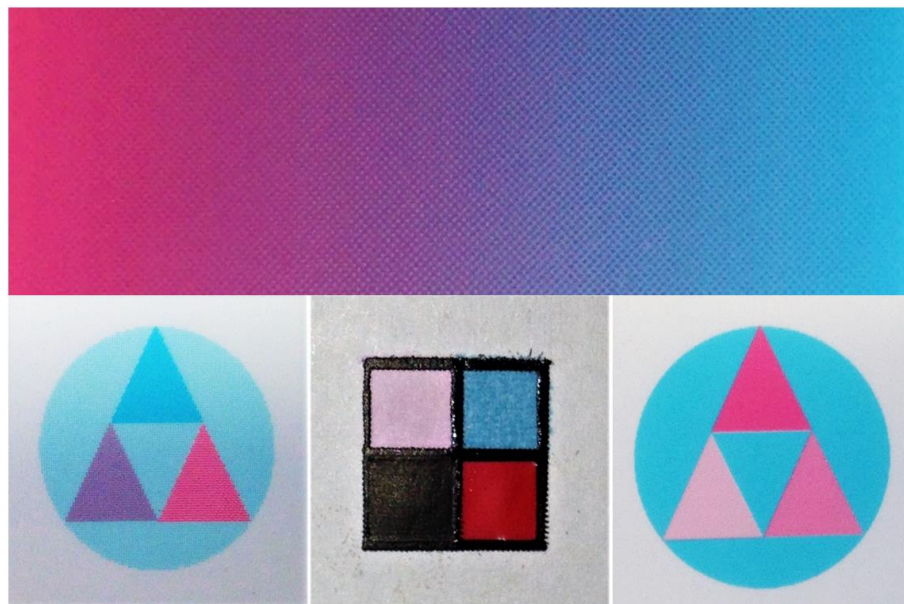


**Figure 52:** **Top** image shows a gradient created with blue and pink inks on conventional inkjet printheads. In the **bottom** row, examples of multi-material placement and mixing are displayed. In the left and right images, only 2 low viscosity materials are used and the different colours are the result of various printing patterns, different resolutions and material mixing. In the middle image the 4 heads of the assembly were working in the same process, depositing high viscosity (black and red paint) and low viscosity (pink and blue) materials.

### Design, slicing and printing strategy

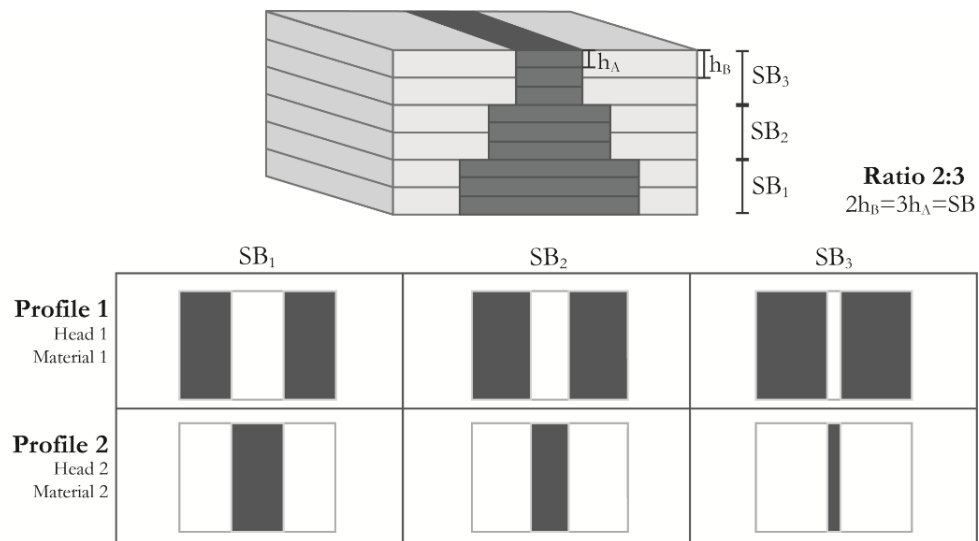


**Figure 53:** Printing strategy diagram showing the structural blocks (SB) and material layers ( $h_A$  and  $h_B$ ) for a simple multi-material structure. The ratio 2:3 corresponds to this example, where 2 layers of material B are needed to achieve the same height than 3 layers of material A. This reduces the effect of layer-mismatch and allow successful 3D fabrication. The printing files for each profile and structural block are also given.

The layer-by-layer approach of AM seems ideal for a process like inkjet, where only one 2D pattern can be produced at a time. However, when it comes to design it is impractical to conceptualise the object as a collection of individual 2D files. Instead, CAD software is used to create a 3D file that contains the geometry of the object, which can be shared and modified at any given time. Still, this file does not hold any information regarding the process that will be used to fabricate the part and therefore it should be translated into instructions that the system can understand. In the present work, the 3D file is exported in STL format and is later sliced with in house developed code based on Matlab (Mathworks, USA). The algorithm asks the user for an STL file, the desired resolution and the layer thickness for the process, and creates a collection of bitmaps that is saved in a separated folder under a custom naming system that will allow other parts of the software to recognise their position and associated *printing profile*.

Nevertheless, the situation gets more complicated due to the presence of 4 heads depositing materials with very different characteristics. Some of these properties, like the different volume and spreading behaviour of the drops or their solidification requirements can be addressed with customised printing resolutions and post-processing included in their respective *printing profiles*. However, the difference in layer thickness among materials once the films are deposited and treated cannot be compensated easily in these profiles. Therefore, the concept of *structural blocks* is introduced to avoid the related geometric issues that would result from ignoring such height miss-match of certain areas of the part. A

*structural block* is a slice of the object that has the same height for all the materials involved, achieved by an appropriate ratio of material layers, i.e. the height of all the materials is appropriately compensated. The printing file does not change during a *structural block*, it is just repeated the required number of times. Consequently, the thickness of the structural blocks is the main limitation to the resolution of the part in the z-direction. The difference between *structural blocks* and *material layers* is represented in Figure 53 for a simple object made from 2 materials. It is worth remembering that the order of the printing profiles (or printing sequence) is under user control through the *part configurator*. The order of the material deposition is typically defined by either the spreading behaviour or post-curing conditions of each material. For instance, fluids that spread less on the substrate are generally deposited first to increase the resolution of the rest of materials, since the first fluid can create a barrier or hole to be filled. A similar approach of height compensation via *structural blocks* is followed when a solid component is embedded on the printing part during the building process.

### **Printing**

The printing stage, once the file and dispensing head are selected and the printing path has been calculated, has remained mainly unchanged compared with the original process. The main difference resides on the addition of z-movement between layers to ensure consistent standoff distance (or gap) between the nozzle plate and the substrate. This is addressed by incrementing the reference position of the substrate after each layer according with the expected layer thickness. Errors in the estimation of the material thickness affect the process after several layers. Specifically, an overestimation of such thickness would lead to printing distances larger than 1 mm, which can potentially introduce errors in the positioning of drops. This, however, has proven not to be very problematic for the micro-dispensing valves, which are more standoff independent than typical PIJ printheads due to their increased drop speed. An underestimation of the layer thickness can lead to a decreasing distance between the nozzle plate and the substrate, which in extreme cases can result in fluid dragging and failed prints. For instance, a layer underestimation of 10  $\mu\text{m}$  will cause the nozzle plate to drag on the deposited material after 100 layers assuming a standoff distance of 1 mm. Considering that the layers for high viscosity materials are in the order of tens of microns and that the system can only move in the z-axis 25 mm, this is not normally a real problem. Since the micro-dispensing valve is less sensitive to print height, this potential issue can be minimised by increasing the standoff distance to 1.5 or 2 mm.

### **Post-processing**

The main aspects for post-processing have already been discussed in previous sections. The only part left to explain are the actual processing options, but before going into detail for each method it is worth explaining their common general approach. Specifically, even though the lamps are placed in different positions on the machine, both approaches are based on the movement of the platform respect to the radiant elements at a controlled speed. This allows for more control over the process and helps to homogenise the power distribution on the sample, since the area directly below the centre of the lamps is more exposed to radiation than the neighbour sections. This inhomogeneity is more relevant for the NIR lamp than for the UV, since the latter is LED-based and presents a more consistent emission, but its larger area compared with the printed samples helps to minimise this effect.

In the case of the **NIR treatment** the available parameters are the power level of the unit, the height of the lamp, the speed of the platform and the number of repetitions. The power level of the lamp is controlled by the micro-controller and the external dimmer and was discussed in an earlier section. In the current thesis, the power level associated to a *printing profile* remains unchanged under the assumption that the objects are of small height and the process relatively short. There is an obvious relation between the height of the sample relative to the lamp and the radiation intensity that it experiences. This could be addressed in the future by introducing a decreasing heat ramp that compensates for the part growth, but this is not pursued for this work. The height of the lamp is manually adjustable, but it stays at 10 mm unless stated otherwise. Variations are possible to accommodate different sample heights. This adjustability provides an alternative way of reducing the amount of power received by the substrate but is more ineffective than the power regulation and therefore will not be used. Similarly, the lateral position (x-direction) of the lamp should be manually placed before the beginning of the fabrication process, which should overlap with the print origin. The length of the NIR lamp allows for the creation of sufficiently large samples for the present study but it limits the maximum building envelope nonetheless. An easy way of solving this constraint would be to introduce a motorised holder capable of moving in the x-direction and perhaps also in the z-axis to provide further flexibility. This would be entirely compatible with the current process flow based on sub-systems and was not implemented for the solely reason of time constraints.

The case of the **UV-lamp** is simpler than the NIR emitter because it is mounted on the print assembly itself, does not heat up as much and has its own cooling fan that can be activated independently. The main decision regarding the UV-curing of materials is when to do it, since this will decide the amount of spreading that is allowed and consequently controls the size of the drops. For materials of high viscosity like the UV-resin used in this work it is possible to print the whole layer and cure it at the end, which results in slightly bigger features but ensures a smooth finish without distinction between individual rows of fluid. An advantage of this method is that the process is independent of printing, which allows the selection of parameters such as the distance between the sample and the lamp (curing gap) and the speed. Alternatively, the UV-lamp can be working during the printing stage, which cures the deposited materials faster if a permanent offset is included in the printing path. This results in smaller droplets and is decisive for materials with lower viscosity and faster spreading, like the TPGDA also used in this work. However, since it is linked to the printing stage, the curing gap and speed are determined by the generated printing path.

### **Pattern inspection**

Inspecting a printed pattern and comparing it with the original file is an effective way of understanding the process further and identify potential sources of error. However, storing numerous samples for future reference is not always possible or effective and to analyse them individually with external tools like optical microscopes tends to be slow. Therefore, it seems natural to use the native vision system on the printing platform to photograph the samples for analysis and future reference. When an image of the sample is required, the system moves the printview camera to the calibrated print origin, illuminates it with the adjustable light sources and takes a monochrome image of the field of view (FOV). This approach was further refined to provide more functionality and the following picture modes were created:

- **Scanning mode:** The assembly moves the camera in a scanning pattern of defined dimensions, taking one picture at a time until the whole area is covered. These images can be stitched together later using external software.
- **Timed mode:** A single area is photographed at a timed interval that allows for monitoring of dynamic processes such as drying or spreading. The camera is limited to 30 FPS, which combined with the time required to move the camera on top of a printed feature causes this mode to be incapable of recording immediate response after ejection, like drop impact or recoiling.

### 3.2.2.4 Final set-up

After the additions and modifications described in this chapter, the hybrid printing system developed for this work is ready. Figure 54 shows an image of its final form and highlights the following improvements over the original system.

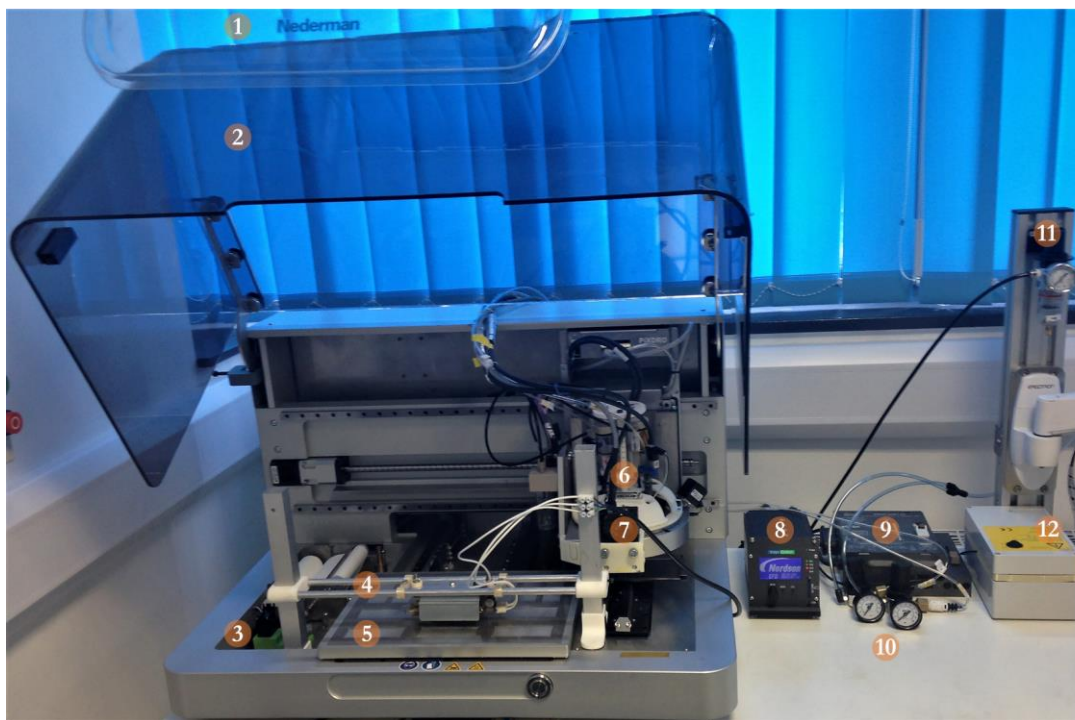


**Figure 54:** Final form of the developed hybrid system highlighting the modifications realised during the present work. The numbers correspond to: air extractor (1), UV-blocking case (2), automated cleaning station (3), IR-lamp (4), positioning plate for glass-slides (5), hybrid assembly holding 4 heads (2 micro-dispensing valves and 2 inkjet printheads) (6), UV-lamp (7), Digital Controller for the valves (8), dimmer module for the IR-lamp (9), pneumatic regulators (10), air filter (11) and Control unit for UV-lamp (12).

## 4. Experimental Methods and Materials

To fulfil the objectives described in section 1.3 and contribute to fill the identified gap in the knowledge of the use of HVJ and PIJ as a combined AM tool, the methodology described in this chapter is followed in the present work. The explanation of the various sub-systems included in the used apparatus are explained in Chapter 3.

### 4.1 Statistical analysis

Every observation has been recorded numerous times ( $N$ ) unless noted otherwise. Observations were recorded in random order whenever this was possible to mitigate unaccounted factors during the experiments and potential bias.

Direct measurements are represented as **measurement  $\pm$  instrument precision** and such precision is assumed to be of the same order of magnitude than the last significant figure given by the instrument if no precision is specifically stated. Alternatively, average results are expressed as **mean of  $N$  observations ( $\bar{x}$ )  $\pm$  sample standard error of the mean (SE)** (Montgomery & Runger 2011).

**Confidence intervals** based on the t-distribution are often presented to provide a clearer view of the results validity. This requires the assumption of a normal distribution for the collected observations, which is a reasonable and common conjecture in experimental sciences dealing with random errors. Moreover, the assumption can be justified appealing to the Central Limit Theorem of statistics, which states that the sum or average of a distribution of independent random variables approaches a normal distribution for sufficiently large number of measurements ( $N$ ) (Montgomery & Runger 2011). The values for the t-distribution can be calculated using the number of degrees of freedom ( $N-1$ ) and the desired percent confidence as inputs. The interpretation of these confidence intervals should not be made directly in terms of probability, since the true value for the magnitude under study will either be contained within the calculated range or it will not. Instead, this confidence interval states that regardless if the true value is contained in the interval, the method used to obtain such boundaries is correct  $100(1-\alpha)\%$  of the time (Montgomery & Runger 2011).

The uncertainty of indirect calculations ( $\delta f$ ) involving other magnitudes is calculated using the well-known approach of **propagation of uncertainties** based on the

partial derivatives of the function respect to each magnitude, providing that the measurements are independent from each other.

Additionally, in instances with a known relationship between variables, **least squares regressions** are used to obtain relevant information from the fitted function coefficients. This approach is more robust than an individual calculation because it allows the evaluation of the trend of data, which can be used to check the goodness of the relationship assumption in different situations and the experiment itself. Examples of this can be found in the experiments calculating the density of the fluids or the mass of individual drops, where obtaining negligible intercepts and linear trends for the tested ranges allows to discard significant influence of external effects such as solvent evaporation.

Analytical evaluation of the data fit's goodness is performed via **adjusted  $R^2$** , or adjusted square of the correlation coefficient. This coefficient can be understood as the percent of variance explained by the proposed model or, in other words, the fraction by which the variance of the error is less than the variance of the dependent variable.

The previously described calculations are performed with both Excel 2016 (Microsoft Office 2016, Microsoft Corporation, USA) and Wolfram Mathematica (Wolfram Mathematica 10.2.0.0, Wolfram Research, USA), unless noted otherwise.

## 4.2 Chosen materials

Following the reasoning explained in the Literature Review (Chapter 2), several materials were chosen for this work. The materials were used as provided by the manufacturers within their shelf life and under their recommended environmental conditions.

### 4.2.1 *Carbon Paint dispensed by HVJ*

A water-based **carbon paint** (Electric Paint, Bare Conductive, UK) was chosen as a conductive material and soluble support. The formulation consists of a natural resin (gum arabic) as the polymeric component, glycerin as humectant, water as solvent and activated carbon as conductive filler. This formulation fulfilled most of the requirements of an ideal testing material, such as electrically conductive, low-cost, non-toxic, easy to clean, high solid loading and non-Newtonian behaviour. The bottle was sealed and kept in an extra container, also sealed, to avoid solvent evaporation and kept at room temperature for storage.

#### 4.2.2 Photo-curable resin dispensed by HVJ

A transparent stereolithographic resin (Clear Resin FLGPCL03, Formlabs, USA) composed of a mixture of methacrylic acid esters and a photoinitiator with a curing wavelength of 405 nm was selected as a structural material. This fluid was kept in a sealed amber bottle capable of blocking UV-radiation to prevent partial curing before printing. The main reason for choosing this material is its low-toxicity and high viscosity compared with other available photo-curable resins. Moreover, this formulation has already proven to be useful for Additive Manufacturing, since it is an unaltered fluid used in stereolithography.

#### 4.2.3 Photo-curable low viscosity ink (TPGDA) dispensed by PIJ

Tripropylene Glycol Diacrylate (TPGDA) is one of the most common acrylate monomers used for photo-polymerisation (its chemical structure is shown in Figure 55). It was chosen as a low viscosity UV-curable ink due to its demonstrated printability, transparency and reasonable mechanical properties (He et al. 2017).

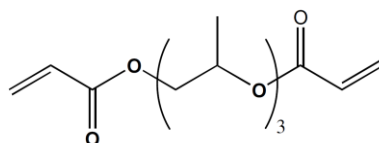


**Figure 55:** Skeletal formula of Tripropylene Glycol Diacrylate (TPGDA). In this convention, the lines represent chemical bonds between species. Carbon atoms are implicit at line ends and vertices unless another element is shown. Carbon-hydrogen bonds are assumed to complete the valence of 4 of each C atom. Figure from (Magdassi 2010).

TPGDA has been shown to withstand up to 350 °C without relevant loss of mass via decomposition (He et al. 2017), which is crucial considering that it must survive the thermal post-treatment that the conductive materials often require. The material was prepared in house by Dr Fan Zhang following the process described by He *et al.* 2017.

#### 4.2.4 Conductive polymer (PEDOT:PSS) dispensed by HVJ

A high viscosity aqueous dispersion of Poly(3,4-ethylenedioxythiophene)-poly(styrenesulfonate) (PEDOT:PSS) (Clevios S V3, Heraeus, Germany) was used as a conductive polymer (Figure 56). This material was chosen for its combination of conductivity, flexibility and transparency. Also, since this formulation in particular was designed for screen printing, notable shear thinning and apparent yield stress are expected. This commercial dispersion is synthesised as a polyelectrolyte complex that consists of polymeric cationic PEDOT and a polymeric counter ion, in this case polystyrenesulfonic acid (PSS) (Kirchmeyer & Reuter 2005). PSS is soluble in water, transparent and can easily

form films. By this method, gel nanoparticles with diameters in the range of 10 – 500 nm of PEDOT stabilized by PSS are formed, which explains why it is often referred as a dispersion rather than a solution. However, this structure of PEDOT at the core of the particles and PSS on the outside can be a problem for the conductivity of deposited films, since a dielectric barrier of PSS is formed, hindering the charges path. This is the reason why many commercial dispersions also include high boiling solvents such as dimethylsulfoxide (DMSO) and ethylene glycol (Elschner et al. 2012) as conductivity enhancers. In the present work, the organic solvents are Propylene Glycol and Diethylene Glycol, according with the provided technical information. These modifiers act as a plasticizer during the drying process, rearranging PEDOT and PSS chains within the film, producing larger interconnected conductive regions in the deposited layer. Therefore, a successful formulation needs to find a trade-off between higher conductivity with lower PSS concentrations or high dispersion stability at high PSS content. This equilibrium is typically found at the PEDOT:PSS ratio of 1:2.5 (Elschner et al. 2012). However, the delicate balance of these dispersions limits the total solid content of the material, which is typically kept below 5 wt% (Elschner et al. 2012).

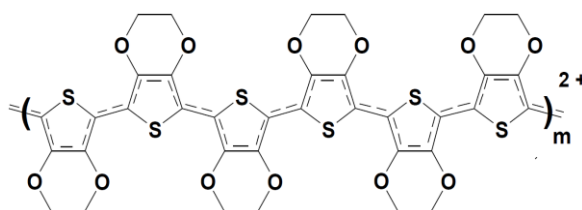


**Figure 56:** Skeletal formula of Poly(3,4-ethylenedioxythiophene)-poly(styrenesulfonate) (PEDOT:PSS). Figure from (Heraeus 2010).

#### 4.2.5 Hybrid silver paste dispensed by HVJ

A hybrid paste (TEC-PA-010, InkTec, South Korea) combining silver nanoparticles (<50 wt%), a soluble silver complex (< 50 wt%) and  $\alpha$ -Terpineol as a solvent (< 10 wt%) was selected. This paste combines two of the main areas regarding nanoparticle-based materials that were previously covered in the literature review (Chapter 2), i.e. solid-loaded formulation and metal-organic decomposition. Thus, the final solid volume deposited is not only dependent on the nanoparticle concentration but is further increased by the transformation of the organic silver compound into silver during the heating step. Specifically, the recommended thermal treatment for this formulation is 140 °C for 5 minutes, which are reasonable conditions for our printing system.

#### **4.2.6 Substrates**

Three main substrates were used in this work: glass slides, polycarbonate films and epoxy fiberglass boards.

##### **Glass slides**

Soda-lime glass substrates are attractive because they are optically transparent, can be manufactured in a wide range of thicknesses, are mechanically stable and can withstand temperatures up to approximately 500 °C (Malou et al. 2013)(Pilkington North America 2013). In contrast, these substrates are rigid, brittle and heavy compared to polymeric films. Pre-cleaned microscope glass slides (Cole-Parmer, UK) of 25 x 75 mm and a thickness of 1 mm are used. The box was kept in sealed, cool and dry environment. The slides were swept with compressed filtered air and pre-exposed to UV radiation at full intensity, 4 mm gap and 5 mm/s scanning speed to prevent potential surface differences based on later uneven exposure to UV.

##### **Flexible polymeric films**

Thin films of polymers such as polyethylene terephthalate (PET) and polycarbonate (PC) are a popular substrate for printed electronics due to their optical transparency, flexibility and low cost. Their main drawback is their poor heat capability, which limits the process to low applied tension and temperatures below 130 °C (Suganuma 2014) to avoid deformation and degradation of the films. Temperatures as high as 300 °C can be reached for polyimide (PI) (Suganuma 2014) at an increased cost. In this work, untreated polycarbonate films (Makrofol, Bayer) of 125 µm thickness are used. This film is selected as a substrate when flexibility is necessary. Temperatures above 130 °C could be used with minimal deformation of the films due to the vacuum capabilities of the printer substrate, which maintained the films flat when the polymer was softening due to excessive heat.

##### **Epoxy fiberglass and printed circuit boards (PCB)**

Printed circuit boards based on materials like epoxy fiberglass with integrated copper tracks are the most used substrate in multi-component electronic devices. These boards with pre-existing conductive tracks also solve another problem commonly encountered in printing electronics, which is the contact of the printed tracks with external devices and circuits. Thus, printing on the copper pads allowed easy access to the tracks with minimal added resistance, which facilitates the repeatable measurement of the conductivity of the tracks without altering them with external devices like the probes of a

multimeter. Since most PCBs are designed to be soldered on, they can withstand the effects of mild thermal treatments required to dry or sinter the conductive materials deposited on them. The chosen boards for the present work are FR4 epoxy fiberglass laminates (RE932, Roth Elektronik, Germany) of 1.5 mm thickness. FR4 is a fire retardant composite material composed of woven fiberglass cloth and an epoxy binder that can withstand temperatures up to 300 °C before degrading (Roth Elektronik GmbH n.d.)(Haugan & Dalsjo 2013). The copper pads are spaced 1.27 mm and have a thickness of 35 µm, while the through holes are 1 mm in diameter. Because these through holes act as a heat conductor towards the bottom of the plate and change noticeably the temperature recorded on its surface when they contact the metallic printer platform, a glass slide is always introduced between the PCBs and the printbed. This hinders heat transfer and narrows the thermal differences between the tests performed on glass slides and epoxy boards. The PCBs were rinsed with IPA, dried with filtered compressed air and stored in a sealed, dry and cool container. The boards were pre-exposed to UV radiation at full intensity, 4 mm gap and 5 mm/s scanning speed to prevent potential surface differences based on later uneven exposure to UV.

### 4.3 Materials characterization

#### 4.3.1 Density

The density of the fluids was calculated by depositing known volumes of material with a 500 µl glass syringe (Gastight 1700, Hamilton Company, USA) on intervals of 25 µl on an analytical laboratory balance (ABT 100-5M, KERN & SOHN GmbH, Germany) with a read-out of 0.01 mg at room temperature. The temperature of the syringe before deposition is monitored and set to  $25.00 \pm 0.05$  °C with a computer controlled air-cooled liquid recirculating chiller (ThermoCube, Solid State Cooling Systems, USA). The consecutive deposition of small volumes of material was performed as fast as possible and always concentrated in a single body of fluid to reduce the effect of evaporation. Instead of single measurements, 10 volume-mass points were captured per test spanning from 25 to 250 µl and repeating the test 3 times per fluid. A linear regression is performed on the data to obtain the density from the slope as explained in section 0.

#### 4.3.2 Particle size and size distribution

Dispersions of particles or flakes were studied with a laser diffraction particle size analyser (Mastersizer 3000, Malvern Instruments Ltd., UK) with exchangeable modules for wet (Hydro EV) and dry (Aero S) samples. The wet module was used to test the size of

the carbon flakes on the electric paint, the sample was dissolved in 550 ml of deionized water. Such dissolution is facilitated by the in-line stirring and sonicating elements. This distribution is commonly characterised by the d-values, which represent the diameter of the particle that divides the sample at a specific percentage. Particularly, D10, D50 and D90 mark the points at which 10, 50 and 90% of the particles are contained below these respective values. This technique requires the previous knowledge of the refractive index of the main components of the sample, but it has a wide database of materials to choose from, where common substances such as water ( $n_w = 1.33$ ) and carbon ( $n_c = 2.42$ ) can be found. Each sample was scanned 10 times and then averaged using the provided software (Mastersizer v3.40, Malvern Instruments Ltd., UK) to obtain a highly repeatable distribution with reduced noise. The same approach is used for the dry module with the difference that no solvent is required and the powder is carried by pressurised air. The samples are shaken at high frequencies to break potential agglomerates and facilitate the measurement of individual particles.

#### **4.3.3 Thermogravimetric Analysis (TGA)**

The solid loading of the materials characterised in this work and their behaviour at high temperatures was studied using a Thermogravimetric Analyser (TGA 4000, Perkin Elmer, USA) under nitrogen flow (20 ml/min). The experiments were performed with samples of approximately 10 mg at a 40 °C/min heating rate in the 30 – 800 °C temperature range. Temperatures higher than 350 °C are not expected during the post-process stage of the fabrication method, but testing at such high temperatures allows to observe evaporation patterns and degradation of the involved polymers, which in turn affects their mechanical stability. Therefore, both the TGA and its derivative, Derivative Thermogravimetric (DTG), are measured. Their  $T_{5\%}$ ,  $\Delta m_{250}$  and  $\Delta m_{600}$  parameters are tabulated, these being the temperature at which the sample has lost a 5% of mass, the mass loss at 250 °C and the mass loss at 600 °C, respectively. The fluids used in this work are compared to other materials to either clarify their structure or give an idea of their solid content in the jetting context. Particularly, the carbon paint was compared with a dissolution of gum arabic in water (Winsor & Newton, UK), PEDOT:PSS was matched to a jettable ink with lower viscosity (Clevios P Jet 700, Heraeus, Germany), the UV-curable resin was compared with TPGDA and the high viscosity silver paste is displayed alongside a jettable silver-based ink (Silverjet DGP-40LT-15C, Advanced Nano Product, Korea).

#### 4.3.4 Surface Tension

The **surface tension** of the fluids on air at 25 °C was characterised with a Drop Shape Analyser (DSA100, KRÜSS GmbH, Germany) (schematically described in Figure 57) by the Pendant Drop Method (Song & Springer 1996) on 15 drops of each fluid using the instrument's native software (DSA4, 1.1a, KRÜSS GmbH, Germany). Since the actual volume of the drop is used in the calculations, the images should be calibrated by reference with an object of known dimensions. It is common to use the outer diameter of the dispensing needle for this purpose, which can be measured with an electronic external micrometre (Schut Geometrical Technology). Two different blunt end stainless steel needle sizes were used, a G18 ( $1.270 \pm 0.013$  mm of outer diameter) for the carbon paint and photo-polymerisable resin and a G25 ( $0.510 \pm 0.002$  mm of outer diameter) for the PEDOT:PSS and the silver paste.

At the tip of the needle a suspended drop is allowed to form and rest. In this situation the profile of the drop is governed by the gravitational acceleration ( $g$ ) and surface tension ( $\sigma_{ST}$ ) and obeys the Young-Laplace equation, where  $R_1$  and  $R_2$  are the principal radii of curvature,  $\Delta P$  represents the difference in pressure due to hydrostatic effects respect to a reference point ( $P_0$ ) at the apex ( $z=0$ ) and  $\Delta\rho$  denotes the difference between the density of the fluid under study and the external phase, in this case air.

$$\sigma_{ST} \left( \frac{1}{R_1} + \frac{1}{R_2} \right) = \Delta P \equiv \Delta P_0 - \Delta\rho g z \quad (40)$$

This equation is typically used in its cylindrical coordinates form under the assumption of axial symmetry (Song & Springer 1996), which results in the dimensionless drop profile being described by a shape parameter ( $B$ ).  $B$  is defined as follows for a liquid-gas system:

$$B = \frac{1}{k_{apex}} \sqrt{\frac{\Delta\rho g}{\sigma_{ST}}} \quad (41)$$

In the case that the radius of the drop at the apex is used as the characteristic length for the system,  $B$  corresponds with the square root of the Bond number ( $B_0$ ) defined in equation 29. Therefore, providing that the density difference between the air (0.0012 g/ml at 1 atm and 25 °C (David R. Lide 2005)) and the fluids under test is known, a numerical method can be used to vary the value of  $B$  until the calculated drop profile

coincides with the actual recorded shape. It has been demonstrated that the aspect ratio of the drop plays an important role for the adequate fit of the model, determining the ideal range of  $B$  as between 0.6 and 0.7, since  $B < 0.5$  result in nearly spherical drops with little gravitational deformation and  $B > 0.75$  yields relatively short drops (Song & Springer 1996). Consequently, only measurements with  $B$  between 0.5 and 0.75 are accepted. As an additional check of the measurement, the software records the fit error (*FitE*) for each measurement as the mean deviation of the calculated contour line from the profile determined by the greyscale analysis. This was used to repeat observations that provide values for the fit below 10  $\mu\text{m}$ .

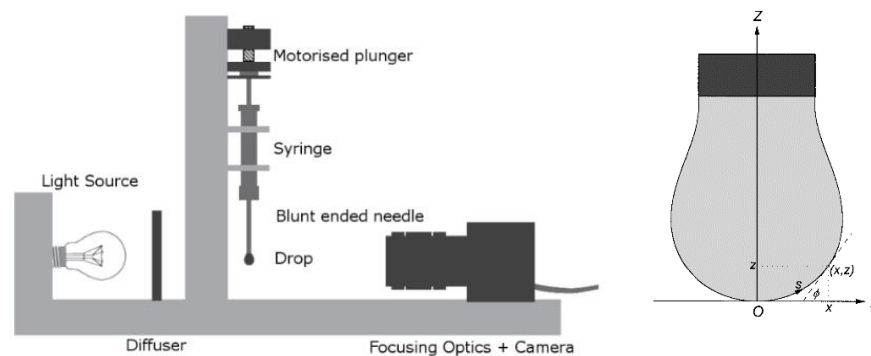


**Figure 57: Left)** Drop Shape Analysis schematics showing the optical and dispensing systems. **Right)** Geometry and graphical definition of the main parameters describing the drop profile, adapted from (Song & Springer 1996).

### 4.3.5 Viscosity

#### 4.3.5.1 Shear viscosity measurements and considerations

During inkjet printing the fluids are highly sheared in the internal pipes and ultimately in the micrometric nozzle. The applied shear rate range can be estimated from the discussion previously presented about flows in a pipe of known dimensions (equations 9 and 18) as  $10^5 - 10^7$  /s. This range is 2 to 4 orders of magnitude larger than the maximum achievable shear rate in a rotary rheometer. This is not generally a problem for Newtonian fluids if there is enough evidence to justify the extrapolation from medium shear rates to this upper range, however it is not that simple for the non-Newtonian fluids, which are expected to shear-thin according to the power-law up to a point where the upper Newtonian plateau is reached (Barnes et al. 1989). Therefore, to get a description of the fluids in the relevant shear region it is important to use shear rates as close to these values as possible.

Rotary rheometers are a well-known and effective method of measuring the shear viscosity of steady-state flow but the achievable shear rates are limited by several factors. Leaving aside the restriction imposed by the intrinsically limited applied stress, the main

problems arise below that technical threshold in the form of instabilities in the fluid, resulting in inaccurate data. One of these sources of error is the generation of **secondary flows** due to the high rotational speed required to achieve high shear rates, which in turn causes an artificial torque and apparent viscosity increase. For instance, it has been reported (Barnes 2000) that the critical angular speed ( $\omega_c$ ) in a cone-and-plate geometry (with known radius ( $a$ ) and angle ( $\theta$ )) for Newtonian fluids can be estimated based on a critical value for the Reynolds number as:

$$\frac{\rho\omega\theta^2 a^2}{\eta} > 10 \quad \rightarrow \quad \omega_c = \frac{10\eta}{\rho\theta^2 a^2} \quad (42)$$

The last expression show that more viscous flows are less affected by this issue, as it is expected, since the viscous forces help to dissipate the internal instabilities. However, more important is the fact that  $\omega_c \propto 1/(\theta^2 a^2)$ , which suggests that a cone with the smallest possible radius and angle would result in more stable measurements, or in other words, a smaller gap between the plates (since  $\theta a \sim h$  at small angles). Nevertheless, this problem is not the only influence of inertia in a rotary rheometer that can lead to artificial results, since at high rotation rates the centrifugal stresses will eventually become large enough to overcome the surface tension ( $\sigma_{ST}$ ) that keep the liquid between the plates of the rheometer, resulting in **radial sample migration** (Connelly & Greener 1985) and a subsequent decrease in the apparent viscosity. This can be estimated for a Newtonian fluid in a parallel-plates geometry of known radius ( $a$ ) and gap ( $h$ ) as:

$$\frac{3}{20}\rho(\omega_c^2 r^2) > \frac{\sigma_{ST}}{h} \quad \rightarrow \quad \dot{\gamma}_{app,c} = \frac{\omega_c r}{h} = \sqrt{\frac{20\sigma_{ST}}{3\rho h^3}} \quad (43)$$

The previous expression, as it was the case for the secondary flow example, shows an improvement of the shear range achievable for the instrument at reduced gaps. This, however, introduces the problem of accurate alignment of the plates (or **instrument zeroing**), since its influence on the measured viscosity increases as the gap decreases. Thus, correcting for such alignment and using gaps down to 30  $\mu\text{m}$ , shear rates of  $10^4 \text{ s}^{-1}$  have been achieved reliably (Pipe et al. 2008) (Connelly & Greener 1985). This maximum shear rate is still far from the jetting region and consequently a microfluidic rheometer, which takes advantage of its narrow dimensions, is used in combination with the rotary instrument to extend the shear rate as much as possible. Consequently, in this work a rotary

rheometer is used for the low and medium shear rate region ( $10^{-2}$  to  $\sim 10^2$  s $^{-1}$ ) and a micro-channel based rheometer is used for the higher range ( $>10^1$  s $^{-1}$ ). Then, a descriptive equation such as the Sisko model described in Equation (15), can be used to obtain their characteristic indexes and compare them in a common context. To do this in a consistent manner, the data obtained on the rotary rheometer was down-sampled from 10 to 5 points per decade to be more comparable to the 4 points per decade of the microfluidic instrument and only the highest 4 orders of magnitude of each flow curve were used, spanning approximately 20 points in each case.

#### **Rotary rheometer for shear viscosity characterisation**

The low shear was measured with a rotational rheometer (Kinexus Pro, Malvern Instruments Ltd., UK) with a cone-plate ( $a = 20$  mm,  $\theta = 4^\circ$ ) and a gap of  $150$   $\mu\text{m}$  between the lowest point of the cone and the lower plate. This geometry was chosen over parallel-plates due to its constant shear rate across the geometry (Barnes 2000). A solvent trap (or vapour hood) loaded with the appropriate solvent for each tested fluid was used in combination with the cone-and-plate geometry to reduce the effect of drying and skinning effects on the exposed edge of the sample by creating a semi-saturated atmosphere around the spinning disc (Barnes et al. 1989). The temperature was kept at  $25 \pm 0.01$   $^\circ\text{C}$ .

The loading of the materials into the rheometer's geometry was performed with a spoon to minimise uncontrolled applied stresses and preserve their shear history. Furthermore, the storage modulus ( $G'$ ) was monitored using the oscillatory tests described in the following section to check that no noticeable re-building of the microstructure was taking place before initiating the measurement, i.e.  $G'$  has a negligible slope within 0.5% for at least 5 min. Each flow curve was recorded 3 times with fresh sample in every instance and then the average  $\pm$  standard error of viscosity and shear stress are plotted in a double logarithmic plot against the shear rate in the range of  $10^{-2}$  to as high as  $10^3$  s $^{-1}$ , depending on the properties of the fluid. Every point was captured under steady-state conditions according with the live monitoring performed by the rheometer, where the value is accepted only if it stays stable within a 5% tolerance for 10 s.

#### **Microfluidic rheometer for shear viscosity characterisation**

The high shear region was measured with a microfluidic rheometer (hts-VROC, RheoSense, USA) equipped with a slit of  $100$   $\mu\text{m}$  depth containing 3 embedded Micro Electro Mechanical System (MEMS) pressure sensors along its length. The ratio length to width is big enough so developed flow can be assumed for the fluids here studied (Pipe et

al. 2008). The temperature in the channel is controlled in real time by a refrigerated/heated liquid circulator with an accuracy of  $\pm 0.01$  °C, which similarly than in the rotary rheometer allows to compensate any temperature fluctuation that can arise in the fluid or the surrounding environment, leading to stable viscosity results. A positive pressure is generated using a syringe pump controlled by the instrument, which results in a flow of material from the containing glass syringe (Gastight, Hamilton, USA) to the micro-channel, where the viscosity is calculated from the measured pressure drop along the slit in a similar way than it was described for cylindrical pipes in Chapter 2.4. However, in order to account for non-Newtonian behaviour and potential wall slip the Weissenberg–Rabinowitsch–Mooney correction is used (Pipe et al. 2008) under the assumptions of steady and 2-dimensional flow. The effects of viscous heating are neglected due to the high surface-to-volume ratio in the microchannel (Kang et al. 2005)(Pipe et al. 2008). Once the above-mentioned corrections are applied, the instrument calculates and displays true shear stress and viscosity. This approach has the advantage over rotary rheometry that it can reach higher shear rates without evaporation or sample migration effects, but it has some drawbacks such as potential blockage due to excessive particle size or immiscibility of consecutive samples, tedious cleaning and the requirement of using a combination of different channels and syringes if one wants to cover a wide range of shear rates.

The operating procedure starts with sample loading, however in this case it is not possible to use a very low shear rate method to do it, like a spoon, and one or many loading-unloading cycles of a syringe are required. This, with some practise, can lead to appropriate loading of the material on the instrument without air bubbles, which is crucial due to their different compressibility than the measured fluids, however it often also results in an over-stress of the fluid prior measurement. However, since the measurements are performed at shear rates higher than the ones suffered by the fluid during the loading process it is reasonable to neglect the effects of such shear history variation. Once the material is loaded in the syringe, preliminary tests are run to observe the general behaviour of the fluid and to fill the micro-channel so the real tests do not suffer an abrupt fluctuation in pressure due to an empty chamber. Then, 3 flow curves per sample are measured and averaged in the range of shear rates that the combination of its viscosity, the volume of the syringe and the dimensions of the micro-channel allow for the achievable pressure. As a general rule, at equal geometric conditions, lower viscosities allow for higher shear rates, as it was represented by the PEDOT:PSS dispersion that was measured above  $10^5$  s<sup>-1</sup> due to its remarkable shear-thinning. The flow curves were measured with a glass syringe of 0.5 ml at 25 °C, while the temperature dependent experiments were performed at a constant

apparent shear rate of  $1000 \text{ s}^{-1}$  for a range of temperatures from 20 to 60 °C. It is noteworthy that in this case, since only one shear rate per temperature is recorded, it is not possible to apply the Weissenberg–Rabinowitsch–Mooney correction to the apparent viscosity. The Arrhenius model shown in equation 3 is compared to the obtained data to evaluate its coefficients for the different tested liquids.

#### 4.3.5.2 Viscoelastic measurements via oscillatory tests

A similar set-up as the one used to measure the shear viscosity was used to measure the elastic ( $G'$ ) and viscous modulus ( $G''$ ) over a range of time-scales. These tests, as it was explained in section 2.4, do not produce a steady state flow and are limited to a linear assumption for the viscoelastic response of the material, which would limit their use for the description of complex flows but is a reliable tool for characterising the microstructure of the fluids at moderate shear rates. The range of accessible frequencies is limited by the torque operating range of the instrument ( $10^{-8}$  to  $10^{-1} \text{ N}\cdot\text{m}$  in the present work) and the system inertia (Barnes 2000), which typically does not allow the observation of the complete viscoelastic curve (Figure 30) but a part of it instead. Nevertheless, the achievable range for the stress-controlled rheometer is enough to study the microstructure of the fluids at slow flow-rates and compare between them. Consequently, the same combination of rheometer (Kinexus Pro, Malvern Instruments Ltd., UK), cone-and-plate ( $a = 20 \text{ mm}$ ,  $\theta = 4^\circ$ , gap = 150  $\mu\text{m}$ ) and solvent trap than in the low shear rate measurements is used. The temperature is kept at  $25.00 \pm 0.01 \text{ }^\circ\text{C}$ .

The loading of the sample in this case is performed analogously as in the shear tests, minimising the application of stresses as much as possible and allowing time for the material to reach its rest state. Then, the linear viscoelastic region (LVER) is located by conducting amplitude sweep tests at a constant frequency of 1Hz. The LVER test leads to the identification of the maximum strain amplitude that can be applied to the system before encountering nonlinearities, i.e. the maximum deformation that the system can recover without affecting the microstructure of the fluid. These amplitudes were identified between 0.02 and 0.1 % for the fluids characterised in this work. Once identified such amplitude, 3 frequency sweeps per material are performed between 0.01 and 30 Hz and the curves are averaged.

## 4.4 Printing characterization

Once the materials were characterised, their performance in the different stages of printing was evaluated. In this work said stages are divided as follows: *jet formation*, *drop landing* and *post-processing*. Since an additive process is under study, these stages are repeated every layer until the 3D structure is formed. Each stage is monitored looking at measurable features to find working combinations of printing parameters.

### 4.4.1 Drop formation and deposition

#### 4.4.1.1 Advanced Drop Analysis (ADA) for low viscosity fluids

The drop formation process for the low viscosity materials jetted by PIJ printheads is monitored and analysed following a stroboscopic approach using the native dropview camera and LED on the printer (Pixdro LP50, Meyer Burger, Netherlands). This consists on a CCD camera taking snapshots of subsequent drops at regular intervals, creating the impression of static events or slow-moving drops depending on the synchronization between the jetting and the images, as it is summarised in Figure 58, which includes both a schematic representation of the different parts of the system and the relation between trigger pulses of the camera shutter, jetting head and LED. This approach assumes high repeatability of the drops dimensions, as it is expected from jetting printheads working within their operation range. However, if the drop ejection is irregular the images obtained are not sharp, since the results are a combination of multiple ejections and not a recording of a single event.

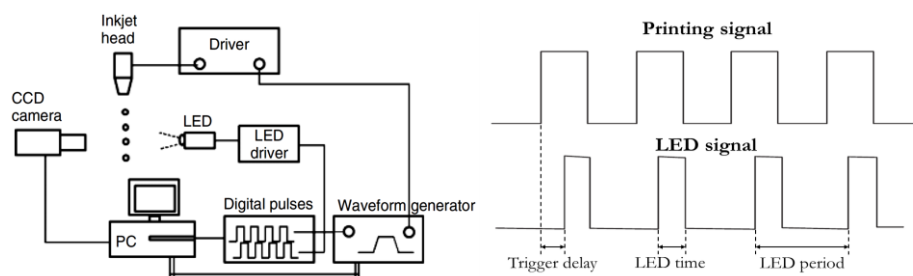


**Figure 58:** Stroboscopic imaging system integrated on the printer. **Left)** Schematic of the different parts of the set-up. The camera, printhead and LED are all controlled by the printer, which regulates their synchronization. Figure from (Kwon 2012). **Right)** Printhead and LED driver signals. The lamp is switched ON during the LED time, which is when the image is captured. Variations on the delay and relative frequency of both signals result in static images at different positions or a slow video of the falling drops.

Since the vision system is integrated on the printer it is possible to modify several printing parameters such as peak time, frequency, pressure, trigger delay or the overall voltage applied to the head, which allows for a dynamic study of the effects of these variables on the drop formation and jettability of the inks. Additionally, since the stage can

move the assembly in front of the camera, different nozzles can be monitored to assess repeatability across the printhead and identify potential malfunctions. Moreover, the **speed** of the drops is calculated using the difference in position of the drop's centre in two consecutive moments (double strobe) while their **volume** is obtained by the disc method (Hutchings et al. 2007), which assumes radial symmetry and treats every row of pixels as a disc of known thickness and diameter. This native analytical function of the unmodified printing platform is referred by the manufacturer as Advanced Drop Analysis (ADA) and it is used in this work without modification for the PIJ printheads.

The possibility of monitoring the shape and speed of the drops at different printing configurations allows for the optimization of the printing pulse according with the previously described method based on the selection of the fastest stable drop (Bogy & Talke 1984). This optimization is ultimately dependent on the geometry of the nozzle channels, since the optimum pulse would be one that allows for the main generated pressure wave and its reflections to interfere constructively, which also explains why there is not a unique set of optimum parameters but several of them at different peak times. Consequently, a series of consecutive experiments where the only varied parameter is the peak, rise and falling times are performed until the fastest drop is obtained. Then, a similar test is performed with the applied voltage as the only variable to tune the speed for the specific application, which is typically accepted between 6 to 12 m/s. Each test was performed for 5 drops per configuration. Finally, the obtained set of parameters is checked in different nozzles across the printhead to verify repeatability and a sample of 20 drops is used to calculate the average speed and volume together with their standard error.

#### 4.4.1.2 High frame-rate videos

Preliminary tests showed that the ejection events on the high viscosity micro-dispensing valves differed from the low viscosity ejections recorded with the stroboscopic approach previously discussed. Particularly, the speed and volume of the high viscosity jets are higher and their repeatability is lower than the low viscosity drops. More importantly, the maximum jetting frequency achievable by the micro-dispensing valves is 500 Hz, which is at least an order of magnitude lower than the common frequencies used in inkjet. This is relevant because in a strobe the jetting frequency is coupled with the LED flashing frequency and lower frequencies result in darker images, which were incompatible with the intended image analysis. Consequently, for the analysis of the ejection of viscous fluids, a set-up based on a high-speed camera is used. First, a matrix experiment where the closing time of the valve is varied between 120 and 1300  $\mu\text{s}$  at 3 different applied pressures (0.1,

0.3 and 0.5 MPa) was performed. Stable printing configurations were chosen for each material and another set of videos, this time with drops impacting pre-cleaned microscope glass slides (Cole-Parmer, UK), was recorded. Both experiments were performed at 25 °C and using the same optical configuration and calibration.

### **Set-up**

A digital high-speed camera (FASTCAM-APX RS, Photron Inc., Japan) with a resolution of 1024 x 1024 pixels and a pixel size of 17  $\mu\text{m}$  was mounted on a geared tripod (Manfrotto, Italy) and appropriately levelled using the inbuilt spirit levels. A long-distance microscope lens (Navitar 12X Zoom Lens System, USA) was combined with an adaptor tube (1 X) to create an optic system with a fixed working distance of 86 mm. This resulted in a manually adjustable magnification of 0.58 – 7.0 X and a field of view of 30.0 to 2.5 mm. A dimmable high intensity fibre-coupled illuminator (150 W bulb, 3200 K Colour Temperature, 680 nm peak intensity) equipped with a collimator (OSL2, Thorlabs, USA) was used as a light source for the system. The optical fibre was held in place by a laboratory clamp and kept aligned with the optical axis of the camera. It is noteworthy that in this configuration the light is constantly ON and the exposure time is controlled by the fast electronic shutter of the camera with a minimum open time of 1  $\mu\text{s}$ . This shutter will be kept as close to the minimum as possible to avoid blurred images resulting from movement during the exposure time, however this also limits the amount of light that gets to the detector per event, which results in darker images. The printing head was placed on a 3-dimensional linear stage (Aerotech, UK) and near of the end of the optical fibre, this configuration allowed simple focusing and free movement of the micro-dispensing valve to select the region of interest (*ROI*) for the videos. The schematics of the set-up are shown in Figure 59.

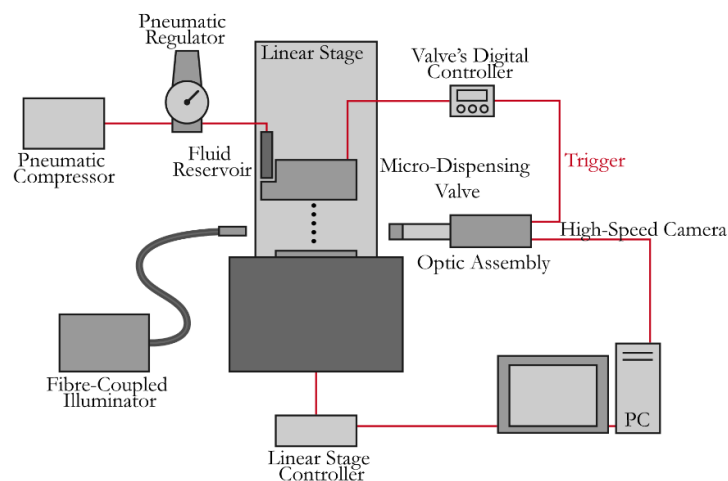


**Figure 59:** Schematics of the high-speed imaging set-up including the optics, illumination and printing sub-systems.

### **Video recording procedure**

The camera is calibrated using the external diameter of a metallic needle that was also measured with an electronic outside micrometer (Schut Geometrical Technology). Table 3 shows the values for the main parameters used in this work unless stated otherwise. The illumination and ambient conditions were also kept constant for all the recordings.

**Table 3:** Main parameters used for high-speed imaging of the ejection on a micro-dispensing valve

<b>Frame-rate</b>	<b>Shutter</b>	<b>Window size</b>	<b>Calibration</b>
20,000 FPS	1 $\mu$ s	128 x 544 px	8 $\mu$ m/px

### **Image analysis**

Once the videos were successfully recorded and transferred to a PC by Ethernet cable they were further manipulated and analysed with editing software (*Wolfram Mathematica 10.2.0.0*, Wolfram Research, USA and *ImageJ v1.50*, Wayne Rasband, National Institutes of Health, USA). Since the acquired images from the camera have normally a bit depth of 8 pixels, they can display a grey value between 0 and 255. However, to study these videos, it is common to start the process with a binarization step or gray-to-binary process that assign a value of 0 or 1 to each pixel of each frame based on a binarization threshold (Kwon 2012). Then, a background frame consisting of an average of 5 empty images can be subtracted to the stack of images to reduce image noise. The resulting black and white videos are ready for automatic analysis but are too long (more than 3000 frames per video) and too numerous (approximately 20 videos per material, 4 materials) for human monitoring. Therefore, following an approach similar to the stroboscopic method used for the lower viscosity material, the 30 recorded events in each video were merged into a single ejection by adding together every 100<sup>th</sup> frame, which at 20,000 fps corresponds to the cycle time of the experiment (5 ms). The good overlap between successive events is an indication of the high repeatability and constant frequency of the printing signal and camera trigger. Additionally, from the analysis of these videos it is easier to identify unstable configurations, which result in non-overlapping events.

To analyse each event, the leading part of each jet was monitored from its conception until it reached the end of the visible window, counting the frames required to cover such known distance to provide the average speed. It is significant that due to the intrinsic discrete nature of the recording process, the exact moments of jet start and end-of-screen reaching are not always captured, which adds uncertainty to the measured time interval. In particular, these moments would take place between 2 recorded frames, but there is no way of knowing if they happen closer to one or another. Thus, it is assumed

that both limit moments of the jet are located exactly between 2 frames with an uncertainty of half the time between frames ( $\pm 25 \mu\text{s}$  for 20,000 fps). Since the total elapsed time depends on the number of captured frames displaying the jet between these two limit moments and the uncertainty is constant, it is expected that the accuracy of the experiment improves with the number of frames. It is also noteworthy that all the recordings have a shared trigger moment, so despite the uncertainty regarding the initial time of the jet, this uncertainty affects consistently to all samples.

The shutter time of the videos can be used to validate qualitatively some of the observations regarding velocity, since that is the time that the camera is recording and a perfectly sharp image would only be obtained if the jet travels a negligible distance during that time. Therefore, if a blur spanning less than 12 pixels is consistently observed with a  $1 \mu\text{s}$  shutter, it means that the jet is traveling slower than 96 m/s, which can be taken as the maximum threshold for the speed in this experiment.

The outside of the nozzle plate is monitored during and after the 30 ejection events to assess any wetting effects that may have arisen from insufficient energy being imparted to the jet. Then, the width and radius of the hanging drop are obtained from the last image and its volume is estimated assuming a spherical cap geometry.

For the videos of individual representative drops impacting on a glass substrate, the width of the drops was automatically monitored over time to study the spreading behaviour of the fluids. The diameter of each drop was normalised in relation with its final diameter after 149.5 ms, which allows for direct comparison between materials.

#### **4.4.1.3 Footprint analysis of ejection and deposition on the substrate**

The previous methods of stroboscopic and high speed imaging are invaluable when the drop formation and flight evolution is under study but they can be slow and often require additional hardware that cannot be integrated into the main system. Additionally, they do not provide information about the size or shape of the deposited drops, which is crucial for the optimisation of 2D films and 3D structures. To cover this gap in the process optimization cycle a top view analysis of the drops' footprints was performed.

The footprints of deposited drops on pre-cleaned plain microscope glass slides (Cole-Parmer, UK) resulting from different settings of pressure (0.1 – 0.5 MPa) and valve closing times (120 – 1300  $\mu\text{s}$ ) were studied with the monochrome camera integrated in the printer. Specifically, the images were taken after the printing of the pattern was finished by

moving the camera over the sample at discrete intervals equal to its FOV, which creates a non-overlapping collection of pictures that cover the entire region. These images were later stitched together and analysed by a semi-automatic custom code developed in Mathematica (Wolfram Mathematica 10.2.0.0, Wolfram Research, USA). The first step consisted on the creation of a **background average** frame from 5 empty images that describes the illumination gradient of the samples without including distinct features from the substrate. This frame was later averaged with each image under study to equalize the illumination of the background and facilitate drop detection. The individual images were then **stitched** together and its **grey levels adjusted** to cover the full range between 0 and 1, which increased the overall contrast to help the user distinguish the features. This was followed by a **morphological binarization** step, which created a black and white image using two threshold values ( $th_1$  and  $th_2$ ). The highest one ( $th_1$ ) is the absolute cut-off value that determines the resulting colour of each pixel while the secondary threshold ( $th_2$ ) is only effective for pixels in direct contact with one affected by  $th_1$ . This creates a mask containing all the distinctive features of the image, including substrate marks and reflection artifacts. Consequently, the detected components were **filtered according with their pixel count** to eliminate noise and a **filling transformed** is applied to complete hollow components affected by glare. The resulting collection of grains was visually inspected by the user to verify that no anomalous shapes were included. For each profile a minimum of 40 drops were analysed. However, this method based on binarization does not cope well with transparent materials such as the UV-curable resin, since the intensity inside the drops matches the background. Therefore, in such cases the morphological binarization was substituted by **edge detection**, followed by a **convex hull detection** step that effectively closed the detected shapes and allowed for the continuation of the process. Furthermore, in cases where the fluid depositions were connected with each other neither of the previously mentioned approaches was capable of resolving them individually and therefore a **manual mask** accommodating the shape of the main bodies of fluid was used instead.

Regardless the method used to detect the drops, the resulting components were studied in terms of their area ( $A$ ) and perimeter ( $P_L$ ) using a calibration of  $3.04 \mu\text{m}/\text{px}$ . However, since these magnitudes are not immediately relevant to the printing process, the **equivalent radius** ( $r_{eq}$ ) and **circularity** ( $f_{circ}$ ) were presented instead. The former is the radius of a circle with area  $A$  and provide and understandable metric for the size of the drop while the latter is a shape factor that determines how circular a shape is, being 1 the value for a perfect disc. In both cases the results are presented as average  $\pm$  standard deviation, which provides information about the repeatability of the printing process.

$$r_{\text{eq}} = \sqrt{\frac{A}{\pi}} \quad (44)$$

$$f_{\text{circ}} = \frac{4\pi A}{P_L^2} \quad (45)$$

Furthermore, patterns at **different resolutions** (measured in drops per inch,  $R_{DPI}$ ) were printed and visually assessed by the same optical systems mentioned above. These patterns included originally lines but they were substituted in an early stage by squares, which show drop interactions in 2D and is more relevant to the work here presented. The relation between the resolution and the droplets pitch ( $p_D$ ) in these units is given by:

$$R_{DPI} \left[ \frac{\text{drops}}{\text{inch}} \right] = \frac{25.4 \left[ \frac{\text{mm}}{\text{inch}} \right]}{p_D \left[ \frac{\text{mm}}{\text{drop}} \right]} \quad (46)$$

In this case the objective is to select a DPI high enough that results in films without pinholes but that it is not too high that it leads to a situation where 3D bulging occurs due to an excessive amount of fluid per unit area. These high resolutions would not only provide a surface with pronounced curvature that would affect the geometry of the 3D object being printed, but they would also influence the drying behaviour of the layer, with thicker films requiring more time and/or energy to fully evaporate the solvent. Furthermore, to compare DPI-results among materials with different droplet footprints of different diameter ( $d$ ) it is also possible to represent each resolution with an overlapping ( $O_{\%}$ ) value given by:

$$O_{\%} = \left( \frac{d - p_D}{d} \right) \cdot 100 \quad (47)$$

Several square patterns were printed on pre-cleaned microscope glass slides and/or epoxy fiberglass boards covering drop overlaps from 0 to 50 %. The square size was 5 mm for the glass samples and 3 mm for the epoxy fiberglass boards. The printing settings for each material were selected according the drop formation results presented in Chapter 6. The imaging of the samples was performed using the monochrome camera built-in the system, which was used to take multiple images of 1.99 x 1.74 mm. The images were later assembled together with no overlap.

#### 4.4.1.4 Drop mass and volume

To calculate the volume of individual drops the weight of several drops was recorded. The micro-dispensing valve was held with a laboratory clamp above a disposable weighing boat on top of an analytical laboratory balance (Kern ABT 100-5M, KERN & SOHN GmbH, Germany) with a read-out of 0.01 mg at room temperature (Figure 60). The printing signal and the pressure were supplied to the valve in the same way that it is done during printing, via a digital controller and a system of pressure regulators respectively. The digital controller was then used to dispense numbers of drops ( $N$ ) from 500 to 2500 in intervals of 500 at a jetting frequency of 250 Hz (4 ms cycle time) and a pulse time of 0.30 ms. The pneumatic pressure and valve closing speed were selected as the most appropriate from previous experiments. Each number of drops was deposited 5 times and the results were then plotted in a graph mass against  $N$  to obtain the mass per drop from the slope of a linear regression. This method allows for self-evaluation in the sense that data with high linearity implies that no significant amount of material has been left on the nozzle plate, which would have reduced the recorded mass for high  $N$ , disrupting the linearity. Furthermore, since the experiment only takes between 2 and 10 seconds and the ejection takes place directly on the balance, the evaporation of the solvents during ejection is neglected. In this case too, the linearity of the results indicate if this assumption is acceptable. Similarly, the effect of pulse length and frequency (cycle time) were studied recording the mass of 2500 drops five times per setting, presenting the result as average  $\pm$  standard error. In this case only deionized water, UV-curable resin and PEDOT:PSS in two different jetting configurations (named slow and fast) were tested.

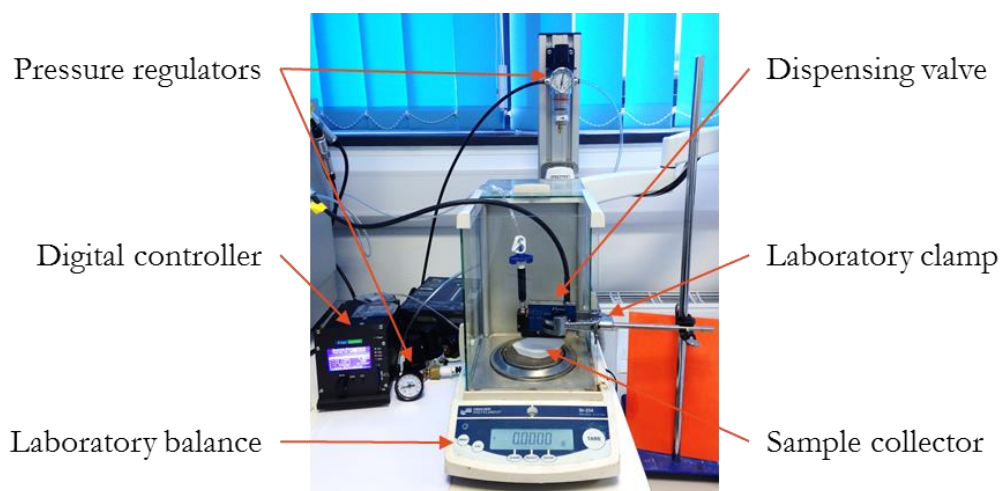


**Figure 60:** Set-up used to measure the weight of consecutive drops jetted by a micro-dispensing valve. It consists on a digital scale and the micro-dispensing valve held in a constant position by a laboratory clamp.

## 4.5 3D geometric analysis

To study the linearity of the height of the samples with the number of layers, a series of multi-layered tracks with increasing thickness were produced using the optimal printing and post-processing settings identified via other experiments shown in this work. The substrate used in each case was either polycarbonate film (for the early experiments on UV-resin and carbon paint), glass slides (carbon paint, TPGDA, PEDOT:PSS) or epoxy fiberglass boards (carbon paint, TPGDA, silver paste), depending on the adhesion and wettability of the fluids in such surfaces. The samples were allowed to rest for at least 24 h in ambient conditions before testing them with a laser profilometer. Particularly, a Point Autofocus Instrument (MLP-3SP, Mitaka, Japan) with a 100× objective was used to measure profiles orthogonal to the direction of the printed tracks. A scanning setting was used to provide 5 µm spacing points along an 11 mm distance to capture a profile cross section of all tracks in a single profile measurement. 9 profiles spaced 450 µm apart were measured to cover the whole sample, with each profile evaluated individually. Specialized surface analysis software (Mountains 7.2, Digital Surf, France) was used to perform levelling by subtraction from the least squares mean plane prior to evaluation of the step heights and area of the tracks as separate profiles. Another set of samples was produced by printing tracks of conductive materials (silver paste and carbon paint) on PCBs, transversal to the copper pads. These longer tracks were scanned 9 to 12 times in the sections between the pads using the same scanning settings to obtain their cross-sectional area and later calculate the resistivity of the materials. Early 3D studies for carbon paint and UV-resin (Appendix A1) were performed with a contact profilometer (Surfest SV-3100, Mitutoyo, Japan) at a point spacing of 50 µm and 3 equally spaced profiles per track. Although these initial tests provided reliable height and area data, they had the drawback of physically contact the samples, which was not viable for weaker materials such as the sintered silver. Therefore, a laser profilometer was used for the latest experiments, which additionally provided an increased resolution respect the contact-based system.

## 4.6 Electrical conductivity and resistivity

### 4.6.1 *Brief magnitudes description*

The electrical properties of a material are determined by its electronic structure and how charge can flow within it. In a solid, the orbitals of an atom overlap with the neighbour atoms and define the finite energy states that an electron can occupy in the system. The

electrons bound to the atoms are said to be in the valence band, while the free charges occupy the conduction band and contribute to the overall electric conductivity. The energy required to promote an electron to the lowest state in the conduction band from the higher state of the valence band is known as **energy gap** or band gap. If a large amount of energy is required to overcome the band gap, a material is defined as an insulator, while a narrower gap is characteristic of semi-conductors. Good conductors, such as metals, have both bands overlapping, which allow high charge mobility even under weak electric fields. Precisely, **conductivity** ( $\sigma_c$ ) in conductors is typically defined in terms of the number of carriers ( $n_c$ ) of charge ( $e$ ) and their mobility ( $\mu_c$ ) (Heeger et al. 2000) or the current density ( $j_c$ ) and the electric field ( $E$ ) required to sustain it:

$$\sigma_c = n_c e \mu_c = \frac{j_c}{E} \quad (48)$$

This property is inherent to the material and is not influenced by the geometry of the sample. However, other properties such as temperature can affect it, since it alters the energy balance in the system. Specifically, metallic materials generally show an increase of conductivity with decreasing temperatures, while insulators and semiconductors display a direct proportionality between these magnitudes (Heeger et al. 2000). Furthermore, any defects or alterations to the microstructure of the material would result in a variation of the conductivity respect of the ideal bulk state, which is why it is common to compare the conductivity of a material processed under specific conditions to its bulk state. Alternatively, the **resistivity** ( $\rho_r$ ) can be used to describe the resistance to flow of the charges through a material, taking advantage of the reciprocal relation between both magnitudes. More detailed information about these magnitudes and their relation with the microstructure of the solids can be found in the literature (Kittel 2004).

From a practical point of view, the **resistance** ( $R$ ) of a structure of length ( $L$ ) and cross-sectional area ( $A$ ) can be related with the resistivity of the material as follows:

$$R = \frac{\rho_c L}{A} \quad (49)$$

Furthermore, following the well-known Ohm's law, it is possible to characterise the resistance of a track by applying a known voltage ( $V$ ) across it and measuring the electric current ( $I$ ):

$$V = IR \quad (50)$$

#### 4.6.2 *Measuring method*

The resistance of the samples produced in this work were measured with a benchtop LCR-meter (HM8018, Rohde & Schwarz GmbH, Germany) with range auto-selection, maximum resolution of  $0.001 \Omega$  and a basic accuracy of 0.2 %. The samples were allowed to reach thermal equilibrium with the environment, which consisted in a controlled room at  $25 \pm 5 \text{ }^\circ\text{C}$  and  $35 \pm 5 \%$  (Hygro-thermometer, AZ8711, AZ Instrument Corp., Taiwan). A warm-up time of more than 30 minutes in ambient conditions was respected before using the instrument and its probes. The small tip of said probes grants repeatable and precise measurement positions but it can result in scratches if the structure being tested is too small or thin, as it was the case with the PEDOT:PSS samples. In these cases, the sides of the sample were fully covered with silver-based electrically conductive paint (RS Pro, UK) and allow to dry for 1 hour before use. Since the resistivity of this material is in the order of  $10^{-5} \Omega \cdot \text{m}$  according with the manufacturer (which is lower than the observed for the carbon paint and the PEDOT:PSS) and the deposited thickness is typically thicker than the samples, it is not expected to add a relevant resistance to the measurements. In the case of samples directly printed on PCBs, the resistance of the pre-existing copper tracks was measured and subtracted to the result.

The dependency of the resistance of an object with its geometry (equation 49) is used in this work to obtain the electric resistivity. The resistance of the multi-layered tracks previously scanned with the laser profilometer was measured with the LCR-meter and plotted against the inverse of their cross-sectional area. A linear regression was used to obtain the slope term, which corresponds to the resistivity multiplied by the track length. This length was measured using the built-in monochrome camera of the system. This was performed for the 5 thickest layer configurations in each material to avoid any potential non-linear wetting in the first few layers.

In some situations, due to the poor adhesion of the material or its fragility, the LCR-probes caused irreversible damage to the samples and prevented consistent measurements. For such situations, another set of samples consisting on single tracks printed across the pads of PCBs were prepared and their topology scanned with a Point Autofocus Instrument as previously described. In this case, the measurement of the resistivity comes from the application of equation 49 to the known geometry of the track between the pads and the resistance measured between them using the LCR-meter. 18 measurements are taken and presented as average  $\pm$  standard error.

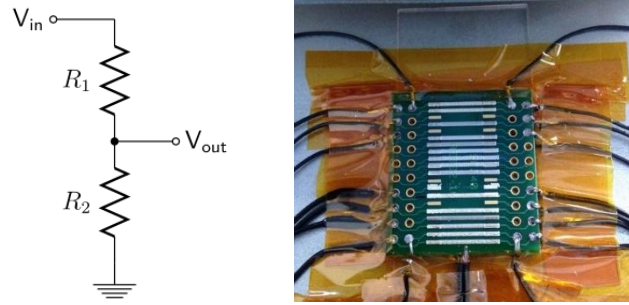


**Figure 61: Left)** Electric diagram of a voltage divider configuration, which controls the relation between the voltage input ( $V_{in}$ ) and output ( $V_{out}$ ) based on the value of 2 resistors ( $R_1$  and  $R_2$ ). **Right)** PCB-based set-up used for real time resistance measurements during post-processing. Printed silver tracks are shown in the image.

Real time measurements of the resistance of tracks printed on PCBs during post-processing were also recorded making use of an additional microcontroller (UNO, Arduino, Italy). The substrates consisted of commercial PCBs (RE932, Roth Elektronik, Germany) with soldered leads of equal length that were connected to the microcontroller via crocodile clips. The total resistance of the PCB's copper tracks, leads and clips was measured and subtracted to the measured resistance. The PCB was placed on a glass slide to avoid contact between the conductive features on the back side of the board with the metallic printbed, which would create an undesirable conductive path for both electricity and heat. The system was held in place with temperature resistant polyimide tape (Kapton tape, DuPont, USA), as it is shown in Figure 61. The temperature was monitored with a K-type thermocouple probe controlled by the microcontroller via amplifier module (MAX31855, Adafruit, USA) and its correspondent code library.

The resistance was measured using a voltage divider configuration (Figure 61), where  $R_1$  is the reference resistor and  $R_2$  the printed track. The input voltage ( $V_{in}$ ) consists of 5 V supplied by the microcontroller, while the  $V_{out}$  is the potential drop measured by an analog pin with 1024 levels in the same controller. The relation between the input voltage and the measurement can be derived using Ohm's law (equation 50):

$$V_{out} = \frac{R_2}{R_1 + R_2} V_{in} \quad (51)$$

To make the most efficient use of the voltage range read by the microcontroller the reference resistor ( $R_1$ ) need to be selected according with the expected resistance range of the tracks. Several measurements of commercial resistors of known value ( $R_{Nominal}$ ) where recorded to test the accuracy of the readings with different reference resistors, as it is shown in Table 4 and Table 5. The readings of the microcontroller ( $R_{Arduino}$ ) are within 5 % error ( $\Delta R$ ) of the LCR measurements ( $R_{LCR}$ ) if the reference resistor is more than 10% of the resistance being tested.

**Table 4:** Nominal and measured values of various resistors. The reference resistance ( $9920 \pm 1 \Omega$ ) is selected to adapt to the range of resistance expected for the carbon paint tracks.

$R_{nominal} (\pm 5\% \Omega)$	$R_{LCR} (\pm 1 \Omega)$	$R_{Arduino} (\pm 0.1 \Omega)$	$\Delta R (\%)$
330	325	330.0	1.5
470	460	467.0	1.5
1000	990	991.0	0.1
10000	10060	10115.0	0.5
1000000	981000	1441000.0	46.9

**Table 5:** Nominal and measured values of various resistors. The reference resistance ( $108.3 \pm 0.1 \Omega$ ) is selected to adapt to the range of resistance expected for the silver paste tracks.

$R_{nominal} (\pm 5\% \Omega)$	$R_{LCR} (\pm 0.1 \Omega)$	$R_{Arduino} (\pm 0.1 \Omega)$	$\Delta R (\%)$
27	31.0	31.1	0.5
43	43.4	43.6	0.6
222	216.5	218.4	0.9
333	322.5	326.2	1.1
470	461.3	468.9	1.6
1000	1010.0	1046.5	3.6
4700	4691.0	5436.3	15.9

The length of the printed tracks was 12 mm, with a resolution of 100 DPI for the carbon paint and 74 DPI for the silver paste. The aqueous PEDOT:PSS dispersion could not be used for this experiment due to the thin nature of the deposited solid films, which were interrupted due to the thickness of the copper pads and the small gap around them. This was not a problem for the other conductive materials, which could overcome these geometric barriers. This is expected to affect the overall resistance of the tracks, but the high repeatability of these irregularities guarantees that relative observations are not affected. Three repetitions of each post-processing configuration were recorded and averaged in the shown curves (Figure 109 and Figure 113), showing their standard deviation as grey areas around the curves. The power conditions for the IR-lamp were varied for the different tests but the height between the samples and the lamp was kept constant at 8 mm during this experiment. The UV-lamp was working at full power at all times and its distance to the substrate was 4 mm. Due the different distance from the thermocouple to each track and the impossibility of placing it on the track path without altering the properties of the printed pattern, the temperature could not be measured simultaneously with the resistance. This was resolved by repeating each measurement in identical thermal conditions with the thermocouple in the focal position of the process, where the track would have laid. Average temperature curves describing the thermal conditions of the tests were obtained and presented together with the resistance vs. time curves. To provide a common starting temperature of  $27 \pm 3 \text{ }^\circ\text{C}$ , the system was cooled down using air extraction and an air blow gun before each measurement.

## 5. Results and discussion:

### Material characterisation

In this chapter the characterisation of the materials used in this work is presented, focusing on relevant magnitudes for printing such as density, surface tension and viscosity.

#### 5.1 Density

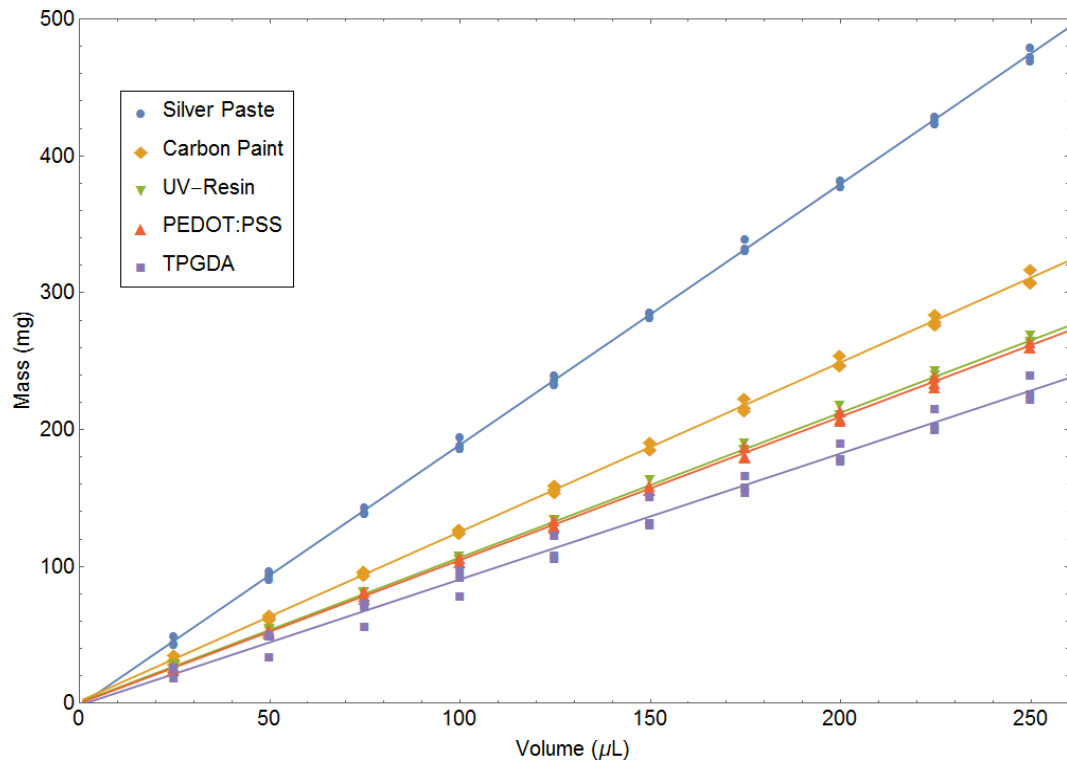


**Figure 62:** Density determination via linear regression of the data obtained by weighting known volumes of each fluid. High linearity and negligible y-axis intercepts are observed.

The results from the density experiment are plotted in Figure 62 and the results of the respective linear regression fits are presented in Table 6. High linearity is observed across the different volumes deposited, which indicates that sources of error such as sample evaporation, air bubble entrapment and material left on the tip of the syringe are not affecting significantly to the density measurements. It is significant that the errors for both the intercept and the slope of the linear model are larger for the TPGDA than for the other materials, which is related to its lower viscosity. Its viscosity results in lower pressure required to induce ejection from the syringe, which makes it more complicated to manually deposit the target volume accurately.

**Table 6:** Density and other fitting parameters of the linear regression with their standard error

Sample	Density (g/ml)	Intercept	Adjusted $r^2$
<i>Silver Paste</i>	$1.905 \pm 0.008$	$-1.5 \pm 1.2$	0.9995
<i>Carbon Paint</i>	$1.237 \pm 0.008$	$1.7 \pm 1.2$	0.9989
<i>UV-Resin</i>	$1.058 \pm 0.007$	$0.8 \pm 1.1$	0.9988
<i>PEDOT:PSS</i>	$1.046 \pm 0.006$	$0.2 \pm 0.9$	0.9991
<i>TPGDA</i>	$0.920 \pm 0.019$	$-1 \pm 3$	0.9881

## 5.2 Particle Size and size distribution

During the jetting process the materials travel through a nozzle of micrometric dimensions, which limits the size of the suspended particles in the jetted materials. Thus, the smaller the components, the better stability the printhead will show, since it is less likely to clog due to particle obstruction. The materials used in the present work can be divided in two categories in this sense, the particle-free and the particle-loaded. The first group includes the stereolithographic resin and the TPGDA, which are photo-polymers and do not require solid content. The carbon paint, the PEDOT:PSS and the silver paste all have different amounts of particles in them. Both the PEDOT:PSS dispersion and the silver material are specified to have nanoparticle content of 10 - 500 nm and 20 – 50 nm respectively. The situation is different for the carbon paint, which is composed by micro-flakes of graphite of undetermined size. Therefore, a laser diffraction particle size analyser was used to measure the particle size distribution of the carbon paint, as it is shown in Figure 63. The volume density is normalized to the total of particles detected and do not represent their concentration in the paint formulation.

A tri-modal distribution is observed with peaks at 0.13  $\mu\text{m}$ , 0.68  $\mu\text{m}$  and 14.50  $\mu\text{m}$ , which is expected to result in compact structures since the smaller particles can fill the voids left among the larger ones, increasing their connectivity and therefore the overall conductivity of the composite (C. Yang et al. 2013). More relevant for this study is the value of  $D_{x90}$ , which states that 90% of the particles have an equivalent diameter of 24.1  $\mu\text{m}$  or smaller. This is half the nozzle size, which can cause blocking problems, considering that only one larger particle is required to block the channel. Filtering the paint before loading it to the printing cartridge with a mesh between 2 and 10  $\mu\text{m}$  would be a way to avoid these potential issues, but the high viscosity of the fluid prevented this approach from being viable in useful volumes. The material was tested unfiltered and a stable behaviour was observed despite its particle size distribution, with only occasional blocking encountered. An explanation for this behaviour could be that the material is not pushed

through the nozzle by pneumatic actuation alone, but it is also mechanically actuated by the ball-needle system of the micro-dispensing valve. This can not only provide much higher pressures, but it can also break the carbon flakes and any potential agglomerates into smaller particles that would flow easier through the nozzle. The relatively fragility of graphite compared to the ceramics and stainless steel of the nozzle-shaft system of the valve agrees with this explanation.

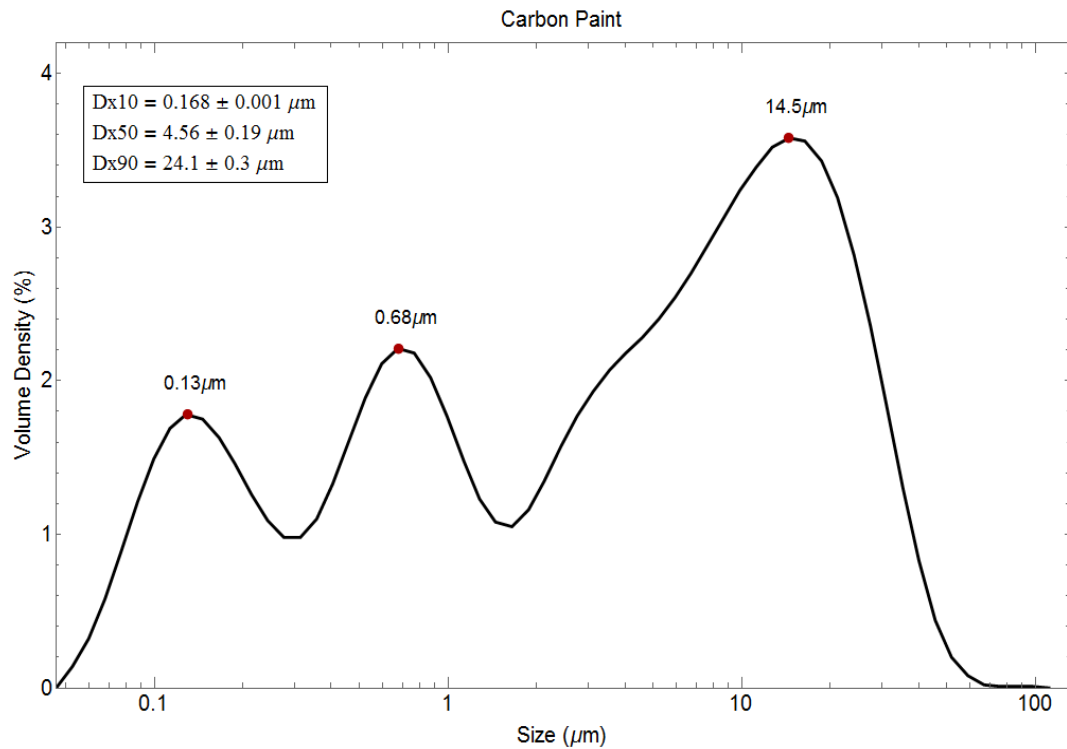


**Figure 63:** Particle size distribution of the conductive flakes in the carbon paint. The maximum values for each of the peaks of the tri-modal distribution are shown in red and the D-values for 10, 50 and 90% are given in the legend.

### 5.3 Solid content and thermal stability

Thermogravimetric analysis (TGA) was used to study the evolution of the samples weight at different temperatures with the intention of assessing their thermal stability at elevated temperatures and the amount of solid residue left after the organic components are removed. The results will be discussed individually for each of the main materials used in this work, comparing them with other relevant fluids used in Additive Manufacturing to provide some context. The Derivative Thermogravimetric (DTG) curve is also presented, providing information on the mass loss rates. The temperature at which a 5% mass loss is achieved ( $T_{5\%}$ ) and the mass variation at 250 ( $\Delta m_{250}$ ) and 600 °C ( $\Delta m_{600}$ ) for each material are summarised in Table 7.

**Table 7:** Results from TGA for different materials used during this work showing their mass loss at different T

Sample	T <sub>5%</sub> (°C)	Δm <sub>250</sub> (%)	Δm <sub>600</sub> (%)
<i>Carbon Paint</i>	44.2	52.32	27.30
<i>Gum Arabic</i>	69.5	29.74	8.10
<i>PEDOT:PSS (high viscosity)</i>	98.9	2.62	0.34
<i>PEDOT:PSS (low viscosity)</i>	42.7	0.89	0.19
<i>UV-Resin</i>	287.8	97.15	0.38
<i>Silver Paste</i>	100.7	59.46	58.03
<i>Silver Ink</i>	151.8	29.56	28.28

The TGA curve and its derivative for the **carbon paint** are shown in Figure 64, along with the TGA curve of an aqueous solution of gum arabic, which is the polymeric binder of the paint. It can be observed that the both the carbon paint and the gum arabic have two main mass loss stages. For the carbon, the first stage displays a peak on its DTG at 109 °C, which is attributed to the evaporation of water (David R. Lide 2005). Then, there is a brief plateau in the region of 200 °C before a second decreasing step is initiated. This second DTG peak is located at 335 °C, which is attributed to the decomposition of the polysaccharides of the gum arabic (Cozic et al. 2009) (Mothé & Rao 2000) (Zohuriaan & Shokrolahi 2004). Analogous peaks are found in the DTG of gum arabic at 124 °C and 320 °C respectively. The graphite will not degrade at a significant rate until approximately the 800 °C region (Kumar et al. 2015) (Choi et al. 2010), which is just outside the range of the performed test. It is expected that the organic residue left after the decomposition of the gum arabic in both cases further decomposes at higher temperatures and more noticeably in the presence of oxygen. The inset of Figure 64 shows the re-scaled curves with respect to their mass at 200 °C, when the solvents have already been evaporated. This allows for a more direct comparison between the carbon paint and the gum arabic, assuming that this particular resin is the same one used in the fabrication of the paint (Pilditch et al. 2009). Comparing their mass loss at 800 °C it can be concluded that the carbon filler accounts for approximately 24 % of the solid residue at 200 °C, i.e. a 13 % of the initial weight of the paint. Thus, assuming that the carbon paint only contains solvent, polymer binder and solid filler, it would be formed by 44 % water (mass loss at 200 °C), 13 % carbon (from the difference in the solid residue) and 43 % gum arabic. This tentative formulation can be validated by calculating the expected density ( $\rho_{paint}$ ) for the carbon paint using known values for its constituents' densities ( $\rho_{water} = 0.997$  g/ml,  $\rho_{graphite} =$

2.50 g/ml and  $\rho_{gum} = 1.35$  g/ml)(David R. Lide 2005) and their assumed mass fractions, resulting in  $\rho_{paint} = 1.23$  g/ml, which is in agreement to the previously measured (Table 6).

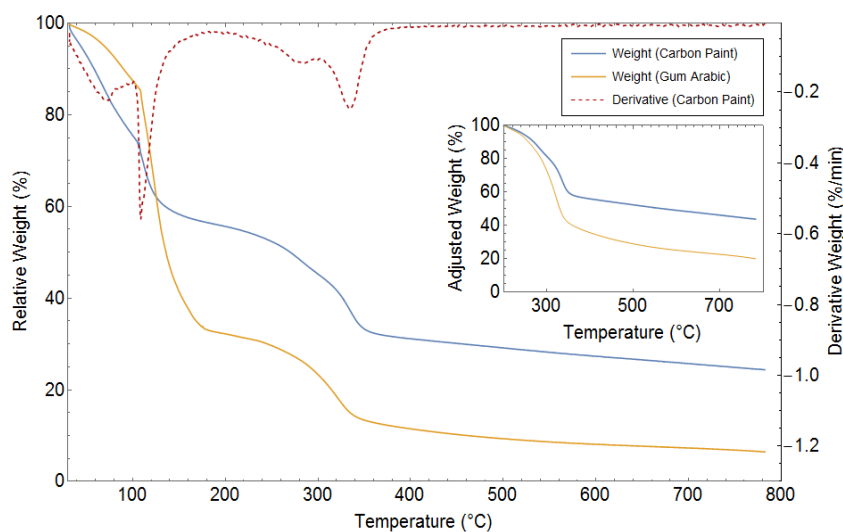


**Figure 64:** TGA data for the carbon paint used in this work and gum arabic, its polymeric binder. Both materials were tested in fluid form with water as their solvent. DTG is also shown for the carbon paint. The inset shows the same data renormalizing both curves to their mass value at 200 °C to show their evolution once the solvent has left the sample.

Figure 65 shows the TGA curves for two **dispersions of PEDOT:PSS**, a high viscosity one designed for screen printing and a low viscosity one formulated for PIJ. Higher viscosity PEDOT shows a single peak in its DTG for the main evaporation event at 199 °C, correspondent to its organic solvents, Diethylene Glycol (245.8 °C (David R. Lide 2005)) and Propylene glycol (187.6 °C (David R. Lide 2005)). According to the technical information there is also a 15-20 wt% of water, which is compatible with the results considering that the peak at 100 °C may be masked by the main evaporation event. This contrasts with the low viscosity version that has a clear bimodal loss with DTG peaks at 116 °C and 172 °C (not shown in the graph). This indicates that water is the main solvent, while the secondary solvent, with a slightly higher boiling temperature, plays a lesser role. The presence of one or multiple co-solvents has mainly two purposes, the first one is to reduce the effect of coffee staining due to different evaporation rates in the middle and the edges of the drop (Magdassi 2010), while the second reason is to increase the conductivity of the films by re-arranging the PEDOT and PSS chains in a way that promotes conductive interconnectivity (Elschner et al. 2012). It is noteworthy that the higher viscosity dispersion requires higher temperatures or longer processing times to fully eliminate the solvent, which in principle is a drawback for the fabrication method, but it is also more stable in the nozzle, since evaporation at room temperature will be minimal and clogging of the nozzle for that reason is unlikely, therefore extending the life of the printheads and improving the repeatability of the process.

The second stage of mass loss of the high viscosity PEDOT:PSS has a DTG peak at 356 °C and later at 579 °C. Similarly, the low viscosity displays a constant decrease in relative mass between 200 and 500 °C with a final peak in the derivative at 594 °C. The peaks around 300 °C and 500 °C are attributed to the rupture of the backbone chain structures of the PSS (Liu et al. 2015)(Jiang et al. 2014) and PEDOT respectively (Liu et al. 2015). It is remarkable that, even though in both cases the solid content at 250 °C is below 3 %, the high viscosity formulation displays almost three times as much non-volatile material (2.62%) than the low viscosity one (0.89%). This solid content is low compared with other materials used in this work but it should be kept in mind that the PEDOT:PSS dispersions are sensitive both to the individual concentration of PEDOT and PSS and their ratio, reaching rarely total solid contents higher than 5 wt% (Elschner et al. 2012).

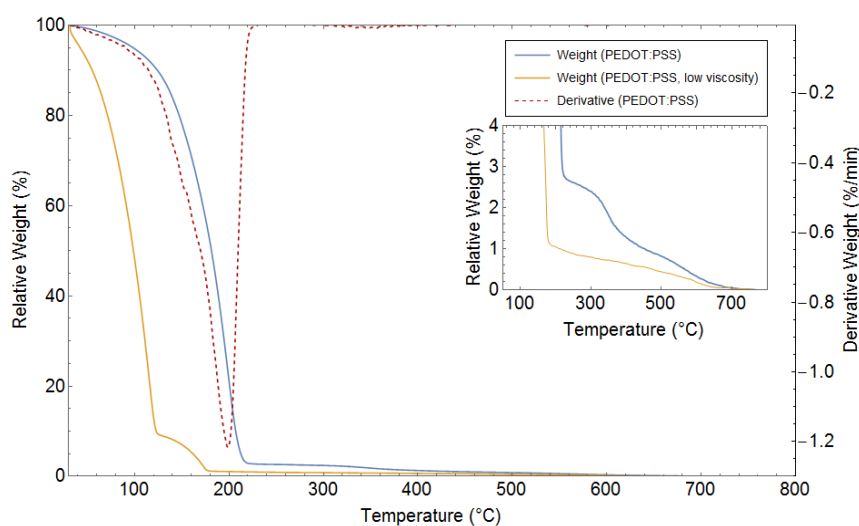


**Figure 65:** TGA data for the high viscosity PEDOT:PSS dispersion used in this work and an analogous PEDOT:PSS-based jettable ink. DTG is also shown for the high viscosity PEDOT:PSS, indicating the temperatures of maximum mass loss. The inset shows a zoomed version of the same curves to provide additional detail.

In Figure 66 the TGA curves for two **silver-based materials** are presented, a high viscosity paste designed for screen printing applications and a low viscosity ink. The high viscosity formulation displays only one mass loss stage with a DTG peak at 157 °C, which means that the several processes controlling mass loss in this sample are happening simultaneously in the range of temperatures between 100 °C and 200 °C. Specifically, this peak can be attributed to the thermal decomposition of the stabilizing polymers coating the silver nano particles and the organic components of the silver complex compound (Smith et al. 2006). Even though the solvent ( $\alpha$ -terpineol) has a boiling temperature of 218 – 221 °C (David R. Lide 2005) it is expected to start evaporating before reaching that point, which is probably the reason why the transition of the mass loss curve is smoother than the low viscosity one. Furthermore, around these temperatures it is also expected that the

sintering of the nanoparticles occurs, but this does not imply a change in the mass of the sample and is not expected to be observable in the TGA results. In the range between 250 °C and 800 °C, the total mass loss is below 2 %, which means that most of the organic components are not present at this point. The low viscosity material displays a clear evaporation DTG peak at 234 °C (not shown in the graph), which corresponds mainly to the evaporation of the solvent TGME (246 °C (David R. Lide 2005)). There is a secondary loss of about 1% at 455 °C, which can be taken as the moment when the last organic compounds are fully decomposed.

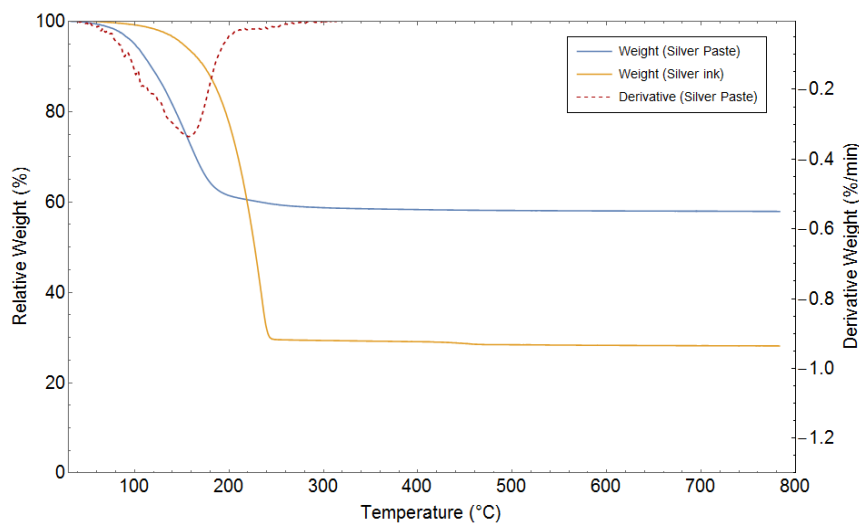


**Figure 66:** TGA data for the high viscosity silver paste used in this work and an analogous silver-based jettable ink. DTG is also shown for the high viscosity silver paste, indicating the temperatures of maximum mass loss.

Apart from their different loss temperatures, the most striking difference between these two silver-based formulations is their solid content. The silver paste shows a metallic residue of 58.03 % at 600 °C, while the ink has 28.28 % of solid content at the same temperature, less than half than the higher viscosity formulation. Furthermore, the main decomposition of organic compounds seems completed for the silver paste before reaching 300 °C, while the low viscosity ink needs to reach 460 °C to achieve the same. Finally, as it will be shown in future sections of this work, it is also relevant that the silver paste has a solvent ( $\alpha$ -terpineol) with a boiling point that overlaps with the thermal decomposition of the organic compounds, which means that it is possible that it starts boiling during the post-treatment step. The lower viscosity ink is less likely to suffer from this effect since its solvent (TGME) has a higher boiling point and allows for a thermal treatment that removes the nanoparticle's ligands before finishing evaporating the solvent.

The TGA and DTG curves for the **photo-polymers** used in this work are shown in Figure 67, this time the samples were already cured, since in this case the focus is on the

thermal stability of the polymers and not in their mass loss due to evaporation. This is relevant since both the high viscosity UV-resin and the TPGDA will act as structural materials in the 3D demonstrators crated in this work, which will be exposed to high temperatures during the thermal post-treatment stages.

The TGA for the UV-resin shows a single mass loss event with two differentiated slopes, corresponding to the DTG peaks at 399 °C and 472 °C. Both peaks can be attributed to polymer degradation, as it was observed in other acrylate-based SLA resins (Salmoria et al. 2005) (Salmoria et al. 2008) (B. W. Huang et al. 2011). However, the fact that the degradation happens in two consecutive steps can indicate either the presence of an additional polymer to modify the properties of the resin or the presence of uncured resin trapped into the tested samples (Salmoria et al. 2005) (Salmoria et al. 2008). Despite this, the material shows good stability until approximately 300 °C, when it displays a mass loss of 6.3 %, before quickly degrading and reaching a negligible 0.38 % of relative mass at 600 °C. The data corresponding to the TPGDA shown in Figure 67 is reproduced from (He et al. 2017), where the heating rate and nitrogen flow were analogous to the ones used in the present study. Their results showed a single degradation step in the range of 350 to 500 °C, with a DTG peak at 404 °C. The observed  $T_{5\%}$  for TPGDA was 308.54 °C, which is very similar to the observed for the UV-resin. In general, both materials behave similarly despite the differences in their rheology, as it will be shown in following sections.

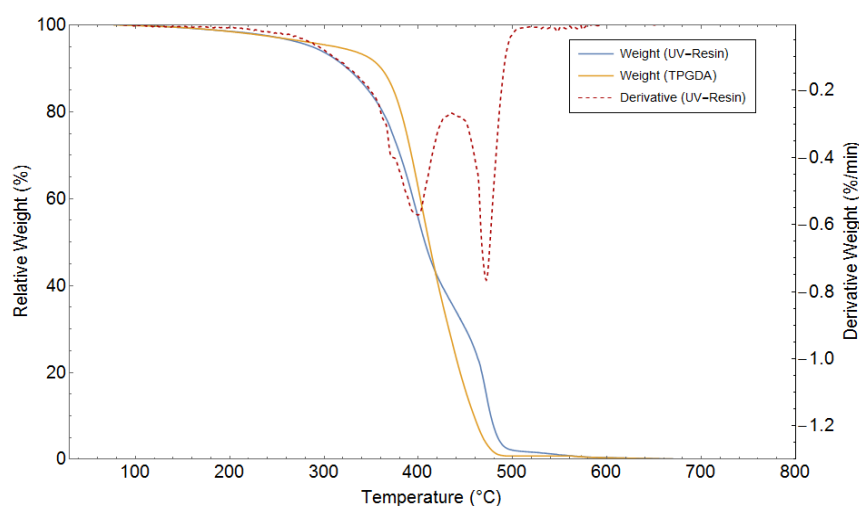


**Figure 67:** TGA data for the two photo-curable materials used in this work, a high viscosity resin and a jettable formulation of TPGDA. Both samples were cured before the test. DTG is also shown for the high viscosity resin, indicating the temperatures of maximum mass loss. TPGDA data reproduced from (He et al. 2017).

## 5.4 Surface tension

The pendant drop method was used to measure the equilibrium surface tension of the high viscosity materials (Table 8). The fit error from the Young-Laplace model (equation 40) to the drops contour performed by the DSA system and the shape parameter ( $B$ ) are also given. The measurements were performed at 25 °C because that is the operation temperature that is used during ejection, however is clear from the literature that an increment in temperature would result in a decrease in the surface tension in all cases (Bhuiyan et al. 2015) (Khaleduzzaman et al. 2013).

**Table 8:** Surface tension and fitting parameters for the high viscosity materials used in this work

Sample	Surface Tension (mN/m)	Fit error ( $\mu\text{m}$ )	B
<i>Carbon Paint</i>	$57.1 \pm 0.8$	$1.9 \pm 0.3$	$0.579 \pm 0.005$
<i>UV-Resin</i>	$36.67 \pm 0.03$	$0.73 \pm 0.05$	$0.5977 \pm 0.0002$
<i>PEDOT:PSS</i>	$17.8 \pm 1.2$	$4.1 \pm 0.5$	$0.600 \pm 0.012$
<i>Silver Paste</i>	$11.0 \pm 0.4$	$3.2 \pm 0.5$	$0.620 \pm 0.013$

The results are repeatable and show a wide range of surface tension values from 57.1 mN/m from the carbon paint to 11.0 mN/m to the silver paste, approximately 5 times smaller. The fit errors are below 5  $\mu\text{m}$ , which compared with the typical diameter of the measured drops (2 mm) was deemed acceptable. This error and the standard error of the surface tension are remarkably small for the UV-resin, but both increase for higher viscosity materials. This can be explained by the shape irregularities observed for these higher viscosity fluids, which occasionally deviated the overall profile of the drop from the assumed axisymmetric shape required for the pendant drop method. Another potentially relevant factor is that, as it will be shown in the following section, all tested materials expect the UV-resin display strong non-Newtonian behaviour, which increases their viscosities at low shear rates like the one applied to the fluids during the present tests. This shear rate dependency is expected to play a relevant role in the dynamic surface tension of the fluids, while the microstructure is re-arranged at medium high shear rates. However, once the drop has reached mechanical equilibrium, which is a requirement of the pendant drop method, and the micro-structure is allowed to relax and re-form, these dynamic effects are expected to become negligible.

The **carbon paint** has the highest surface tension of the set, which is expected considering the high volume of water that it has in its formulation and the high surface tension of water (72 mN/m at 25 °C (David R. Lide 2005)). This value, however, gets

significantly reduced by the presence of gum arabic, which is widely used in industry precisely for its low interfacial activity (Cao et al. 2013).

The **UV-resin** shows a value of  $36.67 \pm 0.03$  mN/m, which is consistent with other SLA photo-polymers of similar characteristics such as the Somos Waterclear 10120 (DSM, Netherlands), which has been reported to have a surface tension of 38 mN/m (Rosen et al. 2008). Interestingly, the UV-resin is also similar to the TPGDA used in this work, as it was in the case of thermal degradation, since He *et al.* (He et al. 2017) showed with an analogous pendant drop method a surface tension for this material of  $30.78 \pm 0.10$  mN/m.

The **silver paste** and the **PEDOT:PSS** dispersion can be discussed together since both are nanofluids. In both cases the values obtained are much smaller than not only the other two tested materials but also the surface tension of their respective solvents. Specifically, the silver material displays a surface tension of  $11.0 \pm 0.4$  mN/m, while its main solvent,  $\alpha$ -terpineol, is at 31 - 33 mN/m. Similarly, the measured surface tension of PEDOT:PSS is  $17.8 \pm 1.2$ , but for its solvents, water, diethylene glycol and propylene glycol are 72 mN/m, 45 mN/m and 36 mN/m respectively (David R. Lide 2005). This reduced surface tension can be explained by the presence of nanoparticles, which have been reported to decrease the surface tension at concentrations lower than a certain threshold, due to the accumulation of particles at the interface and the attractive inter-particle forces (Vafaei et al. 2009) (Khaleduzzaman et al. 2013) (Tanvir & Qiao 2012). More relevant is the fact that both nanofluids have anti-agglomeration mechanisms such as surfactants and steric polymers adsorbed on the nanoparticles' surface. These are crucial for the long term stability of the inks, but since the long chain surfactant molecules form a charged layer around the particles that repels other molecules, inter-particle interactions are decreased and, consequently, the surface tension of the fluid (Tanvir & Qiao 2012).

## 5.5 Viscosity

### 5.5.1 Shear viscosity

The flow curve for the 4 high viscosity materials used in this work was obtained by combining the use of two rheometers, a rotary one and a microfluidic, the results are plotted in Figure 68. All of them show non-Newtonian behaviour in the measured range and display different degrees of shear thinning. The **PEDOT:PSS** dispersion is the most clear example, since it shows a shear viscosity variation of more than 5 orders of magnitude between  $10^{-2}$  and  $10^5$  s<sup>-1</sup>. The high viscosity at low shear rates is explained by the balance

between inter-particle forces, which creates a gel-like microstructure on the fluid. Moreover, the soft nature of the PEDOT:PSS particles allow them to deform at high shear rates, which is responsible of the strong shear thinning behaviour (Elschner et al. 2012). Similarly, the **silver paste** also shows a high viscosity at low shear rates and pronounced thinning slope, which is again related with the stability of the dispersion and the concentration of solids (Barnes 2000). The difference in this case is that, even though the silver particles are also stabilised by polymers adsorbed in their surface, their core is metallic and therefore they do not deform as the gel-particles of the PEDOT:PSS, which together with its higher solids content is a possible explanation of its higher viscosity at the apparent plateau at high shear rates. The **carbon paint** displays a similar behaviour but with a less pronounced thinning slope and a higher final viscosity at high shear rates. This elevated viscosity at  $10^3 \text{ s}^{-1}$  requires a higher pressure from the microfluidic rheometer to maintain the flow, which eventually limits the shear rate achievable by the instrument. This trend is clear for all materials, allowing higher shear rates for lower viscosities, but also increasing the minimum measurable rate proportionally. On the lower side of the viscosity spectrum is the **UV-resin**, which exhibits a small decreasing trend at very low shear rates and later plateaus to a constant viscosity, behaving as a Newtonian fluid between  $1 \text{ s}^{-1}$  and  $10^4 \text{ s}^{-1}$ . This behaviour can be attributed to the absence of particulates or long polymeric chains in the material, which is capable to align with the flow at very low shear rates.

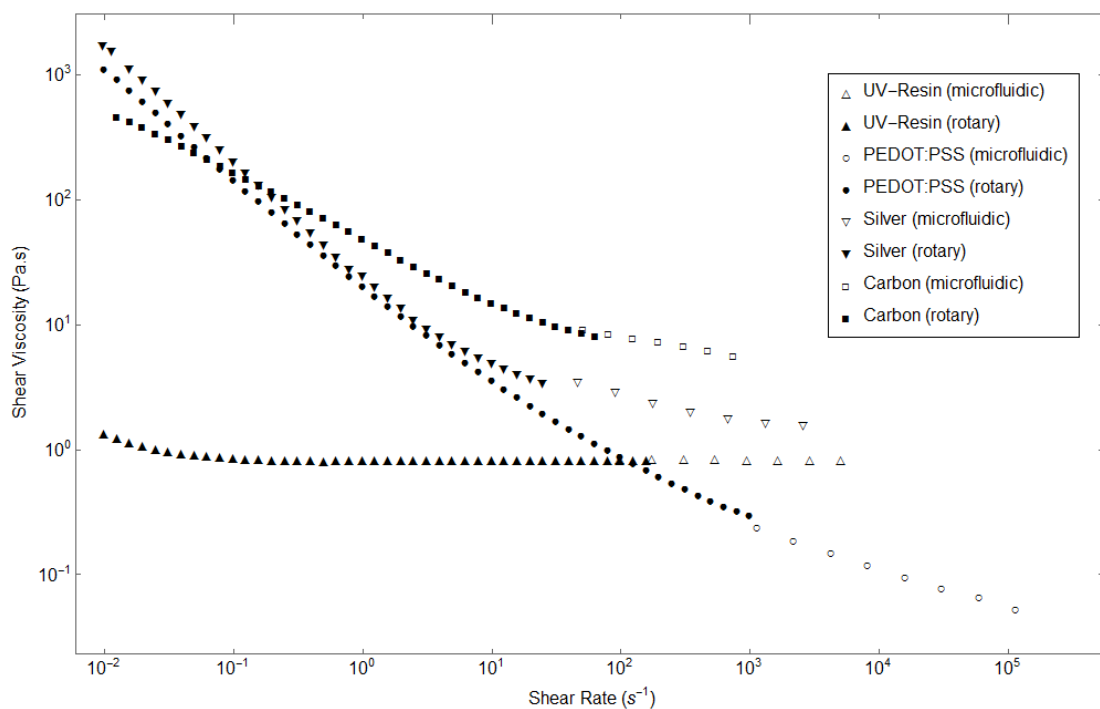


**Figure 68:** Flow curves of the materials used in this work at 25 °C. The solid symbols represent the data from a rotary rheometer while the hollow ones are related to the microfluidic measurements. Good agreement between measuring systems is observed.

The transition between both rheometers is good in all cases and it continues the general trends observed with the rotary rheometer. It is noteworthy that the pressure range of the microfluidic device was used completely to maximise the shear rate range covered. However, it is known that the viscous stresses at low flow rates can become of the order of the resolution of the pressure sensors (Pipe et al. 2008), which introduces noise in the data and explains the initial deviation from the expected trend of some materials. Nevertheless, the fact that both methods provide compatible data seems to indicate that potentially problematic effects such as secondary flows (Barnes 2000), wall-slip (Bertola et al. 2003) or evaporation (Barnes 2000) are negligible in the middle range of shear rates, since due to the great differences between the general operation of both instruments it is unlikely that they affect the results in the same proportion in both cases. In particular, wall slip is based on the depletion of particles near the wall, which is dependent on the particle size and particle size distribution (Barnes 2000) and it is unlikely to affect the results for multi-modal dispersions or nanofluids if the concentration is not very high, which is not the case of the present materials. Additionally, this effect is typically found at low shear rates, when a plug flow of un-yielded core can be maintained due to the lubrication effect near the walls (Bertola et al. 2003), however, the abrupt change in viscosity at low shear rates typical from the transition between wall-slip and non-slip is not observed for any of the materials tested.

In general, all 4 materials show a shear thinning behaviour at lower to medium shear rates, which could be initially represented by the power-law, but later their respective slopes are reduced towards a plateau region that is captured by the experimental data with different success depending of the material. Therefore, in order to describe the fluids near the region of interest for jetting (typically between  $10^5$  to  $10^7$   $\text{s}^{-1}$ ), the Sisko model described by Equation 15 in section 2.4 is used and its results summarised in Figure 69 and Table 9.

The Sisko model describes well the **carbon paint**, displaying a smooth transition between the data from the two rheometers (around  $10^2$   $\text{s}^{-1}$ ) and a narrow 95% confidence interval overall. The **silver paste** shows a slightly less smooth transition (between  $10^1$   $\text{s}^{-1}$  and  $10^2$   $\text{s}^{-1}$ ) but despite the initial bump in viscosity the general trend is well described by the Sisko curve and a high viscosity plateau is anticipated. This local deviation, however, affects the standard error of the coefficients considerably. The **UV-resin** is well captured by the model with almost negligible coefficients and a main contribution from the plateau viscosity. In fact, the final viscosity is maintained from  $1$   $\text{s}^{-1}$  onwards in a very Newtonian fashion. The situation for the **PEDOT:PSS dispersion** is very different, since even

though the change in its thinning trend is obvious from Figure 68, the high viscosity plateau does not seem as close to the measured values as it was with the other materials. Therefore, while the Sisko model describes the general trend of the fluid, the obtained value for  $\eta_{\infty}$  is considerably speculative, which is represented by its high uncertainty. However, since the results for the PEDOT:PSS are the events measured the highest shear rate, the extrapolation at high shear rates is not required and the last observed value would be used instead. The other materials result in more accurate values of  $\eta_{\infty}$  but its validity at higher shear rates will be determined by the ability of the fluids to keep its viscosity in this plateau without noticeable variations in the trend. The most probable deviation from this expected plateau is a shear thickening region, where the viscosity tends to increase again with shear rate. However, the critical shear rate that would initiate the thickening behaviour is known to be approximately proportional to the inverse of the particle size (H. a. Barnes 1999), which for the nanoparticles dispersed in these fluids would situate the hypothetical critical rate beyond the jetting region. Furthermore, this phenomenon becomes relevant at phase volume greater than 50 % (H. a. Barnes 1999), which is not achieved in any of the studied fluids. Particle size distribution with multiple peaks, like the one displayed by the carbon paint, have shown a reduction of the thickening effect (H. a. Barnes 1999).

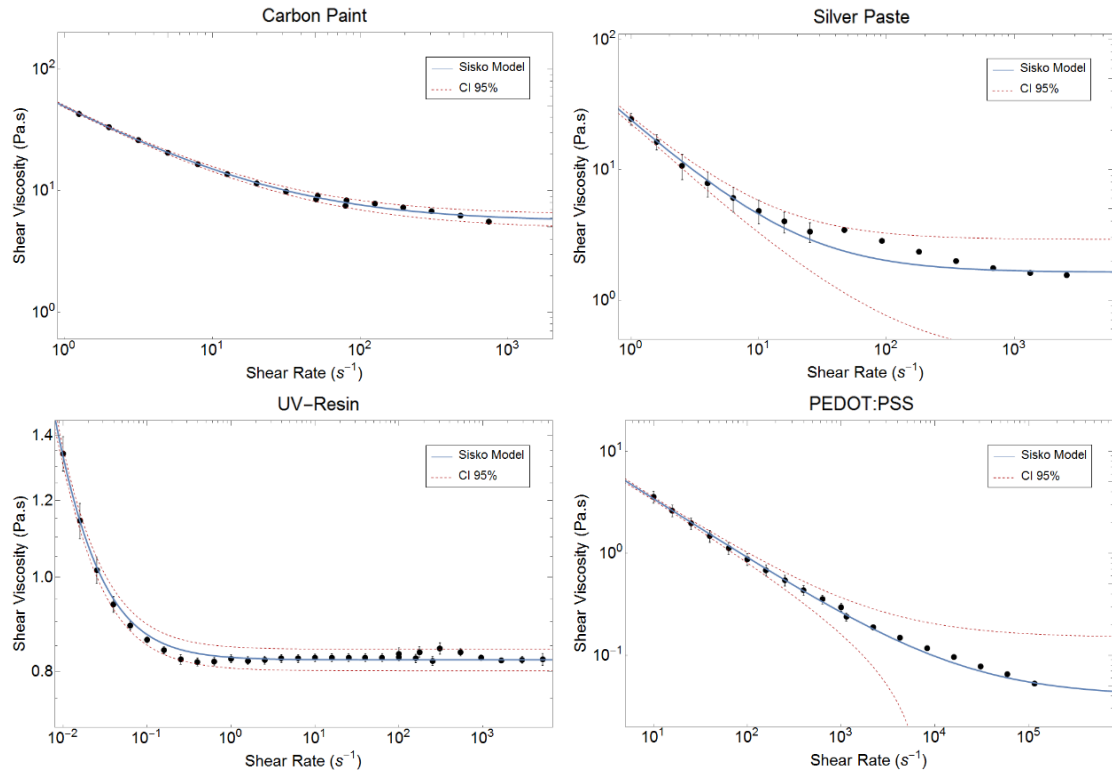


**Figure 69:** Comparison of data with the Sisko model (solid line) and its 95% confidence interval (red dashed lines). The data was taken with two different rheometers, as it is shown in Figure 68, which explains the transition fluctuations observed.

**Table 9:** Sisko model ( $\eta = \eta_{\infty} + K\dot{\gamma}^{n-1}$ ) fitting parameters for the high viscosity materials used in this work. The coefficients are given as average  $\pm$  standard error.

Sample	$\eta_{\infty}$ (Pa·s)	K (Pa·s <sup>n</sup> )	n	Adjusted r <sup>2</sup>
<i>Carbon Paint</i>	5.6 $\pm$ 0.2	43.6 $\pm$ 0.3	0.338 $\pm$ 0.012	0.9996
<i>Silver Paste</i>	1.6 $\pm$ 0.2	22.4 $\pm$ 0.5	0.12 $\pm$ 0.04	0.9961
<i>UV-Resin</i>	0.822 $\pm$ 0.002	0.0051 $\pm$ 0.0008	0.00 $\pm$ 0.03	0.9998
<i>PEDOT:PSS</i>	0.04 $\pm$ 0.02	13.2 $\pm$ 0.5	0.41 $\pm$ 0.02	0.9985

From the same experiments that resulted in the flow curves shown in Figure 68 it is possible to obtain the relation of the shear stress and the shear rate for these materials (Figure 70). This alternative representation helps to assess the stress behaviour of the materials at low shear rates. Especially interesting is the plateau observed for the silver paste and the PEDOT:PSS, which indicates an apparent yield stress. However, since this behaviour cannot be extrapolated to infinitely small shear rates the study of this magnitude will be limited to report the stress value at the lowest measured shear rate, which is  $11.1 \pm 0.9$  Pa for the conductive polymer and  $16.4 \pm 0.3$  Pa for the silver-based material. The stress plateau at low shear rates is not observed for the photo-resin or the carbon paint, which show shear stresses at  $10^{-2} \text{ s}^{-1}$  of  $13.4 \pm 0.5$  mPa and  $5.8 \pm 1.7$  Pa respectively.

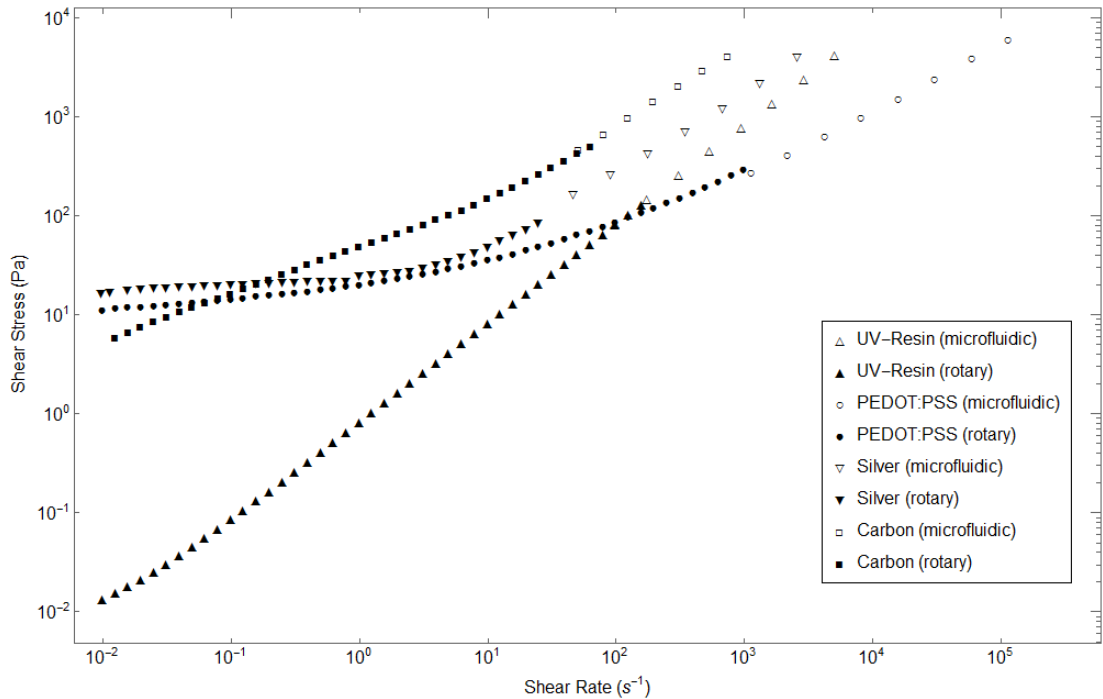


**Figure 70:** Shear stress against shear rate curves for the high viscosity materials involved in this work, measured at 25 °C. The solid symbols represent the data from a rotary rheometer while the hollow ones are related to the microfluidic measurements.

The previous measurements were performed at 25 °C, since that is the jetting temperature that is going to be used in this work. Nonetheless, the flow curves of the viscous materials were also recorded at 1000 s<sup>-1</sup> between 25 °C and 60 °C to assess the variation of their viscosity with temperature (Figure 71). The Arrhenius model (Equation 3) is fitted to the data and the obtained parameters are summarised in Table 10.

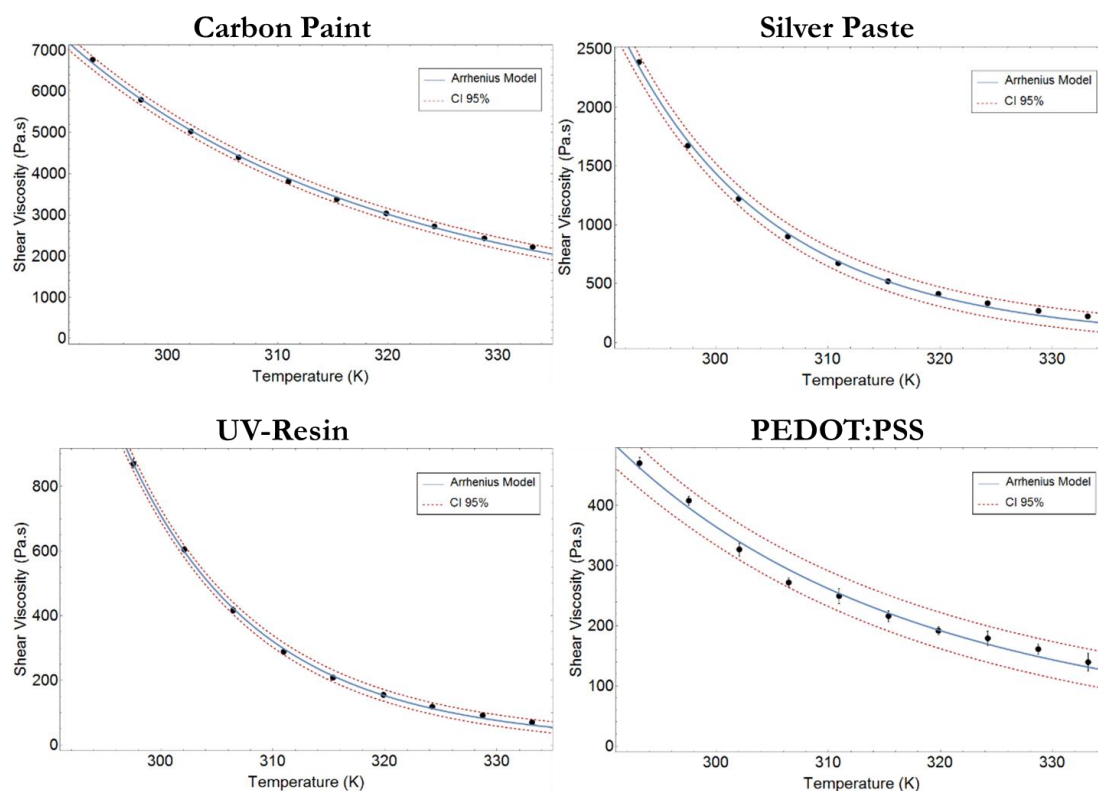


**Figure 71:** Temperature dependency of the shear viscosity at a constant apparent shear rate of 1000 s<sup>-1</sup>. The temperature range is 20 to 60 °C, which is represented as absolute temperature (K) to provide scientific meaning to the Arrhenius model parameters, which can be related with the activation energy of the fluid. Red dashed lines indicate the 95% Confidence Interval of the fit.

It is clear from the obtained  $b$  factors that the photo-curable resin and the silver formulation are the most temperature sensitive materials, which display variations in their viscosity of over 85 % within 35 °C, while the carbon paint and the PEDOT:PSS variation is in both cases below 70 %. Since the relation is exponential, the temperature-induced viscosity variation at high shear temperatures is less pronounced than at near room temperature in all cases. This, if no other considerations were considered, would suggest choosing the highest available temperature to minimise the uncontrolled viscosity variations due to thermal fluctuations in the system, which can cause undesired variations in the jetting process. However, there are many reasons to keep the temperature as low as possible. The first and most important for this work is the fact that the printing assembly was fabricated by LS using nylon (PA12), which can change its shape if the recrystallization temperature is exceeded, affecting the process accuracy. Additionally, even though a

reduction of viscosity can be beneficial in some stages of the process, it will diminish the advantages of non-Newtonian fluids in terms of dispersion stability at low shear rates, since the reduction in viscosity related with an increase in temperature does not discriminate between different shear rates. Furthermore, higher temperatures increment the evaporation rate of the solvents, which can affect the stability of the materials during ejection, specifically during idle times between drops, where a local variation of the concentration can cause blockages and instabilities. Therefore, the temperature for the process will be kept at 25 °C unless specified otherwise.

**Table 10:** Arrhenius model ( $\eta = Ae^{b/T}$ ) fitting parameters for the high viscosity materials used in this work. The coefficients are given as average  $\pm$  standard error.

Sample	$\Delta\eta_{25-60\text{ }^\circ\text{C}}$ (%)	A	b	Adjusted $r^2$
Carbon Paint	$62 \pm 1$	$(5.0 \pm 0.6) \cdot 10^1$	$2780 \pm 40$	0.9998
PEDOT:PSS	$66 \pm 4$	$(1.3 \pm 0.5) \cdot 10^2$	$3100 \pm 120$	0.9981
Silver Paste	$87 \pm 1$	$(1.1 \pm 0.5) \cdot 10^6$	$6300 \pm 130$	0.9990
UV-Resin	$92 \pm 2$	$(1.4 \pm 0.4) \cdot 10^8$	$7400 \pm 90$	0.9997

A low viscosity formulation of TPGDA was also characterised and its flow curve is shown in Figure 72. In this case, only the microfluidic rheometer was used to reach the high end of the shear rate range, which was  $2 \cdot 10^5 \text{ s}^{-1}$  due to its overall low viscosity. The material is very weakly structured, which is manifested by the obtained power-law coefficients ( $K = 0.0205 \pm 0.0005 \text{ Pa}\cdot\text{s}$ ,  $n = 0.957 \pm 0.002$ ,  $r_{adj}^2 = 0.99996$ ). As in the case of the PEDOT:PSS, extrapolation is not necessary since the highest shear rate is already in the typical shear rate region.

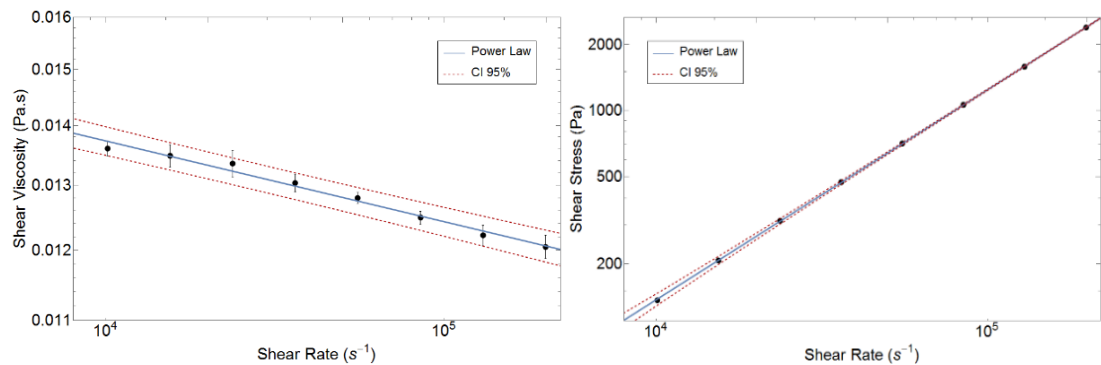


**Figure 72:** Shear Viscosity (left) and shear stress (right) dependency on the shear rate of a TPGDA sample measured in a microfluidic rheometer at 25 °C. The solid line shows the power-law model fit to the experimental data, which results in  $K = 0.0205 \pm 0.0005 \text{ Pa}\cdot\text{s}$ ,  $n = 0.957 \pm 0.002$  and  $r_{adj}^2 = 0.99996$ . The dashed red lines represent the 95% confidence interval of the fit.

### 5.5.2 Viscoelasticity

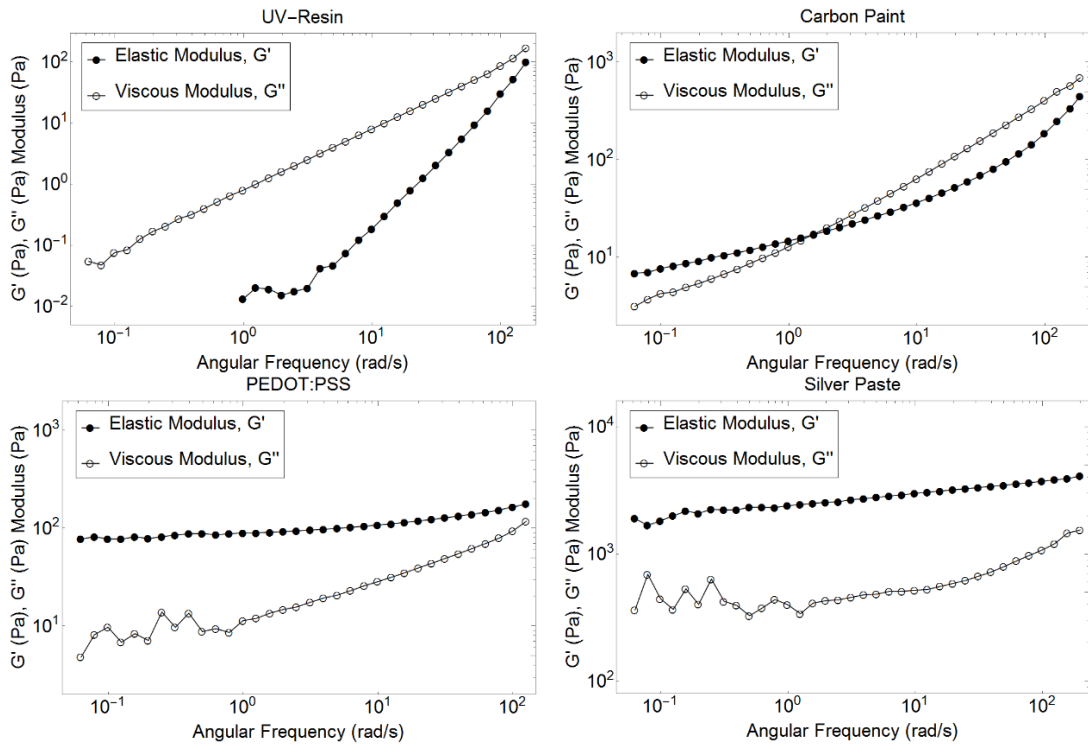


**Figure 73:** Oscillatory spectra of the high viscosity materials used in this work, revealing the evolution of the elastic ( $G'$ ) and viscous ( $G''$ ) moduli across four orders of magnitude of angular frequencies. The measurements were performed at 25 °C in an environmentally controlled rheometer with a cone-and-plate geometry.

The viscoelastic response of the materials was tested by oscillatory measurements, which provided the evolution of the elastic ( $G'$ ) and viscous ( $G''$ ) moduli between 0.01 and 200 rad/s, as it is shown in Figure 73. These frequencies represent different timescales, where low frequencies are equivalent to long timescales and high frequencies are associated to short timescales. It is common to associate a particular frequency (in rad/s units) with a shear rate of the same magnitude in order to compare oscillatory data with shear viscosity measurements. Therefore, the presented results can provide relevant information for the approximate range of shear rates between  $10^{-1}$  to  $10^2$  s $^{-1}$ , which can explain low shear mechanisms such as their quasi-equilibrium structure, their transport through small pipes at low flow rates and the settling and levelling on the substrate after ejection.

The **UV-resin** shows a behaviour very different from the other three materials, since its  $G''$  modulus dominates over the  $G'$  at all times, confirming the liquid-like behaviour that can be anticipated during its manipulation. Additionally, the lack of relevant elastic structure at low frequencies is compatible with the shear stress curve shown in Figure 70, where no apparent yield stress was observed. This means that, without a strong elastic opposition to the surface tension, this material will be more dominated by capillary forces than the other high viscosity fluids, which will result in higher spreading on the

substrate and smoother finishing when settled. Furthermore, even though the crossover frequency between both moduli at the end of the terminal region is not contained in the measured range, it is likely that it will happen between  $10^2$  and  $10^3$  rad/s if both moduli maintain their trends. This means that the longest relaxation time of the material is shorter than, but close to, 10 ms. Which compared to some relevant timescales involved in the jetting process suggests that it will behave solid-like during ejection (timescales in the  $\mu$ s region) but spread in the substrate as a liquid, as it was anticipated above. The noise observed at low frequencies, which also affects the other materials, is a product of the long timescales required to acquire these points, since the measurement is more sensitive to environmental variations during longer tests.

The behaviour of the **PEDOT:PSS** dispersion and the **silver paste** can be described together, since both are stable dispersions of nanoparticles. In both cases the fluids are in the plateau region of the viscoelastic curve with a dominant  $G'$ . This is the consequence of a solid-like structure, where the internal forces between nanoparticles and adsorbed polymers are equilibrated and form a mechanically stable network (Barnes 2000). The larger magnitude of the modules for the silver paste indicates that this material is mechanically stronger than PEDOT:PSS and the rest of fluids here studied. The solid-like behaviour of these nanofluids agrees with the previously observed apparent yield stress (Figure 70), since the materials would withstand moderate stresses before flowing. This mechanical integrity, together with their shear thinning properties, are expected from screen printing materials, since this prevents them from leaking through the mesh before the squeegee is applied, allows flow through it when a stress is applied and minimise capillary spreading on the substrate, which provides higher edge definition and clearer features (Faddoul et al. 2012). These rheological properties have also been identified as desirable for cold extrusion systems, since they allow the retention of shape of the extruded layers and facilitates the creation of 3D features (Lewis 2006). The frequency region tested during the experiment does not provide information about the beginning of the plateau region, which means that the longest relaxation time is largely undetermined apart from the lower limit of 17 s, obtained from the minimum observed frequency of 0.06 rad/s. This indicates that practically all the timescales involved in jetting are much smaller than this relaxation time, and so the material will have a dominantly solid-like behaviour.

The case of the **carbon paint** is closer to these nanofluids than the UV-resin in the sense that it also displays a dominant solid-like behaviour in the lower part of the frequency sweep. However, unlike in the previous cases, the viscous moduli ( $G''$ ) undertake the elastic one ( $G'$ ) at approximately 1.25 rad/s, which marks the beginning of the transition region. Furthermore, both moduli approach again at frequencies higher than  $10^2$  rad/s, anticipating the high frequency crossover that will give place to another relaxation time. Nevertheless, to describe the behaviour at low shear rates the relevant relaxation time would be the one marked by the beginning of the plateau region, which, as in the case of the nanofluids, is outside of the measuring region and can only be generally defined as greater than 17 s.

## 5.6 Conclusions from characterisation

The density, particle size, solid content, surface tension and viscosity of the materials used in this work were characterised and discussed. The high solid content of the inks and their non-Newtonian behaviour stand out from the typical materials jetted on the literature using PIJ. These properties, however, are not expected to hinder their ejection with micro-dispensing valves based on a combination of pneumatic and mechanical actuation. Furthermore, since these valves can also increase their temperature up to 100 °C, material properties such as viscosity and surface tension could be potentially tuned to facilitate their processability. These properties are related with their ejectability in the following section.



## **6. Results and discussion:**

### **Drop formation and deposition**

The materials used in this work were characterised in Chapter 5, while the set-up and printing approach were described in Chapter 3. In this section the same materials were loaded into the developed system and their printability was studied by varying printing parameters such as the firing pulse shape or the applied pneumatic pressure while monitoring the output. The drop formation stage was studied by observing recorded videos under various printing settings, paying particular attention to drop speed and tail-breaking behaviour was obtained. The last one is important because not only it influences the overall speed of the drop but also contributes greatly to the cleanliness of the nozzle plate after each ejection, which ultimately dictates the repeatability of the process. The performance of each fluid was also tested in a simpler experiment where the footprints of deposited droplets are analysed to obtain their equivalent radius and circularity, which is used as an estimator of printing quality. The mass of several drop streams was measured with an external set-up to obtain the volume of individual drops based on the density measured in the previous chapter. The results of the various tests in this section are finally combined in the conclusions sections of this chapter, where a printability window for this process is defined.

#### **6.1 Jettability study of low viscosity TPGDA**

A study of the ejectability of TPGDA ink from PIJ printheads was performed using the Advance Drop Analysis (ADA) native tool of the system. The negative pressure on the head was set at -24.0 mbar and the operating temperatures at 25 °C, which allows ejection without nozzle plate flooding during idle times. The ejection frequency was fixed at 4 kHz, which corresponds to a printing speed of 203 mm/s at 500 DPI. The optimisation consisted in two rounds of experiments, a first iteration where the constant values were chosen arbitrarily and a second one where the optimum values of the first round are used as constant values. The results of both iterations were very similar, with the confirmation experiment yielding the same optimum values than the first, i.e. a peak time of 5  $\mu$ s, rise and fall times of 2  $\mu$ s and overall voltage of 80 V. The results of the second iteration are shown in Figure 74. The responses of the rise and falling times are remarkably similar and present slower drops as the time increases, which is expected considering that this implies

slower contraction and expansion cycles for the piezoelectric actuators in charge of the ejection. Nevertheless, there is still a maximum in speed at  $2\ \mu\text{s}$  in both cases that marks the most efficient time for these pulse sections. Similarly, the peak time also presents a clear maximum in speed at  $5\ \mu\text{s}$ , which is a product of constructive interference between the primary and reflected pressure waves inside the nozzle channel. The voltage however does not display a local maximum in speed in the tested region and instead it shows an increasing trend of the drop speed as the voltage is raised. The resulting drop after pulse optimisation exhibits a speed of  $5.90 \pm 0.13\ \text{m/s}$  and a volume of  $29.80 \pm 0.19\ \text{pl}$ .

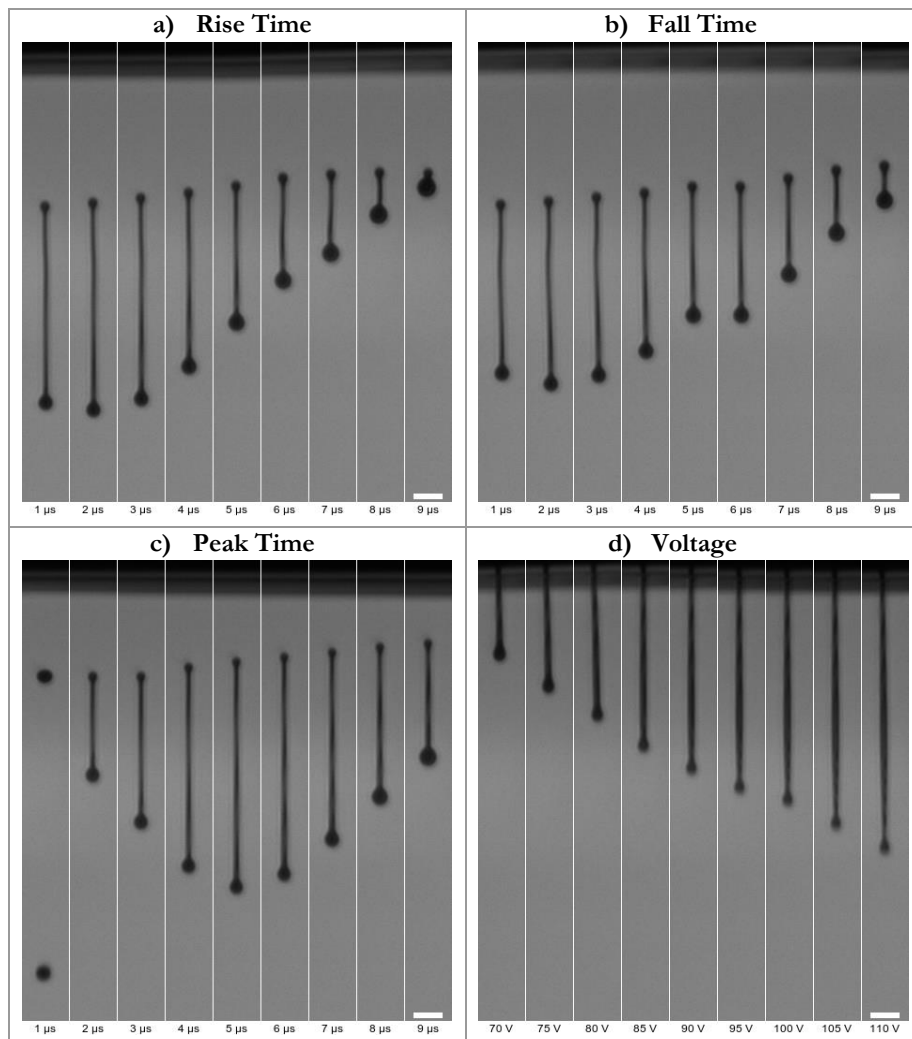


**Figure 74:** Pulse optimization tests performed using the Advance Drop Analysis capabilities of the system. Constant values in each case match the obtained optimum settings of rise time (a), fall time (b), peak time (c) and printhead voltage (d), which are  $2\ \mu\text{s}$ ,  $2\ \mu\text{s}$ ,  $5\ \mu\text{s}$  and  $80\ \text{V}$  respectively. The scale bar is  $50\ \mu\text{m}$  and the overall calibration of the images is  $1.56\ \mu\text{m}/\text{px}$ .

## 6.2 High Speed video analysis

A high-speed camera with a framerate of 30,000 fps and a shutter of  $1\ \mu\text{s}$  was used to observe the ejection of the 4 viscous materials used in this work under 3 different pneumatic pressures (0.1, 0.3 and 0.5 MPa) and 6 valve closing times ( $120\ \mu\text{s}$ ,  $200\ \mu\text{s}$ ,  $300$

$\mu\text{s}$ , 400  $\mu\text{s}$ , 600  $\mu\text{s}$ , 1300  $\mu\text{s}$ ) with a fix valve stroke of 160  $\mu\text{m}$ , a pulse time of 2 ms and a cycle time of 5 ms (equivalent to a jetting frequency of 200 Hz). The systematic study of the combinations between these pneumatic pressures and valve closing speeds is from now on referred as *matrix experiment* in this thesis. The most promising profiles were selected for each material and a second set of videos was recorded in the same conditions except for the glass substrate introduced to observe the impact and spreading of the drops. Both experiments provided valuable information about the process itself and the jettability of each material.

### 6.2.1 *Matrix Experiment*

The discussion of the matrix experiment starts with the results for **PEDOT: PSS** because it displays the most general behaviour in terms of the possible jetting scenarios. This is due to its shear thinning behaviour (as shown in Figure 68), which results in a relatively low viscosity at the high shear rates applied in the narrow nozzle of the system. Therefore, since the required pressure to initiate a continuous stream of fluid through the nozzle is within the pneumatic capabilities of the system, the jetting outcome is split into two main situations depending whether the applied pressure is above or below that critical pressure, resulting in the two modes that will be known in the following as *pneumatically initiated* and *mechanically initiated* ejection, respectively. Thus, when the pressure is 0.5 MPa each jet is started as soon as the valve is open at the beginning of the pulse time and it continues until the plunger mechanically blocks the nozzle. In this configuration, the speed of the last part of the jet depends strongly on the speed of the ceramic ball during the closing stage while the front is a function of the pneumatic pressure, as can be seen in Figure 75. From the figure, it is clear that the speed of the jet's trailing part in relation to its front is a crucial printing parameter, since a pressure perturbation faster than the leading part of the jet results in a fluid rupture known in this work as a splash-in-flight. However, if the closing time is selected such as it results in a slower fluid speed, the jetting event can be finished without a reversal of the jet or atomization, as it is the case of the closing times 600  $\mu\text{s}$  and 1300  $\mu\text{s}$  for the PEDOT:PSS used in this work. Furthermore, if the speed of the closing part of the jet is slower than the front, a reverse situation is encountered where the jet elongates and, depending on properties such as surface tension and viscoelastic behaviour of the fluid, a dumbbell structure like the one described by Bazilevskii *et al.* (Bazilevskii & Rozhkov 2015) and discussed in Chapter 2.4 is formed, which eventually would coalesce into the main drop or break into satellites.

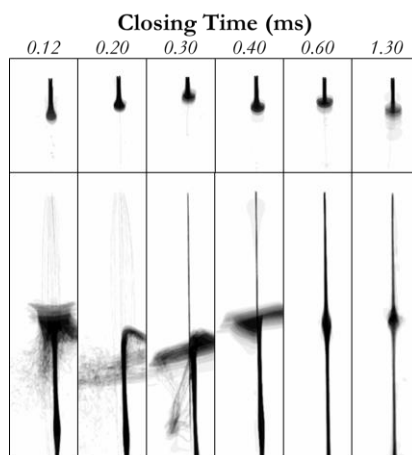


**Figure 75:** Still frames of the ejection of an aqueous dispersion of PEDOT:PSS at an applied pressure of 0.5 MPa and different closing times of the dispensing valve. The top row of images corresponds to the beginning of the pneumatic ejection, while the bottom row shows the fluid-on-fluid collision (or splash-in-flight) caused after  $t_{\text{pulse}} + t_{\text{closing}}$ . The blurring from the images is the result of the superposition of 20 binarized frames. The width of the images is 1.024 mm.

If the applied pneumatic pressure is 0.1 MPa the system operates in mechanically initiated ejection mode and no flow is observed until the closing stage of the valve. This indicates that in this configuration the pulse length is irrelevant and suggests that the deposited volumes would be the smallest that the system can provide for such closing configuration and material. In this case, there is only one body of fluid being ejected at a velocity dependent to the closing speed. It is expected that a difference in pneumatic pressure would also influence the speed of the drop even if it is not enough to initiate ejection on its own, but this was not observed in this experiment due to the temporal resolution of the high-speed camera. Furthermore, it was observed that at slow closing times (600  $\mu\text{s}$  and 1300  $\mu\text{s}$ ) the fluid has not enough kinetic energy to overcome the surface tension and elastic forces on the nozzle, leading to a configuration incapable of generating drops.

An intermediate situation was observed for the 0.3 MPa set of videos, where the pneumatic pressure could initiate the flow in most cases but in a more unreliable way than in both previous configurations. This is attributed to the slower speed of the pneumatically dispensed fluid compared with the 0.5 MPa situation, which either directly wets the nozzle or causes the splash-in-flight to happen closer to the nozzle plate and often results in an irregular wetting of the nozzle. On its own this does not prevent the current jetting event but it changes the initial conditions for the following jet, which must overcome a larger energy barrier to break free and, in case that it does it, it would travel away from the nozzle at a slower speed than the previous ejection. Eventually, the ejection is completely interrupted and each drop attempt only serves to increase the volume of the fluid meniscus hanging from the nozzle plate.

The previously mentioned results are summarised in Figure 76, where the average speed of the leading part of the jet and the volume of material left behind after 30 drops are shown. The speed is obtained from the time that a jet requires to cover a known distance and it has an associate error inversely proportional to the number of frames captured between the start of the event and the passing time. This is particularly noticeable for the fastest profiles that only provide a single frame between those two moments, while the error is greatly reduced as the speed decreases and the number of meaningful frames is increased. Also, it is important to remark that the shown speed corresponds to the front of the jet at the moment of crossing the monitored distance, which explains why all the pneumatically initiated configurations display a compatible speed around 7 m/s independently of their closing time, which is the sole result of the pneumatic pressure. Additionally, some configurations result in very unstable ejection that do not produce the required 30 drops. In these cases, the speed given in Figure 76 describes only the first event, which starts with a clean nozzle plate. These configurations, known in the present work as one-drop observations, are relevant as examples of the minimum speed that a drop of a fluid requires to detach from the nozzle. In the case of the nozzle wetting results, it is notable that most of the events with closing times equal or below 400  $\mu\text{s}$  result in clean ejection due to the higher kinetic energy imparted to the fluid in these cases. The only exception is the profile 300  $\mu\text{s}$ /0.3 MPa, which serves as an example of the previously explained unreliable performance of the intermediate pneumatic profile. Finally, both the 600  $\mu\text{s}$  and 1300  $\mu\text{s}$  closing times are unable to create drops on their own and result in noticeable residual material being deposited on the nozzle plate after 30 drops, but the same closing settings result in clean ejection when a pneumatically initiated mode is used, as is the case for PEDOT:PSS at 0.5 MPa.

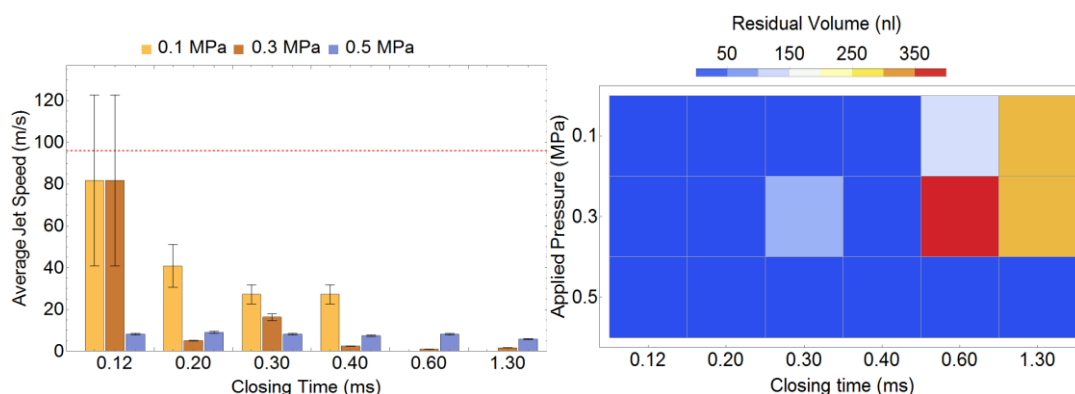


**Figure 76:** Average speed of the leading part of PEDOT:PSS jets (**left**). The red dashed line corresponds to the maximum speed limit of 96 m/s imposed by the shutter of the camera (1  $\mu\text{s}$ ). The events represent the ejection of 30 drops except in the 2 slowest profiles at pressures lower than 0.5 MPa, which resulted in few drops before the accumulated material hindered further ejection (one-drop events). Volume of residue left in the nozzle plate after 30 ejections is shown (**right**).

The **silver paste** shares several properties with PEDOT:PSS, as it was shown in Chapter 5. Both are nano-fluids with low surface tension and a similar shear thinning behaviour at the low and middle range of tested shear rates. The microstructure arising from the interactions between their nanoparticles and the coating agents in charge of their dispersion lead in both cases to similar apparent yield stress and gel-like structure that introduces elastic components to the flow properties. The main difference between these fluids is their solid content, which is much higher for the silver formulation and results in a higher viscosity at high shear rates and an increased density. With these comparisons between both nanoparticle-based fluids in mind it is easier to understand the results of the matrix experiment for the silver material shown in Figure 77.

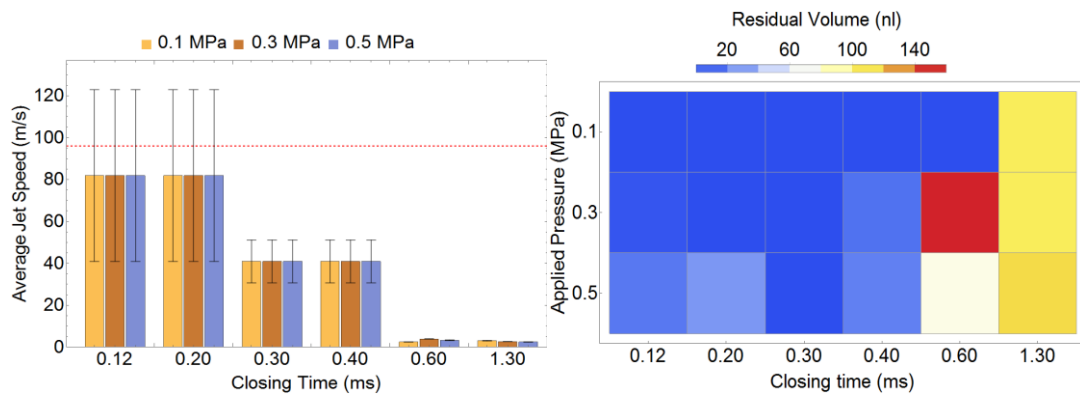


**Figure 77:** The average speed of the leading part of silver paste jets is shown on the **left**, where the red dashed line corresponds to the maximum speed limit of 96 m/s imposed by the shutter of the camera ( $1 \mu\text{s}$ ). The events represent the ejection of 30 drops except in the 2 slowest profiles, which resulted in a few drops before the accumulated material hindered further ejection (one-drop events). On the **right**, the volume of residue left in the nozzle plate after 30 ejections is shown.

In these videos, it is observed that the maximum pneumatic pressure administered by the system (0.5 MPa) is not enough to create a stream of fluid and therefore all configurations correspond to mechanically initiated ejections. However, for both the 0.3 and 0.5 MPa some residual material is left on the nozzle plate after the 30 ejections, which hints at the critical pressure for creating a stable stream being near the 0.5 MPa. As a test, 0.6 MPa was also tested but no noticeable difference was observed. Despite the nozzle wetting, 30 drops were obtained in all cases except for the 3 configurations at 1300  $\mu\text{s}$ , which only could eject between 1 and 3 drops before failing and are therefore represented in the speed figure as one-drop events. Interestingly, the configuration 600  $\mu\text{s}$ /0.1 MPa was able to produce the required drops in several occasions, as can be seen in Figure 78, but it failed 2 out of 5 times tested. The reason for this is that the speed of the drops in this case is very low compared with the other configurations ( $2.49 \pm 0.05 \text{ m/s}$ ) and thus, they have just enough kinetic energy to overcome the opposing forces when the nozzle is clean. Consequently, the ejection is stable for as long as no amount of fluid is deposited on the

nozzle plate but it fails as soon as any residue is left behind. Pneumatic or thermal fluctuations, electronic noise on the jetting signal, entrapped air bubbles on the fluid or flocculations of nanoparticles bigger than the average are potential sources of this instability. It must be noted that these effects do not seem to affect other configurations with faster droplets, which can jet through, and even remove, small volumes of residual material. Apart from the distinctive behaviour of this slow profile, the rest of the results for residual material and average speed of the jets are similar to the observed for PEDOT:PSS.

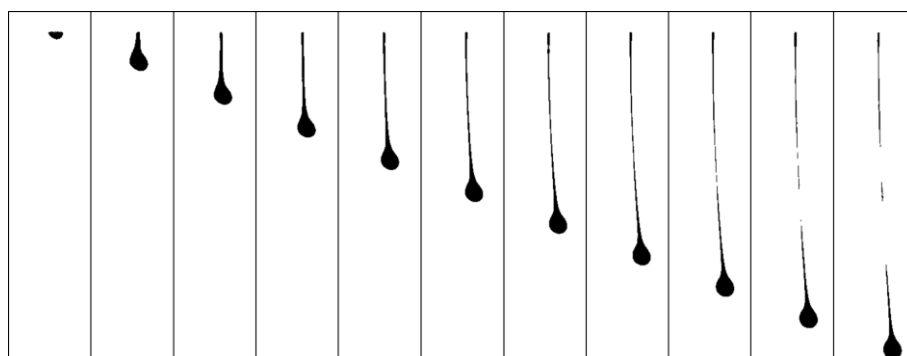


**Figure 78:** Still frames of the ejection of silver paste at an applied pressure of 0.1 MPa and a closing time of 600  $\mu\text{s}$ . Each image is showing the displacement of the drop after 150  $\mu\text{s}$ . The width of the images is 1.024 mm.

The next material evaluated in the matrix experiment was the **photo-curable resin**, which displayed a comparable viscosity at high shear rates to the silver paste without the intense shear thinning experienced by the nano-dispersion. Furthermore, the lack of complex structure also led to an absence of noticeable apparent yield stress and a very weak elastic response. Additionally, the surface tension of the resin is approximately 3 times that of the silver and its density almost half. Despite all these differences, the results for the residual material on the nozzle plate and the average speed of the jets shown in Figure 79 are similar to those obtained for the silver-based material. Specifically, the resin also operates in a mechanically initiated regime at all times but nozzle wetting was observed at 0.5 MPa, which is likely near the critical pressure. Moreover, the profiles with the longer closing times (600  $\mu\text{s}$  and 1300  $\mu\text{s}$ ) were capable of ejecting a few drops but eventually failed at all pressures due to a single disruptive event starting the residue accumulation. It is noteworthy that in the case of the UV-curable resin, the presence of residual material in the nozzle plate is particularly troublesome, since not only it affects the ejection of the subsequent drops but can also lead to nozzle blockage if reflected radiation reaches it, causing it to solidify.

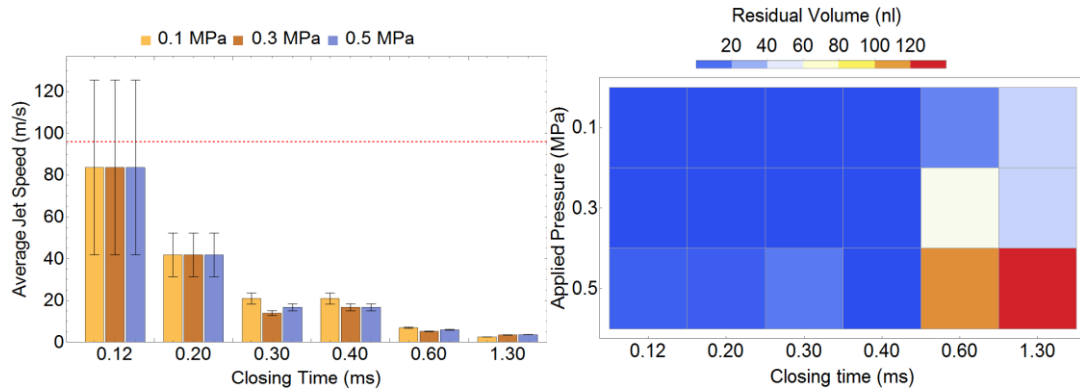


**Figure 79:** The average speed of the leading part of UV-curable resin jets is shown on the **left**, where the red dashed line corresponds to the maximum speed limit of 96 m/s imposed by the shutter of the camera ( $1 \mu\text{s}$ ). The events represent the ejection of 30 drops except in the 2 slowest profiles, which resulted in a few drops before the accumulated material hindered further ejection (one-drop events). On the **right**, the volume of residue left in the nozzle plate after 30 ejections is shown.

The **carbon paint** used in this work has the highest viscosity at high shear rate and surface tension among the tested fluids, which is expected to lead to the highest pressure required to initiate flow through the nozzle. This is reflected in the fact that no consistent stream or nozzle wetting was observed even at the highest applied pressure (0.5 MPa), as can be seen in Figure 80. Instead, the residue left on the nozzle seems to be more dependent on the speed of the jet than on the applied pressure, leaving material behind as a product of insufficient kinetic energy for closing times equal or lower than  $600 \mu\text{s}$ . These profiles, however, were able to eject some drops that were measured as one-drop events, which provided information about the minimum speed required to form a drop. The slower drop was observed for the profile  $1300 \mu\text{s}/0.1 \text{ MPa}$  with an average velocity of  $4.25 \pm 0.16 \text{ m/s}$ , which is almost double than the minimum speed observed for the other materials.

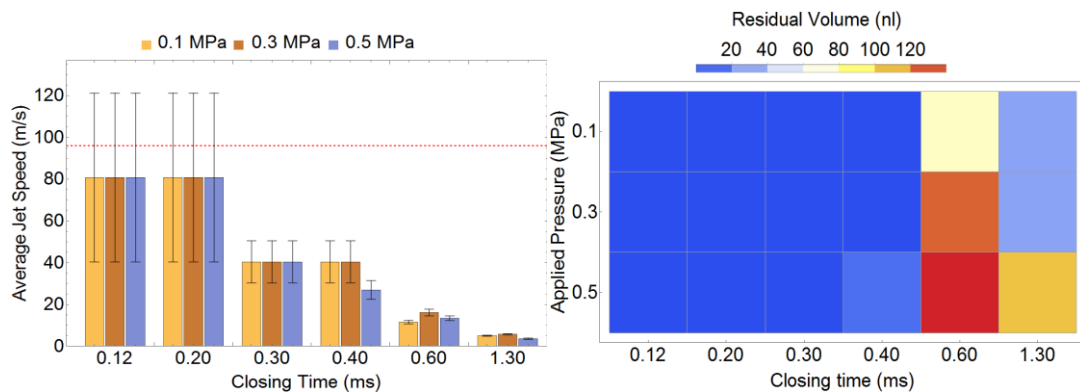


**Figure 80:** The average speed of the leading part of carbon paint jets is shown on the **left**, where the red dashed line corresponds to the maximum speed limit of 96 m/s imposed by the shutter of the camera ( $1 \mu\text{s}$ ). The events represent the ejection of 30 drops except in the 2 slowest profiles, which resulted in a few drops before the accumulated material hindered further ejection (one-drop events). On the **right**, the volume of residue left in the nozzle plate after 30 ejections is shown.

Apart from the high threshold pressure to initiate ejection, this material is different from the others because of the size of the particles suspended on it, which are in the micro-scale rather than nano. This means that in the situations where the fluid arranges itself in a stream or neck, the minimum size that it can adopt is no longer controlled by the capillary and viscoelastic forces alone but it is determined by the physical size of the solids. Furthermore, since the particles are not monodisperse (as it was shown in Figure 63), their distribution along these fluid strings is not homogeneous, which eventually leads to the creation of multiple breaking points (van Deen et al. 2013). This effect, combined with the high exit speeds of certain closing profiles, resulted in atomization, which reduced the repeatability of the ejection at these high speeds, as can be seen in Figure 81.

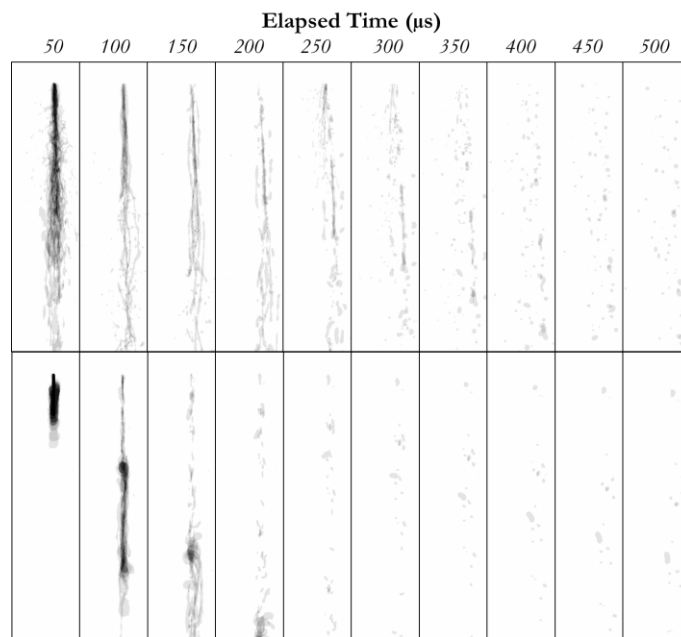


**Figure 81:** Frames of the ejection of carbon paint at an applied pressure of 0.1 MPa and a closing time of 120  $\mu\text{s}$  (**top**) and 120  $\mu\text{s}$  (**bottom**). Fluid atomization is present in both cases but it is more pronounced at a faster closing speed. Each image is the result of a combination of 10 binarized frames. The width of the images is 1.024 mm.

### **Matrix experiment summary and conclusions**

From the previous experiments, it is possible to extract general conclusions for the ejection process in HVJ. These observations are summarised in the processing map shown in Figure 82, where 8 regions of operation are identified along with the threshold parameters that defines them. It is worth mentioning that although in this work the discussion of pneumatic pressure and closing speed are separated to better represent the 2 actuation mechanisms in the system, ultimately they are both referring to a pressure difference applied to the fluid.

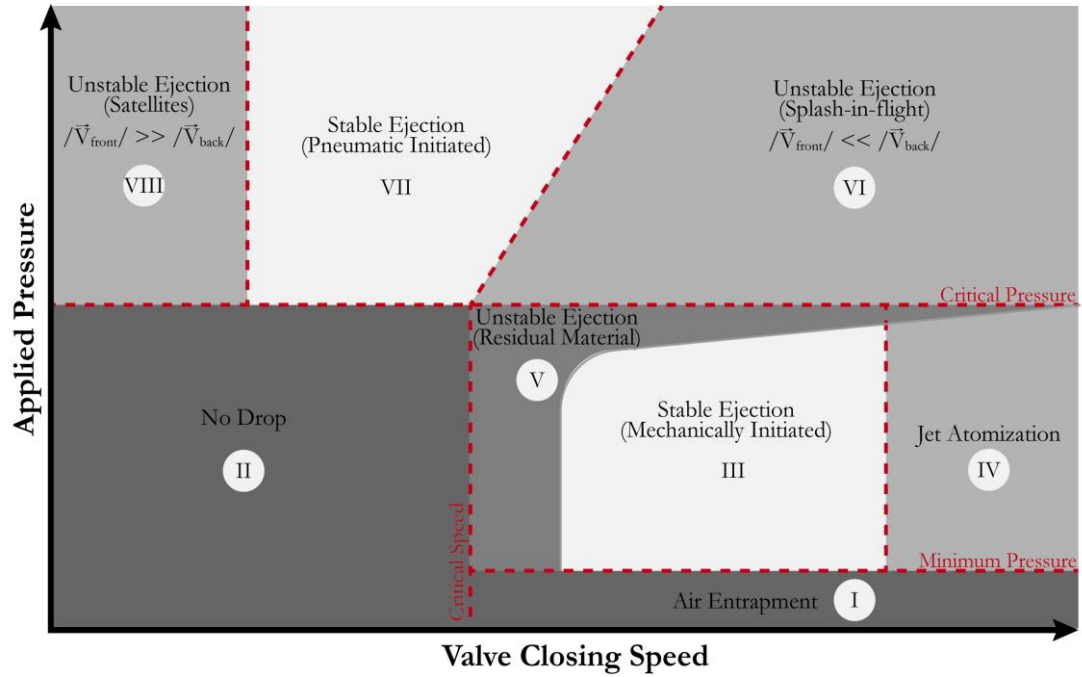


**Figure 82:** Descriptive process map for the ejection of highly viscous materials with the micro-dispensing valves used in this work. The definition of the different regions corresponds to the observed behaviour of 4 materials (a carbon paint, a nanoparticle-based silver paste, a UV-curable resin and an aqueous dispersion of PEDOT:PSS) tested at different pressures (0.1 – 0.5 MPa) and valve closing times (120 – 1300  $\mu$ ) while recording high-speed videos at 20,000 fps.

The first threshold value to consider is the **critical pressure** required to create a constant stream of fluid through the nozzle, which effectively splits the map into pneumatically and mechanically initiated ejections depending on the applied pressure being above or below such value respectively. Additionally, there is another pressure threshold to consider to compensate for the negative pressure created on the nozzle chamber when the plunger is raised to its top position and avoid backflow towards the fluid reservoir. Below this **minimum pressure** air entrapment and material stagnation can occur (region I) according with the literature (Wang et al. 2013). For this reason, the minimum pressure during the present work was 0.1 MPa, which never resulted in interrupted ejection or perceptible decreasing trends on the deposited volumes and is therefore considered successful in preventing material stagnation.

In the mechanically initiated mode, the closing speed of the valve is the main processing parameter, since the plunger is in charge of imparting kinetic energy to the fluid, so it can overcome the energy barrier imposed by surface tension and elastic effects. Thus, if the closing speed is below a certain threshold, the perturbation propagated through the fluid does not have enough speed to break its own meniscus and form a drop, which leads to nozzle wetting and subsequent jetting failing (region II). Alternatively, if the closing speed of the valve is sufficient to break-up cleanly from the nozzle, a stable region of mechanically initiated ejection is found (region III). These drops are the smallest that the

system can dispense for a material at a certain closing speed, since the ejection is only happening during the closing time of the valve. However, if the closing time of the valve is too short, the exit speed of the jets is fast and it leads to atomization (region IV), which affects the quality of deposition negatively.

The previous considerations provide a good understanding of individual drops on the mechanically actuated region, but they neglect the fact the initial conditions of each event are given by the end of the previous jet, which introduces temporal dependences into the jetting process. Specifically, one can apply the energetic arguments previously introduced to the case of a jet being dispensed from a clean nozzle, but the situation is changed by any **residual material** left behind by the previous event. This not only rises the required energy to separate a drop from the nozzle but it also affects its direction and the amount of material left behind after said jet, which complicates even further the following ejection. These situations where the residual material affects the creation of subsequent drops (region V) are found in two different scenarios but ultimately both result in the same behaviour. The first source of nozzle wetting is a pneumatic pressure near the critical pressure, which allows flow through the nozzle but not fast enough to become a stable stream. In this case the perturbation does not come necessarily from the previous event but it affects the initial conditions of the drop anyway. It has been observed that this effect is less problematic at high valve closing speeds, which provide enough kinetic energy to the drops to not only break free from the nozzle but take the initially dispensed fluid wetting the nozzle. The second source of residual material comes from slow closing speeds right above the critical speed necessary to eject a drop. In this scenario, the jet separates from the nozzle but due to its slow speed part of the tail travels back to the nozzle. Part of the fluid is re-absorbed by the nozzle, ready to be jetted in the following event, but in some situations residual material is left behind, which starts forming a wetting film and would affect the next jet.

Pneumatically initiated ejections encounter difficulties, mainly due to the actuation mechanism behind the movement of the front of the jet and the end. Thus, if the speed of the tail of the generated drops is faster than the leading part, the fluid structure collapses in flight and it atomises uncontrollably (region VI), leading to irregular depositions. This situation is reduced as the speeds of both parts of the jet are closer, forming a dumbbell structure that would eventually break-up or coalesce in flight depending on the surface tension, viscoelastic properties of the fluid and time of flight (Bazilevskii & Rozhkov 2015). Therefore, tuning the closing speed in relation to the pneumatically driven speed of the

front can lead to another region of stable ejection (region VII). This configuration is typically slower and more repeatable but it deposits larger volumes than its mechanically initiated counterpart, since there is flow during the pulse time and not only during the closing stage. Finally, if the speed of the tail is considerably slower than the front (region VIII), long tails are observed, which are more likely to break-up into multiple satellite droplets. Furthermore, since this ejection regime requires longer to fire each drop, the deposited volumes are bigger and the overall process speed is slowed down, which in most cases are not advantageous outcomes.

From the process map shown in Figure 82 it is extracted that the smallest and faster stable drops achievable for a high viscosity material with the micro-dispensing valves used in this work are obtained using mechanically initiated configurations. To evaluate the effect of the closing speed on the velocity of these jets, only the observed speeds at 0.1 MPa are shown in Figure 83, including the one-drop events that were only capable of ejecting a few drops before collapsing due to the accumulated residual material on the nozzle plate. In this case the error bars are omitted for clarity, but the uncertainty on the measurements is the same than previously shown for each material individually. Moreover, it is remarkable how despite the crucial differences on the properties of the fluids, they all display a similar dynamic behaviour, which is driven by the mechanical movement of the valve. This is probably due to the valve mechanism being based on the positive displacement of the plunger rather than propagating a pressure wave like is the case for PIJ printheads. However, greater temporal resolution is required in the measurement of the speed to achieve stronger conclusions about the dynamics of these jets and the influence of individual properties such as viscoelasticity, apparent yield stress or surface tension. Furthermore, since a transition from stable to unstable ejection is observed between 400  $\mu\text{s}$  and 600  $\mu\text{s}$ , it would be interesting to explore further that particular region to refine the observations made in this work. This, however, was not possible for the current set-up, which has a discrete amount of closing configurations available. Therefore, in order to modify the printing pulse it would be necessary to override the digital controller of the valves in order to generate custom signals, which is left for future work. Nevertheless, the results obtained agree with the literature, since different authors have reported drop speeds in this range. For instance, Chen *et al.* (Chen et al. 2014) obtained jets of high viscosity silicone with speeds between 20 and 80 m/s using a similar dispensing valve than the one used in this work with an average closing speed of 1.13 m/s. Alternatively, Yang *et al.* (H. Yang et al. 2013) encountered jetting speeds from 6 m/s to above 45 m/s for various

viscous materials dispensed with an older version of the valve used in this work with closing speeds between 0.11 m/s and 1.4 m/s.

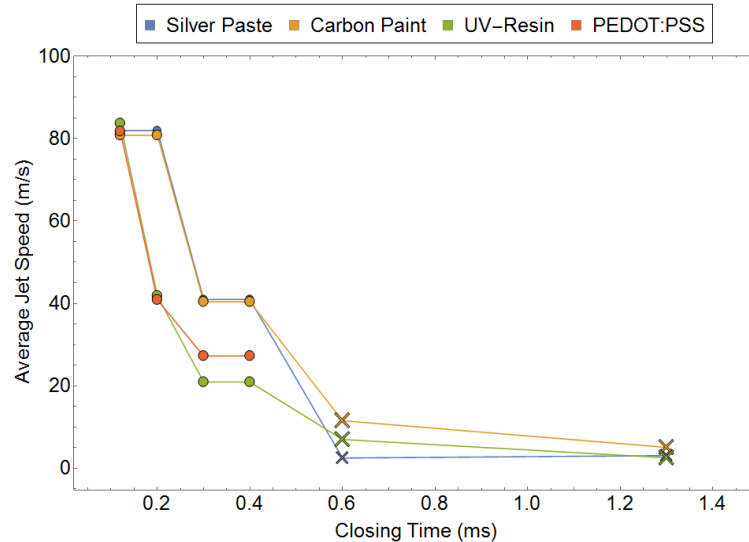


**Figure 83:** Summary of the average jet speed of several viscous fluids with an applied pressure of 0.1 MPa. The cross symbols represent the events that resulted in unstable ejection, in which case only the speed of the first drop is shown (one-drop events). The error bars are omitted in this case for clarity.

After examination of the previous results, the ideal settings are selected as those that lead to repeatable ejection without material residue, provide the slowest droplets to avoid atomization and the smallest deposited volumes to increase the printed resolution. These requirements lead to mechanically initiated configurations with closing times of 300  $\mu\text{s}$  or 400  $\mu\text{s}$  and an applied pressure of 0.1 MPa for all materials. Nevertheless, since PEDOT:PSS is stable in both pneumatic and mechanical modes, a “slow” mode is also defined as the one being initiated by 0.5 MPa and finished at a closing time of 600  $\mu\text{s}$ . However, to fulfil the minimum volume requirement, the pulse time is reduced from 2 ms in the videos previously presented to 0.20 ms, which was the minimum pulse that still resulted in ejection. A still frame of an exemplary drop of each of the selected configurations is shown in Figure 84. Finally, to show the capabilities of the system with low viscosity fluids, drops of isopropanol (IPA) were generated using a purely mechanically initiated configuration consisting on a closing time of 1300  $\mu\text{s}$ , a pulse of 0.15 ms and no external pressure applied to the reservoir, the results are also shown in Figure 84. The difference in viscosity compared with the other fluids, together with its Newtonian and inelastic behaviour, results in a completely different behaviour of the jetted drop, where substantial oscillation of the drop is observed and no fluid tail is encountered. The average speed and observed volume are  $1.77 \pm 0.03$  m/s and  $6.60 \pm 0.03$  nl, respectively.

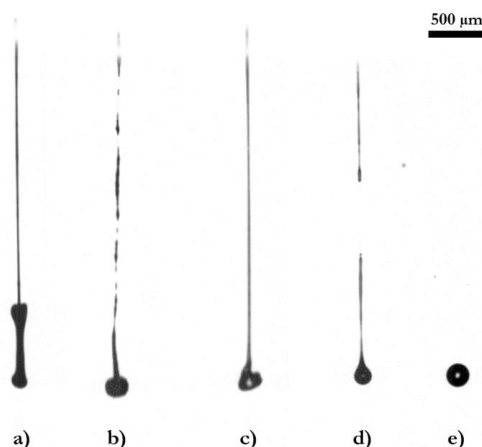


**Figure 84:** Example drops corresponding of suitable jetting configurations for several high viscosity fluids and isopropanol. **A)** Silver paste (closing time 300  $\mu$ s, pulse time 0.20 ms, pressure 0.1 MPa). **B)** Carbon paint (closing time 300  $\mu$ s, pulse time 0.20 ms, pressure 0.1 MPa). **C)** Photo-curable resin (closing time 300  $\mu$ s, pulse time 0.20 ms, pressure 0.1 MPa). **D)** PEDOT:PSS, slow configuration (closing time 600  $\mu$ s, pulse time 0.20 ms, pressure 0.5 MPa). **E)** Isopropanol (closing time 1300  $\mu$ s, pulse time 0.15 ms, pressure 0 MPa). The cycle time is for all materials 2.5 ms, which corresponds to a jetting frequency of 250 Hz.

### 6.2.2 Representative drops impacting on glass substrate

The suitable configurations found for the viscous materials were tested with a glass substrate and recorded at high frame rate to observe the jet formation, impact of the drops and their evolution overtime (Figure 85). From the images, it is observed that the **silver paste** (Figure 85a) and the **photo-curable resin** (Figure 85c) have a similar jetting behaviour. In both cases the fluid reached the substrate in 2 frames and no break-up of the jet was produced before impact due to their relatively fast speed. Therefore, a fluid bridge was formed between the nozzle plate and the substrate, establishing a competition between surface tension and gravity against the viscoelastic forces, as it was discussed in Chapter 2.4. Here is found the first difference between both materials, since the UV-resin broke-up in  $0.40 \pm 0.03$  ms while the silver nano-dispersion did it in  $0.6 \pm 0.03$  ms. The difference between these times can be explained by the higher surface tension and lower viscosity of the photopolymer and the non-negligible difference between the elastic components of both fluids. This variance in the elastic properties is expected to cause a different necking behaviour, which would be exponentially thinning for the resin, closer to a Newtonian fluid, and a transition to a cylindrical neck of constant radius for the silver (Cambridge Polymer Group 2004). Such details, however, require higher spatial and temporal resolution on the images, which were out of reach for the present set-up. After the break-up, the upper part of the tail was reabsorbed by the nozzle and the lower segment was aggregated to the deposited volume for both fluids. At that point another key difference between the materials was found, since it took much longer for the silver-based material to coalesce into a spherical cap that it did for the resin. The reason in this case,

apart from the higher viscosity and lower surface tension of the silver, is the opposition to deformation than the material displays due to its apparent yield stress (Luu & Forterre 2009). These factors were not only responsible for the slower re-arrangement of the silver but also explain its negligible spreading during the test time, which contrast with the increment of the resin's deposit diameter, as can be appreciated in Figure 86.

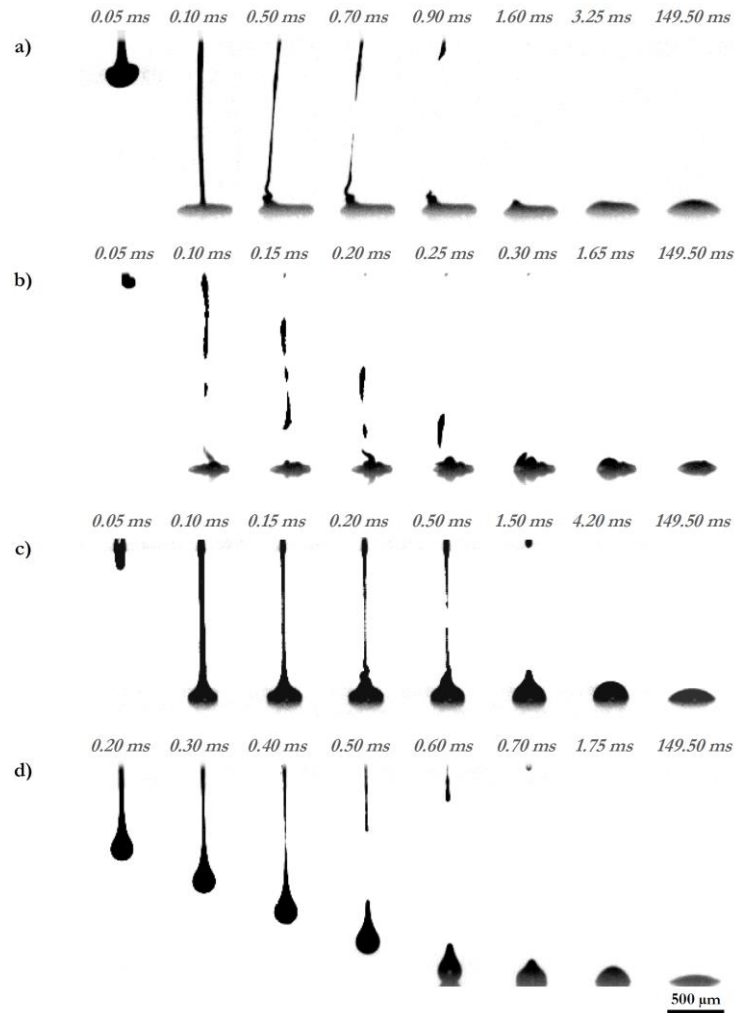


**Figure 85:** Individual drops of high viscosity fluids impacting on a glass substrate, displaying drop formation, impact, jet break-up and preading. **a)** Silver paste (closing time 300  $\mu$ s, pulse time 0.20 ms, pressure 0.1 MPa). **b)** Carbon paint (closing time 300  $\mu$ s, pulse time 0.20 ms, pressure 0.1 MPa). **c)** Photo-curable resin (closing time 300  $\mu$ s, pulse time 0.20 ms, pressure 0.1 MPa). **d)** PEDOT:PSS, slow configuration (closing time 600  $\mu$ s, pulse time 0.20 ms, pressure 0.5 MPa).

The **carbon paint** displayed a very different jetting behaviour. In this configuration, the speed was comparable with the previously discussed materials but the break-up of the jet was not captured in the videos and consequently it is unknown if a fluid bridge was formed or if the jet broke before impact. Independently from the exact moment of the rupture, the break-up time for this material was the shortest of all the tested fluids. This difference may be explained by the particle size of the carbon flakes dispersed on the paint, which were measured in Chapter 5 (Figure 63) and revealed a tri-modal distribution

with peaks at 0.13, 0.68 and 14.5  $\mu\text{m}$ . Thus, when the material stretches the particles arrange along the fluid string, limiting the minimum size that the neck can adopt and creating discrete areas of lower concentration (van Deen et al. 2013), which accelerates the break-up. This effect may also be responsible of the multiple fluid bodies created during the ejection, since many rupture points can occur. In the video, the main volume of fluid reaches the substrate quickly but it is later joined by several slower portions of material that resulted from the inhomogeneous break-up of the tail. Nevertheless, after the deposition was finished, the material coalesced driven by surface tension into a shape resembling a spherical cap. As it happened with the silver paste, the diameter of the drop did not change visibly overtime due mainly to its high viscosity (Figure 86).

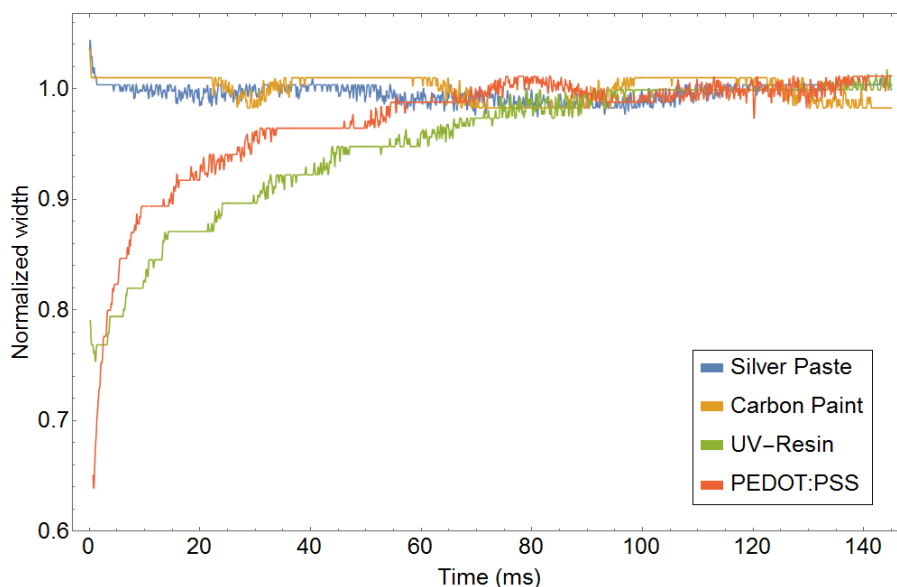


**Figure 86:** Evolution of the diameter of deposited drops of viscous fluids on glass substrates over time. The width has been normalized to the final diameter for each material to provide a comparative result.

The **PEDOT:PSS** dispersion was the only test material jetted under a pneumatically driven configuration, which resulted in a slightly larger volume and a slower speed. The slower pace allowed for the break-up of the tail in flight after  $0.5 \pm 0.03$  ms from the beginning of the ejection, which resulted in a free droplet impacting on the substrate. Then, the coalescence and spreading of the drop took place, which were faster and more pronounced than for any other tested material (Figure 86). This seemed to differ from the expected behaviour considering the high viscosity of the fluid at low shear rates and the measured elastic components, closer to the silver paste than to any other tested material. However, this material is also the most shear thinning and it is expected that even at relatively low speeds the shear rate exerted on the fluid travelling through the nozzle is high enough to break the micro-structure of the fluid considerably, causing its effective viscosity to be low until the rebuilding of the internal structure takes place.

To conclude this section, it is interesting to look back at Figure 86 to appreciate the spreading behaviour of the 4 materials as a whole. The silver paste and the carbon showed a similar trend, which was a constant diameter at all times. This means that all the spreading happened on impact, at a time-scale smaller than the available temporal resolution. This was further confirmed when the Weber and Reynolds number were computed for these configurations (Figure 101) and compared with the results from the literature summarised in Chapter 2.4. Consequently, since the final diameter of the deposited drop is mainly controlled by this parameter, it becomes another reason to try to obtain slower drops in future experiments. Alternatively, the UV-resin and the PEDOT:PSS displayed slower spreading, which was still proportional to the impact speed (Derby 2010) (Schiaffino & Sonin 1997) but less dampened due to the lower viscosity of these fluids at high shear rates. Furthermore, since the internal structure of the materials is not unperturbed at the moment of spreading, concepts like the apparent yield stress do not explain the observed behaviour, since the materials do not have time to re-build its internal networks in the time-scale of the impact driven spreading.

### 6.3 Drop footprint investigation with optical microscopy

In this section, the performance of each material under different printing conditions is evaluated by looking to the deposited drops on a glass substrate. Three aspects of the ejection are monitored with this experiment, namely the shape of the drops, their size and repeatability. The first two are given by the circularity and the equivalent radius while the repeatability can be evaluated by looking at the dispersion of both quantities. It is noteworthy that the shown images are a representative sample of drops of each printing configuration, but the number of analysed events was bigger than 40 in each case.

The results for the **carbon paint** are shown in Figure 87 and Figure 88 and display little size variation across the different jetting profiles, yielding drops of 200 - 240  $\mu\text{m}$  of radius, with no clear relation between this dimension and the printing settings. The situation is different for the circularity, which is higher and more consistent in all cases for the lowest applied pressure (0.1 MPa), indicating a more stable behaviour. This agrees with the high-speed videos previously shown, which exhibited clean ejections at low pressure, since no material flows before the closing stage of the valve or is left behind after each event. However, as the pressure is increased, a small film of fluid is formed on the outside of the nozzle plate, which causes the observed irregularities. This effect was more evident for slower closing profiles, which result in elongated drops. There was an overall decrease

in circularity at all pressures for the fastest closing time (120  $\mu\text{s}$ ), which is likely to be a result of the atomization observed at such high exit speeds. Therefore, some of these small satellites created during the violent closing of the valve landed on the substrate, often on top of previously deposited bodies of fluid, and altered their perimeter causing a reduction in circularity. These satellite drops were slowly re-absorbed into the main volume, but since they were small, their solvent evaporated quicker, leaving an irregular shape. This is compatible with the observed spreading behaviour for this material (Figure 86), which did not visibly change its diameter after the inertial time-scale of the impact. From these observations, it is concluded that an ideal configuration for the carbon paint should be one with an applied pressure of 0.1 MPa and a relatively high closing speed to avoid the previously mentioned problems with nozzle-flooding and inconsistent ejection. However, if the closing speed is high, the material leaves the nozzle too fast and it causes atomization and potential splashing on the substrate. These requirements are fulfilled by the profile 0.1 MPa/ 300  $\mu\text{s}$  previously selected following the analysis of the high-speed videos.

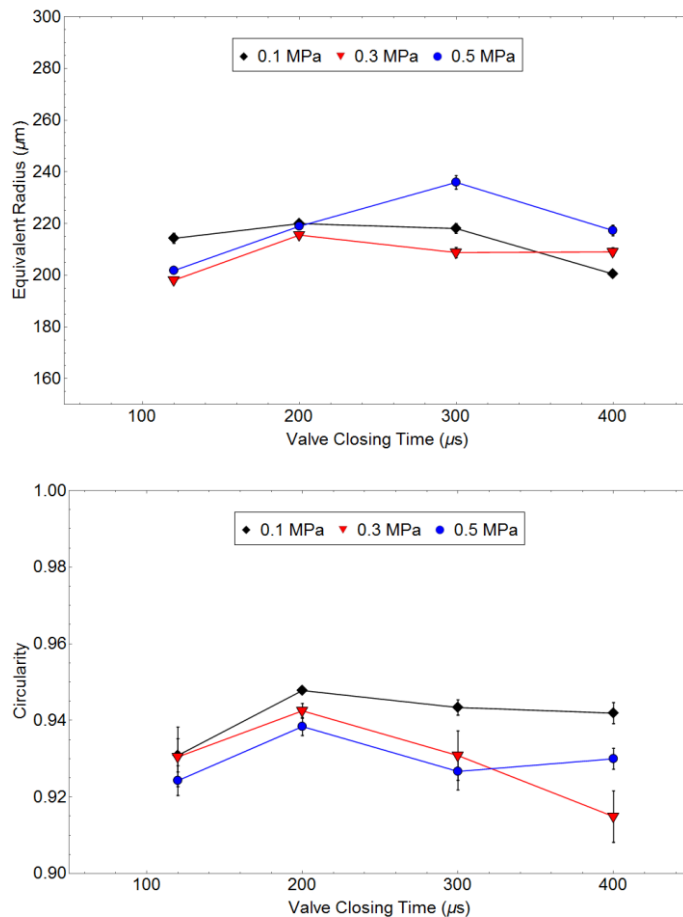


**Figure 87:** Equivalent Radius (**top**) and circularity (**bottom**) of carbon paint's droplets ejected at different valve closing times and applied pressures. Both values are calculated from the area and perimeter of the drops, automatically detected. Closing times longer than 400  $\mu\text{s}$  did not produce stable ejection.

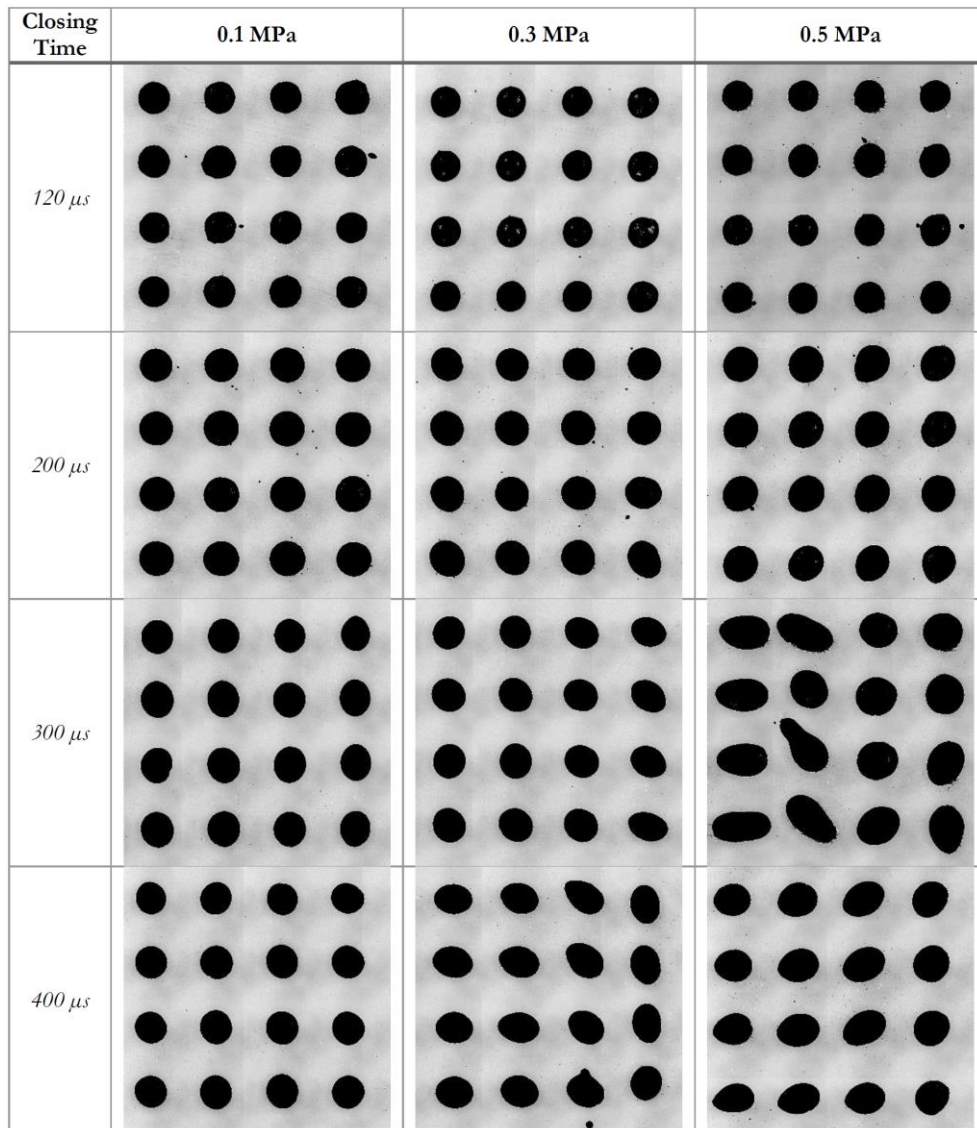


**Figure 88:** Representative drop samples of carbon paint produced at different valve closing times and applied pressures. Closing times longer than 400  $\mu s$  did not produce stable ejection. The pulse and cycle times are constant and have values of 0.5 ms and 4 ms, respectively. Each square image is 3.34 mm long.

The footprints of the **photocurable resin** displayed a markedly different behaviour, as can be seen in Figure 89 and Figure 90. The most notable feature is the high circularity and smoothness of the drops in all cases. This is due to the absence of atomization and a higher spreading tendency than other materials, as was observed in previous experiments (Figure 86). There is a decreasing trend in the equivalent radius as the closing speed decreases, which is a result of the lower impact speeds in these configurations. Moreover, for fast profiles (120 and 200  $\mu s$  closing) the equivalent radius is also correlated with the pressure, obtaining bigger drops at 0.5 MPa, which further suggest a direct relation between the impact speed and the final diameter of the drop in this range of closing times. This trend is lost at closings higher than 300  $\mu s$ , probably due to the interference caused by the residual present in the nozzle at slower closing speeds.

Moreover, nozzle flooding also caused the accuracy to be reduced, as it is clear in Figure 90, which shows positional and shape irregularities in those configurations that previously proved to leave more residual material behind (Figure 79), as is the case of the profiles with a pneumatic pressure of 0.5 MPa. Alternatively, the impact speed also presented a correlation with the presence of air bubbles on the drops, as these were present only for the shortest closing time (120  $\mu\text{s}$ ) at all pressures and the second fastest (200  $\mu\text{s}$ ) at all but 0.1 MPa. Since the total pressure applied on the fluid inside the nozzle chamber is a combination of both forms of actuation, it is reasonable to expect these profiles to be the ones leading to faster jet exit speeds. The nature of these entrapped bubbles into fluid drops impacting a solid plane has been found to be a consequence of the deformation of the bottom part of the jet prior impact, as a result from an increased pressure due to the incoming drop (Mehdi-Nejad et al. 2003) (van Dam & Le Clerc 2004). Moreover, due to the high viscosity of the resin, once the bubble is created it is less likely to escape through the surface of the drop.

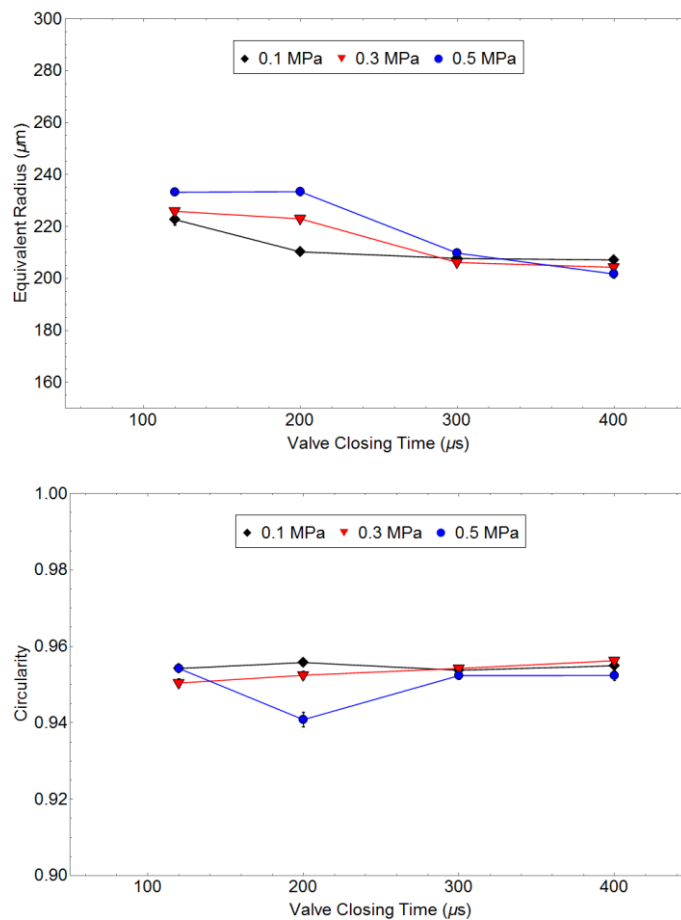


**Figure 89:** Equivalent Radius (**top**) and circularity (**bottom**) of UV-curable resin's droplets ejected at different valve closing times and applied pressures. Both values are calculated from the area and perimeter of the drops, automatically detected. Closing times longer than 400  $\mu\text{s}$  did not produce stable ejection.

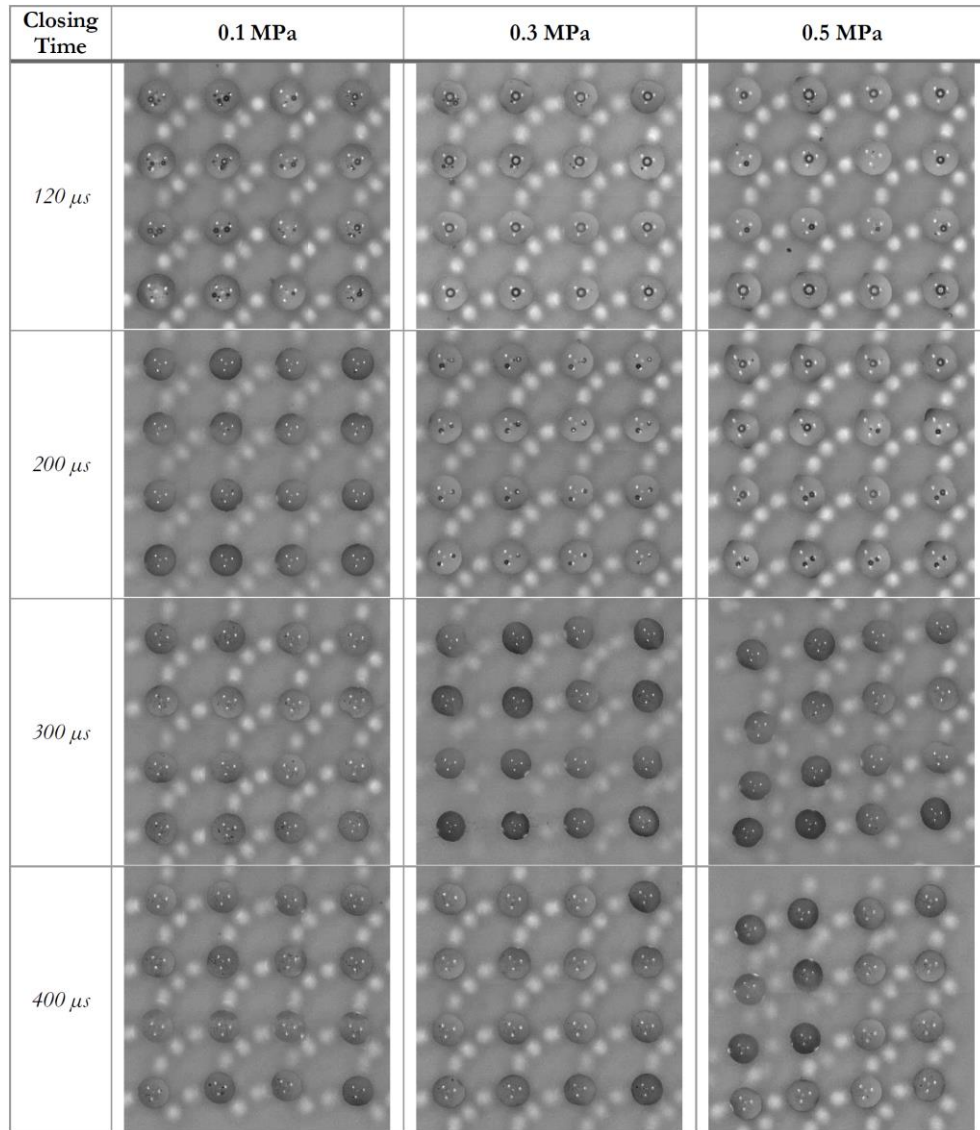


**Figure 90:** Representative drop samples of photo-curable resin produced at different valve closing times and applied pressures. Closing times longer than 400  $\mu s$  did not produce stable ejection. The pulse and cycle times are constant and have values of 0.5 ms and 4 ms, respectively. Each square image is 3.34 mm long.

The **silver paste** results shown in Figure 92 and Figure 91 contrast with the previously discussed materials, since the window of acceptable ejection is narrower. For fast profiles (closing time equal or lower than 200  $\mu s$ ), evident splash on the substrate was observed for all pneumatic pressures, which is a direct effect of the high impact speed of the jets in these configurations. The area of these depositions was higher than for slower drops but also more irregular, which led to circularity values below 0.7. This material also exhibited shape variation previously associated with the presence of residual fluid on the nozzle plate before the closing moment of the valve. Specifically, all the configurations with a 0.5 MPa applied pressure with all the tested closing profiles and the 0.3 MPa at 400  $\mu s$ , showed elongated depositions that in occasions joined with neighbour drops. Eventually, the nozzle flooding was so severe that it impeded the detachment of any drop

at slower closing speeds, which resulted in a growing volume of fluid on the nozzle plate and no stable ejection. Additionally, not even the drops deposited in stable configurations had circularities higher than 0.9. This behaviour can be partially explained by the break-up of the fluid bridge between the nozzle plate and the substrate, which is the slowest of all the materials tested, as was shown in Figure 85. These fluid filaments are under tension until they suddenly break and collapse in both directions, which in some occasions result in visible strings pointing towards the drop's centre. Moreover, since the spreading behaviour in this material is dominated by the viscoelastic forces, there was little re-configuring of the deposited material, resulting in drops with lower circularity than capillary driven materials. With these considerations in mind the profile with a closing time of 300  $\mu\text{s}$  and an applied pressure of 0.1 MPa or 0.3 MPa are selected as the most suitable for this material, since they result in repeatable events, the highest circularity and a relatively small equivalent radius. This choice is compatible with the observations from the high-speed experiments.

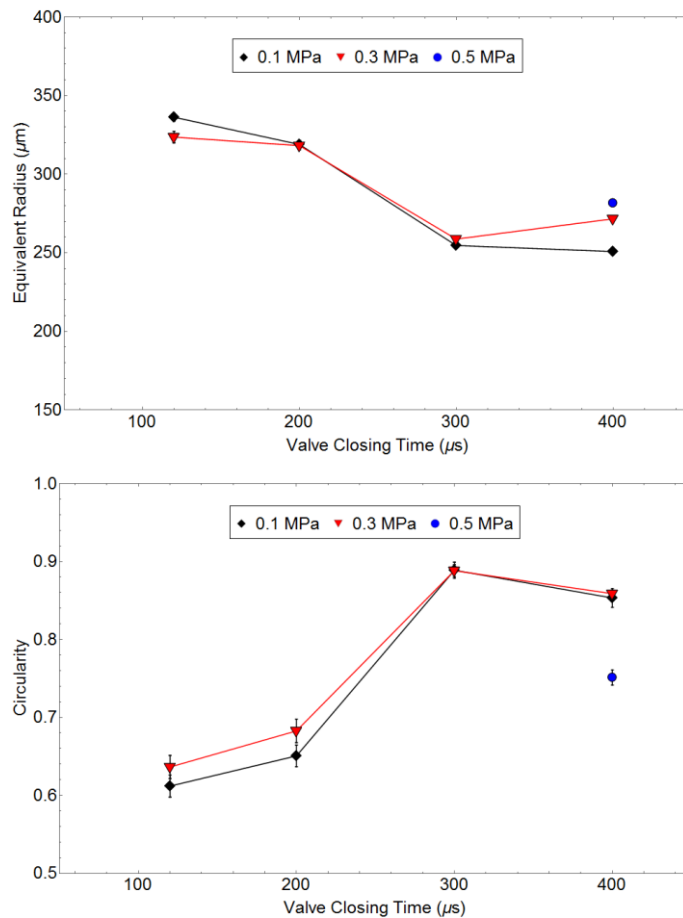


**Figure 91:** Equivalent Radius (**top**) and circularity (**bottom**) of silver paste droplets ejected at different valve closing times and applied pressures. Both values are calculated from the area and perimeter of the drops, automatically detected. Most events at 0.5 MPa resulted in joined features that could not be individually analysed. Closing times longer than 400  $\mu\text{s}$  did not produce stable ejection.

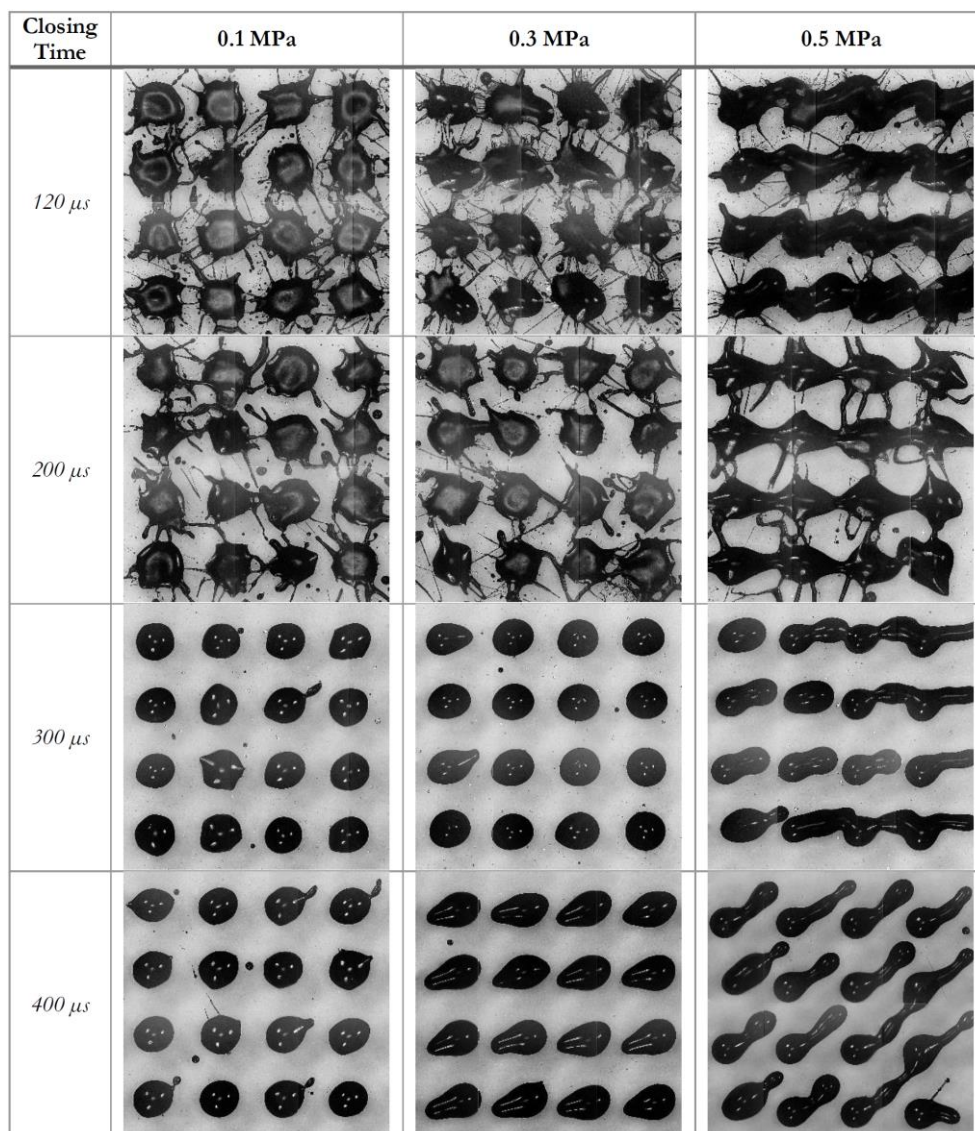


**Figure 92:** Representative drop samples of high viscosity silver paste produced at different valve closing times and applied pressures. Closing times longer than 400  $\mu$ s did not produce stable ejection. The pulse and cycle times are constant and have values of 0.5 ms and 4 ms, respectively. Each square image is 3.34 mm long.

The aqueous dispersion of **PEDOT:PSS** used in this work allows the observation of pneumatically initiated ejections, as it is shown in Figure 94 and Figure 93. The first consequence of this is that stable configurations were found for all the tested closing times, up to 1300  $\mu$ s, when the highest pressure was applied (0.5 MPa). This, as it was demonstrated in the high-speed video experiment, is due to the applied pressure being enough to initiate a stable fluid stream on its own, leaving the closing stage of the valve to finish the ejection. This, however, imposes a restriction on the closing speed, since a faster tail than the drop's head would result in a situation previously referred as splash-in-flight, as it was shown in Figure 75. Nevertheless, if the substrate is close to the nozzle plate this fluid-on-fluid collision would happen on the substrate instead of during flight. This explains the characteristic shape of the closing times 120  $\mu$ s and 200  $\mu$ s at 0.5 MPa.

Similarly, since 0.3 MPa also showed capability of initiating the jets, although more inconsistently, the fluid-on-fluid scenarios affected also the profiles with closing times equal or lower than 300  $\mu\text{s}$ . The results for these configurations yielded apparently inconsistent results in terms of their shape and size compared with the closing speed (Figure 93). However, it is noteworthy that these patterns were not the sole product of the splash of a fast jet against a flat substrate but a fluid-on-fluid collision and factors such the distance between the nozzle plate and the substrate, the speed of both parts of the jet and the volume deposited before the impact, should be considered. Understanding this behaviour further would require new videos showing the impact of these jets and modelling their behaviour, which is outside of the scope of this work. Nevertheless, these fluid-on-fluid collisions were not observed when the closing time was sufficiently slow and stable ejection was achieved.

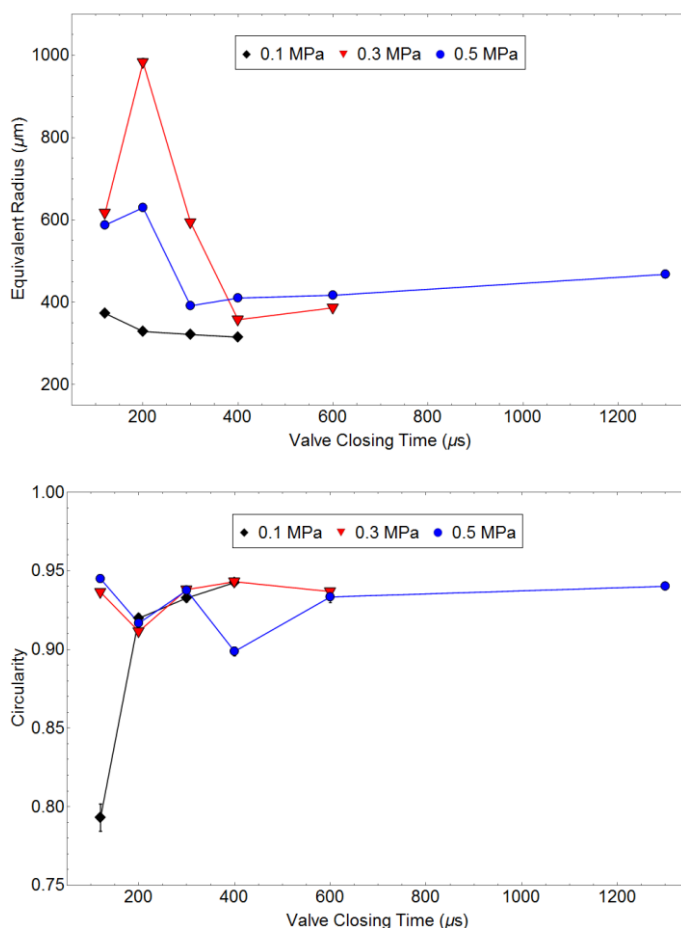


**Figure 93:** Equivalent Radius (**top**) and circularity (**bottom**) of an aqueous dispersion of PEDOT:PSS's droplets ejected at different valve closing times and applied pressures. Both values are calculated from the area and perimeter of the drops, automatically detected. Most events at 0.5 MPa resulted in joined features that could not be individually analysed.

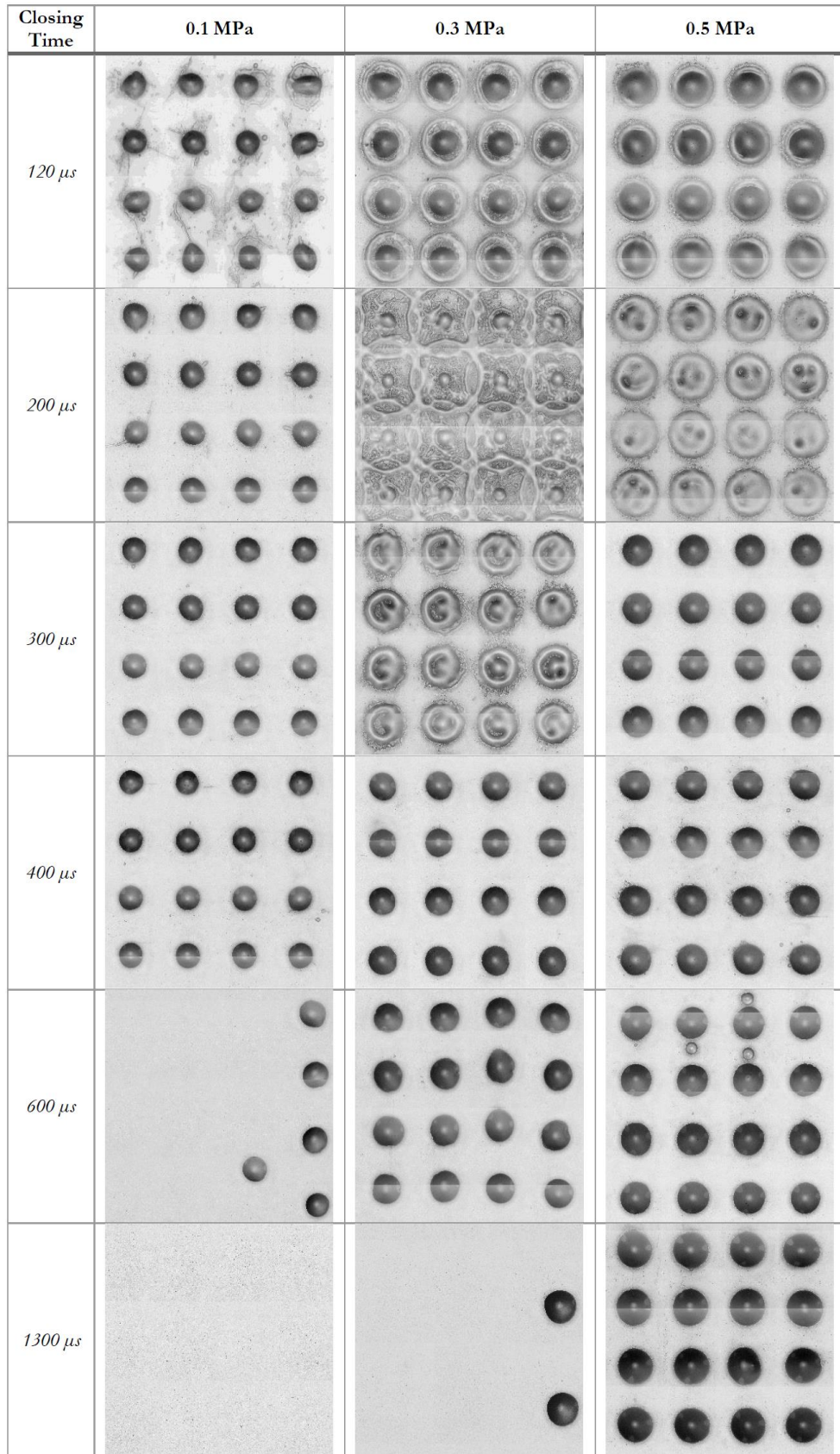


**Figure 94:** Representative drop samples of an aqueous dispersion of PEDOT:PSS produced at different valve closing times and applied pressures. The pulse and cycle times are constant and have values of 0.5 ms and 4 ms, respectively. Each square image is 5.90 mm long.

Mechanically initiated profiles (0.1 MPa) were stable for closing times up to 400  $\mu\text{s}$  and displayed a stable behaviour. This is consistent with the results of previous sections, where nozzle flooding or fluid-on-fluid collisions were not observed. Furthermore, these profiles showed a clear trend of increased circularity and smaller size as the closing time was increased, which agrees with the impact driven nature of these ejections. However, the difference in the output is decreased with the closing speed, leading to very similar results for 300  $\mu\text{s}$  and 400  $\mu\text{s}$ , which would be both accepted as suitable profiles for this material. Moreover, a closer look at the images in Figure 94 reveals signs of splash for the fastest closing configuration, which provides valuable information about the suitable jet's speed range, as it will be discussed in the following section.

Finally, it is notable that despite the different splashing scenarios encountered for this material, the circularity of the events was generally high (between 0.90 and 0.95). This was similar to the results for the photo-curable resin (Figure 89) and consistent with the observed spreading behaviour of both fluids (Figure 85), which displayed a quick response after impact and a strong capacity to re-shape the deposited volume into a spherical cap.

### **6.3.1 Footprints experiment summary and conclusions**

From the present experiment, it was observed that the application of pressure above 0.1 MPa introduced irregularities to the results in the form of elongated or irregular drops for most materials. The reason is a transition from a mechanical ejection event to a pneumatically initiated event, where the material jetted first interfere with the deposition of the main body of fluid.

This is typically in the form of a flooded nozzle plate, which alters the speed and direction of the ejected drop, but for some materials, such as the dispersion of PEDOT:PSS, the applied pressure is enough to create a stable stream of fluid that travels towards the substrate before the mechanically driven tail, which creates a fluid-on-fluid collision. Furthermore, even stable pneumatically driven configurations have the disadvantage of leaving the nozzle open for longer, which results in bigger volumes. Consequently, it is reasonable to operate in a region of low pressure where the main actuating force comes from the valve's closing plunger. These configurations are summarised in Figure 95 and show a common trend towards smaller and more circular depositions as the closing time is reduced. This behaviour is typical from impact driven events, as it was shown in Chapter 2.4 (Figure 34 and Figure 35), where the initial spreading is governed by the impact speed, opposed mainly by viscoelastic forces, followed by a

secondary spread ruled by the competition of surface tension with the same viscoelastic dissipative forces. It is noteworthy that the results obtained for this experiment are obtained with a flat glass substrate and it is expected that the spreading behaviour changes with other substrates. However, the behaviour of the valve is independent of the substrate and therefore the conclusions about the performance of these printing configurations are general. Moreover, these observations are compatible with the high-speed experiments previously performed, which not only reinforces the findings but also opens the possibility of only performing the footprint experiment in future optimisation processes for different materials. This is beneficial because the footprint experiments are faster and can be carried out within the printing system without additional instruments, which allows for higher levels of automation.

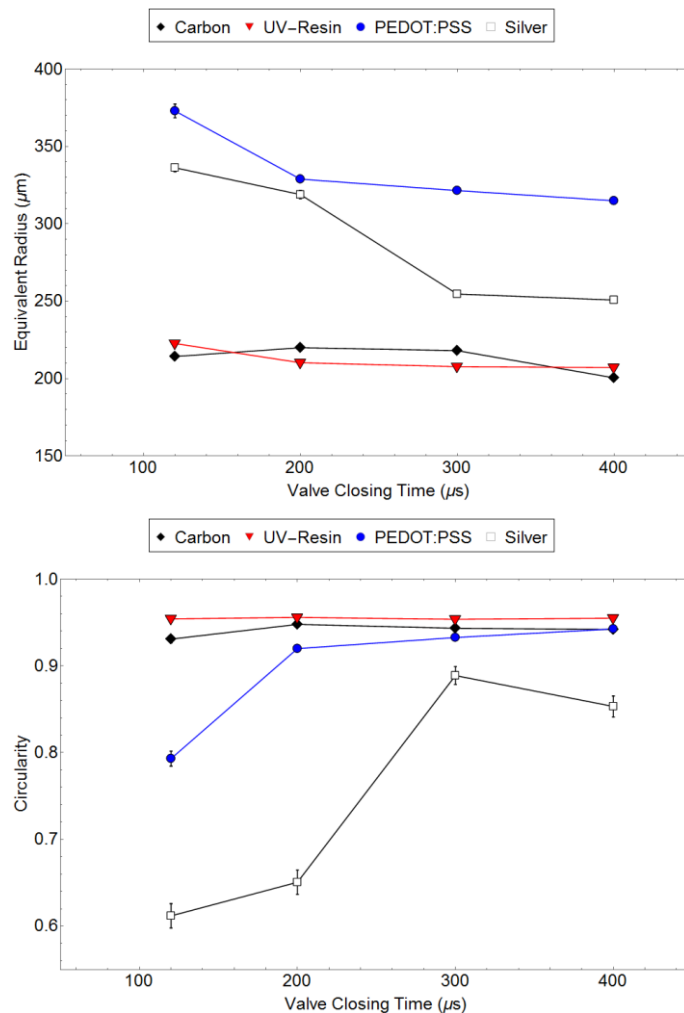


**Figure 95:** Equivalent Radius (**top**) and circularity (**bottom**) of droplets of several high viscosity fluids ejected at different valve closing times and an applied pressure of 0.1 MPa.

## 6.4 Drop mass and volume

From the previous experiments, a working set of parameters was identified for each material. Typically, they involve a relatively fast closing speed of the valve and a low pneumatic pressure that is lower than the ejection threshold previously mentioned. The settings used for each material are the ones previously identified as suitable for these materials (Figure 84). In the case of PEDOT:PSS, however, due to its shear thinning behaviour, it was possible to successfully eject in two different configurations, one pneumatically initiated (slow) and one mechanically initiated (fast). The fast one consisted in a closing time of 300  $\mu\text{s}$ , a pulse of 0.2 ms and an applied pressure of 0.5 MPa. To the viscous materials used during this work it has been added deionised water as an example of a low viscosity fluid of known properties (1.002 mPa·s and 72.75 mN/m at 20 °C (David R. Lide 2005)). Isopropanol was originally considered for consistency with previous experiments but its high evaporation rate is a potential problem to the method here used, where the mass of each drop is calculated from the weight of a larger number of events. The settings used for the water involved a closing time of 300  $\mu\text{s}$ , a pulse of 0.2 ms and an applied pressure at 0.1, 0.3 and 0.5 MPa. These settings were not chosen following the criteria for optimum ejection previously given but for comparative reasons with the other materials.

The results from the **weight of multiple drops** for the different materials are shown in Figure 96 and Figure 97, where the average mass of a drop was obtained from the slope of the linear fit. A high linearity was observed for all samples, which suggests that there was no fast evaporation of the solvent, residual material was not being left on the nozzle plate after repeated ejections and there were no signs of material stagnation on the nozzle due to low pressure. However, it is worth noting that the dispersion of the results for  $N = 2500$  for the slow configuration in PEDOT:PSS is distinctively greater than in any other measurement for this fluid. This does not indicate that material is left on the nozzle plate because most of the values are above the existent linear trend instead of below, which is the expected sign of lost mass. Instead, this dispersion may be caused by a fluctuation on the pneumatic system or in the temperature of the material, which would reduce the viscosity of the fluid and increase the flow rate at the same pressure. This variation is not observed for the mechanically actuated configurations, which are repeatable and do not display signs of fluctuations on the system performance.

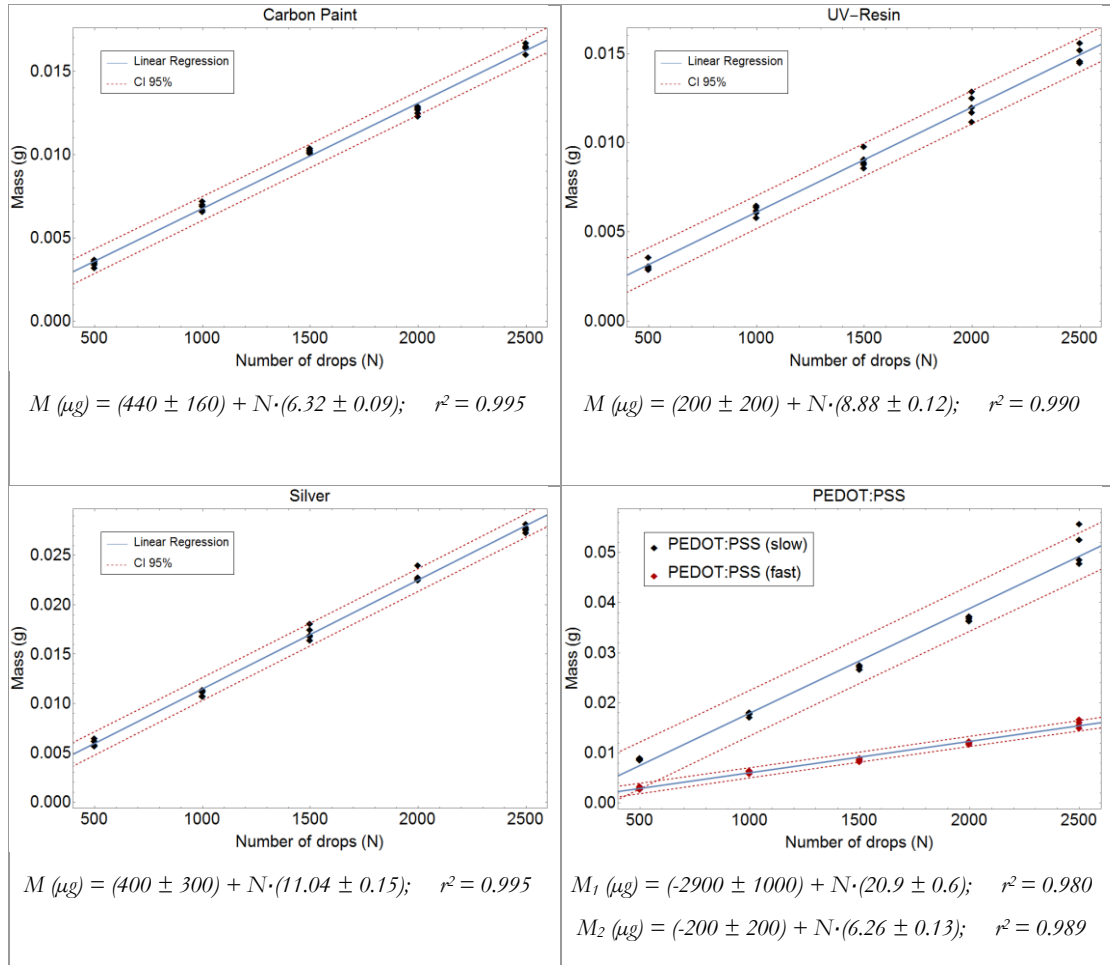


**Figure 96:** Mass of different numbers of drops for a carbon paint, a UV-curable resin, a silver paste and a PEDOT:PSS dispersion. A linear regression (blue line) is used to extract the slope of the linear trend, which is interpreted as the mass per droplet in each case. The results for the linear fit are given in each case. The red dashed lines indicate the 95% Confidence Interval of the fit.

The case of water (Figure 97) is illustrative of the situation where not only one tested pressure is above the critical threshold for stable ejection but all of them. It is clear that as the pressure was increased the flow rate increased with it, leading to greater dispensed volumes. This is a useful tool for volume adjustment, but since it requires to operate in pneumatically dominated configuration, it increases the minimum material potentially dispensed by the system. The dispersion of the data for  $N = 2500$  was also higher than at lower ejection numbers, but it was not as characteristic as it was in the case of PEDOT:PSS. A thermal or pneumatic fluctuation cannot be ruled out in this case either but considering the very low expected threshold pressure for water and the relatively aggressive closing speed used in this experiment, it is likely that a situation of splash-in-flight, as it was previously explained (Figure 82), was happening, which would affect to the repeatability of the measurement more visibly as the number of events increased.

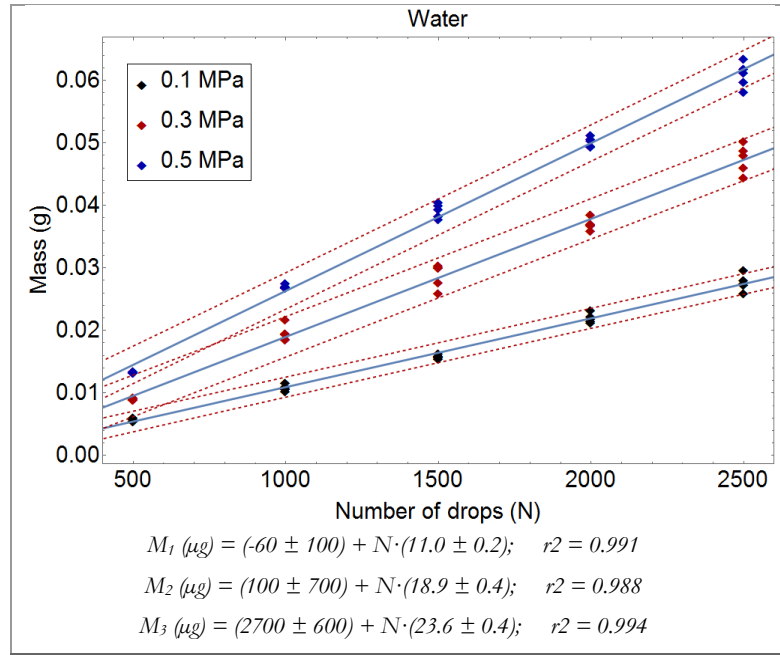


**Figure 97:** Mass of different numbers of drops for deionized water at 3 different applied pressures. A linear regression (blue line) is used to extract the slope of the linear trend, which is interpreted as the mass per droplet in each case. The results for the linear fit are given in each case. The red dashed lines indicate the 95% Confidence Interval of the fit.

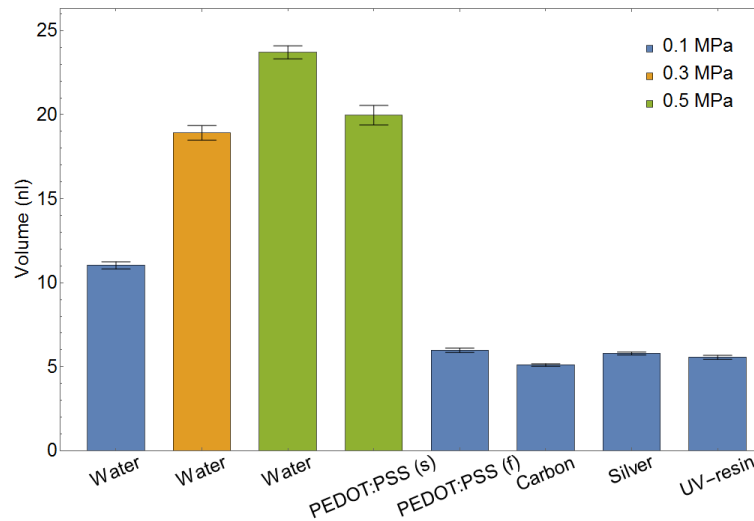


**Figure 98:** Volume per drop generated for different materials. The colour of each bar represents the pressure of that profile to highlight the effect of this magnitude on the deposited volume. All instances of water and the slow profile for PEDOT:PSS correspond with pneumatically initiated ejection, while the other configurations are mechanically initiated.

The results for the average mass of a single drop in each case are divided by the correspondent density measured in the previous chapter (Table 6), or  $0.998 \pm 0.001$  g/ml for water at 20 °C (David R. Lide 2005), and the resulting **volumes per drop** are displayed in Figure 98. The difference between the pneumatically and mechanically initiated profiles is clear, resulting in higher volumes for configurations with pressures above the threshold for ejection and lower, comparable results for the mechanically dominated profiles. It is noteworthy that water shows a greater volume than PEDOT:PSS (slow) at the same pressure (0.5 MPa) even though the closing time in the case of the polymeric dispersion is

slower (300  $\mu\text{s}$  for water and 600  $\mu\text{s}$  for PEDOT:PSS), which gives it more time to flow. This is attributed to the higher viscosity of the dispersion, even at high shear rates, which results in a lower flow rate under the same geometric conditions and applied pressure. The settings with mechanically induced ejection display remarkably lower volumes than the ones initiated by pressure, as it was previously hypothesised. This is because in pneumatic profiles there is ejection happening during the whole pulse time, while in mechanically initiated ejection the material only flows during the closing stage, leading to a reduced volume independent from the pulse length. Moreover, it is noted that in these cases the volume is not only lower than for the pressure driven configurations but it is also consistent across materials despite the strong differences between fluid properties measured during the present work. This could be explained considering that the dispensing device used in this work is a positive displacement valve, which physically moves a certain distance each cycle, as was explained in Chapter 3 (Figure 38). Thus, considering that both the stroke of the valve and the geometry of the nozzle chamber remain constant, it is reasonable that the jetted volume is constant even for different materials. The only deviation from this scenario arises from the flow-back towards the material reservoir during the closing of the valve, which would be dependent again on the fluid properties and the applied pressure. Nevertheless, the proportion of material flowing back to the reservoir compared with the amount that is dispensed through the nozzle does not seem to be introducing a remarkable deviation in the observed volumes. Therefore, the stroke of the valve seems to be the main driver of the dispensed volumes in mechanically initiated configurations and consequently it is a valid candidate to optimise in the future to further reduce the size of the jetted drops to improve the resolution of the system. However, these tests would require the modification of the printing signal sent to the valve and are therefore left for future work.

Using a similar approach, the effect of **pulse length** was tested for a selection of materials and configurations, representing both pneumatically and mechanically initiated ejections (Figure 99). These results confirm that the pulse length has no noticeable effect on materials being ejected with pressures below the ejection threshold, as is the case for the UV-resin and the polymeric dispersion in fast mode. The situation is remarkably different for the water and PEDOT:PSS in slow configuration, both pneumatically initiated, since they display an increasing drop volume as the pulse gets longer. The observation of volume increase with the pressure and pulse time for pneumatically driven configurations agrees with the results of Yang *et al.* (H. Yang et al. 2013), which used a

similar valve than the used in this work with several viscous materials under pressure. However, they also tested higher viscosity materials on mechanically driven settings and found an increasing trend on the dispensed volume with the pulse time that eventually saturated into a constant value. They attributed this effect to the refilling of the nozzle chamber between ejections, ejecting more fluid at longer re-fill times until the chamber was completely full and the volume maximized. This behaviour was not observed in our experiments, perhaps due to the lower viscosity of our materials or the lower applied pressure. Thus, in case that this saturation effect is present, it is possible that it is reached within the minimum tested pulse time (0.3 ms) for the fluids used in this study, which would be compatible with the constant volume observed regardless the pulse length.

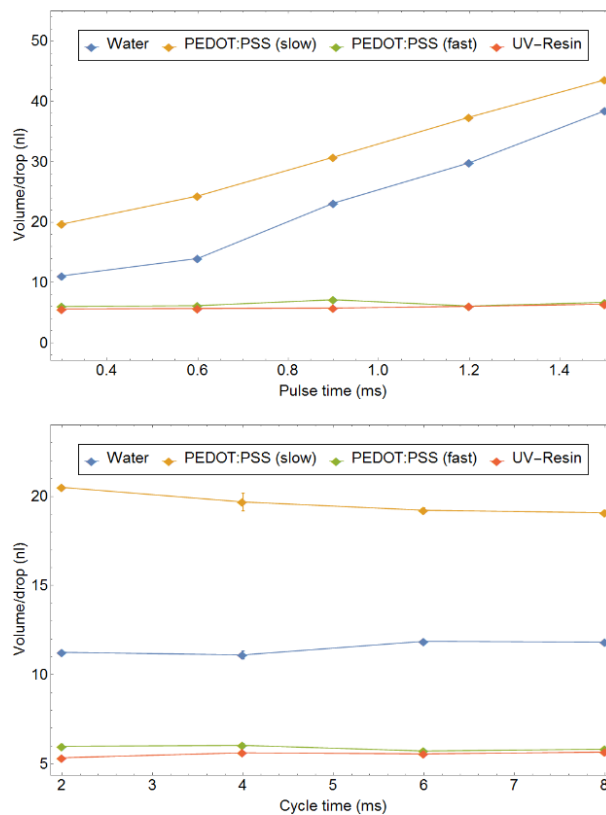


**Figure 99:** Influence of pulse time (top) and cycle time (bottom) for 4 different printing configurations. The constant cycle time in the pulse experiment is 4 ms, while the constant pulse time during the cycle tests was 0.3 ms. The water pressure is 0.1 MPa.

Similarly, these 4 configurations were studied under different **cycle times** to check the reliability of the valves across the range of frequencies between 125 and 500 Hz, as shown in Figure 99. It is important to bear in mind that 500 Hz is the maximum operation frequency recommended for these valves, which would behave in a non-linear manner outside said range. The volumes obtained are consistent with previous experiments and constant across the whole frequency range, as it was expected according with the operation recommendations of the manufacturer.

## 6.5 Discussion and printability calculations

### 6.5.1 *Experiments performed: evaluation and potential improvements*

Several experiments have been carried out to characterise the jetting performance of various fluids under different printing settings. First, the low viscosity photopolymer (TPGDA) that was deposited with a PIJ printhead was studied via **stroboscopic imaging** while the waveform was modified, allowing for the selection of the profile most energetically efficient. This method proved to be accurate and simple, especially since it did not require any external equipment to record the images or analyse them. The volume and speed of the obtained drops were  $29.80 \pm 0.19$  pl and  $5.90 \pm 0.13$  m/s respectively. Similarly, a series of **high-speed videos** were recorded for the viscous materials jetted with the micro-dispensing valve, where both the closing time and the pressure were modified to study their effect on the process. Valuable conclusions about the stability of the jets, their different stages, an estimation of their average speed were obtained from these recordings. However, since the speed of the jets in some configurations exceeded 40 m/s, the events were captured only in a small number of frames, which limited the accuracy of the results and did not allow the analysis of fine mechanisms like tail break-up. Likewise, the temporal resolution of the present experiment limited the conclusions extracted from the deposition of these drops on glass substrates, since most of the impact driven spreading happened in a timescale shorter than 1 frame. It is expected that to successfully monitor events of this speed in a length scale of a few millimetres, a frame-rate between  $10^5$  and  $10^6$  fps (Davidson & Abramowitz 2002) and a resolution of approximately 100 x 200 px would be required. Alternatively, a stroboscopic imaging system could be used, but since the frequency of ejection is 1 or 2 orders of magnitude lower than in PIJ, the required intensity of the lamp would be higher than the available source.

Alternative performance tests of the same configurations were carried out by the optical analysis of the resulting footprints on glass substrates. This method yielded results consistent with the high-speed videos in a shorter time and with all the experiments contained in the printing system. This opens the possibility of further automation in the future, since the calculation of the circularity and equivalent radius that are currently performed in a separated computer could be implemented into the system's software to allow for live results or even automatic optimization. Nevertheless, even in the current state the process of detecting and analysing these drops has proven to be successful, judging by the high number of detected drops per sample and their narrow distribution.

However, there are some aspects that can be improved in future iterations of this experiment, such as the illumination system and the analysed patterns. The former consisted on a combination of a ring light and an axial light, which were regulated to obtain homogeneous illumination without losing the features of the drops. Then, the average light pattern was obtained from numerous empty images and subtracted from each image to equalise the illumination. This approach was successful but it resulted in colour gradients on the drops near the edges, which in some occasions hindered their detection. This inhomogeneity could be reduced greatly by using only an axial illumination system, which is the most typical optical configuration for machine vision applications due to its even illumination and images free from shadows and glare (Edmund Optics 2015). However, the perpendicular direction of the light rays with respect to the sample causes the loss of surface defects and internal features such as bubbles. It was observed during the present experiments that an axial only approach was insufficient for transparent materials like the photopolymers studied here, since their edge was barely detectable. Therefore, the present configuration combining both types of illumination was the best compromise able to work with the most materials. The system could be optimised if some properties of the printed fluids are fixed. Alternatively, the printed patterns could be modified to increase the separation of the drops so only one event is captured per image. This would not only homogenise the effect of the illumination across different drops within the array but also would allow for individual assessment of the position of each deposition respective to the centre of the image. This approach, would require a very precise calibration of the camera movement to avoid deviations between the centre of the image and the landing place of the drops. Moreover, this monitoring method would be slower and generate a higher number of images to analyse, which is the reason why it was avoided in the present work.

Lastly, an experiment based on the weight of multiple ejections was performed to calculate the volume of the drops and to evaluate the impact of parameters such as pressure and pulse length. The main sources of error for these tests were the evaporation of the solvent of the inks during the experiment, the residual fluid left on the nozzle plate after each cycle and the potential material stagnation due to insufficient pressure feeding the material to the nozzle chamber. These critical mechanisms were not observed and did not affect the linearity of the results at different number of events, which lead us to consider this a successful method for the evaluation of potentially stable profiles. However, according with the observations gathered during the high-speed videos and footprint experiments, this mass-based test is not recommended as a screening experiment, since it

is possible that configurations resulting in moderate nozzle flooding display low deposited volumes, which could lead to their misidentification as a suitable jetting configuration.

### **6.5.2 Printing parameters**

From the experiments here shown and other similar tests found on the literature, the effect of each main printing parameter has been clarified and is summarised in the following.

#### **Applied pneumatic pressure**

Experiments have shown that the applied pressure is critical to define the jetting regime in which the ejection happens, being mechanically driven for configurations with a pneumatic force lower than a critical pressure typical for each material or displaying a slow pneumatically initiated jet front followed by a mechanical closing of the valve if the pressure is higher than said pneumatic threshold. **Pneumatically initiated jets** are slower but can lead to splash-in-flight or fluid-on-fluid collisions if the speed of the tail is faster than the front (Figure 75). Furthermore, since the material is ejected for as long as the nozzle is open, there is a clear proportionality between applied pressure and flow rate, which results in greater deposited volumes and faster stream speeds as the pressure increases. Other authors have observed the same trend (Shu et al. 2010) (Wang et al. 2013) (Xie et al. 2010) and established that the required pressure to reach a particular flowrate is proportional with the viscosity of the fluids. This dependency is more complex for non-Newtonian fluids, as it was discussed in section 2.4 (equation 16), but the dependency between the viscosity and the required pressure is preserved at high shear rates for the fluids used in this work. The material that required less pressure to travel through the nozzle of the micro-dispensing valve was the aqueous dispersion of PEDOT:PSS, followed by the photo-curable resin, the silver paste and the carbon paint. The same incrementing order is found on the viscosity at shear rates of  $10^3 \text{ s}^{-1}$  and higher (Figure 68) for the materials used in the present work. This viscosity dependency can serve as a starting point to study the threshold pressure, but other parameters such as nozzle geometry and apparent yield stress are also key factors. In particular, the presence of an apparent yield stress has been found to create a pressure threshold below which no flow is produced in micro-extrusion experiments using viscoelastic fluids (Bruneaux et al. 2008). The authors were able to identify a linear relation between the required pressure to initiate flow, the apparent yield stress of the fluids and a nozzle length-to-radius ratio. This approach was suitable for their experiment because the fluid reservoir was a syringe, with no other narrow

channels before the nozzle and the actuation mechanism was purely pneumatic. Therefore, the material could be considered at rest and unyielded until the extrusion stage. In our system, the feeding mechanism is more complex and a certain degree of shear thinning is expected before the fluid reaches the nozzle chamber, leading to a gradient of effective viscosities along the pressurized path.

It is important to note that the pressure threshold marks the required actuation to initiate flow through the nozzle but not necessarily to form a stable fluid stream or a droplet. This stable ejection requires higher pressure, as was introduced in section 2.4, to overcome the energy barrier established by the surface tension and elastic components of the fluid. Thus, if enough pressure is applied to initiate flow but not to separate the jet from the nozzle, an accumulation of residual material floods the nozzle plate, affecting the repeatability of the following ejections and eventually preventing the formation of drops. This was directly observed in both the high-speed video experiment and the footprint study of the present work.

**Mechanically driven configurations** have shown negligible variations in their behaviour under different applied pressures. This could be due to the small contribution that the pneumatic pressure has in the flow of these high viscous materials compared to the fast closing speed of the valve, which would result in velocity variations below the resolution of our experiments. This, however, does not mean that the applied pressure is irrelevant for these profiles, since several authors highlight the importance of the application of a minimum pressure to compensate the backpressure generated during the opening of the valve, which helps to re-fill the nozzle chamber between cycles (Quinones et al. 2002) and to avoid air entrapment due to said suction force (Wang et al. 2013). These effects, however, were not manifested during our experiments, which were conducted under a minimum pressure of 0.1 MPa.

### **Temperature**

It is well known that the viscosity and surface tension of most fluids tend to decrease as the temperature is raised as a consequence of an increased Brownian motion of the constituent molecules (Barnes 2000). Thus, since both magnitudes are opposed to the flow and drop formation mechanisms it is reasonable that the required pressure for jetting is reduced for heated materials, which generally leads to an improved ejection of viscous materials (H. Yang et al. 2013) (Quinones et al. 2002) (Shu et al. 2010) (Wang et al. 2013). The variation of the shear viscosity with temperature for the viscous fluids used in

this work was characterised in the range of 20 to 60 °C (Figure 71 and Table 10) and showed good agreement with the Arrhenius model (equation 3). Although a reduced viscosity would require lower applied pressures, the rest of the experiments were performed at 25 °C to avoid excessive heat exposure to the nylon-based printhead holder fabricated for this work, which could result in geometric alterations and subsequent printing inaccuracies. Also, the dispersion of the pastes is expected to be more stable at lower temperatures.

### **Cycle time**

The valves used in this study have an specified maximum jetting frequency of 500 Hz, non-linear deformation of the piezoelectric elements and potential damage to the system is expected outside this range (Nordson EFD 2013). The deposited volumes were tested for several fluids operating in both mechanically and pneumatically initiated jets in the range of 125 to 500 Hz (Figure 98). The measured volumes were constant at all frequencies with deviations below 3 %, which limits the effect that the re-filling time of the chamber can have on the process. However, despite its observed independence with the dispensed volume, the cycle time plays a crucial role in the process governing the separation of consecutive events. Specifically, it is expected that to obtain jets that are not connected to the next, the following separation condition needs to be fulfilled:

$$t_{pulse} + t_{closing} + t_{break-up} < t_{cycle} \quad (52)$$

Since most configurations tested in this work were mechanically initiated and consequently independent from the pulse time, the previous condition was not compromised for this jetting regime. The case of the aqueous dispersion of PEDOT:PSS was different, since at 0.5 MPa was able to produce pneumatically initiated jets and therefore a test of the previous separation condition was conducted, as it is shown in Figure 100. In the figure, two configurations were monitored with the same pulse time (2.0 ms) and closing time (0.3 ms) but different cycle time (2.5 and 3.0 ms). The small variation in the frequency resulted in a transition from individual events to joined consecutive jets. From equation 52 it is possible to calculate a range for the break-up time that goes between 0.2 and 0.7 ms, which in fact is compatible with the observed break-up shown in Figure 85. Thus, the maximum jetting frequency that would result in individual events for this material with the given settings would be lower than 400 Hz. Similar joined jets have been observed in the literature for pseudoplastic fluids with long break-up times dispensed with a micro-dispensing valve (H. Yang et al. 2013) but no separation condition was provided.

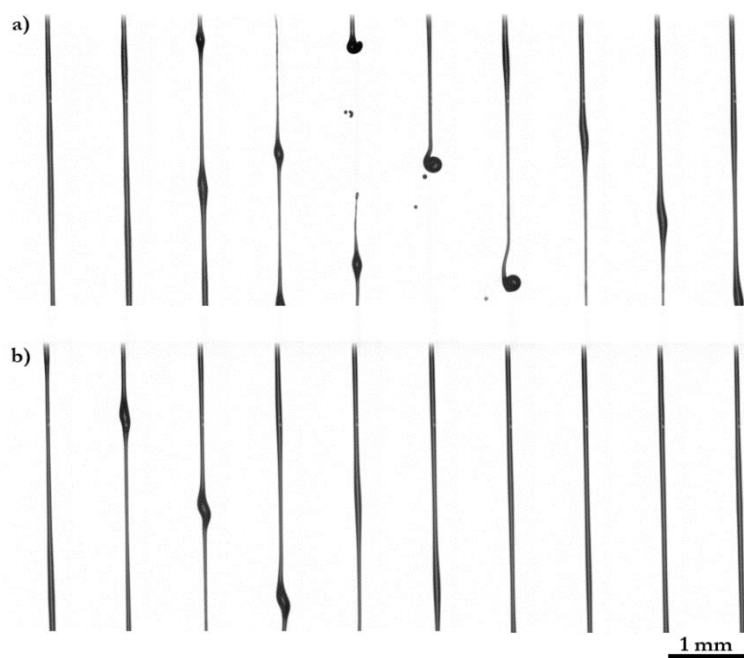


**Figure 100:** Still frames recorded at 4000 fps and 1  $\mu$ s shutter for an aqueous dispersion of PEDOT:PSS at 0.5 MPa with a pulse time of 2.0 ms, a closing time of 0.3 ms and cycle times of 3 ms **(a)** and 2.5 ms **(b)**. In both cases the closing and re-opening of the valve is shown in the middle frames. The top image displays a clear separation between consecutive events due to its lower jetting frequency while the bottom one shows indistinguishable events.

### Pulse time

The discussion of this parameter is similar to the applied pressure in the sense that its effect on the ejection depends on the main driver of the ejection, i.e. mechanical or pneumatic. Thus, for mechanically initiated configurations the pulse time does not affect the dispensed volume, as was shown in Figure 99. These experiments were performed at minimum pressures of 0.1 MPa, which seems to be enough to re-fill the nozzle chamber between cycles for the fluids tested in this work. However, it is possible that at higher viscosities the required pressure for re-filling is higher and failing to provide that would affect the dispensed volume, as it was observed by Yang *et al.* (H. Yang et al. 2013). For pneumatically initiated jets the pulse time is directly proportional with the dispensed volumes (Figure 99), since the flow is initiated as soon as the valve opens. This dependency between volume and pulse time is in agreement with the results of several authors using various micro-dispensing systems (H. Yang et al. 2013) (Shu et al. 2010) (Wang et al. 2013) (Xie et al. 2010).

### Closing time

During this chapter, several closing times have been tested with a common and fixed stroke of 160  $\mu$ m, resulting in average closing speeds between 0.12 and 1.33 m/s. The effect of the closing time had a different impact on each material depending on their properties but the shared outcome is an increase in the exit speed of the fluids as the

closing time is reduced. This is most evident when the pneumatic pressure is kept low, as was shown in (Figure 83). Thus, the closing time is the most important printing parameter in the system, since it determines if a drop is ejected, its stability and the eventual shape on the substrate (Figure 95). In the present work, the available closing speeds were limited to 6 pre-sets, which allowed for a general mapping of the process but presented limitations for a more individualised study of the transition between stable and unstable configurations for each material. Consequently, it is advisable for future experiments to gain further control over this parameter, which can be achieved by developing a bespoke digital controller.

### **Stroke length**

The stroke length of the valves was constant at 160  $\mu\text{m}$  in the present work due to the limited control over the printing pulse provided by the current digital controller. Therefore, direct experiments could not be performed to study the effect of this parameter on the ejection. Nevertheless, its role in the jetting mechanism is well understood as another governing factor on the local pressure at the entrance of the nozzle, often linked to the closing speed. In fact, typical systems provide control of either the stroke length or the closing time, leaving the other constant, allowing for different closing speeds. Selecting the closing time, as it is the case in the present study, is more accurate in terms of digital control but it does not allow variation of the amplitude of the plunger's displacement, which is related with the dispensed volume. Several reports of smaller deposited drops using shorter stroke lengths are available in the literature (Gu et al. 2016) (Shu et al. 2010) (Wang et al. 2013). This direct dependency of the deposited volumes with the plunger movement was suggested in the droplet's mass experiment (Figure 98), since constant volumes close to 5.5 nl were observed for materials of very different flow properties at the same closing speed. Thus, reducing the stroke length of the valve while maintaining its closing speed is a potential method to reduce the deposited volumes. More experiments using different stroke lengths and closing speeds are required to prove this capability but they require the modification of the digital controller of the valve and consequently are left for future work.

### ***6.5.3 Printability map***

To study the effect of different flow properties and drop average speeds in the jetting process, a printability map is created following the guidelines given in section 2.4. The results for the tested jetting configurations are represented in a parametric space

defined by the Weber (equation 27) and Reynolds (equation 10) numbers (Figure 101). It must be noted that the definition of these dimensionless numbers assumes a constant value for the viscosity, but this is generally not the case for the materials used in this work (Figure 68). However, since the shear rate applied to the fluids in the nozzle walls during jetting is estimated to be in the range of  $10^5 - 10^7 \text{ s}^{-1}$  (from equations 9 and 18), the constant viscosity at infinite shear rate ( $\eta_\infty$ ) obtained from the Sisko model fit of the rheological data (Table 9) is used for the calculations. However, since actual viscosity measurements are available for TPGDA and PEDOT:PSS due to their lower viscosity, these are used instead of the extrapolation. Other required fluid properties such as density (Table 6) and surface tension (Table 8) were also characterised in Chapter 5. The nozzle diameter ( $50 \mu\text{m}$  for the micro-dispensing valve and  $35 \mu\text{m}$  for the inkjet printhead) is used as the characteristic length. The speed of the drops in each case is taken as the average speed measured from the high-speed videos for the viscous materials and from the ADA tests for the TPGDA (Figure 74). The stability of the ejection is assessed from the videos and the obtained footprints with the following criterion:

- **Substrate splash:** Distorted shape deposited on the glass substrate with low circularity values and repeatability. Splatter due to fluid-on-fluid collision is not considered substrate splash since it does not depend mainly on the surface or the impact speed but on the pressure and relative velocity between the front and the end of the jets.
- **Stable ejection:** 30 drops are successfully ejected with a residual volume on the nozzle plate at the end lower than 20 nl.
- **Unstable ejection:** 30 drops are ejected but a residual volume greater than 20 nl is left on the nozzle plate at the end. The drops in these situations are visibly affected by nozzle flooding and their direction is irregular.
- **One-drop events:** These are configurations so unstable that only originate a few drops before the residual fluid on the nozzle stops the ejection. In these cases, since the first drop is the only event unaffected by nozzle flooding, only the speed of the first one is considered. These measurements do not represent useful jetting configurations but are crucial to understand the minimum drop speed that a drop requires to be ejected.

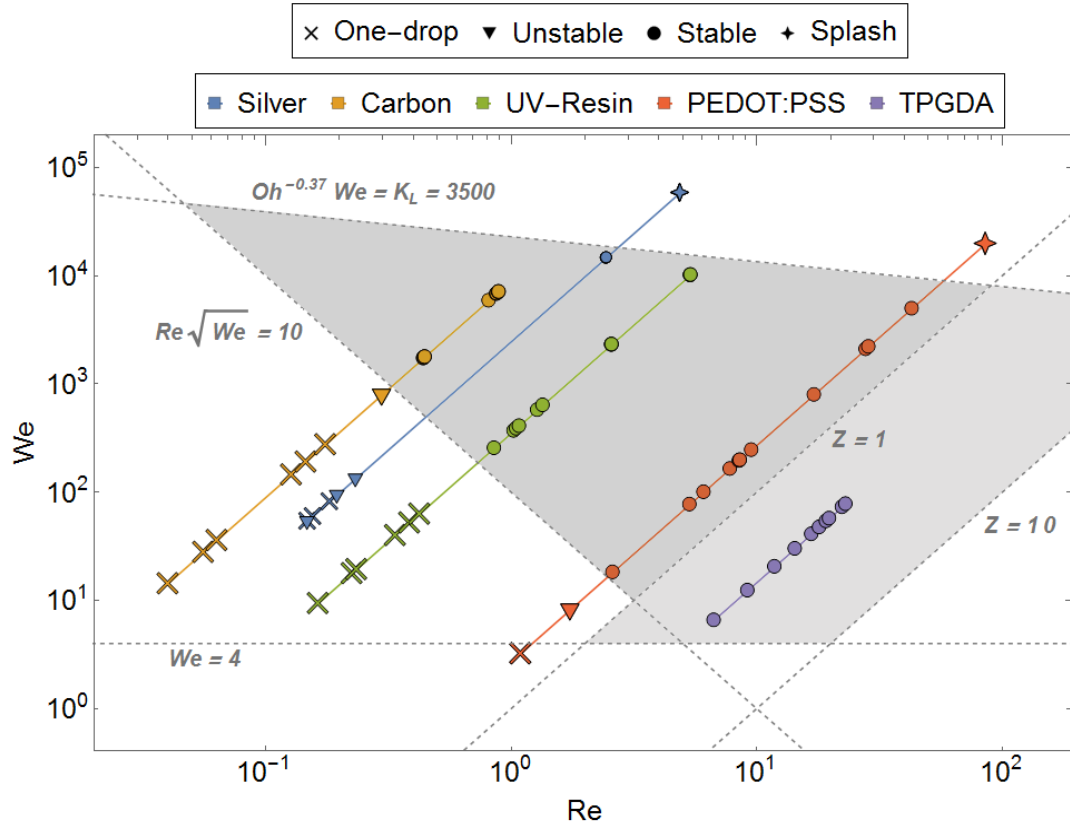


**Figure 101:** Parameter space defined by the Weber ( $We$ ) and Reynolds ( $Re$ ) numbers displaying the results collected during this work. Different symbols represent the performance of the jets, considering their repeatability and spreading on a glass substrate. The barrier for minimum velocity is given by  $We = 4$  (Derby 2010), the splash threshold by  $Oh^{-0.37}We = K_L$  (Cossali et al. 1997) and the lines of  $Z = 1$  and  $Z = 10$  define the printability region for drop-on-demand inkjet printing (Derby 2010), coloured in light grey. A stability threshold following  $Re\sqrt{We} = 10$  is suggested by the author from the observed trend in the data, which allows the creation of an extended printability region for micro-dispensing valves (dark grey).

Figure 101 is a generalization of the well-known printability map for inkjet printing provided by Derby (Derby 2010). In its original version, the printability window for drop-on-demand inkjet is suggested to be in the range of  $10 > Z > 1$ , where  $Z$  is a printability parameter that corresponds to the inverse of the Ohnesorge number (equation 28). Precisely in this region, are located all the configurations tested for the TPGDA deposited with a conventional inkjet printhead. Higher values of  $Z$  than 10 are supposed to lead to excessive satellite droplets, while lower than 1 correspond to viscous materials traditionally impossible to jet. Nevertheless, it is in this region where all the viscous materials dispensed in this work are positioned.

The line at  $We = 4$  represents the suggested **minimum speed** that a drop requires in order to overcome the surface tension of the fluid and break-free (Derby 2010). This threshold is respected by all fluids and configurations except for the PEDOT:PSS with a closing time of  $600 \mu s$  and an applied pressure of  $0.3 \text{ MPa}$ , which results in  $We = 3.2$ . However, considering the approximations and assumptions performed in this analysis in

terms of the flow properties of the fluids, this result is compatible with the lower boundary suggested by the literature. Similarly, a **splash threshold** is calculated following equations 34 and 35 (Cossali et al. 1997), accepting  $Ra = 6 \text{ nm}$  for the average surface roughness of standard microscope glass slides (Li & Logan 2004) and a radius of the drops in flight resulting from the assumption of spheres of known volume (Figure 98). This splash threshold is expected to be underestimated due to the elastic effects not being taken into account (equation 36 (Cossali et al. 1997)) but in the current form it already successfully defines the splash region, where both the PEDOT:PSS dispersion and the silver paste are located when the closing time is lower or equal to  $120 \mu\text{s}$  and  $200 \mu\text{s}$  respectively.

It is noteworthy that the transition between unstable and stable ejection seems to happen for all the tested materials following a trend close to  $Re\sqrt{We} = C$ , where  $C$  is a constant. Later, values were given to  $C$  until both regions were successfully defined for the observed events, which resulted in the following **stability threshold**:

$$Re\sqrt{We} = 10 \quad (53)$$

Thus, with this additional condition, a new printability window is defined for the viscous fluids. This region shrinks as the Reynolds and Weber numbers are reduced, which effectively corresponds to a decrease of dominance from the inertia of the system in favour of the viscosity or the surface tension, respectively. This agrees with the theory reviewed in section 2.4, since it represents the conditions in which the kinetic energy imparted to the drop is not enough to overcome the opposing forces. This observation, however, requires of further experiments to be confirmed. A good starting point would be to focus on the transition region and obtain new videos at a higher frame-rate to reduce the uncertainty of the data. Also, following these initial observations, it would be beneficial to test other fluids in the region of  $1 > Re > 0.01$  with common characteristics such as density, particle size or surface tension to decrease the number of variables. Furthermore, considering that neither  $Re$  or  $We$  contemplate extensional or viscoelastic effects, it would be interesting to either select only Newtonian fluids for the second round of experiments or consider these complex mechanisms by studying other relevant dimensionless numbers such as the Deborah (equation 25) or elastocapillary (equation 33) numbers, both including the relaxation time of the fluid as an indicator of its elasticity.

# **7. Results and discussion:**

## **2D & 3D deposition of functional materials**

Before attempting to produce multi-material 3D structures, it is crucial to optimise each material individually for 2D depositions. Thus, multitude of square patterns at different resolutions were printed to obtain repeatable layers with suitable material coverage, considering both geometric and functional factors. Later, the 3-dimensional parts were created by the characteristic layer-by-layer approach of Additive Manufacturing, which eventually required the fluid materials to be solidified via a material-dependent post-processing. In this work, the processes used were solvent evaporation, UV-curing, or a combination of solvent evaporation, chemical conversion and nanoparticle sintering.

Once the printing and post-processing conditions of 2D patterns were studied and working sets of parameters were selected, multi-layered geometries were produced and the evolution of both their height and cross-section with the number of layers were characterised via laser profilometry. The objective of these experiments is twofold, to determine the average layer thickness of each material and to measure the resistivity of the conductive materials in these specific processing conditions. This information was then used for the design and fabrication of multi-material parts with pre-defined dimensions, which is the objective of the final section of this chapter. There, several proof-of-concept devices are presented to showcase the present and future capabilities of the system, showing promising results in the areas of flexible and printed electronics, electroluminescent applications and functional 3D-structures.

### **7.1 2D-tests: Resolution and post-processing conditions**

Inkjet printing is based on the discrete deposition of drops on a substrate following the directions of a digital file. Since the original application for this technology was the reproduction of images and documents in a physical format, many methodologies have been developed or adapted from other printing areas to improve shape and colour representation (Lau & Arce 2008)(Hutchings & Martin 2012). An example of this is found in the strategies of dithering and halftoning that combine arrays of dots of a limited number of basic colours to simulate an increased colour depth for a viewer at sufficient distance.

This was previously shown in Chapter 3 (Figure 51), where the multi-material calibration of the hybrid system was addressed.

These strategies based on the deposition of discrete dots are not suitable to impart other functionalities such as electrical conductivity to the printed samples, since this physical property requires continuous paths for charge transfer and any discontinuity, either arising from the patterns or due to low printing accuracy, would result in interrupted circuits. Therefore, the drops need to land in close proximity to one another to merge and fill any pinholes within the boundaries of the printed patterns. However, the deposition of adjacent droplets does not always lead to satisfactory shapes, as it is shown in Figure 102 for a series of linear trains of drops, where only a range of drop-to-drop distances result in constant-width features. This was studied in detail by Duineveld (Duineveld 2003), who proposed that the observed regularly spaced bulges of liquid were the effect of competing flow paths for a newly arrived droplet. This means that if a recently deposited droplet encounters another droplet or a fluid bead while it is spreading due to capillary action, there are two flow scenarios. If the spacing between droplets is short and the deposition rate is relatively slow, the curvature on the new droplet is greater than the one in the bead, thus the Laplace pressure will push material from the new droplet into the main body of liquid. This increase of volume comes with an associate increase in contact angle, which can create instabilities and therefore the bulges. However, at higher rates and drop spaces, the situation is reversed and the spreading of the droplet is favoured, resulting in a train of discrete drops. This instability has been experimentally observed numerous times (Soltman & Subramanian 2008) and later analytically modelled (Stringer & Derby 2009). In this work, this linear approach was originally followed to optimise the resolution of the printed patterns, as it is shown in Figure 102. Nevertheless, it was early observed that the suitable resolution range for these patterns was always higher than the obtained for square patterns, as it is expected due to the 4 neighbours contributing to re-locate fluid in a 2D pattern compared with the only 2 neighbour drops in a line. Consequently, since the objective of this work is to create 3D objects by stacking numerous 2D films, the test patterns were modified to create squares instead of lines.

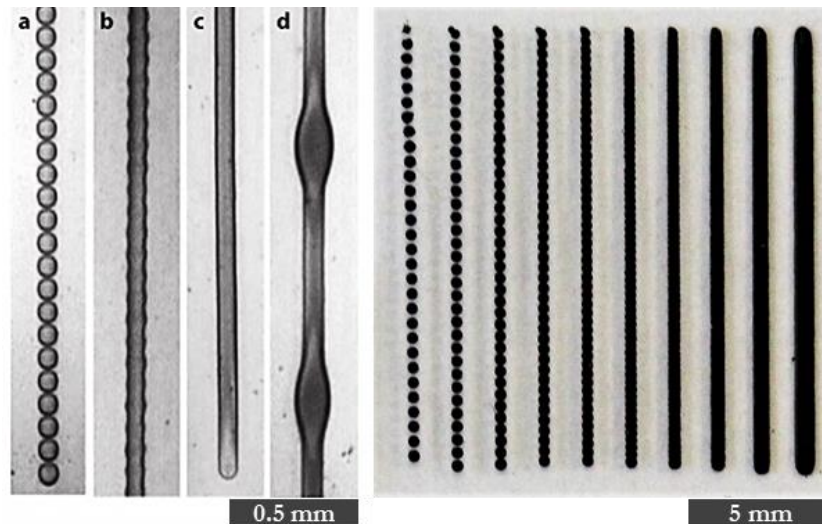


**Figure 102: Left)** A continuous liquid bead (c) can be obtained for the right combination of parameters such as droplet spacing and deposition rate. Droplet spacing too large will hinder coalescence (a) but a spacing too short (d) can result in inhomogeneous redistribution of the fluid, which creates bulging instabilities. Image from (Soltman & Subramanian 2008). **Right)** Early 1-dimensional resolution test for the carbon paint used in this work on a polycarbonate substrate. The overlap (%)/resolution (DPI) for the tracks from left to right are: 0/50, 0/56, 2/63, 13/71, 25/83, 38/100, 50/125, 63/167, 75/250, 88/500.

Once the layers are printed with satisfactory resolution, they need to be post-treated to solidify them, which in the present work is performed by either solvent evaporation, UV-curing, and a combination of solvent evaporation, chemical conversion and nanoparticle sintering. However, as important as the type of process that each material requires is the moment at which it is applied, since the solidification step can be performed either at the end of the fabrication stage or after the deposition of each layer, resulting in different properties for the printed geometries. For instance, the former approach of wet-on-wet printing provides good merging between layers and can result in stable structures if the rheological properties of the green part are enough to hold the shape until the firing process is finished. Consequently, this approach is typically used in the extrusion of highly loaded pastes (Marchelli et al. 2011) (Billiet et al. 2012). However, if the rheological properties are not finely tuned, the layers tend to grow laterally instead of vertically, showing a non-linear growing in the z-direction (Sridhar 2010). Also, this approach has the disadvantage of trapping inside the created structure some materials that should be removed, such as solvents and other volatile compounds, which typically result in either undesirable contamination (Jolke Perelaer, Smith, and Mager 2010) or high porosity (Marchelli et al. 2011). Alternatively, the wet-on-dry approach of treating each layer individually, generally results in a more linear relation between the height of the structure and the number of layers (Sridhar 2010) and limits the entrapment of solvents to the expense of longer processing times. This is the approach traditionally followed in material jetting and therefore it would be adopted in the present work.

### 7.1.1 *UV-curing*

UV-curing with LED lamps has some advantages over other energy transfer methods such as fast on/off cycles, uniform radiation, long service life and absence of IR in the emission spectrum that can be absorbed by other polymeric materials involved in the process (Suganuma 2014). The UV-lamp used in this work was described in Chapter 3 together with its curing modes. The evaluation of the curing state of the samples is performed via a two-stage shape integrity test. First, the sample is scratched with the plastic part of a cleaning swab (Foamtips swabs, Chemtronics, USA), then isopropanol is applied on its surface and the swab is used to try to smear any uncured material that could be present. If both checks result in an unmodified surface, the sample is deemed cured. This is not proof that the inner parts of the sample are 100 % cured, but it ensures the retention of the printed geometry and the avoidance of material mixing prior the deposition of the following layer, which are the requirements for this process. Full curing is likely to be achieved during the successive irradiation of the sample and can be further ensured by applying a UV-bath on the same set-up before the sample is removed. In this section, the study of the suitable printing resolution on different substrates and the UV-curing conditions for the low viscosity TPGDA and the higher viscosity UV-curable resin are discussed.

#### 7.1.1.1 **Stereolithographic Resin**

The stereolithographic resin was printed with the PICO valves on microscope glass slides using pressure of 0.1 MPa, a closing time of 0.30 ms and 25 °C. The square samples were cured after each was printed at 10 mm/s, which is within the range of curing speeds successfully tested in early experiments (Appendix A1). This approach was chosen over live curing due to the single nozzle configuration of the micro-dispensing valves, which increases the number of passes required to complete a square compared with a multi-nozzle printhead. Thus, if the UV-lamp is always on, the first deposited drops would be exposed to the radiation tens of times more than the last printed lines, which could have adverse effects. The non-negligible time between the droplet landing on the substrate and the curing would result in poor feature resolution for fluids with fast spreading, but this is not the case for the high viscosity resin used in this work, which allows shape retention of the uncured material until the UV-lamp pins everything in place. This type of curing allows for homogeneous and smooth surfaces, since the resin is cured once all the drops have coalesced and the fluid has settled.

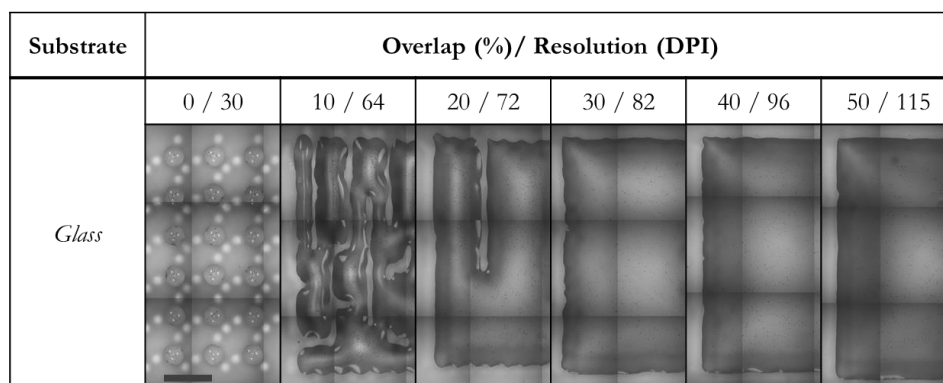


**Figure 103:** Square patterns printed with UV-resin on a glass slide to test different drop overlaps from 0 to 50 %, starting with individual drops of 440  $\mu\text{m}$  in diameter. The curing was applied after the print of each pattern was completed at 10 mm/s. The images were automatically taken with the integrated monochrome camera on the system and later stitched to visualise the full samples. The scalebar in the image is 1 mm.

Keeping the curing and printing conditions constant, several square samples were produced exploring drop overlaps between 0 and 50 %, as are shown in Figure 103. Fully closed patterns were observed from 30 % overlap onwards, with improved edge definition as the resolution increases. This trend, however, is accompanied by an overall increase of the square area due to the greater fluid volume contained in the fluid film, which is particularly evident at an overlap of 50 %. Since this uncontrolled spreading reduced the minimum possible printed features and could result in the unwanted closing of holes in the future patterns, the selected resolution was 89 DPI, which corresponds to an overlap of 35 %.

#### 7.1.1.2 TPGDA

The second UV-curable material used in this work was TPGDA, which was deposited by PIJ printheads due to its low viscosity. However, since this material spreads faster than the resin previously discussed, the possibility of curing the printed patterns at the end of the printing stage loses its attractiveness, since it would result in rounded patterns with very little detail. Thus, the live curing approach was used instead, which involved the UV-lamp being on during the printing phase, curing the drops as soon as they are deposited on the substrate. There is no risk of over-exposing the samples due to the 128 nozzles on each printhead, which are able to print considerably big sections in a single pass. The limitation of this curing mode, however, is that both the height and speed of the UV lamp respect to the substrate are fixed by the printing conditions, which limit the adaptability of this process stage. This was not a problem in the present case, since a printing speed of 100 mm/s and a gap size between the UV-lamp and the substrate of 4 mm was enough to produce samples that passed the curing tests based on scratching and IPA dissolution previously described.

Following this printing and curing configuration, several square samples were printed on both glass and epoxy fiberglass boards (or PCBs) to find a suitable range of print resolution that results in fully dense layers (Figure 104). Patterns with holes were obtained for both materials at drop overlapping at or below 40 %, with full coverage at 50 %. In both cases the resolution of 500 DPI resulted in an overlap close to 50 % and displayed no internal holes. Consequently, 500 DPI is chosen as the printing resolution for this material in the rest of this work.

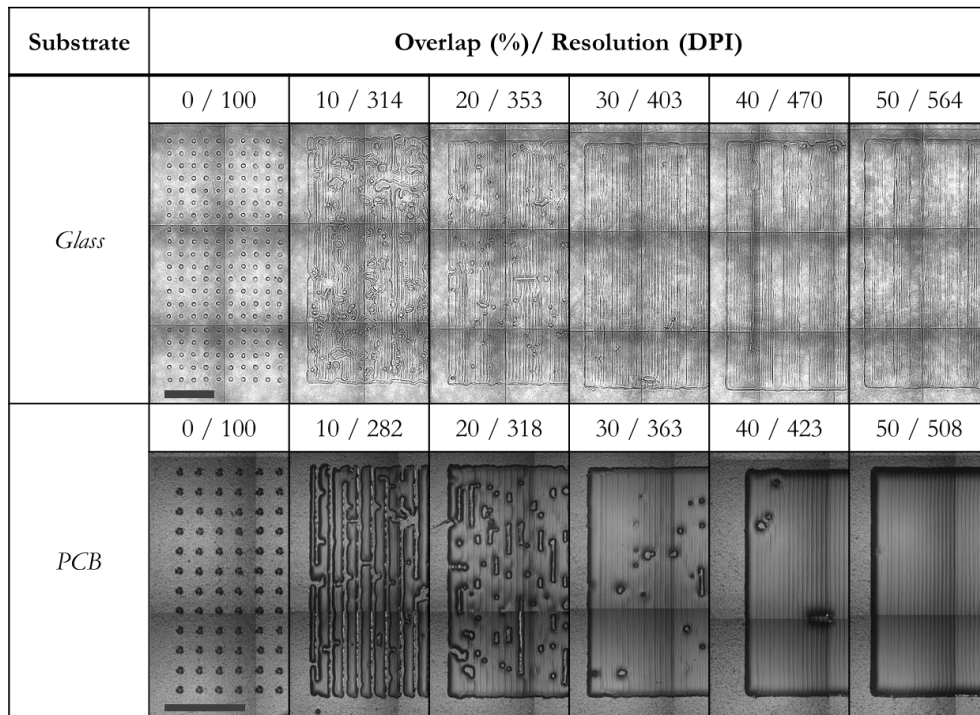


**Figure 104:** Square patterns printed with UV-curable TPGDA on a glass slide and an epoxy fiberglass board (PCB) testing different drop overlaps from 0 to 50 %. Individual drops display a diameter of 90  $\mu\text{m}$  and 100  $\mu\text{m}$  in glass and PCB respectively. The curing was applied during the printing at a speed of 100 mm/s and a distance between the lamp and the substrate of 4 mm. The images were automatically taken with the integrated monochrome camera on the system and later stitched to visualise the full samples. The scalebar in the image is 1 mm.

### 7.1.2 Solvent Evaporation

Solvent evaporation is the most typical post-treatment in PIJ, since most inks have volatile elements that need to be either evaporated or absorbed by the substrate. This process takes place from the first moment that the fluid is ejected and the length of time required to complete it depends on the vapour pressure of the involved solvents (Magdassi 2010). It is a common practice to heat either the substrate or the printing environment to speed this process up but it is important not to reach excessively high temperatures in the vicinity of the fluid reservoir and printhead because this can lead to material degradation and nozzle blockages. Although heating the substrate has been shown to be a decisive control parameter for droplets spreading (Soltman & Subramanian 2008)(Redinger et al.

2004), it is expected to introduce a thermal gradient in the z-direction that can cause inhomogeneities at sufficiently high number of layers. Thus, in the present work both the substrate and printing environment are kept at room temperature (25 °C) and any form of energy transmission would come from radiation emitted at a constant height of the newly printed layers.

In this section the results from 2-dimensional resolution tests and details about their respective post-process requirements are provided for the aqueous dispersion of PEDOT:PSS and a viscous carbon paint.

### 7.1.2.1 PEDOT:PSS

The aqueous dispersion of PEDOT:PSS was printed with the micro-dispensing valves on microscope glass slides using an applied pressure of 0.1 MPa, a closing time of 0.30 ms and a surrounding temperature of 25 °C. The square samples were dried after each sample was printed by a thermal treatment consisting on 2 passes of the lamp at IR Set 29% (as described in the calibration section dedicated to the IR-lamp, Chapter 3) and 0.1 mm/s, which resulted in approximately 100 s at a temperature close to 100 °C. This proved to be enough to dry the solvents present on the inks without causing apparent boiling, which resulted in smooth and transparent conductive films, as it is shown in Figure 105. This thermal treatment is in agreement with the suggestions of the manufacturer, also shown in Figure 105. Later experiments were performed at higher power settings (IR Set 34%) with similar results and shorter processing time.

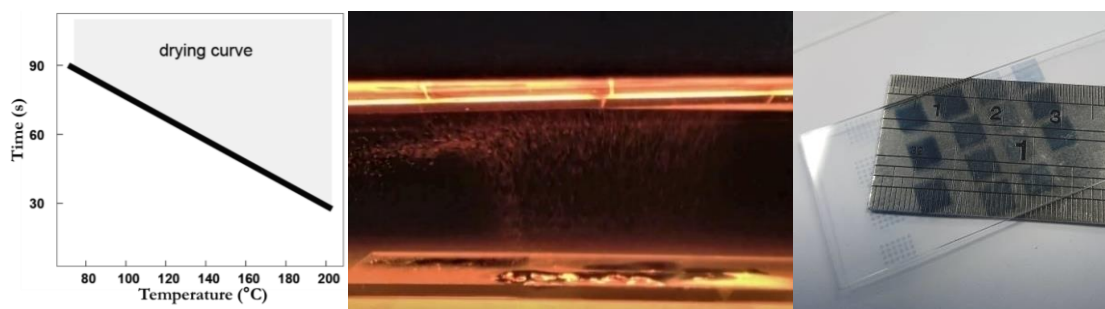


**Figure 105:** **Left)** Technical information provided by the manufacturer of the PEDOT:PSS dispersion regarding its drying conditions (Gaiser 2013). **Middle)** Image of a sample of PEDOT:PSS being dried by the IR-lamp in the system. Vapour coming from the sample towards the lamp is observed. **Right)** Picture of mono-layered square samples of PEDOT:PSS printed on a glass slide displaying more transparency in the optical spectrum for lower printed resolutions.

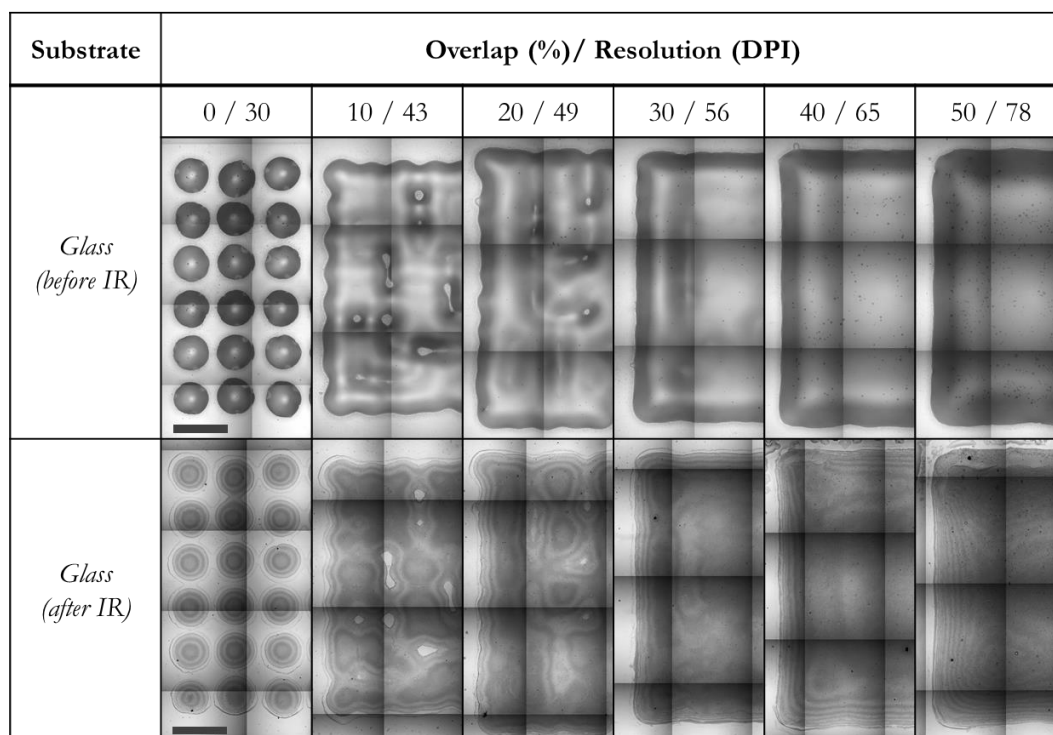


**Figure 106:** Square patterns printed with an aqueous dispersion of nanoparticles of PEDOT:PSS on a glass slide to test different drop overlaps from 0 to 50 %, starting with individual drops of 650  $\mu\text{m}$  in diameter. The drying was applied after the print of each pattern was completed with the IR lamp at 29% of its maximum power at 0.1 mm/s. The images were automatically taken with the integrated monochrome camera on the system after 2 minutes of printing to allow spreading equilibrium. The scalebar in the image is 1 mm.

The 2D resolution tests (Figure 106) show a similar behaviour to the UV-resin (Figure 103) before the fluid is dry, with some holes interrupting the films below 30 % overlap and an increasing total area as the resolution increases. In this case the squares at 50 % are not only slightly darker but also display rounded edges, both signs of a greater volume deposited in a similar area. The situation after the IR-drying of the samples results in almost identical patterns overall, proving that the holes are not filled even at higher temperatures when the spreading of the fluid is increased by a decrease in viscosity. Thus, the ideal resolution in terms of material coverage is 30 and 40 % overlap, and consequently 65 DPI is used for the rest of this work unless stated otherwise. Nevertheless, a correlation between lower resolutions and an increased transparency was observed for all samples, which is explained by the higher optical transitivity of thinner films. Similar results were obtained when samples of different number of layers were printed at a constant resolution. However, thinner films would result in higher resistance of the PEDOT:PSS sheets, which could be a problem for certain applications such as electroluminescent lamps, where lower resistance would result higher luminosity. Therefore, even though 65 DPI was accepted as the ideal resolution from a geometric point of view, it is expected that other resolutions would result in different thicknesses and affecting in turn the transparency and resistance

of the film, making this printing variable a crucial functionality control parameter. Experiments in this regard, however, are outside of the scope of this project and are left for future exploration of the capabilities of PEDOT:PSS as a high viscosity conductive material.

### 7.1.2.2 Carbon Paint

The conductive carbon paint was printed with the micro-dispensing valves on microscope glass slides and epoxy fiberglass boards (or PCBs) using an applied pressure of 0.1 MPa, a closing time of 0.30 ms and a surrounding temperature of 25 °C. The drying conditions recommended by the manufacturer are 24 °C during 5 to 15 minutes (Bare Conductive Ltd 2016), depending on the thickness of the deposited patterns. However, since the patterns here printed are smaller and thinner than the conventional applications of this paint, a drying test was performed by printing a square of 5x5 mm at 100 DPI on a glass slide and letting it dry in ambient conditions (25 °C) while the printing system was used to take a picture every second (Figure 107). From the stack of images, it is possible to see how the material dries faster on the edges and only after approximately 100 seconds the texturized surface in the upper right corner does not change its appearance. After 2 minutes, a foamtip cleaning swab was used to check if the paint was still fresh, but no pattern variation or material transfer to the swab was observed, which was accepted as a sign of drying. An additional test was conducted during the early stages of this project (Appendix A1), where 3 different drying times (0 s, 30 s and 300 s) were tested in a multi-layered sample. It was shown that drying times between layers of 30 s or below resulted in bulged tracks, while 5 minutes was enough to provide linear growth of the samples height as the number of layers was incremented. These results are in agreement with the technical information provided by the manufacturer and the experiment shown in Figure 107.

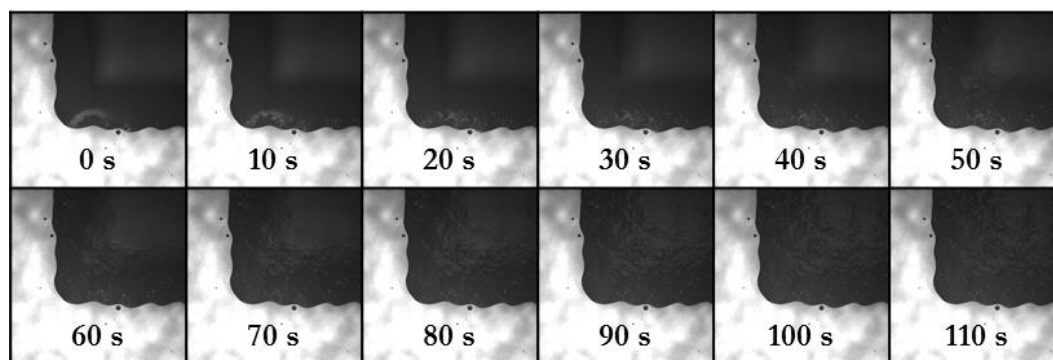


**Figure 107:** Bottom-left corner of a square pattern of carbon paint printed at 100 DPI. A picture every second was taken with the integrated monochrome camera on the system to monitor the evaporation of the water at room temperature (25 °C). Each image is 1.5 x 1.5 mm.

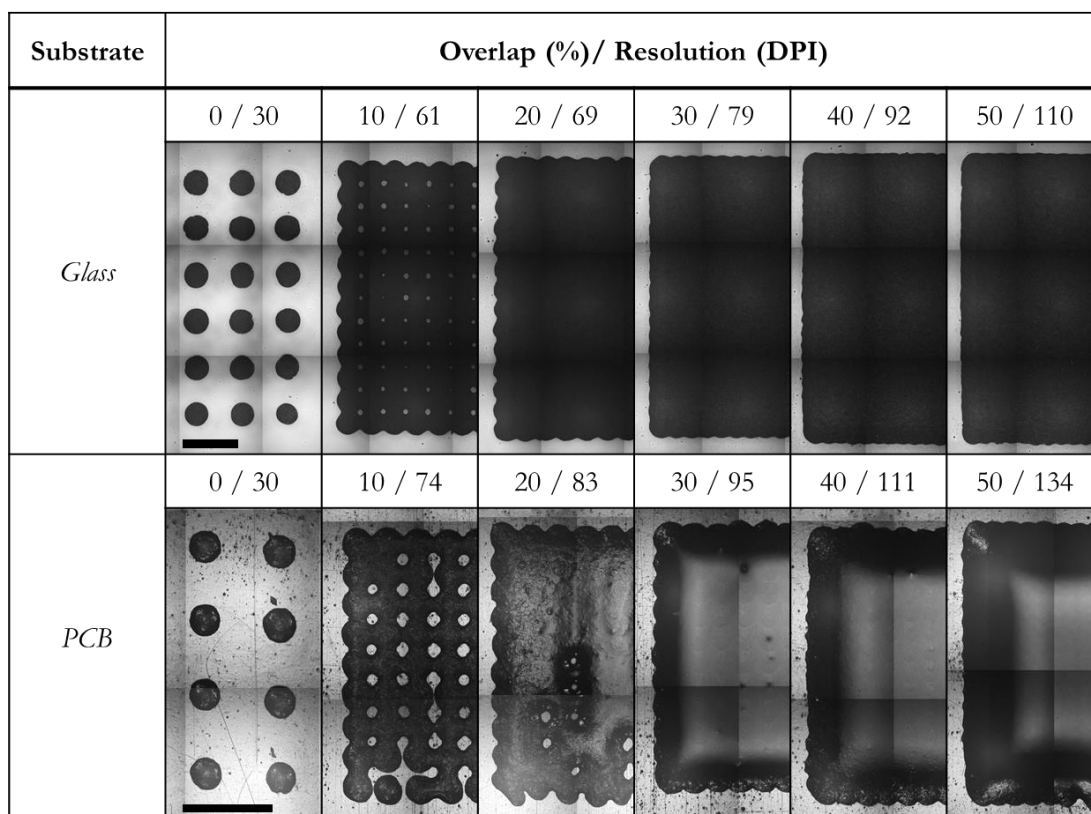


**Figure 108:** Square patterns printed with carbon paint on a glass slide and an epoxy fiberglass board (PCB) testing different drop overlaps from 0 to 50 %. Individual drops display a diameter of 460  $\mu\text{m}$  and 380  $\mu\text{m}$  in glass and PCB respectively. The patterns were left to dry at room temperature (25  $^{\circ}\text{C}$ ). The images were automatically taken with the integrated monochrome camera on the system and later stitched to visualise the full samples. The scalebar in the image is 1 mm.

Making use of the room temperature drying and the printing conditions previously discussed, several square samples were created on both glass and PCBs to assess the range of usable resolution (Figure 108). On glass, the minimum drop overlap that results in a dense layer was 20 %, while in the epoxy fiberglass surface the drops spread less and a 30 % overlap was required for the same effect. Furthermore, due to the reduced spreading of the carbon paint previously reported and attributed to its complex rheology, the edges of the squares at medium overlap values were scalloped, which requires an increase in the drop overlap of 10 % on each material to hide the individual contribution of the drops.

Drying the samples at room temperature, even if the drying time is reduced to 2 minutes, slowed down the overall process considerably, especially when the required number of layers was increased. Furthermore, since the previous considerations for dryness were purely macroscopic, there is no guarantee that part of the solvent was not trapped between layers as the part is produced, which can decrease its overall conductivity. To this end, alternative forms of drying based on the application of IR and UV radiation were explored with promising initial results, since both lamps fully dried the samples under one minute. However, to relate the drying tests with the magnitude of interest and be sure

that the samples were fully dry, a series of experiments where the resistance of printed tracks was monitored in real time were conducted. Figure 109 shows the evolution of the resistance of the tracks over time while UV and IR radiation is applied to them at full lamp power and IR Set 24%, respectively, at a moving speed of the samples respect to the sources of 0.2 mm/s. A third set of samples were left to dry at room temperature ( $27 \pm 3$  °C) to compare its drying rate with the irradiated samples. These results show a clear reduction in both the required processing time and the final resistance obtained respect to the air-drying method. Both irradiation approaches show an abrupt reduction in the resistance after approximately 20 seconds, but it is likely that this trend is related with the limitations of the set-up in terms of the minimum voltage that is able to detect, which would result in a constantly high resistance until such potential falls enough to provide a good reading. Below the M $\Omega$  barrier, the data shows a considerable reduction in noise and present a clear descending trend that reaches a more stable section after 60 s, from where the resistance changes only slightly as the time continues.

To directly compare both radiation approaches, another set of experiments was conducted where the temperature instead of the resistance was monitored over time in the same thermal conditions, as it is displayed in the bottom part of Figure 109. This is not a comparison between the lamps themselves, since the distance to the samples and the used power settings are different, instead the interest is on their thermal behaviour. This revealed that the temperature response related with the UV lamp is faster and reaches a higher absolute value. Furthermore, the 3 tests resulted in very similar heating curves, which is not the case for the IR-lamp, which shows more variation. Thus, even though the samples were irradiated during a shorter time in the UV case, this radiation was absorbed more efficiently and resulted in a faster post-process and lower resistance. The UV-lamp also has the advantage of being self-cooled with an integrated fan and being mounted on the printing assembly rather than a separate structure, which also allows for real time drying. Consequently, this approach is selected as the ideal drying approach for the carbon paint for the rest of this work.

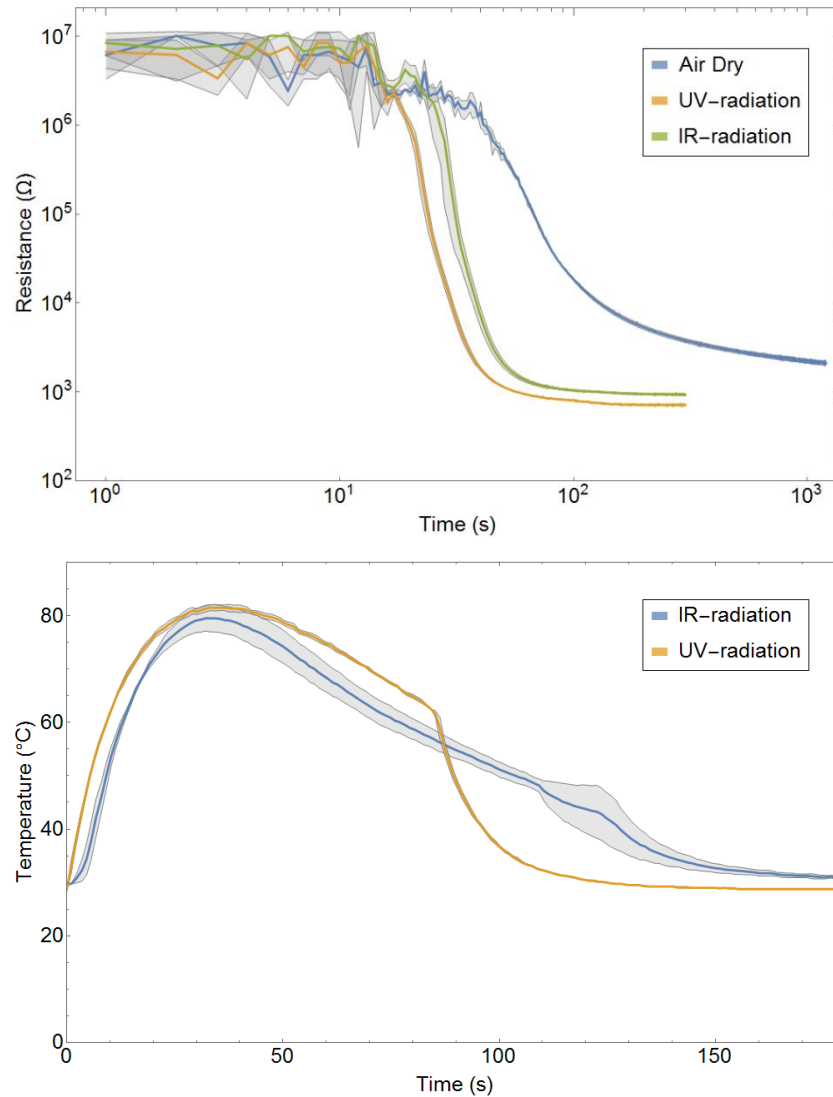


**Figure 109: Top)** IR-radiation at a power set of 24% (0.2 mm/s, 8 mm separation) and UV-radiation at full power (0.2 mm/s, 4 mm separation). The initial constant resistance of several  $\text{M}\Omega$  is attributed to limitations of the set-up in terms of voltage scale. **Bottom)** Temperature response over time in the same heating conditions than the real-time resistance experiment. The initial temperature is  $27 \pm 3^{\circ}\text{C}$ . In both cases the grey areas represent the standard deviation of each curve.

### 7.1.3 Sintering

Metallic inks require a sintering step to merge the constituent particles and thus create continuous pathways for the electric charges to flow. The degree of sintering, and therefore the final conductivity of the tracks, depends on numerous factors such as temperature, particle shape and size, surface additives adhered to the particles, and time (Hutchings & Martin 2012). More details about this process and alternative energy deposition methods were discussed in the literature review (section 2.1.1.2).

### 7.1.3.1 Hybrid Silver Paste

In the present work, the only material that requires sintering is the viscous silver paste. However, as it was discussed in the material selection section (4.2.5), this paste is a combination of silver nanoparticles dispersed in a solvent and a metallic salt that synthesises more nanoparticles in-situ when is heated above a thermal threshold. Therefore, for the first half of the post-processing stage, the volatile materials contained in the ink need to be eliminated via evaporation, while towards the end the energy is required to partially melt the nanoparticles to induce sintering. Nevertheless, the differences in its post-process do not change the way this fluid is jetted with the micro-dispensing valves (closing time: 0.30 ms, pressure: 0.1 MPa, temperature: 25 °C) and, consequently, a 2-dimensional resolution study (Figure 110) is performed on glass and epoxy fiberglass to find the appropriate drop overlap range. These experiments revealed that for both substrates, holes interrupt the printed films with overlaps below 20 % but scalloped edges are formed until overlaps of 40 %, which increase up to this value the optimal threshold if a criterion based purely on coverage is applied. However, when these samples were left to dry at  $25 \pm 5$  °C for 20 hours, the samples printed at higher resolutions displayed a cracked surface that in some cases had collapsed on their hollow core (Figure 110). When the glass slide was picked up from the machine and tap a few times on a solid surface, all samples with an overlap above 30 % were severely damaged. Similarly, when the surface of the samples was gently swiped with a dry foamtip cleaning swab, only the samples printed with a drop overlap of 10 % survived and even most of the individual drops without an overlap were detached. The poor adhesion and surface cracks of silver nanoparticle-based inks on glass have been widely reported (Hutchings & Martin 2012) (Sanchez-Romaguera et al. 2008) (Jang et al. 2008) and is typically attributed to solvent induced stresses and a mismatch between the thermal expansion of the silver films and the substrate material.

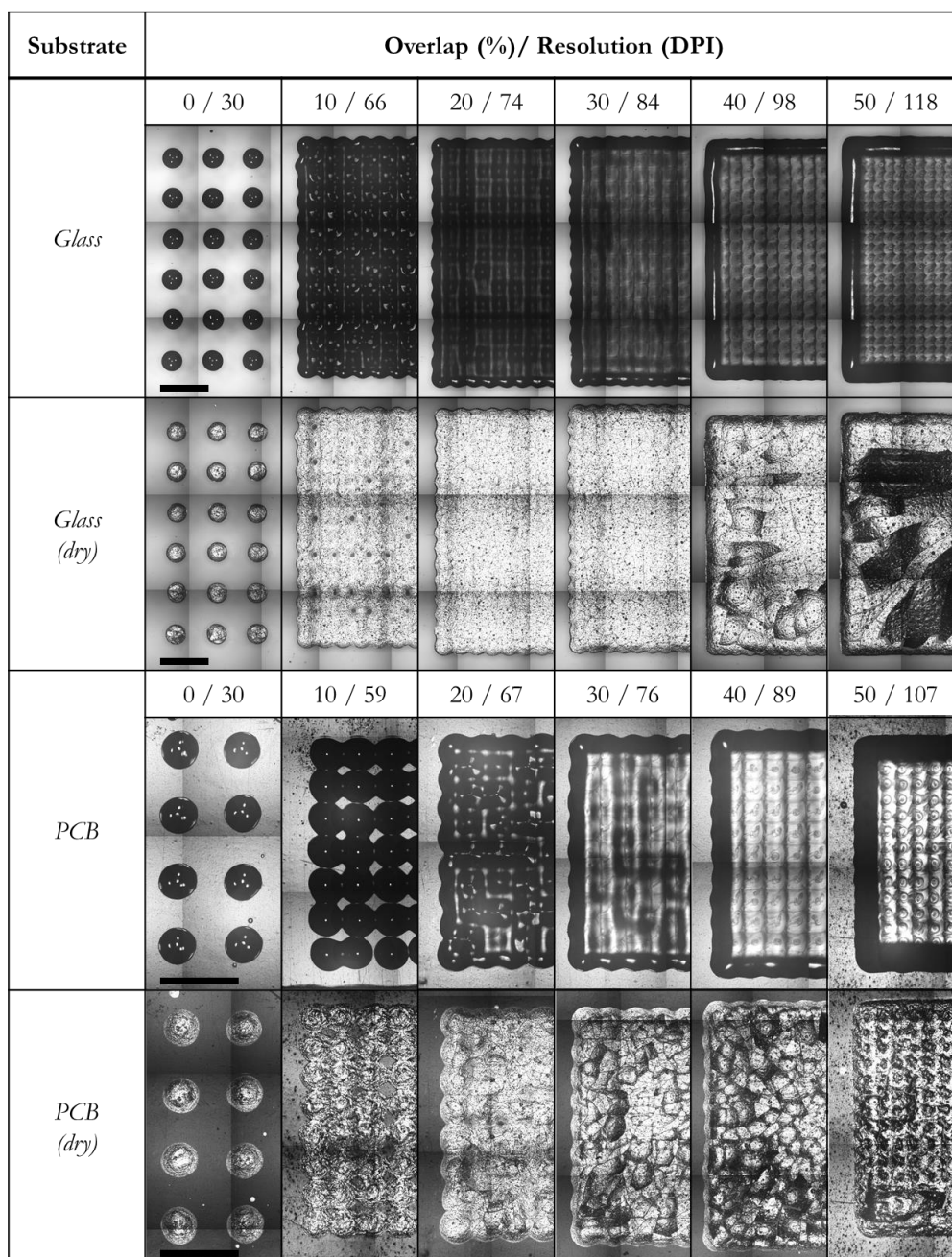


**Figure 110:** Square patterns printed with silver paste on a glass slide and an epoxy fiberglass board (PCB) testing different drop overlaps from 0 to 50 %. Individual drops display a diameter of 430  $\mu\text{m}$  and 475  $\mu\text{m}$  in glass and PCB respectively. The patterns were left to dry at room temperature ( $25 \pm 5 \text{ }^\circ\text{C}$ ) and photographed again after 20 hours. The images were automatically taken with the integrated monochrome camera on the system and later stitched to visualise the full samples. The scalebar in the image is 1 mm.

Another set of samples at drop overlaps (resolution) of 20 % (74 DPI) and 30 % (84 DPI) were printed on glass and post-treated under IR-radiation (Figure 111). Since the manufacturer of this silver paste recommends homogeneous heating up to 140  $^\circ\text{C}$  for 5 minutes to obtain the best results, the power of the IR-lamp was regulated to create 5 heating profiles spanning over such temperature.

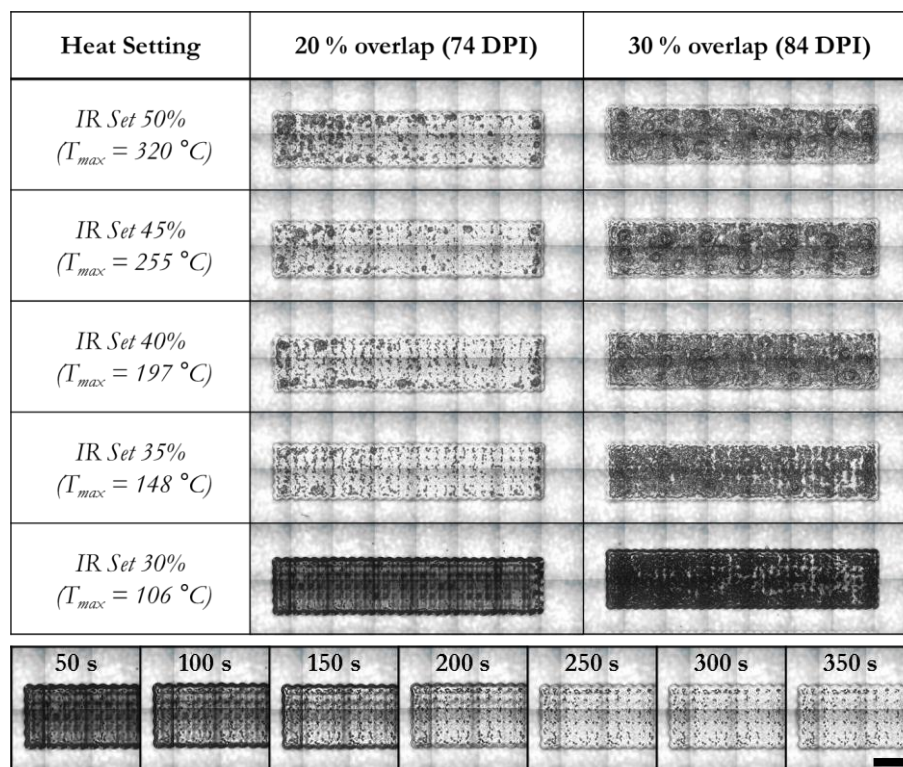


**Figure 11:** **Top)** Rectangular patterns (10 x 2 mm) of silver paste printed on a glass surface at 74 and 84 DPI. On the left column, the power settings of the IR-lamp and the estimated maximum temperature after 1 minute of treatment according with the calibration of the IR-lamp (Figure 48, Chapter 3) are given. The sample-lamp distance was set to 10 mm. The images were automatically taken with the integrated monochrome camera on the system and later stitched to visualise the full samples. **Bottom)** Left part of the sample printed at 74 DPI and treated with the IR Set 30% monitored after 7 consecutive heating cycles.

These images show rough surfaces of the silver patterns due to the violent bubble formation observed during the heat treatments. The bubbles left characteristic dark craters where they erupted from the fluid, as it has been seen in the literature for the same silver formulation (Pagudala 2012). It is expected that a fluid with lower viscosity would have been able to rearrange filling these holes, nevertheless the silver paste has a high viscosity that is increased during the evaporation of its solvents, which hinders any potential re-wetting. This hypothesis of the solvents boiling is not only backed by the visual observation of the event, but also agrees with the TGA information presented in Chapter 5 (Figure 66), where the silver paste was tested up until 800 °C. Then, an apparently double peak was identified in the DTG with maximums at 110 °C and 180 °C, which indicates the presence of more than one volatile species. The main solvent of this paste is  $\alpha$ -terpineol, which has a boiling temperature typically found between 218 – 221 °C (David R. Lide 2005), which can account for the main peak. The other volatile components are not identified due to the commercial nature of the material, but according with the TGA curve, one or more of them have a boiling temperature in the region of 110 °C, which agrees with the observed lack of violent boiling for the samples heated with the IR Set 30% that are

expected to reach a maximum temperature of 106 °C (calibration curve of the IR-lamp shown in Figure 48 (Chapter 3)). Consequently, this lower power setting was used until the images taken with the integrated monochrome camera showed a reflective surface, which is a sign of at least superficial drying (Figure 111). After 5 passes the surface of the track did not show further variation in its colour and displayed mild signs of bubbling.

From the images shown in Figure 111 it is also remarkable that the sample with a higher drop overlap displays increased roughness associated with boiling. This can be explained by the greater volume per unit area, which allows the formation of more and bigger vapour bubbles but presents approximately the same surface for them to escape the fluid. Consequently, even lower overlaps should be used to reduce the overall thickness of the films and reduce the effect of the solvent's boiling, which agrees with the technical information provided by the manufacturer that recommends a thickness of 1 – 2  $\mu\text{m}$  (InkTec Company Limited 2013). However, as it was shown in Figure 110, a lower drop overlap would result in holes in the films, which would compromise their conductivity. Therefore, for this material the resolution criterion based solely on the evaluation of the coverage and edge definition is not valid and the control of the boiling of the solvents has to be taken into account.

To select the appropriate time and power setting for the IR-lamp in terms of the final conductivity of the samples, an experiment where the resistance of the printed tracks is monitored in real time during the sintering step is performed (Figure 113). A separate set of experiments was carried out where the temperature is recorded instead in identical thermal conditions (Figure 113). These experiments reveal similar parabolic temperature curves for all settings, with a peak of maximum temperature registered when the sample is right below the IR-lamp. The temperature peaks are linearly proportional with the power applied to the IR-lamp, as it is expected since no other parameter is varied. The parabolic curves are truncated at the moment when the lamp is turned off, accelerating the cooling rate of the sample from that moment onward. The effect of these thermal profiles on the silver paste is a clear trend of reduced final resistance and time as the energy density is increased, which suggests an increasing percentage of sintering of the nanoparticles contained in the material at higher temperatures. This was in principle not expected, since at least the 2 more powerful heat treatments were considered to fulfil the recommended conditions of this material for full sintering, 140 °C for 5 minutes (InkTec Company Limited 2013). However, even though the IR-lamp reaches high temperatures quickly (Figure 48), the scanning approach used here reduces the time that the sample experiences

a temperature above 140 °C. Specifically, the IR setting at 27 % does provide approximately 5 minutes of suitable sintering conditions while the setting at 24 % operates only around 2.5 minutes in the desired range, this could explain the difference observed in the tracks treated with this profile. Similarly, the IR power profile at 22 % does not provide enough energy to sinter completely the nanoparticles but it is likely that partial sintering is initiated. Furthermore, evaporation was completed, which eliminates non-conductive elements from the material and facilitate charge transport. Evaporation was not completed for a power setting of 20 % at 0.05 mm/s, so the scanning speed was reduced to 0.025 mm/s, increasing the total time of the treatment. This, however, permitted evaporation and allowed the sample's surface to turn from grey to a highly reflective silvery appearance. Moreover, it reduced the tracks' resistance close to 3  $\Omega$  after 10 minutes of treatment, which indicates the beginning of the sintering process. These samples, however, did not display the characteristic craters on the surface previously associated with bubble escaping from the surface of the fluid (Figure 112). Conversely, all 3 higher thermal settings showed increasingly rough surfaces due to boiling, which once again agrees with the peaks observed at 110 °C and 180 °C in the thermogravimetric derivative study previously performed on the fluid (Figure 66). This establishes a trade-off between the surface finish of the printed samples, the sintering time and the final resistance obtained. In particular, low energy density delivered to the sample would result in smoother surfaces but requires longer processing and yields lower electric performance, while higher thermal settings lead to quicker silver conversion (below 2 minutes per layer) and minimum resistance, but rough surfaces are obtained due to vapour bubbles scaping the interface. The bubbles could potentially disrupt thin tracks if a hole bigger than its width occurs, however, since the process relevant to this work is based on the deposition of multiple layers of material and is unlikely that two consecutive films display holes in the same position, the likelihood of a broken track due to the observed boiling is low.

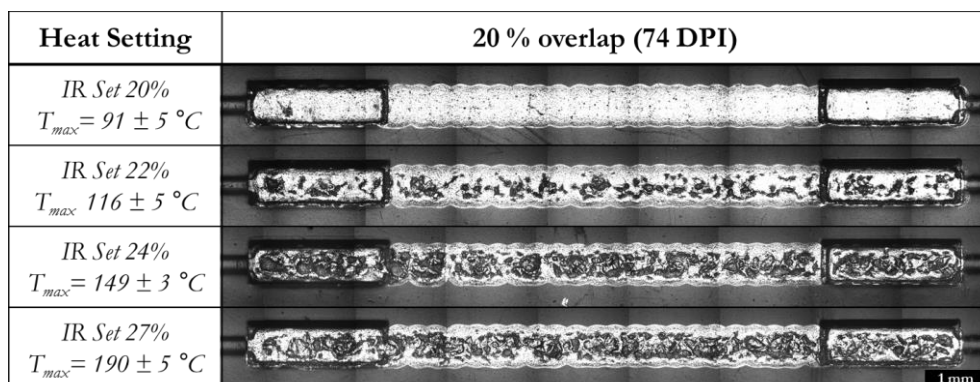


**Figure 112: Exemplar tracks of silver paste dried and sintered at different IR power settings** at 0.05 mm/s (except IR Set 20%, which is 0.025 mm/s), 8 mm of distance between the lamp and the samples. The tracks display an increasing presence of dark craters due to the boiling of the volatile elements at high temperatures. The scale bar is 1 mm.

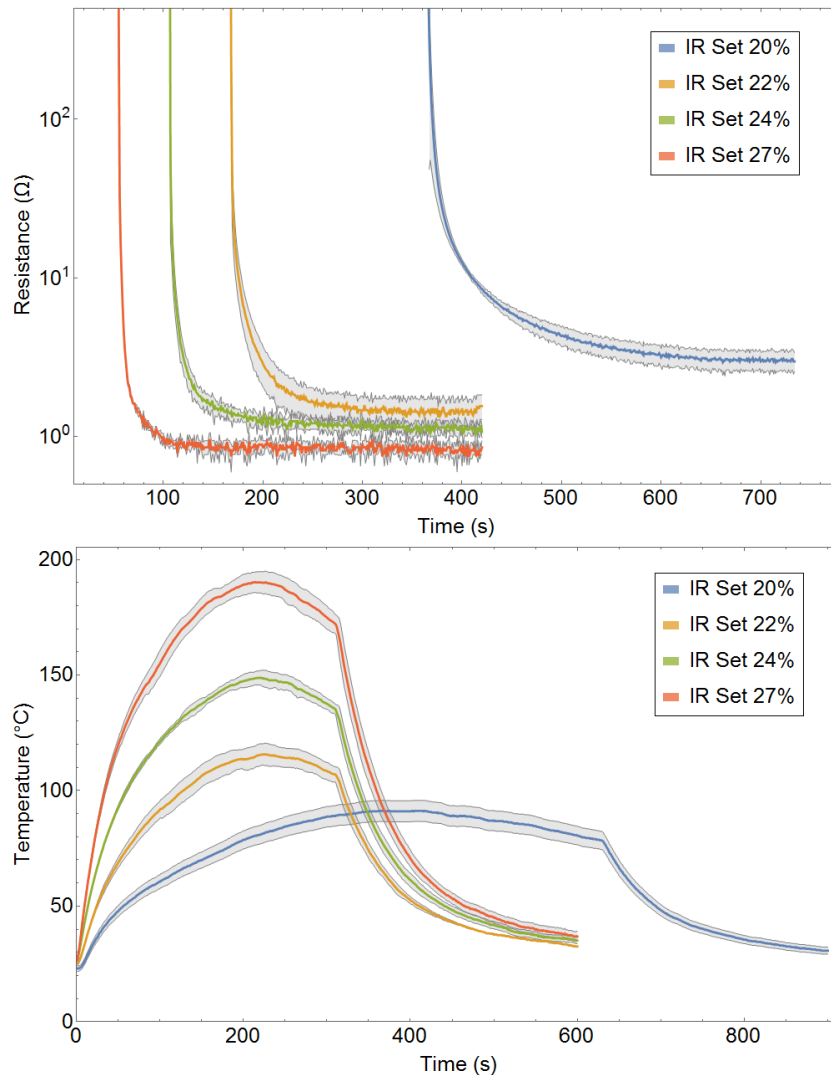


**Figure 113: Top)** Average resistance in real time of 4 sets of 0.5x12 mm silver tracks (74 DPI) being sintered at 0.05 mm/s (except IR Set 20%, which is 0.025 mm/s), 8 mm of distance between the lamp and the samples and different IR power settings between 20 and 27 % of its full capability. **Bottom)** Temperature response over time in the same heating conditions than the real-time resistance experiment. The initial temperature is  $27 \pm 3$  °C. In both cases the grey areas represent the standard deviation of each curve.

#### 7.1.4 Conclusions of the 2-dimensional tests

In this section, several resolution tests were carried out to find the optimal range of drop overlapping resulting in good edge definition and full internal coverage of the films. Despite the differences of the material properties, surface roughness and drop wetting diameter, the **ideal overlap** from a coverage point of view was found between 30 % and 50 % in all cases. This observation agrees with other resolution tests for inkjet printing performed by other authors once their results are adapted from drop spacing to drop percentage of overlap. For instance, Sanchez-Romaguera *et al.* (Sanchez-Romaguera *et al.* 2008) reported that drop overlaps between 0 % and 22 % (45 and 35  $\mu\text{m}$  drop spacing for 45  $\mu\text{m}$  drops) resulted in scalloped edges, while overlaps between 33 and 56 % (30 and 20  $\mu\text{m}$  drop spacing for 45  $\mu\text{m}$  drops) resulted in tracks with good definition when printing

an epoxy insulator on glass for printed electronic applications. Similarly, Ibrahim *et al.* (Ibrahim et al. 2006) found that the ideal spacing for a commercial ink yielding drops with an average diameter of 55  $\mu\text{m}$  was 35  $\mu\text{m}$ , which corresponds to a drop overlap of 36%.

However, the common overlap range follows a purely geometric criterion based on fluid coverage. This neglects the effects that the different post-treatments required to solidify the deposited materials have on the samples when a wet-on-dry approach is followed and each layer is cured before the next can be dispensed. Thus, the three different solidification mechanisms required by the materials used in this work were studied along with the resolution to find an equilibrium between pattern fidelity and functionality. In the case of **UV-curing**, two strategies were investigated: curing after each layer is finished and curing during printing. The former was identified as the suitable option for viscous fluids with slow spreading that are capable of retaining the printed shape until they are pinned down by UV radiation, as it is the case for the stereolithographic resin tested in this work. This approach resulted in smoother surfaces without internal interfaces at the expense of resolution, especially on sharp corners. However, curing the full layer at the end reduces the amount of energy delivered to the sample and it does it in a more homogeneous way compared with real time curing, where the lamp is illuminating the printed dots continuously and the first drops are much more irradiated than the last. For low viscosity photocurable materials like TPGDA, curing in real time is a more appropriate option to stop the fluid spreading as soon as possible. The samples cured in this way usually present visible interfaces between different print swaths or columns, but this is compensated in the case of TPGDA by a much smaller drop size compared with the UV-resin. This increased spatial resolution is the reason why TPGDA is used from this point onwards in this work, since a smaller minimum building block is an attractive property for a structural material.

**Solvent evaporation** was tested for an aqueous dispersion of PEDOT:PSS and a carbon paint, both in ambient conditions and delivering energy to speed the process. In all cases the printing platform was kept at 25 °C to reduce the number of variables. It is known that the heat of the platform can help tuning the spreading of the materials (Soltman & Subramanian 2008) but it can also introduce thermal gradients on the z-direction in parts of inhomogeneous thickness. Thus, any radiation was applied always from the top at a constant distance, to treat each layer as repeatable as possible.

PEDOT:PSS displayed greater wetting on glass than the paint, but once the fluid settled it did not spread more under IR radiation nor showed signs of boiling, so the resolution selected for this material agrees with the coverage criterion previously mentioned. The IR-lamp was used to evaporate the solvents in approximately 100 s reaching temperatures close to 100 °C. The processing time could be potentially reduced by increasing the temperature further, however, since the solvent is mostly water, temperatures above 100 °C combined with thick fluid films could result in violent boiling that can disrupt the surface of the material, as it was observed in the case of the silver paste.

Real time measurements of the resistance during thermal treatment were not possible due to the poor wetting of the PEDOT:PSS on the PCBs and the fact that the thin films resulting after drying were of the same order of magnitude that some surface features, causing uncontrollable track interruptions. The obtained PEDOT:PSS samples are moderately conductive, flexible and transparent. The last property is related with layer thickness (Kirchmeyer & Reuter 2005), which in turn depends on the printing resolution. However, since modifying that would result in a variation in the resistance of the layer, this cannot be generally optimised and further experiments are required for particular applications.

The main difference in the case of the carbon paint was that the drying in ambient conditions was much quicker and consequently was initially considered a valid treatment. Later experiments based on real time monitoring of the resistance demonstrated that this evaporation method was slower and more inefficient than initially thought. Alternatively, both IR and UV radiation were successfully used to accelerate the evaporation rate, reducing the required time to approximately 60 s. Even though the heating profile and final resistance of both tested processes were comparable, UV radiation showed faster reaction times and a more repeatable behaviour. This was attributed both to the LED nature of the source's elements compared with the incandescent filament on the IR and the built-in cooling system on the ultraviolet lamp, which provides a more stable output. Another advantage of the UV approach is the placement of the lamp on the printing assembly rather than in a separate structure, this would allow for a continuous radiation treatment during printing similar to the one used to cure the TPGDA. Ultimately, the decision of one lamp or the other is closely related to the material to be heated and its

surroundings, since an ideal process would be one where the sample has a high absorbance of the emitted wavelength while the rest of involved materials remain unaffected.

Solvent evaporation is also a crucial part of the processing of the silver paste, but in this case, it is accompanied by the in-situ chemical conversion of the silver complex into nanoparticles and the sintering of said particles to create continuous charge paths. Tests under different thermal settings were performed and the violent boiling of the volatile elements contained in the silver paste at high temperatures was identified as the main weakness of the process, since it results in rough and irregular surfaces. This agrees with the study of Pagudala (Pagudala 2012), where the same silver paste (TEC-PA-010, Inktec) was used in a screen printing process yielding an average solid thickness of 3  $\mu\text{m}$ . The bubbles' distinctive craters were noticeably reduced if the temperature was kept below approximately 110  $^{\circ}\text{C}$ , which corresponds with the beginning of the combined peak observed on the thermogravimetric derivative curve of the material (Figure 66). Another resolution experiment was performed involving IR power settings between 30 % and 50 % (at a sample-lamp distance of 10 mm) and drop overlaps of 20 % and 30 %. This test showed a dependency of the boiling surface marks with the resolution, which was interpreted as a dependency with the wet film's thickness. Specifically at higher drop overlap the volume per surface ratio increases which decreases the evaporation rate but favours the creation of bubbles that travel towards the interface to escape, leaving the characteristic craters. Low viscosity fluids would re-fill the holes quickly, but the viscosity of the material at this point is high due to the increased solid fraction, resulting in permanent marks. Therefore, this process imposes a trade-off on the resolution of printed samples, since high drop overlaps result in improved edge definition but poor surface finish and vice versa.

To study the effects of different thermal settings on the final resistance of the printed samples and their processing time, an experiment recording the resistance of the samples in real time, like the one performed for the carbon paint, was carried out. These experiments revealed an inverse relation between the temperature of the samples and the required processing. However, an increase in energy density also increments the boiling marks on the surface. More relevant is the observed dependency of the final resistance with the applied heat, which did not reach a minimum for the 4 heating profiles tested. This indicates that only partial sintering is achieved for the tested configurations, which makes sense if the parabolic thermal profiles measured are compared with the recommended conditions for full sintering (140  $^{\circ}\text{C}$  for 5 minutes)(InkTec Company

Limited 2013), since only during part of the cycle the temperature is above the proposed threshold. This could be improved by slower movement of the sample respect to the lamp, but not only it would increase the length of the process but also would result in higher maximum temperatures, which is likely to increase the presence of boiling marks. Nevertheless, IR Set 27 % with 8 mm between the lamp and the samples and a scanning speed of 0.2 mm/s resulted in silver patterns with rough but continuous surfaces and low resistances and therefore is selected as the ideal post-processing conditions for this paste.

Finally, it is worth reflecting on the usefulness of the experiments recording the **resistance in real time** while different forms of post-processing were applied. This allows for optimization of the thermal conditions based on the real outcome of the main functional property of these materials, their electric resistance. The test is quick, partially integrated in the system and can potentially be operated in conjunction with other sub-systems such as the monochrome cameras to assess shape and colour changes in real time. In future iterations of the system this optical capability could be used to complement or substitute entirely the resistance measurements, since the colour change of the samples has been successfully used in the literature as an indicator of electronic performance of silver-based inks (Cherrington et al. 2012).

## 7.2 3D-tests: Layer thickness and resistivity

Since AM technologies follow a layer-by-layer approach, the properties of the final part depend on the individual characteristics of these films. The effects of printing resolution and post-processing conditions on the general shape and coverage of the layers were studied in the previous section. These tests allowed for the fabrication of repeatable and fully dense 2-dimensional patterns that displayed functional properties such as electric conductivity. However, to create a 3D object a stack of such layers is required, and their properties in the z-axis become relevant. For instance, the thickness of the processed layers not only determines the resolution in that direction but also the processing time and energy consumption, since the thinner the layers the more of them are required to be printed and treated. Therefore, a trade-off needs to be found to obtain objects with enough vertical detail in a reasonable amount of time. This is a limitation of inkjet and transfer printing methods, which typically result in solid thicknesses of a few microns and require more passes than a screen printing process that can deposit films in the range of 100  $\mu\text{m}$  in one cycle (Suganuma 2014). In fact, the high viscosity and non-Newtonian nature of the fluids used in screen printing, not only allow higher aspect ratio of the produced features but also a good shape retention during processing, which is the reason why this technique is widely

used in industry to create dense flat patterns. Furthermore, increased film thickness is an advantage for the deposition of conductive materials, since the resistance of the printed tracks is inversely proportional to their cross-sectional area (equation 49) and, consequently, less layers are required to fulfil a particular functional requirement.

In this section, various multi-layered structures are created according with the processing parameters selected from previous experiments and 3D-scanned to study the layer thickness of each material. This information is used in a later section to create multi-material structures by compensating the layer thickness miss-match between different materials. Furthermore, the cross-sectional area obtained from the scans of the tracks is used in combination with their measured resistance to obtain the electric resistivity of each conductive material under the used processing conditions.

### 7.2.1 Layer thickness

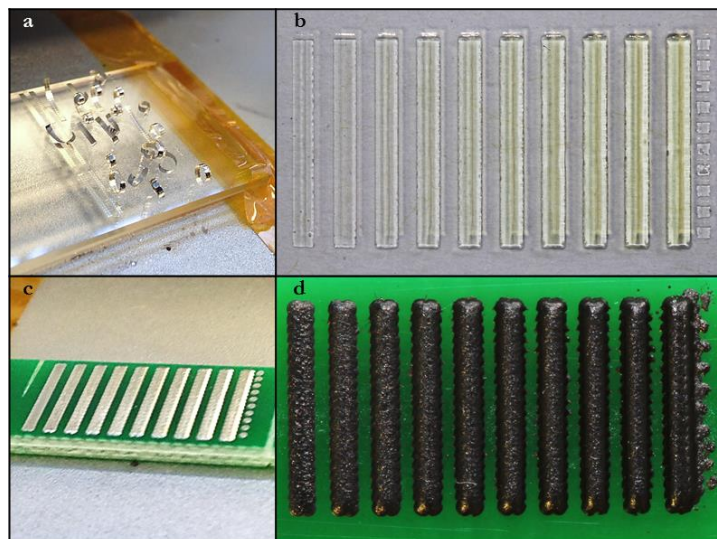


**Figure 114:** Multi-layered tracks printed on glass slides and epoxy fiberglass substrates. The number of layers goes from 1 (left) to 10 (right) in all samples. **a)** Silver paste printed and sintered on glass, displaying delamination due to poor adhesion to the substrate. **b)** TPGDA printed on glass, showing an increasing yellow tint with the number of layers. **c)** Silver paste successfully printed and post-treated in an epoxy fiberglass board of 1.5 mm thickness. **d)** Carbon paint printed on epoxy fiberglass and dried via UV-radiation.

Samples with several tracks of an increasing number of layers were printed and post-treated according to the optimum settings previously found on polycarbonate, glass and epoxy fiberglass substrates (Figure 114). Specifically, glass slides were used for TPGDA, carbon paint and PEDOT:PSS with good results. Silver was also tested on this substrate but the poor adhesion of the solid silver to the glass and the thermal tension on the track's surface resulted in detached curled structures (Figure 114). The weak adhesion of printed silver to glass is a known issue that is typically overcome by adding other materials to the formulation, such as resins and polymers to increase the interaction with

the substrates (C. Yang et al. 2013). Since one of the objectives of this work is to use the materials without modification, the silver paste was printed on epoxy fiberglass boards instead (Figure 114), which allowed the completion of the multi-layered test structures. The carbon paint and TPGDA were also printed on the epoxy boards to compare their behaviour in different substrates. This will be relevant for the multi-material structures produced in the last section of this chapter, where silver, carbon and TPGDA are printed on PCBs. The UV-resin was tested in an early experiment on polycarbonate (PC) films at 2 different curing speeds (6 and 150 mm/s) (Appendix A1). This experiment, however, was not repeated in glass because by this time the TPGDA had successfully being used as a structural material instead of the stereolithographic resin due to its higher resolution in the z-direction. Nevertheless, the results obtained on PC films are included in the combined height vs. number of layers curve shown in Figure 115 and its fit parameters table (Table 11) for comparative reasons.

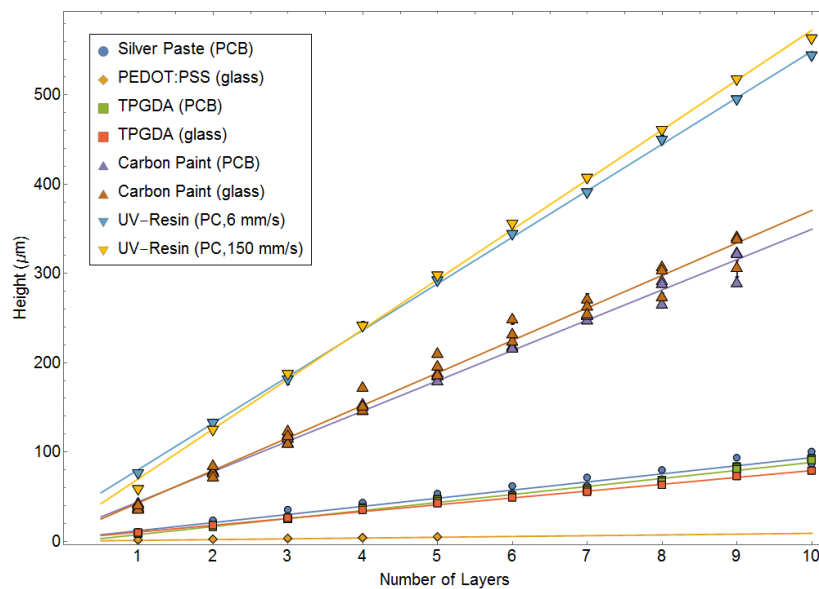


**Figure 115:** Samples' height obtained via 3D-scan (optical profilometry for all samples except UV-resin, that was characterised by contact profilometer) compared with their number of layers. The terms in parenthesis denote the substrate and the scan speed in the case of the stereolithographic resin. The lines are linear regressions whose fit parameters are shown in Table 11.

In both Figure 115 and Table 11 a high linearity of the growth of all the samples with increased number of layers is observed. This is crucial for the representation of 3-dimensional objects and is a result of efficient post-process conditions that do not allow excessive lateral spreading or fluid transport between consecutive layers. It is therefore possible to assume that this trend would continue and provides confidence to the values of the layer thickness obtained from the linear regression of the data. Similarly, the intercepts of these linear fits are close to zero in most cases, which further reinforces the

selection of a linear model to describe this data. Nevertheless, the observed deviations can be explained in terms of the variations between samples, the imperfections of the substrates (particularly relevant for the epoxy fiberglass boards) and the distinct wettability of the first few layers compared with the rest. The intercepts associated with the UV-resin are particularly high, which may be explained by the fact that the polycarbonate substrates were flexible films that can be deformed during the curing process and the profilometry measurement, causing a shift of the baseline. This, however, is not expected to affect significantly to the obtained thickness, since this is calculated from the slope of the linear trend.

**Table 11:** Linear regression fitting parameters ( $\pm$  standard error) of the height vs. number of layers data (Figure 115).

Sample	Substrate	Post-process	Layer thickness ( $\mu\text{m}$ )	Intercept ( $\mu\text{m}$ )	Adjusted $r^2$
<i>Silver Paste</i>	Glass	IR Set 27%, 0.2 mm/s	$9.1 \pm 0.4$	$3 \pm 2$	0.967
<i>Carbon Paint</i>	Glass	UV, 0.2 mm/s	$36.4 \pm 0.9$	$7 \pm 5$	0.985
<i>Carbon Paint</i>	Epoxy Fiberglass	UV, 0.2 mm/s	$33.9 \pm 0.6$	$10 \pm 3$	0.993
<i>UV-Resin</i>	Polycarbonate	UV, 6 mm/s	$52.1 \pm 0.4$	$28 \pm 3$	0.999
<i>UV-Resin</i>	Polycarbonate	UV, 150 mm/s	$55.9 \pm 0.7$	$14 \pm 4$	0.998
<i>PEDOT:PSS</i>	Glass	IR Set 34%, 0.1 mm/s	$0.875 \pm 0.013$	$0.09 \pm 0.04$	0.997
<i>TPGDA</i>	Glass	UV, real time	$7.66 \pm 0.12$	$2.6 \pm 0.7$	0.998
<i>TPGDA</i>	Epoxy Fiberglass	UV, real time	$8.97 \pm 0.17$	$-1.5 \pm 1.1$	0.989

In terms of the thickness of these solid films, the first notable result is that the measured height for glass and PCB substrates is comparable for the 2 materials that were printed in both surfaces (TPGDA and carbon paint), where the difference between both substrates was within  $3 \mu\text{m}$  in both cases. This variation is more relevant for the TPGDA than for the carbon due to its overall thinner layers, but it is a promising result that points towards minimum variation of the printed results in different substrates. The increased dependency on the substrate for the TPGDA in relation with the carbon paint is attributed to their different rheology, both in terms of absolute viscosity (remarkably lower for TPGDA) and internal microstructure. The absolute layer thickness obtained for the measured materials varies from  $0.875 \pm 0.013 \mu\text{m}$  for the aqueous dispersion of PEDOT:PSS on glass to  $55.9 \pm 0.7 \mu\text{m}$  for the UV-resin on polycarbonate film UV-cured at the fastest setting. The fact that the minimum thickness is obtained for PEDOT:PSS despite being printed with the micro-dispensing valve with drops of approximately 5 nl (Figure 98) indicates that the solid content of the fluid played a larger role than the volume deposited. In particular, from Table 7 and Figure 65, a solid content at 250 °C of 2.6 wt%

is observed, which means that most of the fluid is evaporated at the end of the thermal cycle, leaving a thin film of PEDOT:PSS nanoparticles behind. Similarly, the solid residue at 250 °C for the silver paste and the carbon paint is 59.5 wt% and 52.3 wt%, respectively. At first glance, these comparable values do not seem to explain the difference in layer thickness observed for these materials, especially considering that they too were printed with the micro-dispensing valve in similar drops of approximately 5 nl. However, once the density of pure silver (10.5 g/cm<sup>3</sup>), graphite (2.2 g/cm<sup>3</sup>) and gum arabic (1.4 g/cm<sup>3</sup>) are considered (David R. Lide 2005), the difference in thickness can be explained as a result of volumetric shrinkage. Both photopolymers showed in previous experiments that their mass loss below 300 °C was lower than 5 wt% (Figure 67), which agrees with the negligible expected evaporation and volumetric shrinkage. Thus, the difference in layer thickness for these materials is directly proportional with their printing resolution and the volume of each drop, which in the case of the UV-resin would be again close to 5 nl while the TPGDA drops were observed to be near 30 pl. The fact that the drops of UV-resin were as big as for the other viscous fluids together with the absence of volatile species on the fluid explains the highest thickness observed for this material.

### 7.2.2 *Electrical performance*

#### **PEDOT:PSS**

The aqueous dispersion of PEDOT:PSS was printed on glass, treated with IR radiation (IR Set 34%, 0.1 mm/s) and scanned to obtain the cross-sectional area of the tracks, which proved to be linear with the number of layers (Figure 116). The inverse of the area was plotted against the measured resistance of the tracks to obtain another linear plot, from which the electric resistivity is calculated by dividing the slope term ( $0.97 \pm 0.04 \text{ } \Omega \text{ mm}^2$ ) by the length of the tracks ( $6.3 \pm 0.2 \text{ mm}$ ), following equation 49, obtaining  $(1.54 \pm 0.08) \cdot 10^{-4} \text{ } \Omega \text{ m}$ . This result is contained within the  $10^2 - 10^{-5} \text{ } \Omega \text{ m}$  range of commercially available PEDOT:PSS dispersions (Gaiser 2013). More specifically, the manufacturer provides a sheet resistance of 700  $\Omega$ /square (Heraeus 2010) for the formulation used in this work (Clevios S V3), but no test thickness is provided, which hinders the comparison with the obtained result. Thus, based on the experiments shown in Table 11, a dry thickness between 0.1 and 10  $\mu\text{m}$  is assumed, which results in an expected range for the electric resistivity of  $7 \cdot (10^{-5} - 10^{-3}) \text{ } \Omega \text{ m}$ , compatible with the measured value. Furthermore, the same formulation of PEDOT:PSS was used in the literature to study ways of improving the conductivity of conductive polymers by adding different conductive additives (Dilfer

& Schmitt 2012). Their results for unaltered PEDOT:PSS deposited as wet films thinner than  $1\ \mu\text{m}$  via offset printing on PET flexible films show resistivity values as low as  $10^{-3}\ \Omega\ \text{m}$  after drying the samples at  $100\ ^\circ\text{C}$  for 5 min. These values are compatible with both the range previously estimated based on the manufacturer specifications and the result obtained for the conductive polymer in this work.

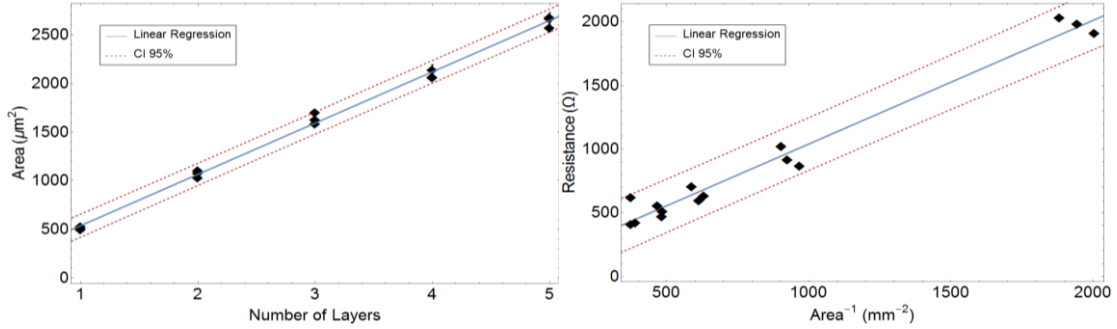


**Figure 116:** Data obtained via Point Autofocus profilometry for an aqueous dispersion of PEDOT:PSS printed on glass and dried by IR-radiation. The blue line shows the linear regression fit while the red dashed lines indicate the 95% Confidence Interval. **Left)** Area of the tracks in relation with their number of layers ( $A_{\text{layer}} = 527 \pm 9\ \mu\text{m}^2/\text{layer}$ ). **Right)** Measured resistance vs. the inverse of the cross-sectional area to calculate the electrical resistivity from the slope ( $\rho_r = (1.54 \pm 0.08) \cdot 10^{-4}\ \Omega\ \text{m}$ ).

### Carbon Paint

The area evolution of carbon tracks with the number of layers and their measured resistance are shown in Figure 117, where linear trends are observed for both experiments irrespectively of the substrate. As expected, the section area per layer is very close for both glass and epoxy boards, since the volume of the drops, printing resolution and solid content of the paint are the same in both scenarios. This result, together with the measured height per layer for both substrates (Table 11), agrees with the observed geometric similarity of the samples printed on the 2 materials. However, this geometric correspondence results in different values for the electric resistivity (Glass:  $(3.7 \pm 0.5) \cdot 10^{-3}\ \Omega\ \text{m}$ , Epoxy Fiberglass:  $(6.0 \pm 0.6) \cdot 10^{-3}\ \Omega\ \text{m}$ ), that although are comparable, seem to indicate that the difference in thickness, composition and roughness of the substrates play a role in the final resistance of the tracks. To confirm this observation, however, a thorough characterisation of the geometric and thermal properties of both substrates would be required, which is outside of the scope of this work. Alternatively, a similar experiment was performed by printing 3-layered carbon tracks directly onto PCBs, to compare their cross-section to the measured resistance between the pre-existing copper pads. This approach ensured repeatability in the length of the tested conductors and prevented the samples to be damaged during the repeated contact of the LCR-meter's probes. Histograms showing the resistance and cross-sectional area of different points of these

transversal tracks are displayed in Figure 118. Both quantities were then used in equation 49 to obtain a resistivity of  $(5.3 \pm 0.2) \cdot 10^{-3} \Omega \text{ m}$ , which is in good agreement with the result calculated from the previous multi-layered experiment on the same substrate.

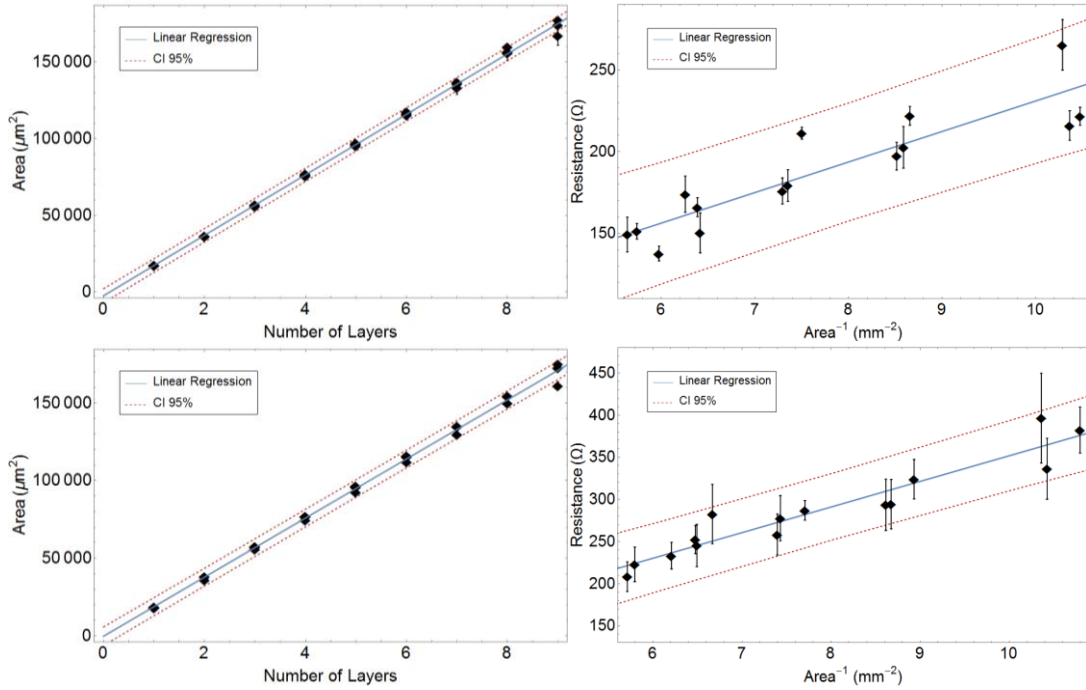


**Figure 117:** Data obtained via Point Autofocus profilometry for carbon paint printed on glass (**top**) and epoxy fiberglass boards (**bottom**). The length of the tracks is  $5.1 \pm 0.2 \text{ mm}$ . The evaporation of the solvent was accelerated by UV-radiation. The blue lines show the linear regression fits while the red dashed lines indicate the 95% Confidence Interval. **Left)** Area of the tracks in relation with their number of layers (Glass:  $A_{\text{layer}} = 19730 \pm 150 \mu\text{m}^2/\text{layer}$ , Epoxy Fiberglass:  $A_{\text{layer}} = 19000 \pm 200 \mu\text{m}^2/\text{layer}$ ). **Right)** Measured resistance vs. the inverse of the cross-sectional area to calculate the electrical resistivity from the slope (Glass:  $\rho_r = (3.7 \pm 0.5) \cdot 10^{-3} \Omega \text{ m}$ , Epoxy Fiberglass:  $\rho_r = (6.0 \pm 0.6) \cdot 10^{-3} \Omega \text{ m}$ ).

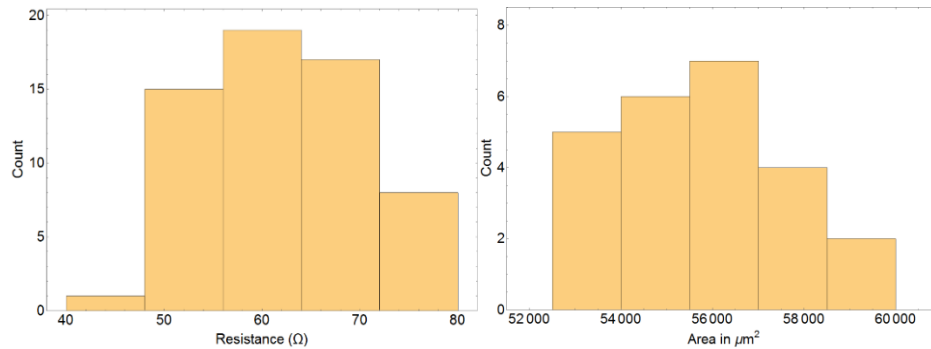


**Figure 118:** Histograms from the measurement of the resistance (**left**) and cross-sectional area (**right**) of 3-layered carbon tracks printed between the copper pads of a PCB. The average ( $\pm$  standard deviation) resistance is  $62 \pm 8 \Omega$ , while the area is  $55600 \pm 1900 \mu\text{m}^2$ . This results in an electric resistivity of  $(5.3 \pm 0.2) \cdot 10^{-3} \Omega \text{ m}$ .

The results obtained in the 3 experiments compare well with the expected resistivity of the material ( $2.75 \cdot 10^{-3} \Omega \text{ m}$ ) (Bare Conductive Ltd 2016). These results are an order of magnitude lower than the observed electric resistivity for the carbon paint in early experiments (Appendix A1), which was  $(1.2 \pm 0.5) \cdot 10^{-2} \Omega \text{ m}$ . This experiment was performed on a different substrate (polycarbonate films) with different track sizes and scanned with a contact profilometer rather than a Point Autofocus instrument, which can

account for part of the observed differences. Nevertheless, the main difference between both processes was the post-processing applied to the printed samples, since in the early attempts the tracks were allowed to dry in ambient conditions for 5 minutes instead of applying UV-radiation to speed up the evaporation. This difference in the thermal conditions during the solvent evaporation stage have already proved to cause an order of magnitude difference in the resistance of the treated tracks in the same amount of time (Figure 109), despite of the dry appearance of the samples after just 1-2 minutes (Figure 107). Thus, it is possible that part of the solvent was not completely evaporated during the post-processing of each layer, trapping part of it inside the sample when the next layer was deposited. This would result in pockets of fluid sample or hollow porous depending on the thickness and diffusion ability of the solid shells, but would explain the reduced electric resistivity and increased layer thickness observed for the samples dried in ambient conditions (Appendix A1). To validate this hypothesis, characterisation experiments of the microstructure of the tracks' cross-section via Scanning Electron Microscopy or Atomic Force Microscopy would be required, which are outside of the scope of this work. Nevertheless, a UV-radiation treatment has been identified as the most efficient post-treatment for the carbon paint, resulting in fully-dried conductive samples with a linear growth in the z-direction as new layers are deposited.

### **Silver paste**

Silver multi-layered samples were created on epoxy fiberglass only, since the sintered metal demonstrated poor adhesion to the smooth surface of glass. The marginally improved adhesion to the PCBs, however, did not stop the samples from breaking under minimal interaction, which severely affected the repeatability of the experiments involving this material. An example of this is found on the evolution of the 3 multi-layered samples printed and post-treated to assess their growth in the z-direction and resistivity. One of the tracks fractured during the set-up of the profilometer and another during the resistance characterisation due to the contact with the LCR-meter's probes. These tracks could have been replicated but restrictions on the equipment availability prevented their 3D-scan within the time-frame of the project. Furthermore, without modification of either the material or the epoxy fiberglass surface, the same fragile samples are expected. Despite these setbacks, the resistance of the remaining track was compared to the average cross-section area (Figure 119) to obtain an electric resistivity of  $(4.7 \pm 0.7) \cdot 10^{-7} \Omega \text{ m}$ . To validate this result, longer tracks printed perpendicularly to the copper pads of a PCB were created and sintered accordingly, as it was previously successfully done for the carbon paint. These allow easy access to the tracks via pre-existing conductive tracks, which prevent the direct interaction between the probes and the samples. This experiment was also used to compare

the sintering step performed via IR-radiation (IR Set 27%, 0.2 mm/s) directly on the printing system with the oven conditions (140 °C, 12 min) recommended by the silver paste's manufacturer. Histograms showing the resistance and cross-sectional area of different points of these transversal tracks sintered by the 2 proposed methods are displayed in Figure 120.

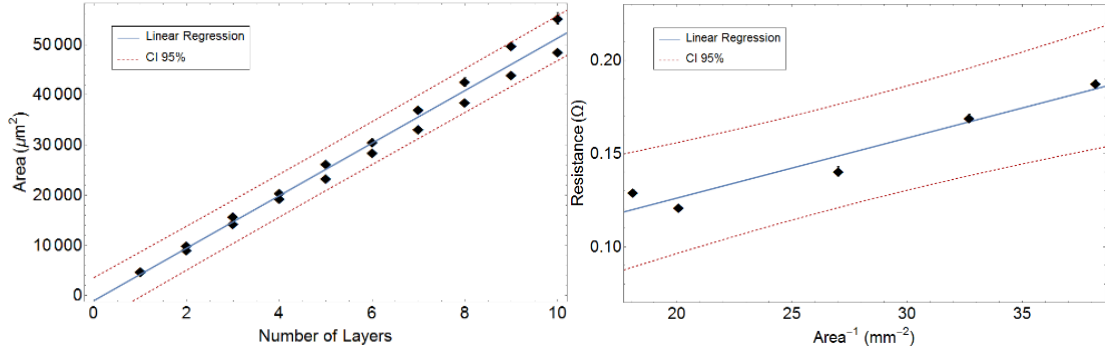


**Figure 119:** Data obtained via Point Autofocus profilometry for silver paste printed on epoxy fiberglass boards. The length of the tracks is  $6.8 \pm 0.2$  mm. The sintering step was performed via IR-radiation (IR Set 27%, 0.2 mm/s). The blue lines show the linear regression fits while the red dashed lines indicate the 95% Confidence Interval. **Left)** Area of the tracks in relation with their number of layers ( $A_{\text{layer}} = 5230 \pm 150 \mu\text{m}^2/\text{layer}$ ). **Right)** Measured resistance vs. the inverse of the cross-sectional area to calculate the electrical resistivity from the slope ( $\rho_r = (4.7 \pm 0.7) \cdot 10^{-7} \Omega \text{ m}$ ).

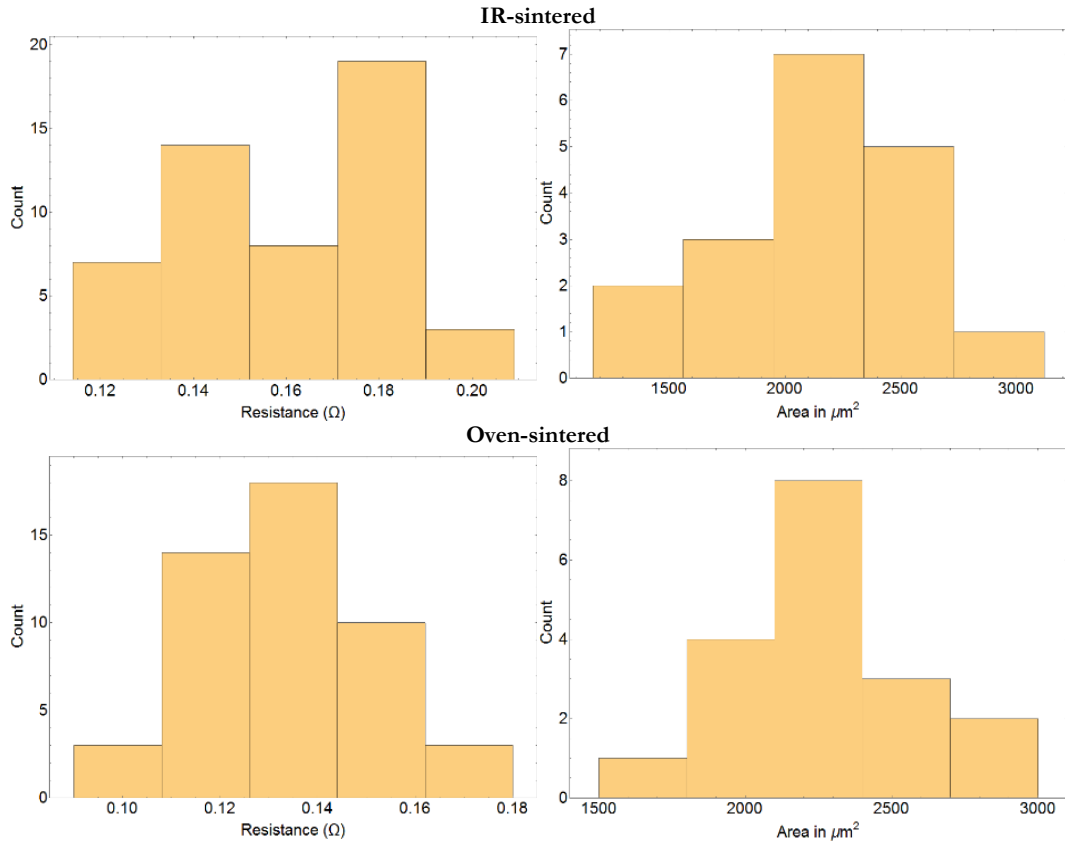


**Figure 120:** Histograms from the measurement of the resistance (**left**) and cross-sectional area (**right**) of silver tracks printed between the copper pads of a PCB. **Top** results correspond to samples sintered by IR (IR Set 27%, 0.2 mm/s), while **bottom** ones were heated in an oven (140 °C, 12 min). The average ( $\pm$  standard deviation) resistance is (IR:  $0.16 \pm 0.02 \Omega$ , Oven:  $0.13 \pm 0.02 \Omega$ ) and the section area is (IR:  $2100 \pm 400 \mu\text{m}^2$ , Oven:  $2300 \pm 300 \mu\text{m}^2$ ). The calculated electric resistivity is (IR:  $(5.2 \pm 0.3) \cdot 10^{-7} \Omega \text{ m}$ , Oven:  $(4.7 \pm 0.2) \cdot 10^{-7} \Omega \text{ m}$ ).

The resistivity achieved by the IR-sintered tracks is  $(5.2 \pm 0.3) \cdot 10^{-7} \Omega \text{ m}$ , while the oven samples yielded a result of  $(4.7 \pm 0.2) \cdot 10^{-7} \Omega \text{ m}$ . Although the resistivity obtained by oven treatment was marginally lower, both results are compatible and agree with the observations extracted from the multi-layered experiment. However, these results are approximately 8 times higher than the expected resistivity of this material ( $6 \cdot 10^{-8} \Omega \text{ m}$ ) according with the manufacturer (InkTec Company Limited 2013). This discrepancy can be partly explained by the bubble marks on the surface of the tracks, that even though had been minimised compared with earlier experiments at higher temperatures, are still visible and can disrupt the continuity of thin films. Similarly, internal microfractures caused by inhomogeneous thermal expansion and mechanical perturbations can reduce drastically the measured conductivity of the tracks (Hutchings & Martin 2012) (Sanchez-Romaguera et al. 2008) (Jang et al. 2008). This last phenomenon, however, is not likely to result in repeatable values of the resistivity and is therefore not identified as a main source of error for the present work. Another factor to consider is the difference between the solid thickness of the printed samples ( $9.1 \pm 0.4 \mu\text{m}$ , Table 11) and the recommended thickness for the screen printing process ( $1 \mu\text{m}$ ) for which the material is formulated (InkTec Company Limited 2013), which can increase the thermal barrier for complete sintering beyond the conditions tested in this experiment. However, it is more likely that the reason behind the reduced resistivity is related with partial sintering of the nanoparticles and organic residue left behind after the thermal step, as was observed by Jung et al. (S. Jung et al. 2016). In their screen printing experiment with the same silver paste used in this work, wet films of  $4 - 6 \mu\text{m}$  were deposited on polycarbonate (PC) and polyimide (PI) substrates and sintered via thermal and carbon nanotube assisted micro-wave radiation. They reported an electric resistivity of  $1.6 \cdot 10^{-7} \Omega \text{ m}$  (10 % bulk silver) for the thermal treated samples, which had spent 60 minutes in an oven at  $140 \text{ }^\circ\text{C}$ . This resistivity, however, improved to  $2.4 \cdot 10^{-8} \Omega \text{ m}$  (66 % bulk silver) when their microwave-sintering process elevated the temperature of the samples above  $350 \text{ }^\circ\text{C}$ . They then analysed the atomic carbon content of the samples resulting after high temperature treatments and observed an inverse relation with the temperature, which shows the continuation of the removal process of organic components at such temperatures. Finally, they related these results with the approximately 2 wt% drop above  $300 \text{ }^\circ\text{C}$  in the thermogravimetric curve of the material, which agrees with the TGA results shown in this work (Figure 66). Therefore, the obtained electric resistivity results are reasonable and consistent with the literature.

### **7.2.3 Conclusions of the 3-dimensional and functional tests**

Several multi-layered samples were printed, post-processed and 3D-scanned to study the growth of the structures as layers are added, paying attention both to geometric and functional characteristics. The fluids were printed on three different substrate materials, namely polycarbonate foil, glass slides and epoxy fiberglass boards. The choice of substrate depends on the printing material, the experiment to perform and the final application for the part. Nevertheless, some of these materials do not survive high temperatures and can be deformed during the printing or characterisations processes, which can affect the obtained results regarding the geometry of the samples. A different approach to solve compatibility issues between substrates and printing materials could be to modify such inks to promote adhesion. This can be done by adding polymeric additives to the fluids, as it is the case for the carbon paint and the photopolymers used in this work, or nanoparticles that would bond with the substrate during the sintering step, such as nanosized glass frit (Jang et al. 2008). Nonetheless, since the objective of the present work is to create and understand a multi-material process rather than to optimise a particular material, this route based on the re-formulation of the fluids was not investigated.

Despite these substrate's choice limitations, both the TPGDA and the carbon paint were printed on glass and epoxy fiberglass. Their results regarding the layer thickness were similar in both substrates, with discrepancies of their respective average values in each material below 3  $\mu\text{m}$ . This difference, however, is comparatively higher for the TPGDA due to its thinner layers, but it shows that even for low viscosity fluids the spreading on a different substrate and its effect on the overall height of the sample is small. This observation cannot be widely applied to any pair of substrates but it indicates that the role of the substrate for 3D-fabrication is not as important as in single layer 2D-printing. This reduced effect on the height of the structure is due to the fact that only the first layer is directly interacting with the substrate, while the following ones are deposited on the solidified printed material instead. This trend continues for all the layers in the structure, minimising the substrate's choice impact on the final geometry as the number of levels is increased. Additionally, it is worth considering that the measured film thicknesses in this study are related to specific 2D patterns, but different geometries would present variations to the thickness based on the number of neighbours that each drop encounters. Also, since there are different materials involved in the process, each layer can be printed on a variety of substrates that often would present mixed compositions and non-flat surfaces, which complicates the absolute prediction of the thickness in each point. Nevertheless, the

relative results here discussed were performed with typical printing conditions in mind and are expected to be valid in a wide range of situations, providing a good starting point for future research.

Apart from the influence of the substrate, the evolution and absolute value of the layer thickness for each material is interesting for processing reasons. All the materials displayed linear growth with increasing number of layers, which indicates that the process is stable and the samples can be scaled-up homogeneously in all directions. Also, it demonstrates that the post-processing conditions used to treat these materials, were enough to retain the shape of the layers without lateral spreading or fluid exchange across consecutive planes. Furthermore, the absolute layer's height for each material was characterised (Figure 115 and Table 11) and will be used to create multi-material structural blocks of constant thickness following the approach described in Chapter 3 (Figure 53). The range of thicknesses measured varies from  $0.875 \pm 0.013 \mu\text{m}$  for the aqueous dispersion of PEDOT:PSS on glass to  $55.9 \pm 0.7 \mu\text{m}$  for the UV-resin on polycarbonate film UV-cured at the fastest setting. Assuming a similar volume for all the viscous fluids deposited via micro-dispensing valves and comparable drop overlap between 20 and 40 %, it was determined that the main factor governing the thickness of the films is the solid content of the inks after their post-treatment and the density of such solid materials. Alternatively, since each photocurable formulation was deposited by a different type of printhead and their volumetric shrinkage is comparable, drop volume was established as the thickness driving factor for these fluids. Thus, the system allows some thickness control by selecting the printing resolution and jetting parameters driving drop volume, but ultimately the main factors controlling layer height are the solid content of the formulation and the printhead used to deposit it. Therefore, it is worth planning the thickness requirements beforehand and assign the printing fluids to the dispensing systems accordingly. Thicker layers can be an advantage for functional materials, since they speed up the process and limit the exposure to radiation of the surroundings. However, this can hinder or complicate the control of some properties such as transparency, where the ideal film thickness can be thinner than the minimum thickness achievable. Also, thicker wet films at high temperatures can lead to rough surfaces due to violent evaporation of the solvent, as it was observed in the previous section with the silver paste (Figure 111 and Figure 112). Thinner layers improve the z-resolution and facilitate the thickness compensation required to obtain homogeneous multi-material structural blocks (Figure 53). Applying this logic to the materials tested in this work, it is determined that the

TPGDA printed with PIJ is a more suitable structural material due to its increased resolution in the 3-dimensions respect to the stereolithographic resin and its faster processing due to multi-nozzle jetting and the possibility of curing during printing. Furthermore, due to the observed sub-micrometric film thickness for PEDOT:PSS, it does not seem worth jetting it with the micro-dispensing valves. Instead, low viscosity formulations, like the one tested in the thermogravimetric section in Chapter 5 (Figure 65), would be recommended in combination with the other free inkjet printhead in the system. The reduced solid content of said formulation is expected to result in layers with a thickness of approximately a third of the observed for the viscous variety, which can help to find the equilibrium in the trade-off between transparency and conductivity. Lastly, both the silver paste and the carbon paint are benefiting from the high viscosity approach and can yield tracks of useful resistance in a single pass, so they are a good fit for the micro-dispensing valves.

The resistivity of the 3 conductive materials was tested using the same approach based on surface profilometry and resistance characterisation. First, the resistance of the tracks in the multi-layered structures previously used for the layer thickness study was measured and the electric resistivity obtained from a linear regression following equation 49. This method yielded good results but it proved to be too invasive for the silver samples, which cracked easily in contact with the LCR-meter's probes. Thus, a second set of experiments was carried out by printing and 3D-scanning longer constant-section tracks transversal to the copper pads of PCBs. This allowed the characterisation of the resistance without direct contact with the samples at constant distances, which improved the overall repeatability of the experiment. The resistivity results for both methods and different substrates were compatible with each other and the literature. Particularly, the samples of PEDOT:PSS printed on glass yielded a resistivity of  $(1.54 \pm 0.08) \cdot 10^{-4} \Omega \text{ m}$ , while displaying homogeneous deposition and optical transparency. The carbon paint resulted in a resistivity of  $(5.3 \pm 0.2) \cdot 10^{-3} \Omega \text{ m}$  in the experiment based on longer transversal tracks. The results for the multi-layered samples in glass and epoxy boards were  $(3.7 \pm 0.5) \cdot 10^{-3} \Omega \text{ m}$  and  $(6.0 \pm 0.6) \cdot 10^{-3} \Omega \text{ m}$ , respectively. Interestingly, these values of resistivity are an order of magnitude lower than the measured in an early experiment based on multi-layered samples dried in ambient conditions printed on polycarbonate film  $(1.2 \pm 0.5) \cdot 10^{-2} \Omega \text{ m}$ , (Appendix A1). More experiments would be required to determine the role of the geometry of the samples and the variation in substrate, but it is reasonable to assume that this difference stems from the discrepancies on the thermal conditions during the post-process.

Specifically, the solvent evaporation per layer in the newer samples was accelerated via UV-radiation at a scan speed of 0.2 mm/s, while in the early tests 300 s of waiting time in ambient conditions was the only treatment applied to the tracks. The study of the samples' resistance under these different post-treatments (Figure 109) revealed an order of magnitude difference, despite the apparent dryness of the samples after less than 2 minutes (Figure 107). Thus, it is possible that part of the solvent is trapped within the sample when only 5 minutes of dry time in ambient conditions is allowed, which would explain the lower conductivity of the samples. Consequently, the UV-treatment of the carbon tracks is maintained as the main post-process treatment.

The silver samples printed on PCBs displayed poor adhesion and fragility, especially when the samples had to interact with the probes of other instruments. Nonetheless, a resistivity of  $(4.7 \pm 0.7) \cdot 10^{-7} \Omega \text{ m}$  was obtained from the resistance and cross-sectional area of the tracks in a multi-layered experiment. Later, a test involving long tracks transversal to the copper pads of the PCBs was carried out and a similar result of  $(5.2 \pm 0.3) \cdot 10^{-7} \Omega \text{ m}$  was obtained. The compatibility of both results despite differences in the method such as geometry and IR-radiation exposure, provides more confidence to the results. Furthermore, it rules out the significant presence of internal fractures, since it is unlikely that such defects affect in the same proportion to both sets of samples. Alternatively, other tracks were printed directly on the pads of a PCB but sintered in the oven at 140 °C for 12 min, exceeding the thermal requirements specified by the manufacturer (InkTec Company Limited 2013) in order to obtain the lowest resistivity. This, however, yielded a value of  $(4.7 \pm 0.2) \cdot 10^{-7} \Omega \text{ m}$ , which is compatible with the previous tests for IR-sintered tracks but remains almost 8 times higher than the expected resistivity ( $6 \cdot 10^{-8} \Omega \text{ m}$ ). The most reasonable explanation found for this discrepancy was the presence of organic residue that was not completely removed during the thermal processes (S. Jung et al. 2016). This was backed up by the nearly 2 wt% drop in the silver paste thermogravimetric curve (Figure 66) above 300 °C. This opens the possibility of obtaining lower electric resistivity at higher processing temperatures, but that would reintroduce the boiling issues encountered for thick wet films at high temperatures (Figure 111) that resulted in rough and often discontinuous surfaces. Thus, the wet thickness of the deposited layers is again identified as a main processing factor driving not only the final height of the solid layer but also its surface quality and functional properties.

### 7.3 Multi-material proof-of-concept functional structures

The knowledge regarding the used materials gathered during the previous chapters is used to create functional demonstrators that showcase the present and future capabilities of the hybrid approach proposed in this work. These include multi-material patterns with designed local physical properties, 2D and 3D functional circuits, flexible multi-layered devices, 3D structures with embedded components, and all-printed electroluminescent devices as an example of advanced functionality. Furthermore, since this is the first time that the materials come in contact with one another, a multi-material matrix experiment is performed to assess the compatibility and interactions of the used formulations.

#### 7.3.1 *Multi-material interaction matrix*

A frequent challenge in multi-material inkjet printing is the interaction between the jetted materials, since any unplanned physical or chemical reaction between adjacent elements can result in geometry distortions and functionality loss. For instance, if two inks share their main solvent they are likely to mix in wet form or re-dissolve previously deposited solid layers. This mechanism can potentially be used to smooth transitions between materials and promote inter-layer adhesion, but due to the difficulty of predicting the outcome reliably it is common to formulate the different inks with orthogonal solvents to avoid such mutual dissolution (Singh et al. 2010). Furthermore, since each material require a different treatment to form a solid film, it is possible that said process affects negatively other elements of the process. This is the main drawback of polymeric materials, both substrates and inks, since they cannot survive the high temperatures required to sinter nanoparticle-based formulations (Suganuma 2014). Consequently, two sets of experiments based on printing arrays of drops of each ink on top of the other involved materials were performed (Figure 121). In the present case, the samples were generated using the automated material selection strategy implemented, but the imaging of the samples was performed externally using an optical microscope. Nevertheless, there is nothing preventing this step being performed with the mounted monochrome camera, which would be more compact from a process point of view.

In the first iteration of this test, the stereolithographic resin was used as a structural material, the carbon paint as the functional component and polycarbonate foil was selected as substrate. No obvious signs of interaction between materials were observed apart from the different wettability experienced. The carbon paste wets all the surfaces less than the photo-reactive resin, leading to smaller footprints, despite having an approximately similar volume. The sample of carbon on a carbon displayed individual drops on the edge of the

squares but none were observed in its middle, which seems to be an indication that the substrate material may not have been totally dry on the centre and facilitated the incorporation of the drops into the previous layer. Nevertheless, the drops that were left are smaller than the ones printed directly on the polycarbonate film. Alternatively, the UV-curable resin shows bigger drops on the polycarbonate film and slightly smaller on the carbon substrate. In the case of the photoactive resin on a substrate of the same material, there are no discernible drops, which are an indication of enhanced wetting respect from the other substrates. This could be partially explained by the smooth surface created by the cured resin and the chemical compatibility between liquid and solid phases. However, it is noteworthy that the drops did not create a homogeneous film on top of the previous layer but a bumped surface, indicating that the spreading of the wet film was not as pronounced as it seems in the picture. Therefore, there is an optical component to be considered, since imaging the interface of two bonded bodies with the same refractive index is virtually impossible. Apart from their respective post-processes, the samples were irradiated with UV light at 0.1 mm/s 5 times but no signs of degradation were found on either material.

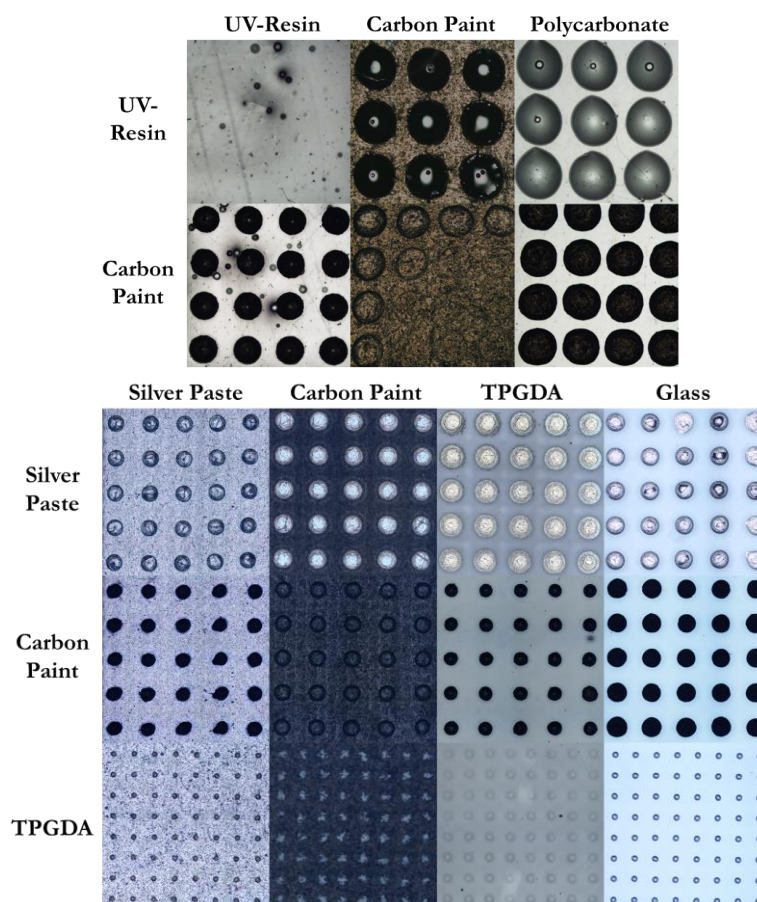


**Figure 121:** Material interaction experiments involving 2 sets of materials. **Top)** Carbon paint, UV-resin and polycarbonate film. The squares are 2 mm. **Bottom)** Silver paste, carbon paint, TPGDA and glass. Each square image has a 4 mm side. All samples were subjected to 5 cycles of each post-process required for at least one of the involved materials.

The second set of samples was produced using TPGDA as a structural material, carbon paint and silver paste as functional components and glass as a substrate. No issues with cross-dissolution or chemical interaction were observed in this case either and the differences in the wettability were again the main distinction among the tested substrates. The carbon paste performed similarly on top of the 3 printed materials but displayed a relative bigger area on the glass slide. Alternatively, the biggest silver droplets were found in the TPGDA, performing similarly on the other materials. The TPGDA also spread the most on a layer of cured photopolymer, as it was the case with the UV-resin, this time however, the drops could be identified due to the UV-curing occurring during printing, which allowed them to retain their shape and relative height respect to their surroundings. All samples were treated by 5 cycles of UV radiation and IR (Set 29%) at 0.1 mm/s with no degradation effects visible. The silver drops collapsed due to the room temperature drying of their solvent before the thermal treatment was applied, as it was already observed and discussed in Figure 110.

In conclusion, no potentially problematic interactions were detected among the involved materials, which is mostly due to their orthogonal solvents and the fact that they are sequentially treated, so no 2 fluids coexist in a given time. Moderate differences in the drops' wettability on the various surfaces has been observed but is not in general a concern since the printing resolutions had been selected with ample margin for overlap. Variation of the spreading behaviour of the drops is expected as the substrate material and deposited film are altered. This is the reason why the structural material is typically printed in first place, so negative volumes can be created that later accommodate the functional fluids, controlling their shape despite the effects observed in Figure 121.

### ***7.3.2 Complex multi-material designs with locally designed properties***

The possibility of accurately deposit micrometric drops of multiple fluids following digital designs allows the creation of parts with unique properties. For instance, not only can various materials be used to fabricate a part in a single process, but the transition between them can be designed to be gradual, preventing the discontinuities in the physical properties of the object associated with discrete interfaces. This man-made materials with controlled anisotropy are known as **Functionally Graded Materials** and although can be achieved by several established fabrication methods (Kieback et al. 2003), multi-material Additive Manufacturing is one of the most promising approaches. Practical examples of AM techniques creating functional gradients were discussed in section 2.2. Alternatively,

instead of a transition function between two (or more) materials, small functional cells can be tessellated across the structure to control the properties of the final part. These voxels can be made of multiple materials or a combination of one element and empty spaces, but if the resulting structure presents properties different from its constituent components, it is known as a **meta-material**. Due to the typical resolution fabrication in Additive Manufacturing and the fact that even single material processes can contribute to this field, most of the efforts in AM-metamaterials are focused on mechanical properties (Sitthi-Amorn et al. 2015)(Bickel et al. 2010). An exception would be multi-photon polymerization, which can produce nanostructures following an additive approach and therefore is a suitable tool to study optical metamaterials (Farsari et al. 2010). However, as AM multi-material techniques evolve it is likely to see progress in other types of functional metamaterials.

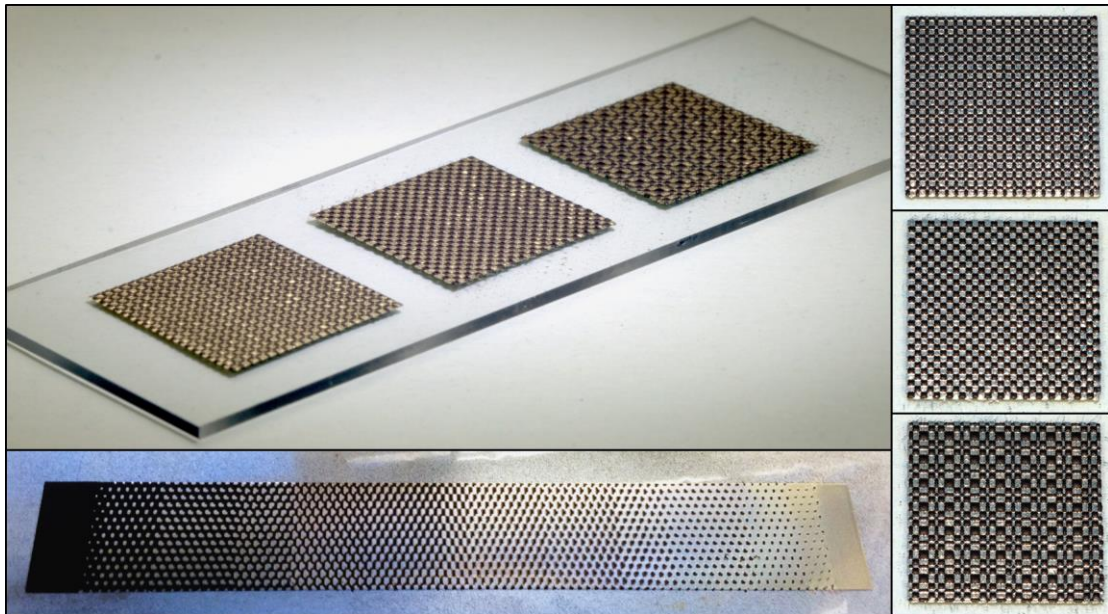


**Figure 122: Top and right)** Checker-board patterns printed with carbon paint and high viscosity silver nano-paste showing the potential application of multi-material jetting systems to functional metamaterials in 2D. The square patterns have a lateral size of 15.24 mm. **Bottom)** Track (99.8 x 14.0 mm) displaying a gradual transition from carbon to silver, printed on polycarbonate foil. The polymeric substrate allows flexibility on the track but the silver cracks after a few cycles due to poor adhesion.

As a proof-of-concept of multi-material functional structures following the previous design routes, several samples using the carbon paint and silver paste were fabricated (Figure 122). A graded carbon-to-silver track was produced on polycarbonate foil following the previously discussed printing settings for each ink. Instead of separated post-treatments, both materials were allowed to coexist in fluid form to promote adhesion and then were treated by a pass of IR radiation. UV was not required to dry the carbon paint, since the heat used to sinter the silver nanoparticles was enough to apparently

complete the evaporation of its solvent. Different sections can be observed along the track with various material ratios, which is purely a feature of the printing file used, since any pattern could be printed as long as it can be digitally created. A smaller size of the functional cells and a randomised distribution along the gradient would be recommended for future attempts. Furthermore, square samples displaying 3 different checker-board designs were created on glass following the same printing settings. In this case the carbon was allowed to dry before depositing and sintering the silver paste, since the focus was the resolution of the pattern. Interestingly, while the samples were being photographed in various lighting conditions they displayed apparently different reflection behaviour. This would not be entirely surprising since the reflectivity of carbon and silver is strikingly different, but it shows another potential application field for the multi-material system developed in this work.

### 7.3.3 Functional circuits in 2D

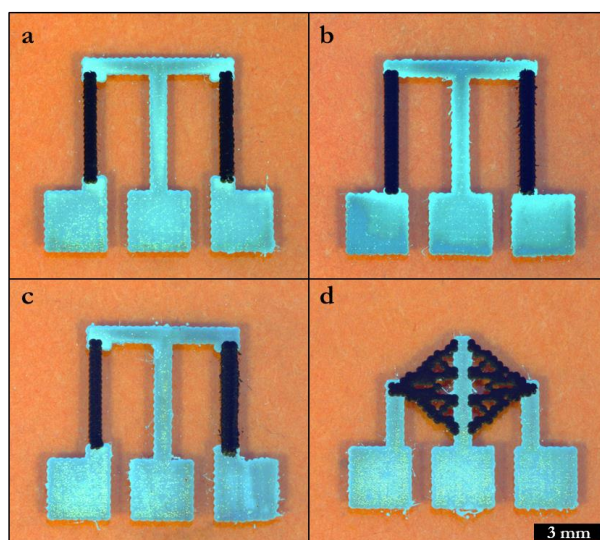


**Figure 123:** Printed voltage dividers using carbon paint and silver paste. Each configuration displays a different resistance ratio due to differences in the number of carbon paint printed layers, this in turn regulates the ratio between output and input voltages. **a)** 2 layers each leg ( $R_1 \sim R_2$ ). **b)** 1 and 2 layers ( $R_1 \sim 2R_2$ ). **c)** 1 and 3 layers ( $R_1 \sim 3R_2$ ). **d)** More complex alternative design of a voltage divider. 1 layer in each side ( $R_1 \sim R_2$ ).

In this section, the creation of functional circuits featuring silver as conductor and carbon paint as a printable resistor are discussed. Specifically, 3 voltage divider configurations like the one described in Figure 61 were fabricated, modifying the ratio between the two involved resistors ( $R_1$  and  $R_2$ ) to control the ratio between the output ( $V_{out}$ ) and input ( $V_{in}$ ) voltages (Figure 123). The rectangular shape of the resistors remained unchanged but the number of layers was modified to create 3 different resistance ratios ( $R_1/R_2$ ), which regulated the output. The electrical potential difference between the

outermost electrodes was applied by a regulable power supply (0 – 30 V Power Supply, TENMA, USA) and read in the different positions using a digital multimeter (72-7720, TENMA, USA). The resistance of the tracks was characterised as the average of 3 measurements with a benchtop LCR-meter (HM8018, Rohde & Schwarz GmbH, Germany) with a maximum resolution of  $0.001 \Omega$  (Table 12). Silver-based electrically conductive paint (RS Pro, UK) was applied on the electrodes to avoid scratching the thin layer of sintered silver and provide good contact for the probes of the measuring instruments. The resistance of this paint and the silver tracks is negligible compared with the carbon resistors, as it was shown earlier in this chapter. The results from the measured voltage output at inputs between 1 and 9 V are plotted in Figure 124. The experimental voltage ratio was obtained from the slope of the linear regression of this data, while the expected value is calculated from equation 51.

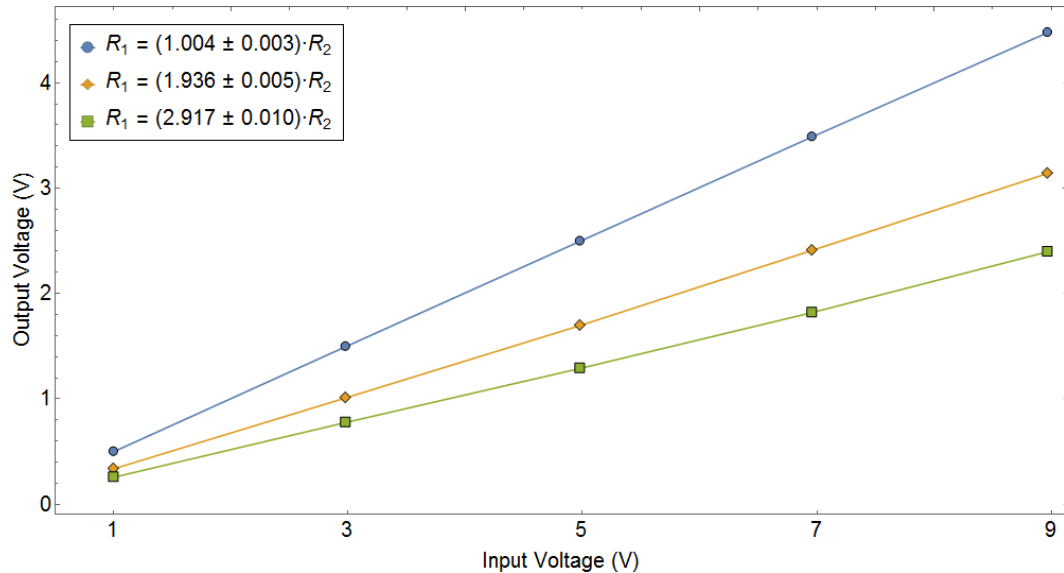


**Figure 124:** Response of the different configurations of printed carbon-silver voltage dividers at input voltages between 1 and 9 V. Each configuration displays a different resistance ratio due to differences in the number of carbon paint printed layers.

**Table 12:** Resistance and voltage relations for 3 different printed carbon-silver voltage dividers.

	Sample 1 ( $R_1 \sim R_2$ )	Sample 2 ( $R_1 \sim 2R_2$ )	Sample 3 ( $R_1 \sim 3R_2$ )
$R_1 (\pm 1 \Omega)$	504	842	862
$R_2 (\pm 1 \Omega)$	502	435	296
$R_1/R_2$	$1.004 \pm 0.003$	$1.936 \pm 0.005$	$2.917 \pm 0.010$
Expected $V_{out}/V_{in}$	0.50	0.33	0.25
Experimental $V_{out}/V_{in}$	$0.499 \pm 0.001$	$0.352 \pm 0.003$	$0.267 \pm 0.003$
$R^2$	0.9999	0.9997	0.9994

The experimental results are in good agreement with the expected voltage ratios, which means that the circuits performed satisfactorily as voltage dividers. It is worth noting that in this case the relevant attribute of the samples is not the absolute resistance of each track but their ratio, thus, the success of the process not only demonstrates the deposition of functional materials in customisable shapes but also the reasonable repeatability of the produced tracks. Furthermore, the printed tracks are not restricted to rectangular shapes, since more intricate designs can be produced to provide specific functionality or adapt to the available space. Figure 123 shows a more complex alternative to the voltage divider structure, where the pattern at both sides is symmetric and, consequently, has an expected voltage ratio of 0.5. The circuit yielded an experimental ratio ( $V_{out}/V_{in}$ ) of  $0.538 \pm 0.002$  at 5V, which is within 8% error of the expected value, proving the suitability of this approach for certain applications where complex shapes are required.

#### **7.3.4 Flat multi-layered devices**

Passive components such as capacitors, resistors and inductors are the building blocks of most electric circuits and, consequently, very little fully-printed applications can exist without addressing their fabrication. Despite their importance, these components are based in fundamental physical principles and often require only one functional material to work, allowing their creation even by simple processes. However, due to miniaturization and efficiency requirements of the electronic industry, the fabrication of these elements typically involve a larger number of constituents, which calls for multi-material approaches. For instance, it is common to use insulator materials to encapsulate components and tracks to protect them from external factors and avoid uncontrolled charge transfer among adjacent elements. Thus, a bi-material printing system loaded with an insulating structural material and a conductive element, is enough to create LCR-circuits (Redinger et al. 2004)(Church et al. 2009). Nevertheless, the successful printing of simple components with conventional geometries is just the first step towards taking full advantage of printed electronics. Once simple inductor coils are achieved, creating customised antennas is the next step (Deffenbaugh 2013)(Adams et al. 2011), which can adapt to the shape and application of each device. Furthermore, these printed antennas can be integrated on objects to allow inductive transfer of energy (Choi et al. 2004) or operate as RFID tags (Quintero et al. 2016)(Redinger et al. 2004)(Subramanian et al. 2005) to allow communication among separated objects. Similarly, long serpentine patterns of resistive materials can be printed to create customised heaters (Dziedzic et al. 1994)(Yao et al. 2016)

and sensors, from humidity and temperature (Quintero et al. 2016) to strain gauges (Correia et al. 2013)(Gooding & Fields 2017)(Muth et al. 2014). It is worth emphasizing that all these components can be fabricated in single additive processes that allow functionality incorporation, which saves both a considerable amount of precious materials and processing time. Furthermore, if the materials and substrates are chosen adequately, flexible and transparent functional devices are possible, which enable the creation of entirely new electronic devices.

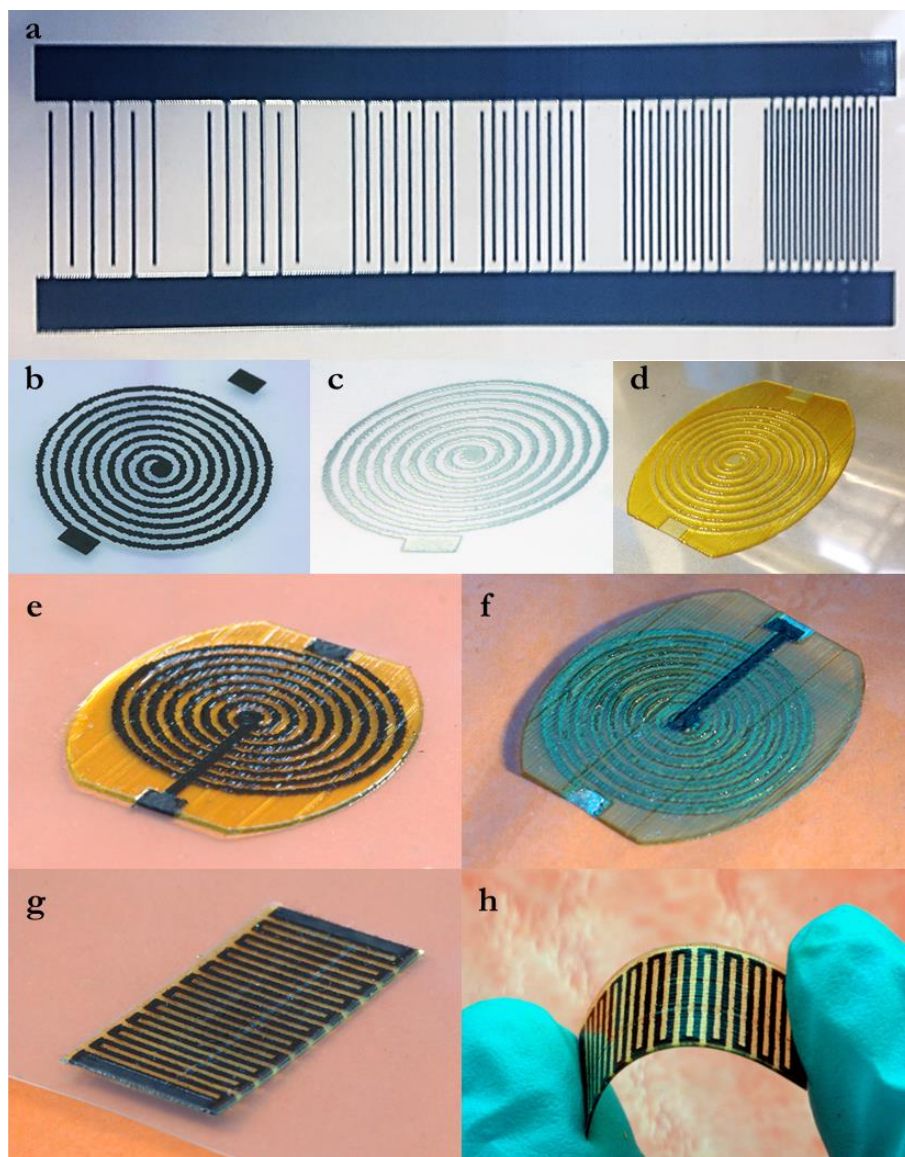


**Figure 125:** Samples printed on polycarbonate foil with common shapes in the electronics industry for the fabrication of sensors and actuators. **a)** Translucent interdigitated tracks (127 x 42 mm) printed with an aqueous dispersion of PEDOT:PSS in 3 consecutive layers before IR-induced drying. **b)** Spiral coil printed with carbon paint (17 x 17 mm) and dried with UV radiation. **c)** Spiral coil printed with silver paste and sintered with IR radiation (17 x 17 mm). **d)** TPGDA base with trenches designed to accommodate the conductive materials (32 x 38 mm). **e)** Encapsulated triple-layered carbon track on TPGDA (32 x 38 mm). **f)** Embedded coil (32 x 38 mm) composed of 3 layers of sintered silver and 1 layer of carbon paint, which resulted in lower resistance than purely carbon coils preserving their mechanical resistance. **g)** Serpentine double-layered carbon track in TPGDA (30 x 15 mm). **h)** Printed resistor displaying flexibility and transparency through the insulator TPGDA areas.

In this section, several proof-of-concept flat passive elements are printed to illustrate the capabilities of the developed system in the aforementioned areas (Figure 125). These interdigitated, coil and serpentine patterns were fabricated on flexible polycarbonate foil, using TPGDA as insulating structural material. Specifically, interdigitated translucent electrodes (Figure 125a, 127 x 42 mm) were produced printing 3 layers of PEDOT:PSS and drying them with IR radiation (IR Set34%, 0.2 mm/s). No electric conduction was detected between both sides despite achieving minimum electrode separations of 200  $\mu\text{m}$ . Spiral inductive coils were created depositing both carbon paint and silver paste directly on the polymeric film (Figure 125b & c) and post-treating them accordingly. However, to provide easy access to both extremes of the conductive track an insulating layer is required, so the returning track can bridge the distance between the middle of the pattern and the connection pads. This was achieved by the deposition of thin films of TPGDA. Furthermore, to create stand-alone devices detached from the substrate, base and top films were also produced to embed the conductive elements except for their connecting pads. These structural patterns were always printed before the functional materials and were designed to restrict the spreading of the tracks, allowing for increased control and resolution in relation with free-wetting drops (Figure 125d). Following this approach several encapsulated conductive coils were created with a containing square of 32 x 38 mm (Figure 125e & f). Minimum resistance of  $14.2 \pm 0.2 \text{ k}\Omega$  was measured for structures with 3 layers of carbon paint and  $6.2 \pm 0.2 \text{ }\Omega$  for single layered silver. However, the silver samples displayed weak mechanical properties and cracked internally with minimal interaction. This could potentially be improved by printing thicker silver films and encapsulating them with more layers of TPGDA, but ultimately is a material dependent drawback of sintered silver tracks. Instead, a layer of carbon paint was printed on top of 3 layers of sintered silver with the intention of bridging the cracks with the more flexible paint. The carbon-silver coil presented cracks visually apparent after removing it from the printing platform but still showed a resistance of  $263 \pm 8 \text{ }\Omega$ , which is between the obtained values for the purely carbon and silver coils, demonstrating that the multi-material approach was successful. Finally, a serpentine double-layered carbon track (30 x 15 mm) was printed and encapsulated in TPGDA following the same approach (Figure 125h & h) to illustrate the creation of customised heaters or sensors. The resistance obtained was  $17.8 \pm 0.2 \text{ k}\Omega$ , which draws a current of approximately 1.7 mA (from equation 50) for the maximum 30 V that the available power supply could provide. This was not enough to produce a significant difference in the temperature, but shows that fabricating this type of

device is entirely possible. Future iterations can be performed with more conductive materials or a thicker carbon track. This sample displayed an increased flexibility and transparency respect previous samples due to thinner TPGDA encapsulating.

### **7.3.5 3D demonstrators**

One of the main qualities of Additive Manufacturing is that it provides fabrication complexity without increasing the cost or the intricacy of the process. Thus, once a multi-material system is capable of creating multi-layered samples like the ones shown in the previous section, producing non-conventional geometries is just a matter of preparing more complex digital patterns. This, however, is often non-trivial, since most tools for complex design are still in their infancy and end up being a bottleneck for the fabrication capabilities of AM. Nevertheless, using a combination of approaches it is possible to create functional multi-material 3D geometries on standard surfaces, as it is shown in Figure 126. Specifically, several multi-layered flat samples (15 x 7 mm) were created first on polycarbonate films to validate the design of 5 independent carbon and silver tracks insulated by TPGDA (Figure 126a & b). The printing cycle for this sample was: TPGDA base with space for the silver track, silver track, carbon paint only on the contacting pads, TPGDA embedding the silver track but leaving the pads exposed, carbon tracks bridging over silver, TPGDA encapsulating carbon and leaving the pads exposed. The resistance of the carbon tracks was  $1057 \pm 7 \Omega$ , while the silver displayed a value of  $0.63 \pm 0.02 \Omega$ , both results are consistent with previous tracks of similar size. The zig-zag profile of the diagonal tracks is due to the reduce resolution (100 DPI) of the file. This, however, is not the resolution of the system and therefore can be improved by designing the files in a larger resolution with individual dots were the drops are expected. This approach, although successful, is time-consuming and can result in damage to the printheads if a frequency higher than their limit is required to print at a particular speed.

After the multi-layered flat test, a 3D structure inspired on the same crossing of diagonal tracks was created in Autodesk Inventor (Figure 126c, render) and sliced into bitmaps using in-house developed code (Wolfram Mathematica 10.2.0.0, Wolfram Research, USA). The key here was not to slice the conductive tracks with the structure and instead print them in one layer as before. The TPGDA provides enough support for them to adapt to their required slope and allows to treat them all at the same time, reducing greatly the energy deposited on the surrounding materials. Nevertheless, this approach, would not be practical with low viscosity materials, since they would likely slip on the

slopes of the structure and accumulate at the base. Furthermore, if the structure is tall, the heat treatment applied to the tracks is not homogeneous, which can cause the conductors to have a different resistance depending on their relative position to the lamp. However, as it was shown during the calibration of the IR-lamp (Figure 48), a height difference of 2 mm displayed a temperature variation of approximately 15 °C, which is typically not enough to create a discernible difference in the properties of the materials. This trend, however, is not expected to be linear once the sample gets closer to the heat source, so it is important to keep a safe distance between the substrate and the lamps. Nevertheless, since most 3D samples printed in this work are shorter than 2 mm these effects are not considered further.

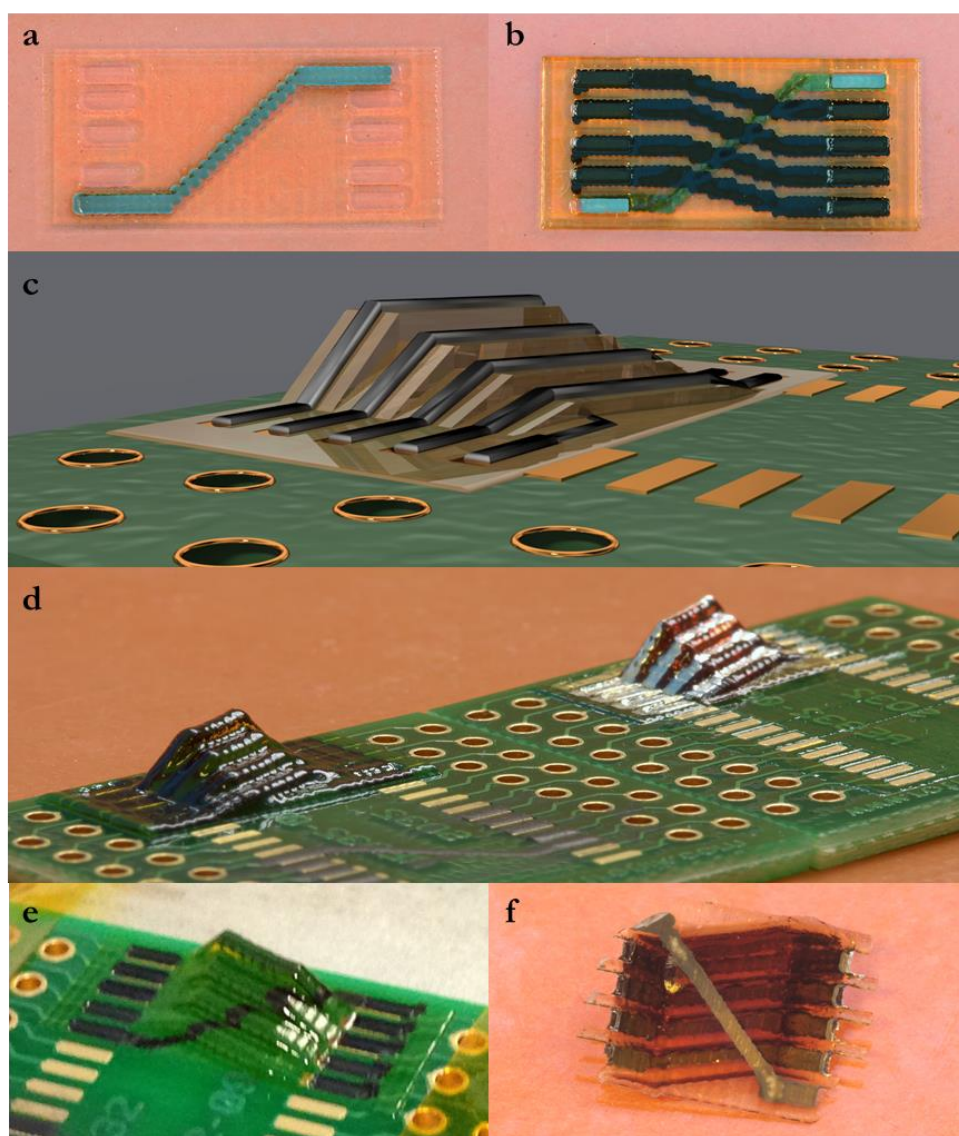


**Figure 126:** **a & b)** Conductive tracks of silver and carbon paint framed and isolated by TPGDA. **c)** Rendered image of the 3D design with added tracks. This file was sliced into bitmaps to create the object layer-by-layer. **d)** Two iterations of the same 3D structure, one with carbon tracks and another with silver. **e)** Detail of the carbon sample before the top tracks were printed, showing good transparency and clarity. **f)** Bottom part of the silver 3D structure that detached due to excessive heat. All samples had dimensions of 15 x 7 mm.

Two samples were printed with carbon and silver as conductive element, PCBs as their substrate and TPGDA as structural material (Figure 126d). The main stepped structure was composed by 4 levels of increasing height reaching a maximum of 1.44 mm, which required 160 layers of TPGDA with thickness of 9  $\mu\text{m}$  (Table 11). The slope of the tilted sides of the steps were designed to be 40°, 30°, 20° and 10°. The fabrication process in both cases lasted approximately 2 h and 45 min, which results in an average processing time per layer of 1 minute. No processing issues were encountered during the fabrication of the carbon sample apart from the tracks being too wide for the width of the steps that they occupy, resulting in material overflow. This, only affected the aesthetics of the part, since it did not cause unwanted connections between consecutive channels, and it could be prevented by designing a raised barrier at the edge of the steps. The resistance of the longer track was  $1610 \pm 10 \Omega$ , while the ones travelling across the 2 lowest steps were  $670 \pm 30 \Omega$ . However, the 2 tracks printed on the higher steps did not show conductivity and, upon closer inspection, discontinuities on the line were encountered. The most likely explanation comes from the resolution of the printing files, since they were 100 DPI and did not allow smooth patterns, this is most noticeable in the diagonal tracks. Furthermore, since these lines were printed on tilted planes, the effective drop-to-drop distance is affected by their inclination and the greater the slope the longer this distance would be. Also, it is noteworthy that the 100 DPI resolution was chosen in base of the spreading of the material on glass and PCBs, however for these 3-dimensional diagonals the substrate was TPGDA, which displayed reduced wetting compared to glass for the carbon paint (Figure 121) and contributed to the discontinuity of the tracks. Consequently, the patterns of the diagonal tracks were redesigned before printing the silver structure to prevent the problems experience with the carbon (Figure 127). In particular, the patterns were scaled up from 75 to 825 DPI, and the position of the drops was denoted by black pixels, as before. The difference is that in these new patterns, the distance between drops is quantised in steps 11 times smaller. The immediate result is that adjacent droplets are not represented as adjacent dots anymore, providing greater freedom to control their position. However, these files need to be handled with care, since it is relatively easy to generate patterns that require printing frequencies outside the recommended range of the dispensing heads. The slope-dependency of the resolution was not compensated, since it requires a more sophisticated and time-intensive approach. Nevertheless, it could be addressed in a similar manner, since once the position of the drops is directly programmed is just a matter of computer power to place them in the right position.

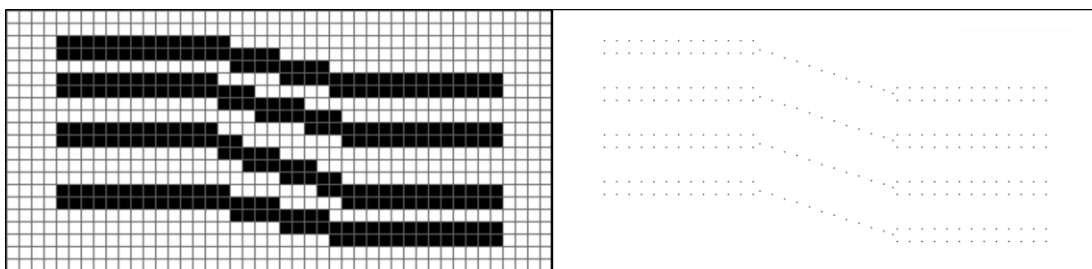


**Figure 127:** Bitmap files used to print the silver diagonal tracks. Black pixels represent the position of the centre of each drop. The minimum distance between dots is determined by the size of the pixels. **Left)** Original bitmap at 75 DPI with a grid showing the divisions between pixels. Adjacent pixels result in connected drops. **Right)** Modified pattern at 825 DPI that allow greater design freedom. Multiple effective resolutions can be used in the same file if this method is used. Disconnected dots still form continuous lines due to the size of the drops.

A 3D silver sample was produced using the same files for the TPGDA than in the carbon case and the upgraded designs for the diagonal tracks (Figure 126d). The resulting structure presented no visual interruptions of the tracks nor overflow of material on the top section of the steps, indicating that the modification of the files was a success. The resistance of the lower track was  $10.2 \pm 0.2 \Omega$ , while the others presented an average value of  $1.14 \pm 0.11 \Omega$ . It is worth noting that the tracks' width was reduced, which can explain the small increment on the resistance of the upper tracks compared with the flat test. The lower track, however, shows almost 10 times higher resistance, which is probably due to a non-critical defect along the printed line.

The aspect of the TPGDA is darker and less transparent than in the carbon case (Figure 126d, e & f), which is likely related with the different post-treatment used to consolidate the conductive materials. Specifically, the carbon paint was dried by UV exposure at a scanning speed of 0.2 mm/s, while the silver was sintered with IR at a power set of 27% at 0.05 mm/s, which at same dimensions results in a longer exposure to infrared. Also, it is likely that the absorption of TPGDA is different for these two sections of the electromagnetic spectrum, so further experiments would be required to unequivocally establish the source of the polymer darkening. However, despite being subjected to temperatures lower than the decomposition threshold measured by TGA (Figure 67), it is possible that the degradation of the material has been initiated. A sign of this is the fact that the main structure was easily detached from the platform after the resistance tests were carried out (Figure 126f). Since the fracture line was between the raised structure and the lower plane, both printed with TPGDA, this is not likely related with the poor adhesion of the silver and instead is possible that it is due to the weaker state of the polymer due to prolonged exposition to IR radiation. The rest of the sample, however, was apparently as stable as the carbon sample and no further fragmentation was detected after extensive manipulation.

The previous samples are examples of 3D multi-material structures but are still limited in their geometry due to the requirement of always depositing material on an existing layer. This eliminates the possibility of internal hollow spaces and overhangs. The way to overcome this in Additive Manufacturing has typically been to use a removable support material. Stereolithography, FFF and Laser Melting normally create a thin scaffold of the same material around the part, while Laser Sintering uses the raw powder as support. However, if the system is multi-material, it is common to use either a soluble or a phase changing material as a support, which typically reduces the chances of damaging the part during the supports removal stage. Thus, the carbon paint is used in this work to illustrate the creation of removable supports making use of its water solubility and demonstrated printability (Figure 128). In these experiments, since they are chronologically previous to the implementation of the low viscosity printheads, the structural material is the UV-resin.

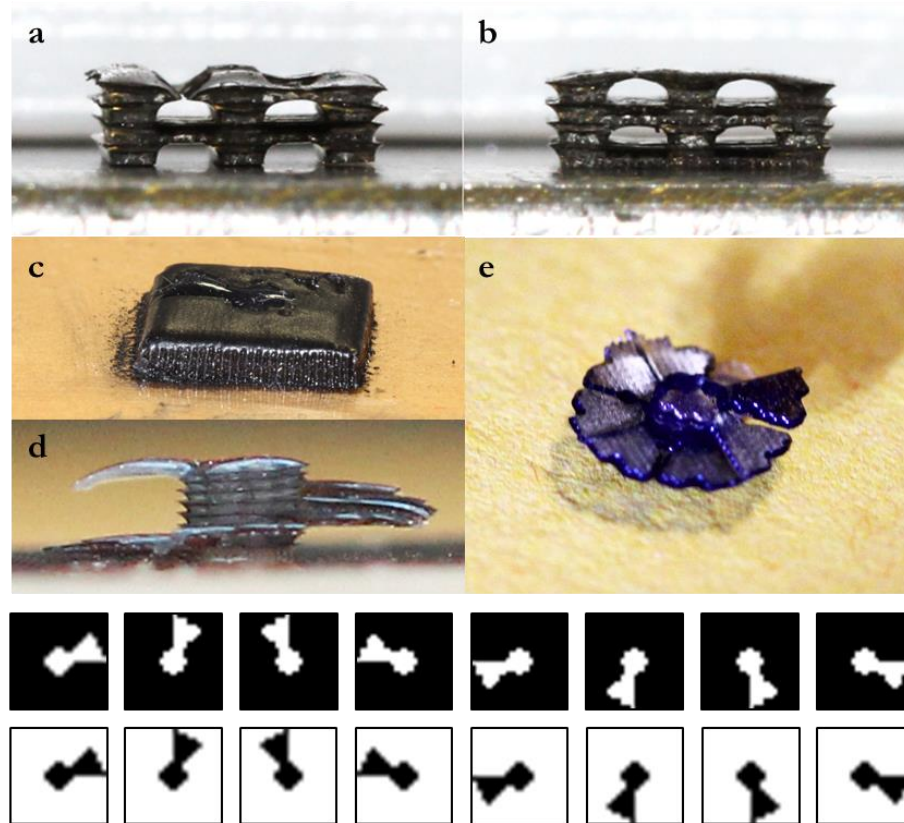


**Figure 128:** **a & b)** Woodpile structure printed with stereolithographic resin and using carbon paint as soluble support (6.0 x 6.0 x 1.4 mm, before dissolving the carbon). **c, d & e)** Spiral staircase-like structure printed by the same method (8.0 x 8.0 x 2.3 mm). The printing files used to produce this 3D structure are shown at the bottom, with the black pixels representing the drop positions.

The first configuration (Figure 128a & b) is a woodpile structure of 3 levels, changing the direction of the beams perpendicularly in each step. The number of layers of carbon and photopolymer in each structural block are 5 and 7 respectively, which are estimated to provide homogeneous thickness. Moreover, the carbon was always printed

first to limit the spreading of the UV-resin, since it was cured after the completion of each layer instead of during printing. The carbon was allowed to dry 5 minutes between layers to allow solvent evaporation. Nevertheless, it is noteworthy that solvent entrapment in the sample due to short drying time is not an issue as relevant as it was when the carbon was used as a conductive material and this drying time could be reduced. Once the printing stage was completed, the carbon was dissolved in deionized water at 60 °C under sonication for 1 hour to reveal the structure. The resin remained translucent but it turned darker due to the incorporation of carbon during its uncured stage. This could be avoided by fully drying the carbon before depositing the resin (perhaps using a forced-drying method involving UV or IR radiation) and curing the photopolymer sooner, so the mixing time is shorter. However, more efficient would be to use a support material that does not contain suspended particles. An aqueous solution of gum arabic seems a suitable option, since it is the binder on the carbon paint used in this work.

The geometric result is satisfactory since it displays overhangs and internal channels that would be impossible to achieve without the use of a support material. Some of these features, however, deviate from the original design and display a more curved nature, as it is the case of the cross-section of the channels or the external sides of the sample. The reason for these variations are a combination of the intrinsic curved shape of a fluid deposited on a flat surface and a miss-match on the layer thickness of both materials. The only thing that can potentially help with the former is to deposit thinner layers, which indicates that the support material would be more successful if printed with the inkjet printheads incorporated later to the system. The height miss-match is a result of a non-optimised materials' ratio, which can be improved by performing experiments like the previously shown in this chapter, where multi-layered tracks are scanned with a profilometer. Nevertheless, these tests are carried out on samples spreading on a flat substrate freely, which is not exactly the situation encountered here, where trenches created by the support are filled with the structural material. Thus, an approach calculating the required volume to fill each pocket would be ideal if the required computational task can be performed in a reasonable time.

A more complex spiral staircase-like structure was created using the same approach and materials (Figure 128c, d & e). In this case, the same curved profiles and pagoda style edges are found, but the overall process successfully produced cantilevers with an approximate thickness of 300 µm.

### **7.3.6 *Embedded components and capacitive sensors***

Despite the great advances in the area of printing electronics experienced in the last decade, the amount of materials and geometric tolerances required to fabricate some components are still outside the capabilities of the additive technologies. Still, the geometric benefits of AM can be harnessed today, even in demanding applications, if pre-manufactured components are automatically integrated during the fabrication process. Automated insertion methods using transfer films and robotic arms are already common in the PCB industry and can be used in conjunction with Additive Manufacturing systems (Parekh et al. 2015). However, depending on the nature of the printing system, the addition of external components can be disruptive for the process. For instance, successful integration of off-the-shelf components has been demonstrated using stereolithography (SLA) as the structural fabrication tool (Lopes et al. 2012)(Navarrete et al. 2007)(Shemelya et al. 2013)(Li et al. 2016), but every time that a component had to be placed or a conductive track deposited, the sample had to be removed from the resin vat, cleaned, rotated, moved towards an additional mechanical stage and brought back to the resin vat to continue the process. The disruptions are less pronounced for FDM processes (Espalin et al. 2014)(Shemelya et al. 2013), since the samples do not need to be transferred to a different stage to receive the components, but the limited functionality of thermoplastic-based materials hinders the possibility of depositing everything in a single process. Alternatively, multi-material jetting is an interesting approach since it allows to combine highly functional materials and the creation of complex geometries. Furthermore, the components can be integrated on the design as empty boxes of equal volume, which produces minimal process disruption. One limitation, however, is that the processing conditions need to be controlled so they do not exceed the maximum temperature allowed for the integrated components, but this is an unavoidable condition for any method that incorporates such elements during the fabrication of the parts.

In the present work, several structures with embedded green LEDs (PicoLED P12 Series, ROHM, Japan) are produced using carbon paint as conductive element and stereolithographic resin as structural material (Figure 129). The LEDs were manually placed using precision tweezers and the monochrome camera incorporated in the printing system. Furthermore, a more complex geometry involving a capacitive sensor, 3-dimensional tracks and the LED was created and connected to a micro-controller (UNO, Arduino, Italy) via solid-core jumpers (Figure 129f & g). These wires (0.66 mm in diameter) were connected to the allocated open spaces and fixed in place by adding a drop of fresh carbon paint. The presented device contains three printed tracks, the one in the middle

runs flat across the length of the structure until it is raised at the other end, leaving its top surface exposed to act as a capacitive sensing electrode. The other two tracks start flat but then are raised to form a bridge over the middle electrode, providing current to the LED. Finally, the three electrodes are connected with jumper wires to different pins on the micro-controller, which is in charge of the capacitive sensor and switches the state of the LED when presence is detected. Additionally, the whole device was encapsulated on the photo-curable resin to extend its lifetime. The sensor itself was left exposed to increase its sensitivity, but a thin film of dielectric material could be deposited to protect it. An external frame of carbon was printed to control the spreading of the resin and increase the sharpness of the design. This guide pattern was later removed with warm deionised water, revealing a sharper edge that would have been possible leaving the resin to spread freely on the polycarbonate foil. Once the component was finished, it was tested with the 5V supplied by the micro-controller, showing the desired behaviour. This indicates that the printed tracks were not interrupted or shorted at any point and that their resistance ( $113 \pm 5 \Omega$ ) was not a hindrance for the emission of light by the LED.

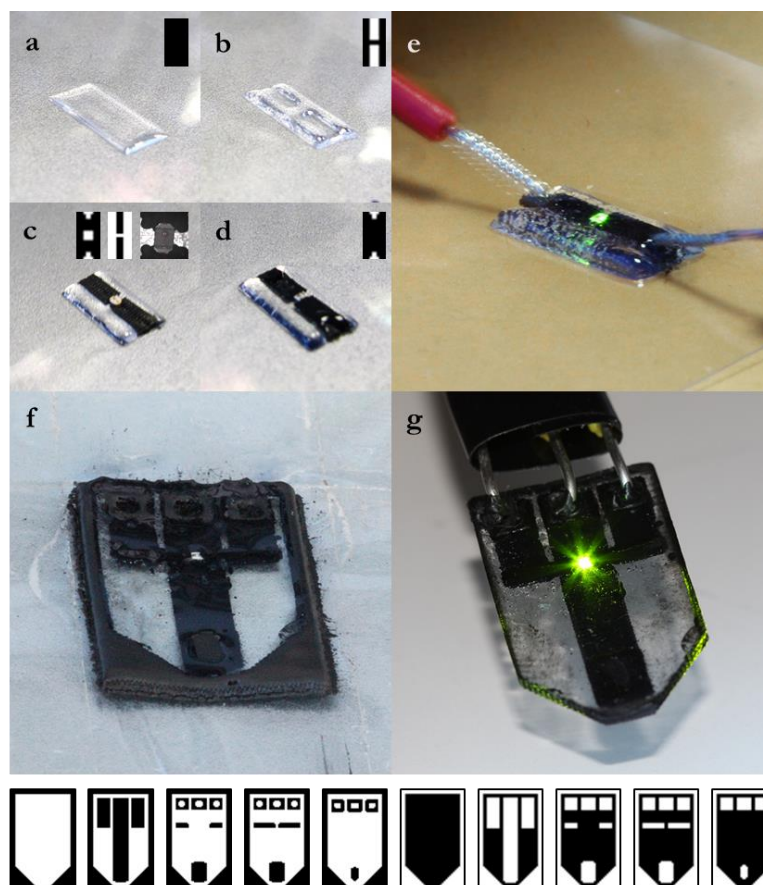


**Figure 129:** a, b, c & d) Steps to print an embedded LED (0.6 x 1.0 mm) and 2 carbon tracks. The insets in each picture show the required patterns and a picture of the LED. e) Finished structure (4.0 x 8.0 mm) showing the green light emitted by the embedded LED when 5 V are supplied. f & g) Embedded LED controlled by an all-printed capacitive sensor with a soluble outer frame to increase the resolution of the part (12.5 x 20.0 mm). Once the supports are removed the part is connected with a micro-controller and the LED is tested with a supply of 5 V. Printing files are shown at the bottom, with the black pixels representing the drop positions.

### 7.3.7 Printed electroluminescent devices

Electroluminescent (EL) materials emit light when are subjected to an electric field and are typically divided in two categories, injection EL and high-field EL. The former takes place under low fields due to the radiative electron-hole recombination at a p-n junction and is the working principle behind the LED, while the latter occurs when “hot” electrons are accelerated by high fields and collide with the dopant sites of the phosphor crystals (Bredol & Dieckhoff 2010). This explains why the typical structure of a conventional electroluminescent lamp is often described as a parallel-plate lossy capacitor, since instead of accumulating charge between the electrodes, part of the energy is emitted as radiation of a particular wavelength. A standard build structure is shown in Figure 130, where the different layers and their functionality are displayed. The phosphor paste is sandwiched between two electrodes, one of which is typically transparent, like PEDOT:PSS or ITO, or presents gaps to let the generated light escape the structure. The other conductor is known as back electrode and is normally chosen as a very low resistive material. Furthermore, if this material is reflective, such as silver or aluminium, it can act as a back mirror to boost the radiance output. The roles of the dielectric layer are multiple, but the main ones are preventing the contact between both electrodes in case the phosphor layer presents pinholes and increase the charge density on the interphase with the phosphor to increase the efficiency of the emission process (Jin-Young et al. 2010). This layer is normally composed of a dispersion of nanoparticles with an increased surface-to-volume ratio and high dielectric constant. Barium titanate ( $\text{BaTiO}_3$ ) is one of the most common choices for dielectric, since at high enough concentrations not only fulfils the previous requirements but also displays good reflectivity, which contributes to increase the output of the lamp in a similar way than reflective back electrodes (Hartmann & Nubler 2010). Having said that, this layer is not strictly essential for a functional lamp (Winscom et al. 2014)(Withnall et al. 2010) but is added to improve efficiency.

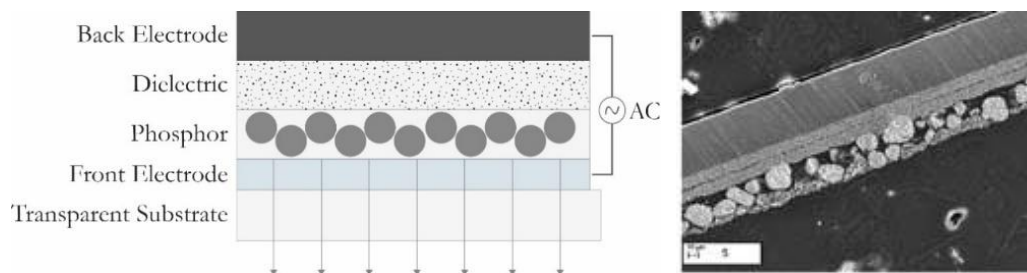


**Figure 130: Left)** Schematic illustration of the different functional layers on an AC powered electroluminescent device (ACPEL) in standard build configuration. **Right)** Cross-section of a screen printed electroluminescent lamp, showing from top to bottom the aluminium substrate, two layers of dielectric, the phosphor layer and a lower transparent film of ITO particles in a resin matrix. The structure without the substrate has an approximate thickness of 60  $\mu\text{m}$ . The image is reproduced from *Withnall et al.* (Withnall et al. 2011).

AC powdered electroluminescent devices (ACPEL), are one of the most common lamps based on this mechanism, and are still in use due to their homogeneous emission, possibility of covering large areas, flexibility and rapid procesability due to their relative insensitivity to oxygen and moisture (Withnall et al. 2010). In fact, thanks to the robustness of the materials involved it is possible to fabricate ACPEL devices by screen printing (Shon et al. 2012)(Toyama et al. 2009), offset lithography (Withnall et al. 2008) or spin coating (Kim et al. 2012) instead of using costly processes that require strictly controlled environments. These techniques, however, are incapable of creating complex multi-material patterns or require various mask per part, which contrasts with the freedom of digital fabrication. Therefore, an inkjet drop-on-demand approach would be advantageous to minimise material waste and increase complexity without additional cost. Promising results were obtained in this area by Angelo *et al.* (Angelo et al. 2013)(Angelo 2013) using ZnS:Mn nanocrystals in various inkjet formulations. However, even though successful DC-LEDs were reported, the ACPEL structure was abandoned due to the thin thickness of each deposited layer compared with the required thickness of the active layer, which not only extended notably the process length but also affected negatively the resolution of the features. This was mainly due to the restrictions that PIJ imposes on the inks, particularly in their viscosity, which in turn limits the particle size and amount of the solid phase. Hence, in the present work a high viscosity jetting approach is explored to produce all-jetted ACPEL devices.

To achieve this objective, a series of initial tests with commercial materials designed for screen printing were realised (Appendix A3). Using the conclusions extracted from these experiments, a UV-curable EL-phosphor composite was formulated and prepared (Appendix A3). The new paste contains a 55 wt% of ZnS:Cu particles with an average size of  $7.08 \pm 0.05 \mu\text{m}$  and demonstrated stable behaviour on the micro-dispensing valve when a  $100 \mu\text{m}$  nozzle is used. A lamp structure similar to the one shown in Figure 130 was followed in all cases with the exception that no dielectric layers were deposited. This is expected to reduce the efficiency of the lamps but, as it was verified during the initial tests (Appendix A3), it does not prevent radiation emission. The phosphor paste was printed at  $25 \text{ }^\circ\text{C}$ , with a pneumatic pressure of 0.2 MPa and a closing valve time of  $120 \mu\text{s}$ . The pulse length was fixed at 0.3 ms and the distance nozzle-substrate was kept at 1 mm, resulting in drops of  $650 \pm 10 \mu\text{m}$  on glass. Printing resolutions of 50 to 65 DPI were tested and 60 DPI was selected for its suitable coverage without pinholes. This resolution represents an approximate 35 % drop overlap, which agrees with the previously

determined optimum range. The materials used for electrodes include silver paste, carbon paint and an aqueous dispersion of PEDOT:PSS, which are printed and post-treated according with the settings previously determined. The printing substrates were alternated between polycarbonate films and glass slides. Since the printing system has a maximum capacity of 4 materials at a given time, with only 2 of them being deposited by the micro-dispensing valves, some viscous materials were hand coated (K Hand Coater, RK PrintCoat Instruments Ltd., UK) to speed the process. In other situations, the materials on the printing system were changed to continue the process. Several material combinations were tested to produce functional lamps, as it is shown in Figure 131. The electroluminescence of the lamps was checked using a 12 V DC to 110 V/400 Hz inverter (12 V EL Inverter, Adafruit, USA). The success of the approaches is based on the production on visible light in a low-light room. Further tests would be required in the future to optimise the design and output of these devices, but that goes beyond the proof-of-concept nature of the presented samples.

An all-printed bi-directional flexible lamp with patterned electrodes and phosphor layers was produced using PEDOT:PSS for both electrodes on polycarbonate foil (Figure 131a & b). The intensity of the emitted light was apparently lower than configurations with a more conductive back electrode, but it was produced under 10 minutes with just 2 functional materials, which makes it an attractive option for applications that require high customization and bi-directional emission with moderate intensities. Another batch of flexible samples was created with carbon paint as back electrode and PEDOT:PSS as patterned top electrode on polyester foil (Figure 131c & d). These structures showed the effect of the film thickness and homogeneity of both active layers on the emission output. Specifically, both samples show a clear increased intensity on the edges of the patterns, which is where the PEDOT:PSS layer is thinner. This is another manifestation of the dependency of both conductivity and transparency with the layer thickness, which suggests that an equilibrium needs to be found for each application. Similarly, a variation of the EL-phosphor layer like the one locally observed in certain areas of the star pattern, also produces increased luminosity, since the excited electroluminophores are closer to the surface. The opposite was tested in a similar structure with 2 layers of phosphor paste, which did not produce any visible light at the tested voltage and frequency. To complete the potential combinations of transparent and opaque electrodes, samples with carbon at both sides were produced with a hand-coated phosphor layer of 40  $\mu\text{m}$  (Figure 131e&f). These samples were not very efficient illuminating their surroundings but displayed

glowing features despite the high opacity of the carbon films, which can be used for printed indicators in many applications. It is noteworthy that in this case the edges of the features were the only illuminated part and little dependency of such light was found with the size of the pores. Since in this case the light cannot travel through the carbon areas, it is unlikely that it is related with the thickness of the deposition. Instead, a more plausible explanation is that the density of the electric field is higher in that area, since the situation is a classic example of a discrete charged flat element in front of a charged plane (Griffiths 2012). It is expected, however, that smaller holes result in brighter spots, since in that situation the contribution of the opposed edges can combine additively.

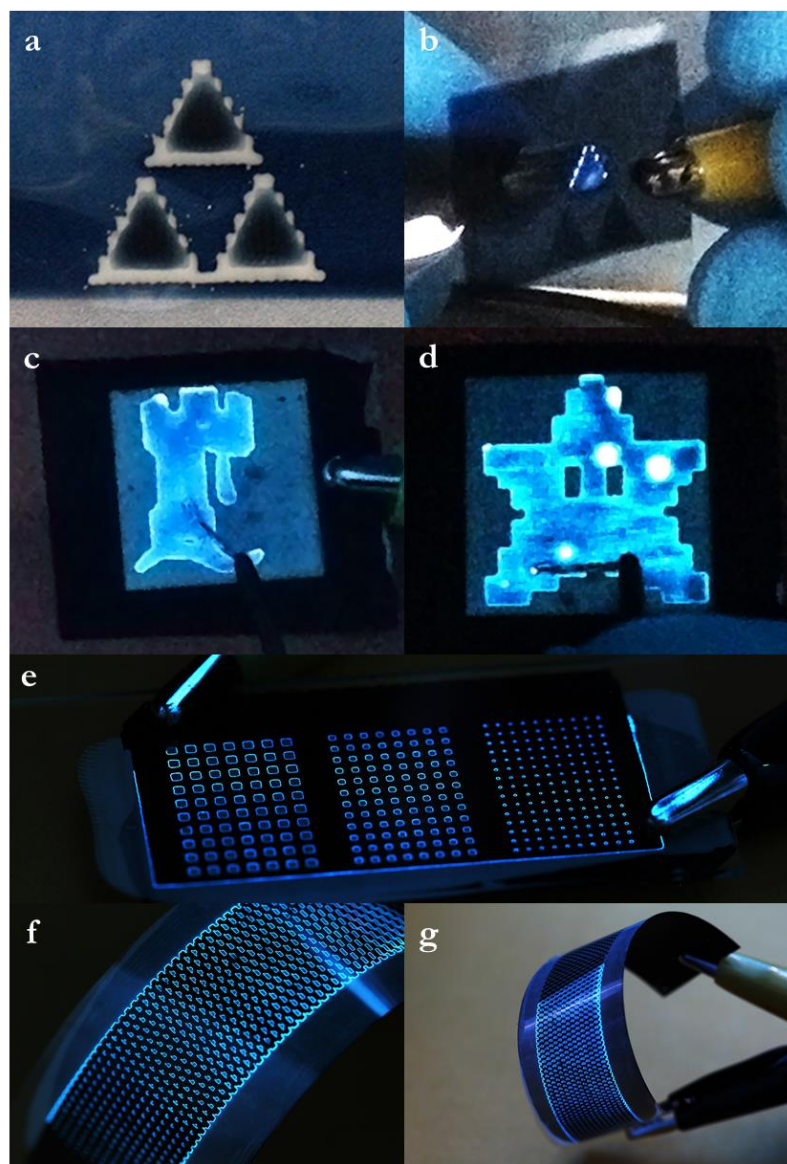


**Figure 131:** **a & b)** All-printed bi-directional flexible lamp with patterned phosphor layer and PEDOT:PSS electrodes. **c)** Electroluminescent lamp featuring the castle from the University of Nottingham logo. The back electrode is coated carbon paint while the front is PEDOT:PSS. **d)** EL-lamp with back electrode of carbon and PEDOT:PSS as transparent front element. Inhomogeneous deposition of the phosphor paste resulted in bright spots of light. **e)** Grid patterns of different pore size showing edge glow despite having both electrodes printed with opaque carbon paint. **f)** Flexible electroluminescent device with both electrodes printed with carbon paint on a polyester film.

The final sample in this section was created with the intention of summarising in one piece the capabilities of the system, since it features TPGDA, silver, carbon paint, PEDOT:PSS and the in-house formulated UV-curable phosphor paste. In particular, the front electrode has a frame of carbon and silver, filled with TPGDA, which shows its potential as a transparent encapsulant (Figure 132). Later a layer of PEDOT:PSS was deposited as a circle pattern, filling all segments in a continuous manner, which would receive a more homogeneous charge distribution thanks to the thick carbon frame acting as a bus bar. The UV-curable phosphor paste was later coated on top of the PEDOT:PSS and a back electrode of carbon was printed to finish the lamp. All materials were post-treated on the system, although the process had to be paused to switch the silver paste for the PEDOT:PSS, which took place in different printing sessions. This is the reason why there is some visible misalignment between the circular front electrode and the carbon frame, but it could be easily overcome by not removing the sample from the system or by using more than a single common indicator as print reference. Regardless, the sample displayed an apparent brighter behaviour than previous samples with only PEDOT:PSS in the front electrodes, which gives another example of the advantage of multi-material fabrication.

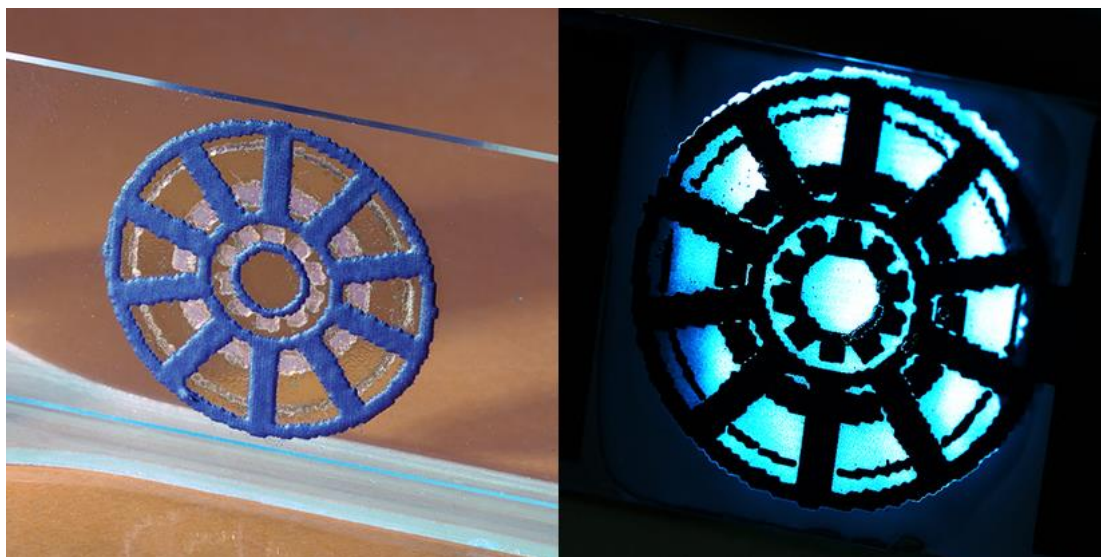


**Figure 132:** Multi-material sample (23.0 mm diameter) displaying a front electrode composed by carbon paint and silver paste partially encapsulated by a film of TPGDA (**left**). The process was then interrupted to change the silver for PEDOT:PSS and the lamp was completed with a layer of the transparent conductor, a layer of phosphor paste, connexion pads and back electrode of carbon. The lamp provided a higher intensity than previous attempts with only PEDOT:PSS as front electrode (**right**).

In conclusion, functional electroluminescent lamps have been fabricated using a multi-material drop-on-demand system capable of combining materials with a wide range of rheological properties. Furthermore, both the printing and post-processing stages took place in most cases in a fully-automated uninterrupted process. The versatility of this approach allowed the creation of functional parts with advanced characteristics such as flexibility and transparency. Future iterations of these experiments would require further characterisation of the produced samples and an optimisation of parameters such as printing resolution and layer thickness, since these were identified as the most relevant features for these applications. To take full advantage of the developed set-up and avoid stopping the process to change materials, it is recommended that a formulation of PEDOT:PSS with lower viscosity is dispensed in one of the PIJ printheads instead of the high viscosity approach here used. This not only would allow for thinner films but it would also provide less difference in the thickness of the edges, which is expected to result in more homogeneous light. Similarly, to improve the coverage of the in-house developed UV-curable phosphor paste, it is recommended to increase the jetting temperature, which would allow to print at lower resolutions without leaving pinholes, obtaining thinner and more homogeneous layers. Alternatively, this paste can be re-formulated in base of its rheology, based on the characterisation of high viscosity materials provided in this work to improve its spreadability. Furthermore, the lack of dielectric layers can be compensated by adding dielectric nanoparticles to the paste (Withnall et al. 2010), as it has been shown to increase the radiative output and improve its coverage. The same goes for its printability, which can be further optimised by carrying out high speed and grid experiments with various printing settings. Finally, it is expected that the printed devices behave differently in other voltage and frequency ranges, so upgrading the driver circuit would also expand the capabilities of these devices.

## 8. Conclusions and future work

The aim of this project was to fabricate functional 3D multi-material samples in a single additive process, which was successfully achieved. To this end, 3 different conductive materials, 2 photo-curable formulations and an in-house prepared electroluminescent paste were co-deposited with a custom AM system capable of ejecting a wide range of viscosities using 2 types of dispensing heads. To discuss the outcomes of the present project, the main objectives initially identified are discussed in the following sections, explaining how they have been fulfilled, the limitations encountered and suitable modifications for future studies. These objectives are:

- Identify **desirable** and **critical features** for a multi-material system capable of dispensing multiple materials with different properties. A digital fabrication approach is preferred to allow the creation of complex patterns without spending additional resources. This review need to include the post-processing required for certain functional materials to reveal their properties.
- **Design, develop** and **calibrate** a manufacturing system fulfilling the requirements previously recognised. This includes the definition and implementation of a clear **printing strategy** capable of dispensing and processing the materials in an efficient way.
- Characterise the **physical and electrical properties** of the fluids involved in the process that can affect their printability and functional performance. These properties include but are not limited to: density, shear viscosity, surface tension, particle size and electric resistivity.
- Test and optimise the **printability** of the selected materials on the developed system. The discussion of their behaviour should be performed in terms of **dimensionless numbers** and **processing windows** to facilitate the comparison of the results with established technologies such as PIJ.
- Study different **post-processing** treatments to polymerise, dry and sinter the selected printing materials. To do this, parameters such as the geometry or electrical resistance of the deposited films can be used to assess the applied post-treatments in terms of the functionality of the produced samples. Furthermore, since the present work is based on a layer-by-layer approach, the speed of the post-processing stage of each layer should also be considered to reduce as much as possible the length of the overall process.
- Use the gathered knowledge about the selected materials and the developed system to build **proof-of-concept parts** displaying high manufacturing freedom and internal electronic tracks.

## 8.1 Identification of required features for a multi-material AM system

After performing a thorough literature review of diverse AM techniques and materials (Chapter 2), it was concluded that a system capable of meeting the objectives of this project was required to at least present the following characteristics:

- **Multiple dispensing elements** to deposit functional and structural materials in 3D by a layer-by-layer approach. These heads are required to function in a **drop-on-demand** approach with resolution in the micro-range to harness the potential of digital fabrication.
- Capability of using **different types of printheads** to allow for a wider range of materials. Different ranges of viscosity would be beneficial to expand inkjet's material catalogue.
- Capable of **reading digital files**, **slice** them into individual layers and find a suitable and **optimised path** to deposit the drops in the minimum possible time adjusting control parameters such as print speed, frequency and resolution.
- **Substrate clamping system** to avoid the samples to move during the jetting process. It needs to be a reversible and repeatable system that permits quick exchange of substrates.
- **Integrated post-processing capabilities** for different materials such as UV-curable polymers, solvent-based fluids and metallic nanoparticles that require sintering.
- **Integrated vision system** to calibrate the printheads, align the printing patterns and inspect the results.

## 8.2 Platform design and development

Platform development was performed by heavily modifying an existing material printer to enable the deposition of multiple materials in 3D. This required the development of a **synchronization circuit** and the fabrication of a **new printing assembly** capable of holding 4 heads, 2 of them micro-dispensing valves to eject viscous fluids (Chapter 3). The assembly development required several prototype cycles before achieving success in all the key areas identified. This stage was clearly speeded up by the availability of other Additive Manufacturing systems such as LS, FFF and material jetting, since each piece could be fabricated, tested, refined and re-manufactured in a matter of hours. Moreover, the virtually limitless nature of AM allowed the creation of complex parts that would have been either impossible or very costly by other means.

The final assembly followed a **modular approach** that not only allowed for quick replacement of damaged or outdated parts but also opens the possibility of implementing different combinations of heads for future studies, such as 3 HVJ valves or 4 PIJ printheads.

The **jetting heads** themselves performed as expected, with the inkjet printheads displaying faster speed and greater resolution for low viscosity fluids and the micro-dispensing valves showing good general performance with more viscous materials. Nevertheless, the drop size of the valves was identified as its weaker attribute. This size was observed to be a result of the combination of drop volume, impact speed and spreadability. The latter is reduced for high viscosity fluids but is eventually dependent on each fluid-substrate combination, while the drop volume and speed can be controlled by modifying printing parameters such as the pneumatic pressure and the closing speed of the valve. However, even after careful tuning of the print settings of the different fluids, a common minimum volume of approximately 5 nl was encountered, which was attributed to the geometry of the nozzle chamber and the stroke of the valve. Thus, considering that modifying the inner geometry of the nozzle is costlier, a study of the effect of different stroke lengths is recommended for future work. In the meantime, higher printing resolution of the functional fluids can be obtained by depositing them on pre-printed negative volumes with smaller sizes than the free-spreading drops. These guiding structures can either be printed with a photocurable structural material or a soluble support.

Apart of the printing assembly, other sub-systems were added or modified, such as the **UV and IR lamps** used for post-treatment, the automated cleaning station and additional micro-controllers that monitored in real time properties like temperature and samples' resistance. Furthermore, the **integrated vision** system was preserved with its hardware unaltered but modifications in its software allowed automatic image scanning and time-lapse videos. The integrated monochrome camera was heavily used to calibrate each dispensing head individually, which is crucial when different interlocking patterns are produced with different materials. This vision system, with additional code modifications, could be used in future experiments to assess in real time the printability of a material looking at the area and circularity of the drops' footprints, similarly to the approach followed in this thesis. Also, it would not require much modifications to use the camera as a 3D scanner based on focus stacking or to assess the sintering degree of a conductive material based on its colour change (Cherrington et al. 2012).

Finally, apart from the hardware modification of the system, a new **printing strategy** was designed and implemented with the objective of creating multi-material parts with minimal geometric distortion. This approach was based on the creation of structural blocks of constant width by combining layers of the different involved materials in specific ratios (Figure 53). The layer thickness information was obtained from the fabrication and 3D scanning of several multi-layered samples that displayed high linearity between the total sample height and the number of layers. This approach, despite being successful in the fabrication of 3D multi-material structures, does not consider the differences in the layer thickness that arise from different pattern geometries and substrates. Thus, in future applications of the set-up developed in this thesis, an approach based on modelled volumes is suggested. This methodology can follow the same strategy here used when the material with reduced spreading was printed first to create negative volumes for the following fluid to fill. However, instead of focusing on the dry thickness of the materials, an approach considering the wet and dry volume of the deposited droplets is likely to result in more accurate representations of the 3D files.

### 8.3 Choice and characterisation of materials

Several formulations were chosen according with their potential usefulness for multi-functional AM, representing areas such as nanoparticle-based fluids, conductive polymers, composites and photocurable materials. It is noteworthy that all the materials selected were originally formulated for other manufacturing techniques such as stereolithography, screen printing and brush painting. The fact that these materials were successfully ejected without modifying their formulation means that the manufacturing approach studied in this thesis already has available a wide catalogue of materials. Furthermore, despite using the same fluids, this multi-material approach can result in more complex structures thanks to its digital and 3-dimensional nature.

The substances used in this work were classified as particle-based **functional materials** and photocurable **structural materials**. The structural materials tested were a high viscosity resin and TPGDA, which displayed similar polymerisation and thermal behaviour (Figure 67) but very different viscosity (Figure 68 & Figure 72). The variation in the last property resulted in their ejection using different dispensing heads, which affected their resolution and processing speed. Consequently, TPGDA printed with PIJ printheads was selected over the resin as structural material for this work.

The functional materials displayed different densities, solid loading and surface tension, but their rheologic response was relatively similar. In particular, all 3 fluids were shear thinning with viscosities in the order of  $10^3$  Pa·s at low shear rate ( $10^{-2}$  s $^{-1}$ ). This feature allowed them to be stable dispersions during storage but flow through the nozzle when a moderate pressure was applied. Furthermore, this internal micro-structure reduced the spreading of the deposited drops, which increased the resolution of the system and reduced the influence of the substrates in the final result. The similarity in their rheological properties did not translate in comparable resistivity after thermal processing, since the carbon paint and PEDOT:PSS displayed electrical resistivities in the order of  $10^{-3}$  and  $10^{-4}$   $\Omega$ m respectively, while the silver paste resulted in  $10^{-7}$   $\Omega$ m. According with these results it seems obvious to select the silver paste as the best option for the current system, however, this material presented numerous processing problems such as poor adhesion to the substrates, tendency to crack and rough surfaces due to solvent boiling (Figure 110 & Figure 111). Furthermore, each layer of this material required a thermal treatment that, extended during a long period of time, can damage the surrounding materials. The aqueous dispersion of PEDOT:PSS also required a thermal step each layer but resulted in flexible and homogeneous films. Its main problem, however, was the thin thickness of these layers (Figure 115), product of its low solid content (Figure 65). This leaves the carbon paint as the best performing material for 3D fabrication of conductive tracks, but it has the downside of displaying the lowest electrical conductivity and occasional nozzle blockage due to the excessive size of its graphite flakes (Figure 63) and the relatively quick evaporation of its solvent. Therefore, the selection of one material over others is ultimately determined by the application. However, if a material was to be formulated for future work following the approach presented in this thesis, a UV-curable conductive composite would be suggested (Sangermano et al. 2013) with carbon nanotubes or silver nanowires as filler to increase the percolation and, consequently, the resulting conductivity. This was the idea behind the in-house formulation of EL-phosphor (Appendix A3), which resulted in a stable paste with quick post-processing at low temperature, imperceptible volumetric shrinkage, acceptable flexibility and high solid loading.

#### **8.4 Printability studies and processing window of the system**

High speed videos, stroboscopic imaging, semi-automatic footprint analysis and drop mass experiments were performed to characterise the printability of the selected fluids. These tests helped to identify 2 distinct modes of ejection, pneumatically initiated

and mechanically initiated, depending if the applied pneumatic pressure was enough to initiate a stream of fluid on its own or not, respectively. The transition between both behaviours was attributed to a critical pressure that is expected to be material and geometry dependent. **Pneumatically initiated** configurations resulted in slower drop velocities but increased their volumes notably, which eventually led to bigger dots on the substrate, limiting the creation of small features. Moreover, these configurations resulted in a fluid-on-fluid collision, often in-flight, if the tail of the jet was faster than the leading part as a result of the closing of the valve, which reduced notably the repeatability of these configurations. Alternatively, **mechanically initiated** configurations led to the smallest drop volumes but their excessive impact velocities occasionally resulted in splashing, affecting negatively to the circularity of the drops.

Independently of the jetting regime, **residual fluid** left on the nozzle plate was identified as the main source of unstable ejection, since it changes the initial conditions of each droplet overtime and can eventually stop the ejection completely. The combination of the observations regarding the critical pressure, the residual fluid on the nozzle, the atomization of the jets and the ejectability of the fluids in general were collected in a single processing map (Figure 82) that described successfully the behaviour of all the fluids tested. This map also identified two stable regions of ejection, one per type of jet initiation. Later, the Reynolds, Weber and Ohnesorge numbers of the fluids in different configurations were computed and a printability window was defined (Figure 101), which combines the results of the previous jettability observations with the splash of the drops observed during the footprint analysis. This representation of the obtained data also revealed an apparent lower threshold related with the stability of the configurations of the form  $Re\sqrt{We} = C$ , where C is a constant that was assigned a value of 10 to separate the stable events from the unstable according with the high-speed videos recorded in this work. Further experiments are required in order to establish and understand such threshold. Especially considering that magnitudes as relevant as the extensional viscosity or the elastic components of the viscosity have not been considered in the present discussion but are expected to contribute to the break-up and spreading mechanisms. The main reasons for this exclusion are the complexity of the characterisation of these magnitudes and the small temporal and spatial scales of their effects, which in most cases were not captured by the high-speed camera used in the present study. Thus, a relevant experiment to deepen the understanding of HVJ would be the recording of new videos with an updated set-up using standard fluids, both Newtonian and non-Newtonian, with known properties. This data,

combined with the characterisation of the inner geometries of the valve, would be enough to model the jetting mechanism and move towards the prediction of the behaviour of other materials, which is a requirement if this technology is expected to be used in real applications. Nevertheless, the results here presented and the provided printability map are expected to be a suitable starting point for future experiments in this field.

## 8.5 Post-processing studies

The post-processing techniques used in the present work consisted on photopolymerisation, accelerated solvent evaporation and a combination of chemical conversion and sintering. These were all realised using the integrated **UV and a IR lamps**, scanning at a certain distance and speed over the samples. The UV lamp was particularly useful since it was capable of curing the photopolymers and heat the carbon paint due to its strong absorption at a wide range of wavelengths. Also, this approach displayed a faster response and lower residual heat due to its LED nature and integrated cooling system.

The assessment of the post-processes success was initially based on the optical inspection of the functional samples' geometry, but later an experiment where their **electrical resistance was measured in real time** was implemented. This process showed the differences that various post-process conditions had on the functionality of printed tracks, helping also to determine the minimum required length of the treatment to speed the process and avoid unnecessary radiation overexposure. These tests were performed on commercial PCBs and monitored with an external microcontroller, but due to geometric restrictions it could not measure the resistance and the temperature at the same time. This limitation was overcome by performing each experiment 2 times in analogous conditions to measure these magnitudes separately, but it would be beneficial for the accuracy of the results and the overall length of the process if both properties could be measured simultaneously. The recommended solution for a future update of the hardware would be the implementation of a contactless thermal sensor, like an IR-camera or a digital pyrometer.

The implementation of such external sensor would also help to improve the control of the emitted radiation, since maintaining a defined temperature on the samples was one of the main challenges regarding the post-process stage. This was particularly relevant for the silver paste, which displayed a narrow window of thermal operation. If the temperature was too low, the nanoparticles did not sinter and their organic ligands were not removed, which resulted in poor electric conductivity. Conversely, a high temperature

induced violent boiling on the liquid phase, resulting in inhomogeneous surfaces with pinholes in the worst cases. Situations like this one are expected to improve with a more precise temperature control, which could be based on a proportional-integral-derivative (PID) control algorithm, using the thermal sensor as input and the lamp intensity as output. A cooling system could be added to increase the responsiveness of the process, but care must be taken not to introduce air currents that disrupt the trajectories of the jets.

## 8.6 Fabrication of 3D multi-material functional structures

The gathered information during the rest of this thesis was applied to fabricate several **multi-material proof-of-concept structures** (section 7.3) to showcase the present and future capabilities of the hybrid approach proposed in this work. These include multi-material patterns with designed local physical properties, 2D and 3D functional circuits, flexible multi-layered devices, 3-dimensional structures with embedded components, and all-printed electroluminescent devices as an example of advanced functionality. Detailed characterisation of each device was not performed but the samples presented functionalities such as electrical conductivity and electroluminescence. Further tests and pattern re-designs would be required to assess the efficiency and suitability of printed devices of these characteristics, but these initial tests are promising.

During the fabrication of these multi-material structures, several **processing limitations** already discussed such as surface cracking, poor adhesion or material degradation due to radiation overexposure were observed. However, since the solutions of these problems have already been discussed and are mostly material dependent, these are not a major concern for the future of this technology. More relevant are the **software and pattern limitations** encountered during the preparation of the files and their fabrication. For instance, since continuous patterns were used for most of this work, the resolution of the files was often limited by the diameter of the drops and the fluid arrangement at certain drop overlaps. This not only reduces the overall resolution of the system, but introduces the problem of incompatible DPIs, which is the situation where 2 files that are supposed to complement do not match due to their different resolutions. This situation can be partially solved by choosing resolutions that are multiples of each other, but this adds unnecessary complexity to the creation of the files. Alternatively, all patterns can be designed with high resolution representing the position of the drops as discrete dots, as it was shown in Figure 127. This approach solves the issue and increases the achievable complexity of the printed patterns, but is even more demanding on the design

stage. Another example of geometric limitation that would benefit from patterns generated with increased complexity is the already mentioned miss-match between the layer thickness of different materials. This was successfully addressed in this thesis by creating structural blocks of constant thickness using a pre-defined material ratio (Figure 53), but it is expected that a volumetric approach would improve the results. However, creating these complex patterns is outside of the capabilities of most commercial design packages.

Similarly, the representation of distinct local properties within a multi-material part is greatly hindered by the **design software** commercially available. Nevertheless, it is expected that the situation changes in the recent future, since many publications report software architectures capable of designing these 3D multi-material structures with programmable properties (Vidim et al. 2013)(Chen et al. 2013) and the computing power of the average computer can handle most of the required calculations. This new approach to design opens the possibility of not only optimise the shape of the parts but also their functionality (Chen et al. 2013)(Panesar et al. 2015). However, to fully solve the bottleneck involving the design of multi-material functional parts and unlock the full potential of advanced AM technologies, the **standard file** should move away from the .STL, which captures only geometric information in a triangle-based mesh, towards richer formats such as AMF (ASTM & International 2013) or 3MF (3MF Consortium 2015), which are capable of storing metadata, local properties, material specifications, curved triangles and generative formulas.

In conclusion, the multi-material fabrication approach presented in this work is fully capable of creating complex functional parts. Some processing drawbacks are still encountered due to the novelty of the methodology but are not major barriers to its wider implementation. Nevertheless, only when the design and pattern generation methodologies are updated, the full potential of this advanced Additive Manufacturing technology would be unleashed.



# 9. Appendices

## A1. Fundamental code for the printing platform

The *part configurator* oversees the switching between printheads and their associated printing parameters (*profiles*) depending on the file to print at any given moment. These structures are written in Visual Basic .NET, which combines logic segments (.CS files) and definition files (.XML files). These structures are based on the existing routines provided by the LP50 manufacturer (Roth & Rau B.V., Netherlands), which make use of several external configuration files and functions not included here.

### Part configurator

#### repMix\_file.xml

```
<?xml version="1.0" encoding="utf-8"?>

<RecipeFlow xmlns:xsi="http://www.w3.org/2001/XMLSchema-instance"
xmlns:xsd="http://www.w3.org/2001/XMLSchema">
  <RecipeScript>repMix_file.cs</RecipeScript>

  <Parameters>

    <Parameter Name="Recipe.Name" Type="Text" Unit="" Default=""
Description="File name" Visible="Operator" Writable="SystemEngineer"/>
    <Parameter Name="Recipe.Recipes" Type="Text" Unit=""
Default="ProfileA,ProfileB" Description="Profiles to run in order"
Visible="Operator" Writable="SystemEngineer" />
    <Parameter Name="Recipe.SB" Type="Number" Unit="" Default="1"
Description="Structural Blocks" Visible="Operator" Writable="SystemEngineer"
/>
    <Parameter Name="Recipe.SB_step" Type="Number" Unit="mm"
Default="0.050" Description="Structural Block thickness" Visible="Operator"
Writable="SystemEngineer" />
    <Parameter Name="Recipe.SB_n" Type="Number" Unit="Times each"
Default="1" Description="Structural Block repetition each"
Visible="Operator" Writable="SystemEngineer" />
  </Parameters>

</RecipeFlow>
```

#### repMix\_file.cs

```
/*
This "Repetier recipe" runs sequentially the specified recipes and adjust
the Z accordingly.
It requires that the settings of the print are selected on the individual
recipes and do NOT change the file to print.
Author: Javier Ledesma (20.10.2015).
*/

public void Initialize()
{
}
```

```

public void Execute()
{
    string Recipelist = Parameters.GetValue("Recipe.Recipes");
    string[] Recipes = Recipelist.Split(',');
    string ParentRecipe = RecipeHandler.activeSetFile;
    string name = Parameters.GetValue("Recipe.Name");

    int sb = Parameters.GetIntValue("Recipe.SB"); //Structural blocks
    double sb_step = 0.01;
    int n = Parameters.GetIntValue("Recipe.SB_n"); //Structural block
    repetitions

    Position SUB = Positions.Get("SubstrateThickness");//Read position of
    #substrate thickness#
    double Zrep = SUB.GetAxisFloat(Position.Axes.Z);
    double ZO = Zrep;//Original Z

    Simulator.Clear();
    Parameters.SetValue("StandardPrint.AutoClearSimulator",false);

    for(int i=1;i<=sb;i++) //Different structural blocks
    {
        for(int j=1;j<=n;j++) //Repetitions of each structural block
        {
            foreach(string Recipe in Recipes)
            {
                string active = string.Format(@"c:\LP50\Recipes\4
Switching\{0}.Recipe.xml", Recipe);
                if(File.Exists(active))
                {
                    RecipeHandler.ActivateSet(active,true);

                    //Test reading "Recipes []"

                    if(File.Exists("C:\\Users\\LP50\\Pictures\\BMPs for
LP50\\Hybrid\\"+name+i.ToString()+"_"+string.Format("{0}",Recipe)+".bmp"))
                    {
                        ParameterHandler.Instance.SetValue("General.ProgressText",name+i.ToString()+
                        "_"+string.Format("{0}",Recipe)+".bmp is coming!");
                        Thread.Sleep(100); // Javier

                        Parameters.SetValue("Recipe.Bitmap","C:\\Users\\LP50\\Pictures\\BMPs for
LP50\\Hybrid\\"+name+i.ToString()+"_"+string.Format("{0}",Recipe)+".bmp");

                        Conversion.StartConversion(Parameters.GetValue("Recipe.Bitmap")); // re-
                        convert the bitmap

                        Script.Run(active);
                    }
                    else
                    {
                        Helper.GenerateScriptWarning("Repeater",string.Format("Could not find: {0},
it is skipped!",name+i.ToString()+"_"+string.Format("{0}",Recipe)+".bmp"));
                    }
                }
                else
                {
                    Helper.GenerateScriptWarning("Repeater",string.Format("Could not find '{0}',
it is skipped!",Recipe));
                }
            }
        }
        //Adjust Z to match Structural Block thickness
        Zrep = Zrep + sb_step;
        SUB.Change(Position.Axes.Z, Zrep);
    }
}

```

```

    //Z correction
    Zrep = Z0;
    SUB.Change(Position.Axes.Z, Zrep );
    //
    Parameters.SetValue("StandardPrint.AutoClearSimulator", true);
    RecipeHandler.ActivateSet(ParentRecipe, true);
}

```

## Profiles

### profile.xml

```

<?xml version="1.0" encoding="utf-8"?>
<RecipeFlow xmlns:xsi="http://www.w3.org/2001/XMLSchema-instance"
xmlns:xsd="http://www.w3.org/2001/XMLSchema">
  <RecipeScript>profile.cs</RecipeScript>
  <Parameters>
    <Parameter Name="Recipe.DoMaintenance" Type="Slider" Unit="" Default="0"
PossibleValues="0;$ (No) ,1;$ (Yes) " Description="$ (RunMaintenance) "
Visible="Operator" Writable="SystemEngineer"/>
    <Parameter Name="Recipe.Bitmap" Type="File" Unit=""
Default="..\SampleBitmaps\" Description="$ (ImageFile) " Visible="Operator"
Writable="SystemEngineer" />
    <Parameter Name="Recipe.X_Resolution" Type="Number" Unit="dpi"
Default="500" Description="$ (XResolution) " Visible="Operator"
Writable="SystemEngineer"/>
    <Parameter Name="Recipe.Y_Resolution" Type="Number" Unit="dpi"
Default="500" Description="$ (YResolution) " Visible="Operator"
Writable="SystemEngineer"/>
    <Parameter Name="Recipe.ImageWidth" Type="Number" Unit="mm" Default="0"
Description="$ (ImageWidth) " Visible="Operator" Writable="SystemEngineer"/>
    <Parameter Name="Recipe.ImageHeight" Type="Number" Unit="mm"
Default="0" Description="$ (ImageHeight) " Visible="Operator"
Writable="SystemEngineer"/>
    <Parameter Name="Recipe.StepSize" Type="Number" Unit="pixels"
Default="1" Description="$ (StepSize) " Visible="Operator"
Writable="SystemEngineer" />
    <Parameter Name="Recipe.IgnoreRecipeSize" Type="Slider" Unit=""
Default="0" PossibleValues="0;$ (Yes) ,1;$ (No) "
Description="$ (IgnoreRecipeSize) " Visible="Operator"
Writable="SystemEngineer" />
    <Parameter Name="Recipe.Mask" Type="Slider" Unit="-" Default="QF2"
PossibleValues="QF1,QF2,QF3,QF4,QF5,QF6,QF7,QF8,QF9,QF10,QF11,QF12,QF13,QF14
,QF15,QF16,PIXDRO_SIGNATURE,SPECTRA_SIGNATURE,SPECTRA2_SIGNATURE,SPECTRA_DUA
L_SIGNATURE,XAAR1001_SIGNATURE,XAAR1001_DUAL_SIGNATURE,KM204_SIGNATURE,KM512
_SIGNATURE,OCECOBALT_SIGNATURE,TRIDENT_SIGNATURE,XAAR1001_SMOOTH_TRANSITION_
1,XAAR1001_SMOOTH_TRANSITION_2,XAAR1001_SMOOTH_TRANSITION_3,XAAR1001_SMOOTH_
TRANSITION_4,XAAR1001_SMOOTH_TRANSITION_5,XAAR1001_SMOOTH_TRANSITION_6,XAAR1
001_SMOOTH_TRANSITION_7,XAAR1001_SMOOTH_TRANSITION_8,XAAR1001_SMOOTH_TRANSIT
ION_9,XAAR1001_SMOOTH_TRANSITION_10,XAAR1001_SMOOTH_TRANSITION_15,XAAR1001_S
MOOTH_TRANSITION_20,XAAR1001_SMOOTH_TRANSITION_30,XAAR1001_SMOOTH_TRANSITION
_40" Description="$ (Mask) " Visible="Operator" Writable="SystemEngineer" />
    <Parameter Name="Recipe.Direction" Type="Slider" Unit="-" Default="1"
PossibleValues="1;$ (Uni-directional) ,2;$ (Uni-directional reverse) ,3;$ (Bi-
directional) " Description="$ (Printdirection) " Visible="Operator"
Writable="SystemEngineer" />
    <Parameter Name="Recipe.Tolerance" Type="Number" Unit="pixels"
Default="0.015" Description="$ (Tolerance) " Visible="Operator"
Writable="SystemEngineer" />
    <Parameter Name="Recipe.TOF" Type="Number" Unit="ms" Default="0"
Description="$ (TOF) " Visible="Operator" Writable="SystemEngineer" />
    <Parameter Name="Recipe.PrintAngle" Type="Slider" Unit=""
Default="90" PossibleValues="0;$ (X-Reverse) ,90;$ (Y-Normal) ,180;$ (X-
Normal) ,270;$ (Y-Reverse) " Description="$ (PrintAngle) " Visible="Operator"
Writable="SystemEngineer" />
    <Parameter Name="Recipe.GenerateData" Type="Slider" Unit=""
Default="2" PossibleValues="0;$ (None) ,1;$ (Before motion) ,2;$ (During

```

```

motion),3;$(OnlyAfterParamChange)" Description="$(GenerateData)"
Visible="Operator" Writable="SystemEngineer" />
  <Parameter Name="Alignment.Activated" Type="Checkbox" Visible="Operator"
Writable="SystemEngineer" />
  <Parameter Name="Alignment.SettingsFile" Type="File" Visible="Operator"
Writable="SystemEngineer"/>

  <!--Parameters added by PixDro Engineer on site-->
  <Parameter Name="Recipe.HeadAssy" Type="File" Unit=""
Default="..\HeadAssy\" Description="Assembly" Visible="Operator"
Writable="SystemEngineer" />
  <!--Parameters added by user Javier Ledesma-->
  <Parameter Name="Recipe.CureSpeed" Type="Number" Unit="mm/s"
Default="50" Description="UV treatment speed" Visible="Operator"
Writable="SystemEngineer" />
  <Parameter Name="Recipe.IRSpeed" Type="Number" Unit="mm/s" Default="50"
Description="IR treatment speed" Visible="Operator"
Writable="SystemEngineer" />

  <Parameter Name="Recipe.x_shift" Type="Number" Unit="%" Default="0"
Description="Shift in x-axis" Visible="Operator"
Writable="SystemEngineer"/>
  <Parameter Name="Recipe.y_shift" Type="Number" Unit="%" Default="0"
Description="Shift in y-axis" Visible="Operator"
Writable="SystemEngineer"/>
  <Parameter Name="Recipe.SizeCorrection" Type="Slider" Unit=""
Default="1" PossibleValues="0;$(Yes),1;$(No)" Description="Size Correction
with shift" Visible="Operator" Writable="SystemEngineer" />
  <Parameter Name="Recipe.PICO" Type="Slider" Unit="" Default="0"
PossibleValues="0;(None),1;(PICO A),2;(PICO B)" Description="PICO valve
used" Visible="Operator" Writable="SystemEngineer" />
  <Parameter Name="Recipe.Repeat" Type="Number" Unit="" Default="1"
Description="Repeat" Visible="Operator" Writable="SystemEngineer" />
  <Parameter Name="Recipe.Step" Type="Number" Unit="mm" Default="0.000"
Description="Thickness per step" Visible="Operator"
Writable="SystemEngineer" />
  <Parameter Name="Recipe.Drying_time" Type="Number" Unit="ms"
Default="100" Description="Drying time between layers" Visible="Operator"
Writable="SystemEngineer" />
  <Parameter Name="Recipe.Additional_Maintenance" Type="Slider" Unit=""
Default="0" PossibleValues="0;$(No),1;$(Yes)" Description="Run additional
maintenance after the file is printed" Visible="Operator"
Writable="SystemEngineer"/>
  <Parameter Name="Recipe.doCure" Type="Slider" Unit="" Default="0"
PossibleValues="0;No,1;At the end,2;Live curing,3;Both" Description="UV
curing" Visible="Operator" Writable="SystemEngineer"/>
  <Parameter Name="Recipe.PICOFrequency" Type="Number" Unit=""
Default="200" Min="1" Max="5000" Description="PICO frequency"
Visible="Operator" Writable="SystemEngineer"/>
  <Parameter Name="Recipe.Zreset" Type="Slider" Unit="" Default="1"
PossibleValues="0;$(No),1;$(Yes)" Description="Z reset after print"
Visible="Operator" Writable="SystemEngineer"/>
  <Parameter Name="Recipe.doIR" Type="Slider" Unit="" Default="0"
PossibleValues="0;None,1;Manual,2;Digital;" Description="IR treatment:
Manual Control" Visible="Operator" Writable="SystemEngineer"/>
  <Parameter Name="Recipe.IRdigital" Type="Slider" Unit="" Default="a"
PossibleValues="a;Set5.5,b;Set6.5,c;Set4.5,d;Set4,e;Set5,f;Set6,g;Set7,h;Set
8,i;Set9,j;Set10" Description="IR digital Setting" Visible="Operator"
Writable="SystemEngineer"/>
  <Parameter Name="Recipe.IRtimetowait" Type="Number" Unit="ms"
Default="0" Description="IR time to reach T" Visible="Operator"
Writable="SystemEngineer" />
  <Parameter Name="Recipe.Service" Type="Slider" Unit="" Default="0"
PossibleValues="0;No,1;Yes" Description="Move to Service Position at the
end" Visible="Operator" Writable="SystemEngineer"/>

</Parameters>
</RecipeFlow>

```

**Profile.cs**

```

/*
    Title:                Printhead Profile
    Author:               Javier Ledesma
    Date:                 2014-2016
    Based on "LP50 Standard printing script (Revision 40)" from GJ Pixdro BV
    (05 March 2008).
*/

public void Initialize()
{
}

public void Execute()
{
    bool z_safe = true;
    bool simOnly = (Parameters.GetIntValue("Simulator.SimulationType")==1);

    Position sub = Positions.Get("SubstrateThickness");//J, multilayer
    double z = sub.GetAxisFloat(Position.Axes.Z);//J, multilayer
    double zOrg = z;//J, multilayer
    double d = 0.03;//J, multilayer
    int r = Parameters.GetIntValue("Recipe.Repeat");//J, multilayer
    int dT = Parameters.GetIntValue("Recipe.Drying_time");//J, multilayer,
    drying time

    double Xdpi = Parameters.GetIntValue("Recipe.X_Resolution"); // Javier,
    shifts
    double dx = 25.4/Xdpi; //J
    double Ydpi = Parameters.GetIntValue("Recipe.Y_Resolution"); // Javier,
    shifts
    double dy = 25.4/Ydpi; //J
    double ax = Parameters.GetDoubleValue("Recipe.x_shift")*dx/100; // Javier,
    shifts
    double ay = Parameters.GetDoubleValue("Recipe.y_shift")*dy/100; // Javier,
    shifts*/

    int corr = Parameters.GetIntValue("Recipe.SizeCorrection"); //Javier,
    check if the Size Correction is active
    double imgw = Parameters.GetDoubleValue("Recipe.ImageWidth");
    double imgh = Parameters.GetDoubleValue("Recipe.ImageHeight");

    int PICO_head = Parameters.GetIntValue("Recipe.PICO"); //J Pico valve
    reader
    string Pico = PICO_head.ToString(); //J Pico valve reader
    int freq = Parameters.GetIntValue("Recipe.PICOFrequency");
    double speed = (freq * 25.4)/Ydpi; // I think taking into account Y dpi is
    enough
    string com = "COM6";
    System.IO.Ports.SerialPort myPort3 = new System.IO.Ports.SerialPort(com);

    HeadAssy.ActivateSet(Parameters.GetValue("Recipe.HeadAssy"), true);
    if (PICO_head!=0)
    {
        Parameters.SetValue("Motion.PrintSpeed[0]", speed);
    }

    Position pos = new Position();
    if (Parameters.GetIntValue("Printview.UseAlignedPos") > 0 &&
    !Positions.Exists("ParentReferencePos"))
    {
        // Use the XY position calculated by the alignment system
        pos = Positions.Get("AlignedStartPosition");
    }
    else
    {

```

```

        // Use the Print Start position parameter to determine the printing
start position
        pos = Positions.Get("PrintStartPosition");
    }
    double X = pos.GetAxisFloat(Position.Axes.X);
    double Y = pos.GetAxisFloat(Position.Axes.Y);

    // Only check z_safe if not in simulation mode
    if(!simOnly)
    {
        Helper.CheckPrintConditions();
        PHD.StopHead(DataGen.Active.HeadInfo);
        z_safe = Motion.CheckHomePos(Position.Axes.Z);
    }

    if(z_safe)
    {
        if ((!simOnly) & (Parameters.GetIntValue("Recipe.DoMaintenance"
>0))
            Script.Run(Helper.GetScriptDir() + "maintenance_Javier.cs");

        if ((!simOnly) &
(ParameterHandler.Instance.GetBoolValue("Alignment.Activated")))
        {
            AlignmentFunc.Align();
            if (!ParameterHandler.Instance.GetBoolValue("Alignment.Success"))
                // generate error!
                return;
        }

        //Serial Communication block
        Parameters.SetValue("General.ProgressText", "Serial Communication");
        Thread.Sleep(50); //Wait X ms

        //Serial communication Open
        System.IO.Ports.SerialPort myPort = new
System.IO.Ports.SerialPort(com);
        if (myPort.IsOpen == false) //if not open, open the port
            myPort.Open();

        if (myPort.IsOpen)
        {
            myPort.DiscardInBuffer();
            myPort.DiscardOutBuffer();

            myPort.Write(Pico);
            Thread.Sleep(50);
        }
        myPort.Close();
    }

    //End Com Block

    /*if(corr==0)
    {
        imgw = imgw + dx; //Correction of image width due to shifts, J
        imgh = imgh + dy; //Correction of image height due to shifts, J
        //ParameterHandler.Instance.SetValue("Recipe.ImageWidth","777");
    }*/

    //shifts, J
    X = X + ax; // J change
    Y = Y + ay; // J change

    pos.Change(Position.Axes.X, X);
    pos.Change(Position.Axes.Y, Y);

    //end shifts, Javier

```

```

        //repeat cycle, always the same file
        for(int i=1;i<=r;i++)
        {
            Parameters.SetValue("General.ProgressText", "Step: " +
i.ToString());
            Thread.Sleep(150); //Wait X ms

            Thread.Sleep(10); //Wait X ms
            if ((!simOnly) & ((Parameters.GetIntValue("Recipe.doCure")==2
|| (Parameters.GetIntValue("Recipe.doCure")==3)))){ // Live curing
                //Serial communication Open (Javier)
                //System.IO.Ports.SerialPort myPort3 = new
System.IO.Ports.SerialPort("COM4");
                if (myPort3.IsOpen == false) //if not open, open the port
                    myPort3.Open();

                if (myPort3.IsOpen){
                    myPort3.DiscardInBuffer();
                    myPort3.DiscardOutBuffer();
                    myPort3.Write("0");
                    Thread.Sleep(100); //Wait X ms
                    myPort3.Write("4");
                    Thread.Sleep(100); //Wait X ms
                }
            }
            Script.Run(Helper.GetScriptDir() + "print.cs"); //PRINT!!

            if ((!simOnly) &
((Parameters.GetIntValue("Recipe.doCure")==2|| (Parameters.GetIntValue("Recip
e.doCure")==3)))){ // Live curing
                if (myPort3.IsOpen){
                    myPort3.DiscardInBuffer();
                    myPort3.DiscardOutBuffer();
                    myPort3.Write("0");
                    Thread.Sleep(100); //Wait X ms
                    myPort3.Close();
                }
            }

            if ((!simOnly) &
(Parameters.GetIntValue("Recipe.Additional_Maintenance") >0)) //Additional
cleaning
                Script.Run(Helper.GetScriptDir() + "maintenance_Javier.cs");

            //Drying step
            Parameters.SetValue("General.ProgressText", "Drying "+
i.ToString());
            if ((!simOnly))
                Thread.Sleep(dT); //Drying stop in ms

            //UV Curing (Javier)
            if ((!simOnly) & ((Parameters.GetIntValue("Recipe.doCure")
==1)|| (Parameters.GetIntValue("Recipe.doCure")==3)))
            {
                Script.Run(Helper.GetScriptDir() + "cure_Javier.cs");
            }

            //IR Treatment (Javier)
            if ((!simOnly) & (Parameters.GetIntValue("Recipe.doIR") == 1))
            {
                Script.Run(Helper.GetScriptDir() + "IR_Javier.cs");
            }

            if ((!simOnly) & (Parameters.GetIntValue("Recipe.doIR") ==2))
            {
                Script.Run(Helper.GetScriptDir() + "IR_digital_Javier.cs");
            }
        }
    }
}

```

```

change      z = z + Parameters.GetDoubleValue("Recipe.Step"); // Ehab's
            sub.Change(Position.Axes.Z, z );

            //shifts, J
            X = X + ax; // J change
            Y = Y + ay; // J change

            pos.Change(Position.Axes.X, X);
            pos.Change(Position.Axes.Y, Y);
            //end shifts, Javier
        }
        //end repeat cycle

        //Restore Print Head Position, J
        X = X - ax;
        Y = Y - ay;

        pos.Change(Position.Axes.X,X);
        pos.Change(Position.Axes.Y,Y);
        if (!(simOnly) & (Parameters.GetIntValue("Recipe.Zreset") >0))
//Reset Z position, l=Yes
        {
            z = zOrg;//J,multilayer
            sub.Change(Position.Axes.Z, z );// J, multilayer Back to initial
height
        }

        //end restoring */

        ParameterHandler.Instance.SetValue("General.ProgressText",
"$ (Finished)");

        //COM close and PICO inicialization
        System.IO.Ports.SerialPort myPort2 = new
System.IO.Ports.SerialPort(com);
        if (myPort2.IsOpen == false) //if not open, open the port
            myPort2.Open();

        if (myPort2.IsOpen)
        {
            myPort2.DiscardInBuffer();
            myPort2.DiscardOutBuffer();

            myPort2.Write("0");
            Thread.Sleep(500); //Wait X ms
        }
        myPort2.Close();
//COM close end*/
        if(!simOnly & ((Parameters.GetIntValue("Recipe.Service") >0)))
            Motion.MoveTo("Service");
    }

```

## A2. UV-resin and carbon paint early post-treatment and 3D-tests

### Experiment description

This early attempt at studying the influence of post-treatment conditions on the 3-dimensional characteristics of the printed structures consisted on the creation and analysis of multi-layered samples of UV-resin and carbon paint on polycarbonate films (Figure 133). Specifically, 3 samples of carbon paint were printed at 100 DPI using a valve closing time of 120  $\mu\text{s}$  and a pulse of 1 ms, allowing 3 different times (0 s, 30 s and 300 s) for the material to dry in ambient conditions before printing the next layer. The UV-resin was printed at 65 DPI with a closing time of 200  $\mu\text{s}$ , a pulse length of 2 ms and a UV-curing step after the printing of each layer at 2 different curing speeds (6 mm/s and 150 mm/s). The samples were allowed to dry in ambient conditions for 24 h before scanning them with a contact profilometer (Surfest SV-3100, Mitutoyo, Japan) at a point spacing of 50  $\mu\text{m}$  and 3 equally spaced profiles per track. In the case of carbon paint, only the sample with a drying time of 300 s was scanned with the profilometer, since the other 2 did not present a constant cross-section across the full length of the tracks.

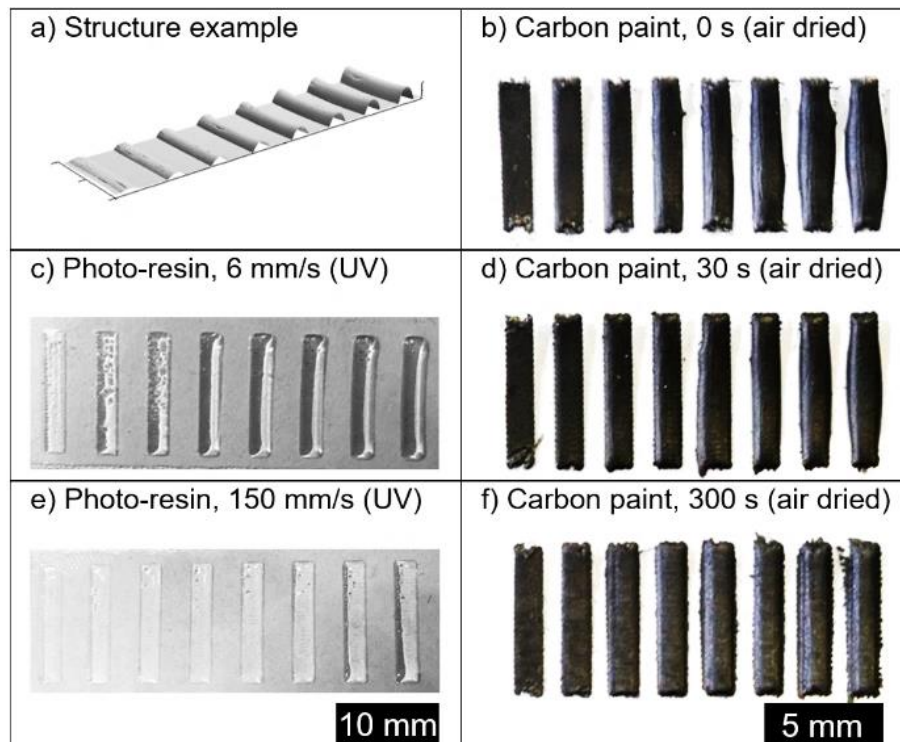


**Figure 133.** Multi-step structures with growing number of layers (a) were produced with different types of post-treatments after each layer. The carbon samples (b,d,f) were allowed to dry at 25°C while the photo-polymer (c,e) was cured by a UV-lamp at different speeds.

### Layer thickness results

The results from the profilometry scans is shown in Figure 134, where good linearity and a comparable slope is observed for the 3 configurations. The linear regression

fitting parameters for the UV-resin are tabulated in the main text (Table 11). The slope value for carbon is  $54 \pm 1 \mu\text{m}$ , which is close to the obtained for the UV-resin but contrasts with the results shown in (Table 11). One possible explanation is the difference in the post-treatment, since the sample shown here did not experience any radiation while the ones in the main text were exposed to UV to accelerate the drying stage. The lack of this thermal step could have caused solvent entrapment that eventually could result in increased porosity. To verify this hypothesis, however, more experiments would be required, which are recommended for future work. Furthermore, it is worth keeping in mind that these results are related with samples printed in different substrates, with different size and analysed by a different instrument than the ones analysed in the main text, which is expected to introduce some variations in the obtained layer thickness. Nevertheless, this experiment provided a good starting point to control the height of printed structures and allow the creation of some multi-material samples involving carbon paint and UV-resin.

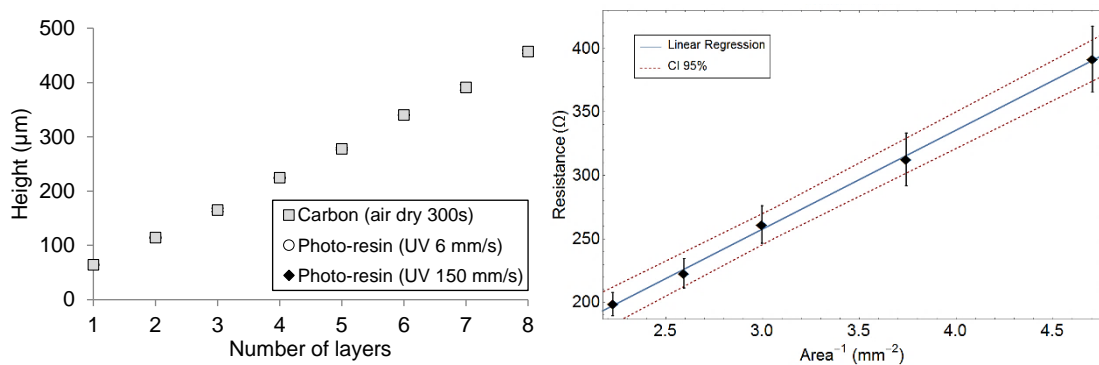


**Figure 134: Left)** Height evolution of samples printed with carbon paint and stereolithographic resin on polycarbonate films. The UV-resin was cured at 2 different scan speeds (6 mm/s and 150 mm/s) while the carbon sample dried in ambient conditions for 300 s before depositing the next layer. **Right)** Resistivity calculation of the carbon paste based on the comparison between the individual resistance of the tracks and their cross-sectional area obtained from contact profilometry. The blue line represents the linear regression and the red dashed lines the 95% Confidence Interval.

### Carbon paint early resistivity results

The contact profilometer was also used to obtain the cross-sectional surface of the conductive tracks, which later was combined with their measured resistance (Figure 134) to obtain the resistivity from a linear regression of the data, following equation 49. This lead to an electrical resistivity value of  $(1.2 \pm 0.5) \cdot 10^{-2} \Omega \text{ m}$  considering a track length of  $6.4 \pm 0.2 \text{ mm}$ . This result agrees with the technical information of the material (Bare Conductive Ltd 2016) and is comparable to the reported volume resistivity for carbon black conductive filament for fuse deposition modelling  $((9 - 12) \cdot 10^{-2} \Omega \text{ m})$  (Leigh et al. 2012). However, the measured value is more than six orders of magnitude higher than the resistivity of bulk silver ( $1.587 \cdot 10^{-8} \Omega \text{ m}$  at  $20^\circ\text{C}$ ) (David R. Lide 2005).

### **Conclusions of experiment**

The present experiment provided working values for the layer thickness of printed carbon paint and UV-resin layers. Moreover, the linearity of the results indicates that appropriate post-processing conditions have been used in the 3 cases, since otherwise deviations from this trend were expected at increased number of layers. This is especially relevant for the stereolithographic resin, which displayed similar growth for both tested curing speeds. Thus, the fastest is used from this moment onwards to reduce the processing time. Moreover, the 3D scans of the samples via contact profilometry allowed for the characterization of the tracks' cross-section, which in turn was used in combination with their resistance to calculate a resistivity of  $(1.09 \pm 0.03) \cdot 10^{-2} \Omega \text{ m}$  for the carbon paint. This was in agreement with the expectations for this material but highlighted the need of inks with increased conductivity to create efficient circuits. This eventually would result in the addition of PEDOT:PSS and the silver paste to the list of materials used in the present work.

This early experiment was also used to identify potential drawbacks of the methodology itself to correct them in future iterations of the tests, as they are shown in the main text. For instance, the polycarbonate films used as a substrate showed signs of thermal degradation under prolonged exposure to radiation. Furthermore, even in their flat state they deflected during the profilometer tests, which can cause the shift of the baseline. Thus, in future repetitions of this experiment glass slides and epoxy fiberglass board will be used due to their increased mechanical and thermal resistance. Additionally, repetitions of each sample are required to increase the statistical validity of the results. This, however, is time consuming and is not an efficient method to assess the validity of the post-processing conditions. Therefore, this experiment will be performed again for the rest of materials to characterise their layer thickness and resistivity but not to investigate the drying or curing conditions, which would be explored in other experiments such as top examination of 2D patterns or real time resistance measurements in different thermal conditions.

### A3. Electroluminescent initial tests and material formulation

#### Initial tests

A commercial green phosphor paste (C2070209P5, Gwent, UK) designed for screen printing electroluminescent lamps was used for an initial feasibility test. This formulation contains an unspecified amount of copper activated zinc sulphide (ZnS:Cu) powder mixed on an organic binder and requires a thermal treatment of 130 °C during 10 minutes after the deposition of the layer to cross-link and eliminate the volatile elements. The recommended dielectric paste (D2070209P6, Gwent, UK) to accompany the previous formulation has nanoparticles of Barium Titanate ( $\text{BaTiO}_3$ ) instead of ZnS:Cu crystals dispersed in the same organic mixture.

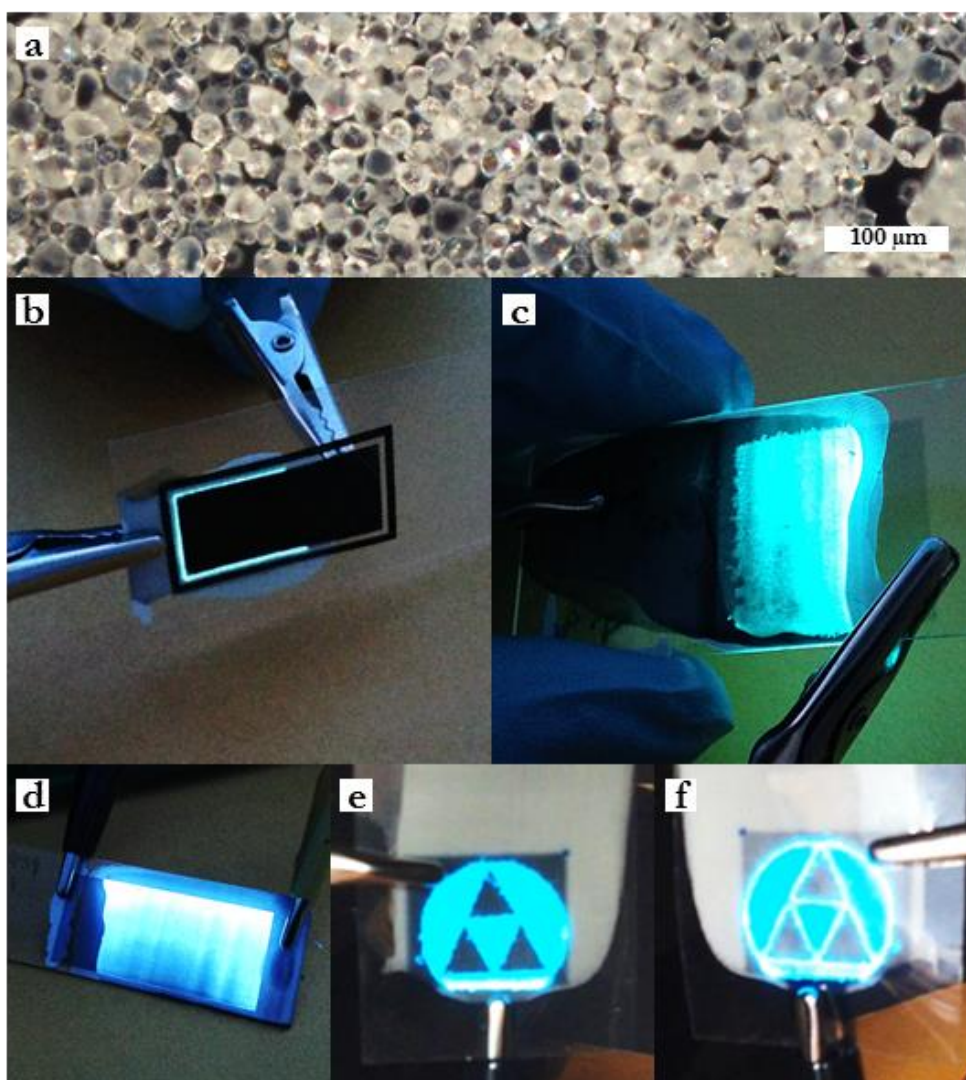


**Figure 135:** **a)** Optical microscope photograph of commercial phosphor powder obtained by dissolving the binder of the paste in acetone. The scale bar is 100  $\mu\text{m}$ . **b)** Test sample with carbon as both front and back electrodes, the light escapes through the gap in the pattern. **c)** Test sample with both electrodes of PEDOT:PSS, resulting in a bi-directional lamp. **d)** Light gradient resulting from an unlevelled hand coating of the phosphor paste, showing the effect of layer thickness. **e & f)** Both sides of a bi-directional lamp with hand coated phosphor paste and both electrodes printed with PEDOT:PSS.

A standard build lamp (Figure 130) can be constructed by stacking layers of conductive material, phosphor paste, dielectric paste and a back conductive electrode on top of a polymeric transparent film. Different combinations of materials were deposited on glass and polyester foil (F2111117D1, Gwent, UK) using the printing system and a K Hand Coater (RK PrintCoat Instruments Ltd., UK) (Figure 135). The samples were then treated in an oven at 130 °C for 15 minutes, placed flat in ambient conditions for 30 minutes and then tested. To check the electroluminescence of the lamps a 12 V DC to 110 V/400 Hz inverter (12 V EL Inverter, Adafruit, USA) was used. The main conclusions extracted from these tests were as follows:

- Lamps displayed similar performance on both polyester and glass substrates, but the polymeric film also allowed for flexible lamps.
- Silver yielded good results as a back electrode in combination with a front layer of PEDOT:PSS but remarkable illumination was also achieved using carbon or PEDOT:PSS back conductors despite their higher resistivity.
- The homogeneity of deposition is directly related with the homogeneity of the lamp.
- Functional devices were obtained even without the dielectric paste but resulted in dimmer intensity.
- Both electrodes can be of the same material and even if they are opaque, like the carbon paint, light is emitted through the gaps. PEDOT:PSS in both sides creates bi-directional lamps.
- Patterned lamps can be easily achieved by printing one of the electrodes and coating the other homogeneously, since the light is only produced in the region between the electrodes. Some lateral leakage is observed, however, which can be used to create luminous patterns with both opaque electrodes.

These initial tests were successful and very promising, but to replicate these results in a single fabrication process some issues needed to be addressed. First, a way to post-treat the materials within the system was required, which was solved by the later addition of the UV and IR lamps. Also, the number of materials need to be reduced if all of them are to be printed with the 4 available heads, taking into account that only 2 of those are capable of dispensing high viscosity materials. Finally, the phosphor paste needs to be reformulated with smaller crystals, since most of the ZnS:Cu particles in the commercial paste were bigger between 20 and 50  $\mu\text{m}$  (Figure 135a), which would be a problem for nozzle diameters of 50  $\mu\text{m}$  and 100  $\mu\text{m}$ . Thus, a new phosphor paste is formulated in the next section.

### Phosphor paste re-formulation

According with the initial results presented in the previous section, the EL-phosphorous paste need to be re-formulated to address two main problems: particle size and processability. The **size and distribution of the electroluminophore crystals** is relevant because they can cause nozzle blockage if they exceed a certain threshold value that ranges between 1 and 10 % of the diameter of the orifice (Hutchings & Martin 2012)(Magdassi 2010)(Angelo 2013), depending on the actuation system and overall fluid viscosity. Increasing the nozzle size is an option, but typically this would result in bigger droplets, which reduces the printing resolution, so decreasing the powder size is a preferred route. Also, smaller particles would result in improved dispersion stability, higher packing fraction and more homogeneous deposited films, which is crucial to obtain homogeneous lamps, as it was observed in the previous section (Figure 135). Consequently, smaller uncoated ZnS:Cu powder with an expected average size of 9  $\mu\text{m}$  was acquired and passed through a metallic wire sieve of 20  $\mu\text{m}$  pore size. Small volumes of both sieved and as-received powder were analysed with a laser diffraction particle size analyser (Aero S Mastersizer 3000, Malvern Instruments Ltd., UK), resulting in very similar results (Figure 136) after 5 scans for each sample. An uncoated sample of sieved powder on a carbon pad was imaged using a tabletop Scanning Electron Microscope (TM3030, Hitachi, Japan), confirming the results of the particle size distribution (Figure 136).

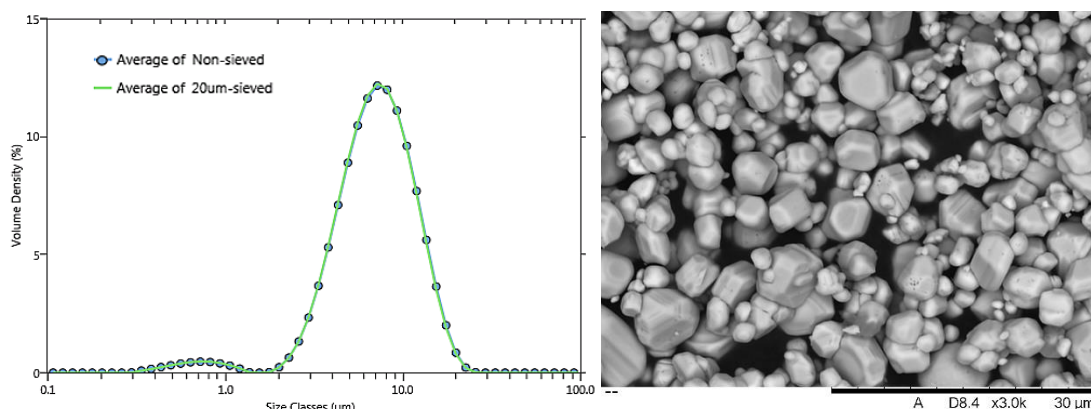


**Figure 136: Left)** Average particle size distribution of ZnS:Cu EL-phosphorous powder samples, one of them was sieved through a 20  $\mu\text{m}$  wire-mesh. **Right)** Image from a Scanning Electron Microscope of the uncoated sieved sample.

The second element to be modified respect the commercial phosphor paste is the binder, since even with the integrated IR lamp would take 5 to 10 minutes to cure each layer, which would increase the total processing time and can damage the surrounding materials. Thus, inspired by the good results obtained printing the stereolithographic resin with the micro-dispensing valves, it was used as a UV-curable binder in the new formulation. This not only allows for faster consolidation of each layer but it also provides

increased dispersion stability due to its high viscosity. Also, since the volatile content of this resin is negligible, volumetric shrinkage is reduced and layer thickness is expected to be in the micron-range, similar to the resulting after a screen printing pass. Similar UV-composites containing luminescent pigments can be found in the literature (Krohn 2001)(Matras et al. 2008)(Hartmann & Nubler 2010). The solid loading of powder on the formulation was 55 wt%, inspired by other electroluminescent pastes encountered in the literature (Chang & Lu 1999)(Hartmann & Nubler 2010)(Krohn 2001), which used concentrations from 30 to 80 wt%. The UV-resin was magnetically stirred (500 rpm) and heated up to 90 °C, which considerably reduced its apparent viscosity, as it was previously observed (Figure 71). Then, small weighted amounts of powder were sequentially added with a spatula, allowing the material to mix thoroughly, until the desired concentration was reached. The mixture was stirred at 90 °C for 2 hours and then at least 12 hours more at room temperature in an in-house made single-barrel rotary tumbler at slower pace. A white-yellow homogeneous paste very similar to the commercial phosphor paste was obtained.

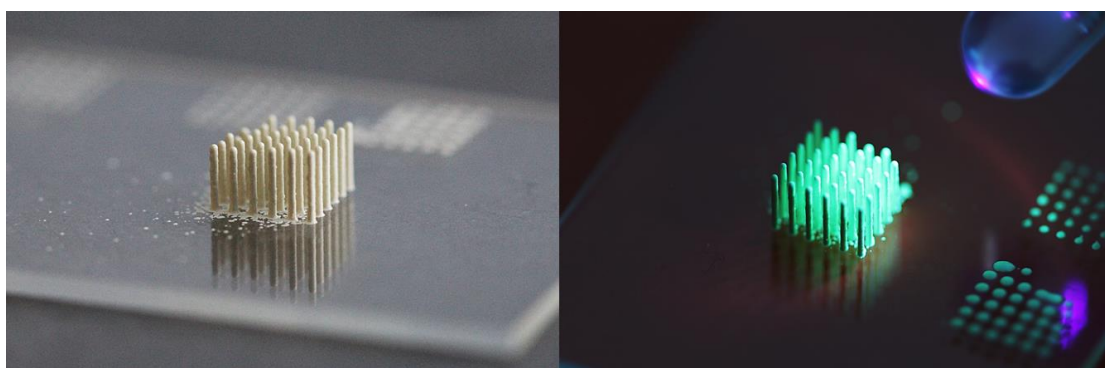


**Figure 137: Left)** Self-standing pillars composed of 50 layers of a UV-curable EL-phosphor composite. The substrate is a glass slide of 1 mm thickness. **Right)** Same structure illuminated by a UV-LED and displaying a characteristic green glow due to the photoluminescence of the ZnS:Cu particles.

The material was loaded on a micro-dispensing valve with a 100  $\mu\text{m}$  nozzle to test its printability and no blockage was experienced, confirming the suitability of the smaller crystals. This behaviour continued for 3 full days, when the material was cleared from the system without a single clogging incident. Printing parameters were determined based on the behaviour observed for the other viscous materials tested in this work. The critical pressure to create a stable stream via pneumatic actuation alone was not achieved within the pressure range tested (0 – 0.6 MPa) at 25 °C, but substantial residual material was encountered on the nozzle plate when 0.5 MPa was tested. Thus, 0.2 MPa was selected as a suitable printing pressure. Similarly, streams of 1000 drops were produced at different valve closing times, which showed that closing profiles equal or above 300  $\mu\text{s}$  leave material

behind in each cycle. Consequently, to avoid stability issues, a closing profile of 120  $\mu\text{s}$  was chosen. The pulse was kept at 0.3 ms, which was the minimum length that still allowed normal ejection. The resulting drops showed an average diameter of  $650 \pm 10 \mu\text{m}$ . It is worth noting that increasing the temperature of the valve would have reduced the viscosity of the material and, in turn, facilitate its printing. This, however, was not attempted to be consistent with the rest of materials printed in this work, also at 25 °C. Once the settings were considered acceptable, the printability and post-processing of the formulated paste was tested in a longer experiment, where the same array of droplets (5 x 5 mm, 30 DPI) was printed 50 times on top of each other, with a UV-curing step each layer at 1 mm/s. This resulted in cured straight pillars, which not only validated the printability and curing of the paste at the used settings but also demonstrated its suitability for 3D applications based on the high aspect ratio of the structures (Figure 137). Furthermore, since the electroluminescent properties of the material cannot be tested without the application of a strong electric field, its photoluminescence (PL) is tested instead by shining a UV-LED (UV/UVA 400 nm purple LED, Adafruit, USA) onto the sample and observing the visible radiation emitted as a result of the excitation and relaxation of the charge carriers (Figure 137). This is a similar process than electroluminescence with the main difference that in PL the electrons are photo-excited by the incoming radiation instead of current injection, as in the case for electroluminescence (Smet et al. 2010). However, since ZnS:Cu presents both behaviours (Withnall et al. 2011), the observation of photoluminescence is taken as an indicator of the good state of its atomic structure, which could have been damaged during the formulation process.

# 10. References

- 3MF Consortium, 2015. 3D Manufacturing Format Specification and Reference Guide, V 1.0. , pp.1–48.
- Ackelid, U. & Wallgren, G., 2010. Apparatus for producing a three-dimensional object. WO 2010095987 A1.
- Adams, J.J. et al., 2011. Conformal printing of electrically small antennas on three-dimensional surfaces. *Advanced Materials*, 23, pp.1335–1340.
- Ahn, B.Y. et al., 2009. Omnidirectional printing of flexible, stretchable, and spanning silver microelectrodes. *Science (New York, N.Y.)*, 323(5921), pp.1590–3.
- Allen, M.L. et al., 2008. Electrical sintering of nanoparticle structures. *Nanotechnology*, 19(17), p.175201.
- Angelo, P.D., 2013. *Inkjet-Printed Light-Emitting Devices: Applying Inkjet Microfabrication to Multilayer Electronics*. University of Toronto.
- Angelo, P.D., Kronfli, R. & Farnood, R.R., 2013. Synthesis and inkjet printing of aqueous ZnS:Mn nanoparticles. *Journal of Luminescence*, 136, pp.100–108.
- ASTM & International, 2013. ASTM ISO/ASTM52915-13, Standard Specification for Additive Manufacturing File Format (AMF) Version 1.1. , 2013.
- ASTM International, 2012. Standard Terminology for Additive Manufacturing Technologies. , pp.12–14.
- Bader, C. et al., 2016. Grown, Printed, and Biologically Augmented: An Additively Manufactured Microfluidic Wearable, Functionally Templated for Synthetic Microbes. *3D Printing and Additive Manufacturing*, 3(2), pp.79–89.
- Bae, S. et al., 2010. Roll-to-roll production of 30-inch graphene films for transparent electrodes. *Nature Nanotechnology*, 5(8), pp.574–578.
- Bare Conductive Ltd, 2016. Electric Paint Technical Data Sheet. , pp.1–2.
- Baren, M.R., 1990. The Ag-Ga (Silver-Gallium) system. *Bulletin of Alloy Phase Diagrams*, 11(4), pp.334–339.
- Barnes, Hutton & Walters, 1989. *An Introduction to Rheology*, Elsevier Science Publishers
- Barnes, H., 2000. *A handbook of elementary rheology*, University of Wales, Institute of Non-Newtonian Fluid Mechanics.
- Barnes, H. a., 1999. Shear-Thickening (“Dilatancy”) in Suspensions of Nonaggregating Solid Particles Dispersed in Newtonian Liquids. *Journal of Rheology*, 33(2), p.329.
- Barnes, H.A., 1999. The yield stress-a review or “ $\pi\alpha\nu\tau\alpha$   $\rho\epsilon\tau$ ”—everything flows? *Journal of Non-Newtonian Fluid Mechanics*, 81(1-2), pp.133–178.
- Bartlett, N.W. et al., 2015. A 3D-printed, functionally graded soft robot powered by combustion. *Science*, 349(July), pp.161–165.

- Bazilevskii, A. V., Meyer, J.D. & Rozhkov, A.N., 2005. Dynamics and breakup of pulse microjets of polymeric liquids. *Fluid Dynamics*, 40(3), pp.376–392.
- Bazilevskii, A.B. & Rozhkov, A.N., 2015. Dynamics of the Capillary Breakup of a Bridge in an Elastic Fluid. , 50(6), pp.800–811.
- Bergeron, V. et al., 2000. Controlling droplet deposition with polymer additives. *Nature*, 405(6788), pp.772–5.
- Bertola, V. et al., 2003. Wall slip and yielding in pasty materials. *Journal of Rheology*, 47(5), p.1211.
- Bhuiyan, M.H.U. et al., 2015. ScienceDirect Effect of nanoparticles concentration and their sizes on surface tension of nanofluids. *Procedia Engineering*, 105(Icte 2014), pp.431–437.
- Bickel, B. et al., 2010. Design and fabrication of materials with desired deformation behavior. *ACM Transactions on Graphics*, 29(4), p.1.
- Bieri, N.R. et al., 2004. Manufacturing of nanoscale thickness gold lines by laser curing of a discretely deposited nanoparticle suspension. *Superlattices and Microstructures*, 35(3-6), pp.437–444.
- Billiet, T. et al., 2012. A review of trends and limitations in hydrogel-rapid prototyping for tissue engineering. *Biomaterials*, 33(26), pp.6020–41.
- Black, K. et al., 2016. Silver Ink Formulations for Sinter- free Printing of Conductive Films. *Nature Publishing Group*, (October 2015), pp.1–7.
- Bogy, D.B. & Talke, F.E., 1984. Experimental and Theoretical Study of Wave Propagation Phenomena in Drop-on-Demand Ink Jet Devices. *IBM Journal of Research and Development*, 28(3), pp.314–321.
- Borel, J.-P., 1981. Thermodynamical size effect and the structure of metallic clusters. *Surface Science*, 106(1-3), pp.1–9.
- Bowyer, A., 2004. RepRap - RepRapWiki. Available at: <http://reprap.org/wiki/RepRap> [Accessed September 10, 2013].
- Bredol, M. & Dieckhoff, H.S., 2010. Materials for powder-based AC-electroluminescence. *Materials*, 3, pp.1353–1374.
- Brescia, R. et al., 1985. Selective ink-jet printing device US 4502054 A.
- Bruneaux, J., Therriault, D. & Heuzey, M.-C., 2008. Micro-extrusion of organic inks for direct-write assembly. *Journal of Micromechanics and Microengineering*, 18(11), p.115020.
- Cambridge Polymer Group, I., 2004. *The Capillary Breakup Extensional Rheometer (CABER)*,
- Cameron, A., 1966. *The principles of lubrication*, Longmans.
- Cao, C. et al., 2013. Effect of gum arabic on the surface tension and surface dilational rheology of trisiloxane surfactant. *Food Hydrocolloids*, 30(1), pp.456–462.
- Chang, D.-A. & Lu, J.-Y., 1999. Screen printing of surface layers.
- Chen, A.U. & Basaran, O.A., 2002. A new method for significantly reducing drop radius without reducing nozzle radius in drop-on-demand drop production. *Physics of Fluids*, 14(1).

- Chen, D. et al., 2013. Spec2Fab: A Reducer-Tuner Model for Translating Specifications to 3D Prints. In *ACM Transactions on Graphics*. p. 1.
- Chen, J.H. et al., 2007. Printed graphene circuits. *Advanced Materials*, 19(21), pp.3623–3627.
- Chen, Y. et al., 2014. Experimental and modeling study of high-viscosity silicone jet dispensing process for LED packaging. *Proceedings of the Electronic Packaging Technology Conference, EPTC*, pp.1431–1436.
- Cherrington, M. et al., 2012. Non-contact assessment of electrical performance for rapidly sintered nanoparticle silver coatings through colorimetry. *Thin Solid Films*, 522, pp.412–414.
- Cherrington, M. et al., 2011. Ultrafast near-infrared sintering of a slot-die coated nano-silver conducting ink. *Journal of Materials Chemistry*, 21(21), p.7562.
- Choi, B. et al., 2004. Design and Implementation of Low-Profile Contactless Battery Charger Using Planar Printed Circuit Board Windings as Energy Transfer Device. *IEEE Transactions on Industrial Electronics*, 51(1), pp.140–147.
- Choi, E.-K. et al., 2010. High-yield exfoliation of three-dimensional graphite into two-dimensional graphene-like sheets. *Chemical communications (Cambridge, England)*, 46(34), pp.6320–6322.
- Choi, H.K. et al., 2008. Scaling laws for jet pulsations associated with high-resolution electrohydrodynamic printing. *Applied Physics Letters*, 92(12), p.123109.
- Choi, J.-W., Kim, H.-C. & Wicker, R., 2011. Multi-material stereolithography. *Journal of Materials Processing Technology*, 211(3), pp.318–328.
- Christanti, Y. & Walker, L.M., 2002. Effect of fluid relaxation time of dilute polymer solutions on jet breakup due to a forced disturbance. *Journal of Rheology*, 46(3), p.733.
- Christanti, Y. & Walker, L.M., 2001. Surface tension driven jet break up of strain-hardening polymer solutions. *Journal of Non-Newtonian Fluid Mechanics*, 100(1-3), pp.9–26.
- Chua, C.K., Leong, K.F. & Lim, C.S., 2010. *Rapid Prototyping: Principles and Applications* 3rd ed., World Scientific.
- Church, K. et al., 2009. Printed electronic processes for flexible hybrid circuits and antennas. In *2009 Flexible Electronics and Displays Conference and Exhibition, FLEX 2009*. pp. 1–7.
- Connelly, R.W. & Greener, J., 1985. High-Shear Viscometry with a Rotational Parallel-Disk Device. *Journal of Rheology*, 29(2), pp.209–226.
- Corbett, J., 2012. *Reprap Colour Mixing Project*. University of Bath.
- Correia, V. et al., 2013. Development of inkjet printed strain sensors. *Smart Materials and Structures*, 22(10), p.105028.
- Cossali, G.E., Coghe, a. & Marengo, M., 1997. The impact of a single drop on a wetted solid surface. *Experiments in Fluids*, 22(6), pp.463–472.
- Cozic, C. et al., 2009. Analysis of arabic gum: Study of degradation and water desorption processes. *Food Hydrocolloids*, 23(7), pp.1930–1934.
- Crooks, R. & Boger, D. V., 2000. Influence of fluid elasticity on drops impacting on dry surfaces. *Journal of Rheology*, 44(4), p.973.

- Cross, M.M., 1965. Rheology of non-Newtonian fluids: A new flow equation for pseudoplastic systems. *Journal of Colloid Science*, 20(5), pp.417–437.
- Cuk, T. et al., 2000. Using convective flow splitting for the direct printing of fine copper lines. *Applied Physics Letters*, 77(13), p.2063.
- van Dam, D.B. & Le Clerc, C., 2004. Experimental study of the impact of an ink-jet printed droplet on a solid substrate. *Physics of Fluids*, 16(9), pp.3403–3414.
- Das, S. et al., 1998. Direct laser freeform fabrication of high performance metal components. *Rapid Prototyping Journal*, 4(3), pp.112–117.
- David R. Lide, 2005. *CRC Handbook of Chemistry and Physics* Internet V., Boca Raton, FL: CRC Press.
- Davidson, M. & Abramowitz, M., 2002. Optical Microscopy. In *Encyclopedia of imaging science and technology*. pp. 1106–1141.
- de Gans, B.-J., Duineveld, P.C. & Schubert, U.S., 2004. Inkjet Printing of Polymers: State of the Art and Future Developments. *Advanced Materials*, 16(3), pp.203–213.
- Deegan, R.D., Bakajin, O. & Dupont, T.F., 1997. Deegan1997. *Letters to Nature*, 389, pp.827–829.
- van Deen, M.S. et al., 2013. Particles accelerate the detachment of viscous liquids. *Rheologica Acta*, 52(5), pp.403–412.
- Deffenbaugh, P., 2013. Fully 3D Printed 2.4 GHz Bluetooth / Wi-Fi Antenna. In *International Microelectronics Assembly and Packaging Society*. pp. 1–7.
- Deganello, D. et al., 2010. Patterning of micro-scale conductive networks using reel-to-reel flexographic printing. *Thin Solid Films*, 518(21), pp.6113–6116.
- Denneulin, A. et al., 2009. The influence of carbon nanotubes in inkjet printing of conductive polymer suspensions. *Nanotechnology*, 20(38), p.385701.
- Derby, B., 2010. Inkjet Printing of Functional and Structural Materials: Fluid Property Requirements, Feature Stability, and Resolution. *Annual Review of Materials Research*, 40(1), pp.395–414.
- Dickey, M.D. et al., 2008. Eutectic Gallium-Indium (EGaIn): A Liquid Metal Alloy for the Formation of Stable Structures in Microchannels at Room Temperature. *Advanced Functional Materials*, 18(7), pp.1097–1104.
- Dilfer, S. & Schmitt, N., 2012. Printing conductive layers using waterless offset technology considering the influences of the low-viscosity polymer inks and the rubber blankets. *Journal of Coatings Technology Research*, 9(4), pp.475–482.
- Duffy, J., 2015. *Measuring the rheology of polymer solutions*, Malvern Instruments White Paper
- Duineveld, P.C. et al., 2002. Ink-jet printing of polymer light-emitting devices. In *Proceedings of SPIE - The International Society for Optical Engineering*. pp. 59–67.
- Duineveld, P.C., 2003. The stability of ink-jet printed lines of liquid with zero receding contact angle on a homogeneous substrate. *Journal of Fluid Mechanics*, 477, pp.175–200.
- Duro-Royo, J., Mogas-Soldevila, L. & Oxman, N., 2015. Flow-based fabrication: An integrated computational workflow for design and digital additive manufacturing of multifunctional

- heterogeneously structured objects. *CAD Computer Aided Design*, 69(Special Issue on Geometric and Physical Modeling for Additive Manufacturing), pp.143–154.
- Dziedzic, A. et al., 1994. Heaters for gas sensors from thick conductive or resistive films. *Sensors and Actuators: B. Chemical*, 19(1-3), pp.535–539.
- Edmond L. Kyser, S.B.S., 1976. US3946398 A.
- Edmund Optics, 2015. *2015 Master Source Book*
- EFD, N., 2013. *PICO™ Driver DCON Operating Manual*
- Elliott, R.P. & Shunk, F.A., 1981. The Au–Ga (Gold-Gallium) system. *Bulletin of Alloy Phase Diagrams*, 2(3), pp.356–358.
- Elrod, S. a. et al., 1989. Nozzleless droplet formation with focused acoustic beams. *Journal of Applied Physics*, 65(9), p.3441.
- Elschner, A. et al., 2012. *ITO Alternative: solution deposited Clevis™ PEDOT: PSS for transparent conductive applications*, Heraeus White Paper
- Emanuel M. Sachs, John S. Haggerty, Michael J. Cima, P.A.W., 1993. Three-dimensional printing techniques US 5204055 A.
- Espalin, D. et al., 2014. 3D Printing multifunctionality: Structures with electronics. *International Journal of Advanced Manufacturing Technology*, 72(5-8), pp.963–978.
- Faddoul, R., Reverdy-Bruas, N. & Blayo, A., 2012. Formulation and screen printing of water based conductive flake silver pastes onto green ceramic tapes for electronic applications. *Materials Science and Engineering B: Solid-State Materials for Advanced Technology*, 177(13), pp.1053–1066.
- Farsari, M., Vamvakaki, M. & Chichkov, B.N., 2010. Multiphoton polymerization of hybrid materials. *Journal of Optics*, 12(12), p.124001.
- Finsky, R., 2004. On the Critical Radius in Ostwald Ripening. *Langmuir*, 20(7), pp.2975–2976.
- Gabi, M. et al., 2009. FluidFM: Combining Atomic Force Microscopy and Nano uidics in a Universal Liquid Delivery System for Single Cell Applications and Beyond. *Nano Letters*, 9(6), pp.2501–7.
- Gaiser, D., 2013. *Clevis™ conductive polymers for Printed Electronic applications*, Heraeus White Paper
- Gao, Y., Li, H. & Liu, J., 2012. Direct writing of flexible electronics through room temperature liquid metal ink. *PLoS one*, 7(9), p.e45485.
- German, G. & Bertola, V., 2009. Impact of shear-thinning and yield-stress drops on solid substrates. *Journal of physics. Condensed matter: an Institute of Physics journal*, 21(37), p.375111.
- Gibson, I., Rosen, D.W. & Stucker, B., 2009. *Additive Manufacturing Technologies: Rapid Prototyping to Direct Digital Manufacturing*, Springer.
- Goldin, M. et al., 1969. Breakup of a laminar capillary jet of a viscoelastic fluid. *Journal of Fluid Mechanics*, 38(04), p.689.
- Goldin, M., Pfeffer, R. & Shinnar, R., 1972. Break-up of a capillary jet of a non-Newtonian fluid having a yield stress. *The Chemical Engineering Journal*, 4(1), pp.8–20.

- Gooding, J. & Fields, T., 2017. 3D Printed Strain Gauge Geometry and Orientation for Embedded Sensing. *58th ALAA/ASCE/AHS/ASC Structures, Structural Dynamics, and Materials Conference*, (January), pp.1–14.
- Griffiths, D.J., 2012. *Introduction To Electrodynamics* 4th ed., Pearson.
- Gu, S. et al., 2016. Design and Experiment of a Solder Paste Jetting System Driven by a Piezoelectric Stack. *Micromachines*, 7(7), p.112.
- Guo, S.Z. et al., 2013. Solvent-cast three-dimensional printing of multifunctional microsystems. *Small*, 9(24), pp.4118–4122.
- Hague, R., Campbell, I. & Dickens, P., 2003. Implications on design of rapid manufacturing. *Proceedings of the Institution of Mechanical Engineers, Part C: Journal of Mechanical Engineering Science*, 217(1), pp.25–30.
- Hara, T. et al., 1981. Ink jet recording device using thermal propulsion and mechanical pressure changes US 4296421 A.
- Hartmann, M. & Nubler, A., 2010. Printing paste and the use thereof for the production of an electroluminescent film.
- Haugan, E. & Dalsjo, P., 2013. *Characterization of the material properties of two FR4 printed circuit board laminates*,
- He, Y. et al., 2017. A Tripropylene Glycol Diacrylate-based Polymeric Support Ink for Material Jetting (accepted for publication). *Journal of Additive Manufacturing*.
- Hedges, M. & Marin, A., 2012. 3D Aerosol Jet® Printing-Adding Electronics Functionality to RP/RM. In *DDMC 2012 Conference*. Berlin, pp. 1–5.
- Heeger, A., MacDiarmid, A.G. & Shirakawa, H., 2000. *The Nobel Prize in chemistry, 2000: conductive polymers*,
- Heeger, A.J., 2010. Semiconducting polymers: the Third Generation. *Chemical Society reviews*, 39(7), pp.2354–71.
- Heeger, A.J., Schrieffer, J.R. & Su, W.-P., 1988. Solitons in conducting polymers. *Reviews of Modern Physics*, 60(3), pp.781–850.
- Heraeus, 2010. *Clevios™ S V3 Technical Data Sheet*
- Hernández, P. et al., 2013. Computer Aided Electroforming. Elecform3D™. *Procedia Engineering*, 63, pp.532–539.
- Heywang, G. & Jonas, F., 1992. Poly(alkylenedioxythiophene)s—new, very stable conducting polymers. *Advanced Materials*, 4(2), pp.116–118.
- Hirsch, A., 2010. The era of carbon allotropes. *Nature materials*, 9(11), p.868.
- Hirt, L. et al., 2016. Template-Free 3D Microprinting of Metals Using a Force-Controlled Nanopipette for Layer-by-Layer Electrodeposition. *Advanced Materials*, 28(12), pp.2311–2315.
- Hoath, S.D. et al., 2009. Links Between Ink Rheology, Drop-on-Demand Jet Formation, and Printability. *Journal of Imaging Science and Technology*, 53(4), p.041208.

- Houben, R.J., 2004. Apparatus and method for printing a fluid material by means of a continuous jet printing technique WO 2004018212 A1.
- Houben, R.J., 2008. Constant flow high pressure printing system WO 2008060149 A1.
- Houben, R.J., 2012. *Equipment for printing of high viscosity liquids and molten metals*. Universiteit Twente.
- Howkins, S.D., 1984. Ink jet method and apparatus US 4459601 A.
- Hu, J. & Yu, M.-F., 2010. Meniscus-confined three-dimensional electrodeposition for direct writing of wire bonds. *Science (New York, N.Y.)*, 329(5989), pp.313–6.
- Huang, B.W., Liu, S.M. & Chen, W.Q., 2011. Preparation of RPSL-01 Type Photosensitive Resin for Stereolithography and Study on the Accuracy of its Fabricated Parts. *Advanced Materials Research*, 239-242, pp.3043–3047.
- Huang, L. et al., 2011. Graphene-based conducting inks for direct inkjet printing of flexible conductive patterns and their applications in electric circuits and chemical sensors. *Nano Research*, 4(7), pp.675–684.
- Hutchings, I.M. & Martin, G.D., 2012. *Inkjet Technology for Digital Fabrication*,
- Hutchings, I.M., Martin, G.D. & Hoath, S.D., 2007. High Speed Imaging and Analysis of Jet and Drop Formation. *Journal of Imaging Science and Technology*, 51(5), p.438.
- Ibrahim, M. et al., 2006. Inkjet Printing Resolution Study for Multi-Material Rapid Prototyping. *JSME International Journal Series C*, 49(2), pp.353–360.
- InkTec Company Limited, 2013. *TEC-PA SERIES (PASTE INK) - brochure*,
- Islam, M.F. et al., 2003. High Weight Fraction Surfactant Solubilization of Single-Wall Carbon Nanotubes in Water. *Nano Letters*, 3(2), pp.269–273.
- Jang, D. et al., 2008. Nanosized glass frit as an adhesion promoter for ink-jet printed conductive patterns on glass substrates annealed at high temperatures. *Advanced Functional Materials*, 18(19), pp.2862–2868.
- Jang, J., Ha, J. & Cho, J., 2007. Fabrication of Water-Dispersible Polyaniline-Poly(4-styrenesulfonate) Nanoparticles For Inkjet-Printed Chemical-Sensor Applications. *Advanced Materials*, 19(13), pp.1772–1775.
- Jang-Ung, P. & Rogers, J.A., 2012. High-Resolution Electrohydrodynamic Inkjet. In D.-Y. S. Jan G. Korvink, Patrick J. Smith, ed. *Inkjet-based Micromanufacturing*. Weinheim, Germany: Wiley-Vch, pp. 57–72.
- Jayasinghe, S.N. & Edirisinghe, M.J., 2004. Electric-field driven jetting from dielectric liquids. *Applied Physics Letters*, 85(18), p.4243.
- Jeon, J. et al., 2015. Design and performance evaluation of a new jetting dispenser system using two piezostack actuators. *Smart Materials and Structures*, 24(1), p.15020.
- Jiang, Q. et al., 2014. Free-standing PEDOT: PSS film as electrode for the electrodeposition of bismuth telluride and its thermoelectric performance. *International Journal of Electrochemical Science*, 9(12), pp.7540–7551.
- Jin-Young, K. et al., 2010. Nanometer-sized BaTiO<sub>3</sub> Dielectric Layer for Inorganic

- Electroluminescence. *Journal of the Korean Physical Society*, 57(6), pp.1799 – 1802.
- Jones, R. et al., 2011. RepRap – the replicating rapid prototyper. *Robotica*, 29(January 2011), pp.177–191.
- Jung, I. et al., 2013. Synthesis of low-temperature-processable and highly conductive Ag ink by a simple ligand modification: the role of adsorption energy. *Journal of Materials Chemistry C*, 1(9), p.1855.
- Jung, J.W., Lee, J.-S. & Cho, D.-W., 2016. Computer-aided multiple-head 3D printing system for printing of heterogeneous organ/tissue constructs. *Scientific reports*, 6(November 2015), p.21685.
- Jung, S. et al., 2016. Sub-second carbon-nanotube-mediated microwave sintering for high-conductivity silver patterns on plastic substrates. *Nanoscale*, 8, pp.5343–5349.
- Kamyshny, A. & Magdassi, S., 2012. Inkjet Ink Formulations. In D.-Y. S. Jan G. Korvink, Patrick J. Smith, ed. *Inkjet-based Micromanufacturing*. Weinheim, Germany: Wiley-Vch, pp. 173–190.
- Kamyshny, A., Steinke, J. & Magdassi, S., 2011. Metal-based inkjet inks for printed electronics. *Open Applied Physics Journal*, 4, pp.19–36.
- Kang, K., Lee, L.J. & Koelling, K.W., 2005. High shear microfluidics and its application in rheological measurement. *Experiments in Fluids*, 38(2), pp.222–232.
- Kenneth H. Fischbeck, A.T.W., 1986. Shear mode transducer for drop-on-demand liquid ejector US 4584590 A.
- Khaleduzzaman, S.S. et al., 2013. Effect of particle concentration, temperature and surfactant on surface tension of nanofluids. *International Communications in Heat and Mass Transfer*, 49, pp.110–114.
- Kieback, B., Neubrand, A. & Riedel, H., 2003. Processing techniques for functionally graded materials. *Materials Science and Engineering A*, 362(1-2), pp.81–105.
- Kim, H.-S. et al., 2009. Intense pulsed light sintering of copper nanoink for printed electronics. *Applied Physics A*, 97(4), pp.791–798.
- Kim, J.-Y. et al., 2012. Inorganic powder electroluminescent devices fabricated by spin coating. *Journal of the Korean Physical Society*, 60(10), pp.1781–1784.
- King, B. & Renn, M., AEROSOL JET® DIRECT WRITE PRINTING FOR MIL-AERO ELECTRONIC APPLICATIONS.
- King, B.H., 2014. Miniature aerosol jet and aerosol jet array US 8640975 B2.
- Kirchmeyer, S. & Reuter, K., 2005. Scientific importance, properties and growing applications of poly(3,4-ethylenedioxythiophene). *Journal of Materials Chemistry*, 15(21), p.2077.
- Kittel, C., 2004. *Introduction to Solid State Physics* 8th Edition., Wiley.
- Ko, S.H. et al., 2007. All-inkjet-printed flexible electronics fabrication on a polymer substrate by low-temperature high-resolution selective laser sintering of metal nanoparticles. *Nanotechnology*, 18(34), p.345202.
- Kolbe, J. et al., 2007. Inkjettable conductive adhesive for use in microelectronics and microsystems technology. *Microelectronics Reliability*, 47(2-3), pp.331–334.

- Kopola, P. et al., 2009. Gravure printed organic light emitting diodes for lighting applications. *Thin Solid Films*, 517(19), pp.5757–5762.
- Kordás, K. et al., 2006. Inkjet printing of electrically conductive patterns of carbon nanotubes. *Small (Weinheim an der Bergstrasse, Germany)*, 2(8-9), pp.1021–5.
- Krohn, R.C., 2001. Uv curable compositions for producing electroluminescent coatings.
- Kumar, K.S. et al., 2015. A new single/few-layered graphene oxide with a high dielectric constant of  $10^6$  : contribution of defects and functional groups. *RSC Adv.*, 5(19), pp.14768–14779.
- Kwon, K.-S., 2012. Vision Monitoring. In D.-Y. S. Jan G. Korvink, Patrick J. Smith, ed. *Inkjet-based Micromanufacturing*. Weinheim, Germany: Wiley-Vch, pp. 127–144.
- Laappo, K., Jackson, B. & Wood, D., 2003. Discrete multiple material selective laser sintering (M2SLS): experimental study of part processing. In *Solid Freeform Fabrication Symposium*. Austin, TX, pp. 109–119.
- Ladd, C. et al., 2013. 3D printing of free standing liquid metal microstructures. *Advanced materials (Deerfield Beach, Fla.)*, 25(36), pp.5081–5.
- Lass, N. et al., 2013. Enhanced Liquid Metal Micro Droplet Generation by Pneumatic Actuation Based on the StarJet Method. *Micromachines*, 4(1), pp.49–66.
- Lau, D.L. & Arce, G.R., 2008. *Modern digital halftoning* 2nd ed., CRC Press.
- Le, H.P., 1998. Progress and Trends in Ink-jet Printing Technology. *Journal of Imaging Science and Technology*, 42(1), pp.49–62.
- Lebel, L.L. et al., 2010. Ultraviolet-assisted direct-write fabrication of carbon nanotube/polymer nanocomposite microcoils. *Advanced materials (Deerfield Beach, Fla.)*, 22(5), pp.592–6.
- Lee, Y.H., Lee, J.Y. & Lee, D.S., 2000. A novel conducting soluble polypyrrole composite with a polymeric co-dopant. *Synthetic Metals*, 114(3), pp.347–353.
- Leigh, S.J. et al., 2012. A simple, low-cost conductive composite material for 3D printing of electronic sensors. *PloS one*, 7(11).
- Lewis, J. a., 2006. Direct ink writing of 3D functional materials. *Advanced Functional Materials*, 16, pp.2193–2204.
- Li, B. & Logan, B.E., 2004. Bacterial adhesion to glass and metal-oxide surfaces. *Colloids and Surfaces B: Biointerfaces*, 36(2), pp.81–90.
- Li, J. et al., 2016. Hybrid additive manufacturing of 3D electronic systems. *Journal of Micromechanics and Microengineering*, 26(10), p.105005.
- Li, Y., Maynor, B.W. & Liu, J., 2001. Electrochemical AFM “Dip-Pen” Nanolithography. *Journal of the American Chemical Society*, 123(9), pp.2105–2106.
- Liu, Q., Huang, C. & Orme, M., 2000. Mutual electrostatic interactions between closely spaced charged solder droplets. *Atomization and Sprays*, 10(6), pp.1–41.
- Liu, Y. et al., 2015. High-Performance Flexible All-Solid-State Supercapacitor from Large Free-Standing Graphene-PEDOT/PSS Films. *Scientific Reports*, 5(October), p.17045.
- Löffelmann, U. et al., 2012. Solvent-free inkjet printing process for the fabrication of conductive,

- transparent, and flexible ionic liquid-polymer gel structures. *Journal of Polymer Science Part B: Polymer Physics*, 50(1), pp.38–46.
- Lopes, A.J., MacDonald, E. & Wicker, R.B., 2012. Integrating stereolithography and direct print technologies for 3D structural electronics fabrication. *Rapid Prototyping Journal*, 18(2), pp.129–143.
- Lu, X. & Chen, Z., 2005. Curved pi-conjugation, aromaticity, and the related chemistry of small fullerenes (< C60) and single-walled carbon nanotubes. *Chemical reviews*, 105(10), pp.3643–96.
- Luu, L.-H. & Forterre, Y., 2009. Drop impact of yield-stress fluids. *Journal of Fluid Mechanics*, 632, p.301.
- Madou, M.J., 2011. *Manufacturing techniques for microfabrication and nanotechnology (Vol. 2)*, CRC Press.
- Magdassi, S. ed., 2010. *The chemistry of inkjet inks*, The Hebrew University of Jerusalem, Israel: World Scientific.
- Magdassi, S. et al., 2010. Triggering the sintering of silver nanoparticles at room temperature. *ACS nano*, 4(4), pp.1943–8.
- Malone, E. et al., 2004. Freeform fabrication of zinc-air batteries and electromechanical assemblies. *Rapid Prototyping Journal*, 10(1), pp.58–69.
- Malone, E., Berry, M. & Lipson, H., 2008. Freeform fabrication and characterization of Zn-air batteries. *Rapid Prototyping Journal*, 14(3), pp.128–140.
- Malou, Z. et al., 2013. Thermal Shock Resistance of a Soda Lime Glass. *Ceramics - Silikáty*, 57(1), pp.39–44.
- Mangal, R., Srivastava, S. & Archer, L.A., 2015. Phase stability and dynamics of entangled polymer-nanoparticle composites. *Nature communications*, 6, p.7198.
- Martin, G.D., Hoath, S.D. & Hutchings, I.M., 2008. Inkjet printing - the physics of manipulating liquid jets and drops. *Journal of Physics: Conference Series*, 105.
- Matras, K. et al., 2008. Composites from luminescent nanosized ZnS and optical polymer. *Matras, K.*, 485(November 2014), pp.776–779.
- McKinley, G., 2005. Dimensionless groups for understanding free surface flows of complex fluids. *Soc. Rheol. Bull*, 74(2), pp.6–9.
- McKinley, G.H. & Sridhar, T., 2002. Filament-Stretching Rheometry of Complex Fluids. *Annual Review of Fluid Mechanics*, 34(1), pp.375–415.
- Meacham, J.M. et al., 2004. Micromachined ultrasonic droplet generator based on a liquid horn structure. *Review of Scientific Instruments*, 75(5), p.1347.
- Mehdi-Nejad, V., Mostaghimi, J. & Chandra, S., 2003. Air bubble entrapment under an impacting droplet. *Physics of Fluids*, 15(1), pp.173–183.
- Mei, J. et al., 2005. Formulation and Processing of Novel Conductive Solution Inks in Continuous Inkjet Printing of 3-D Electric Circuits. , 28(3), pp.265–273.
- Mei, Z., Holder, H. & Plas, H. Vander, 1996. Low-temperature solders. *Hewlett Packard Journal*, (August), pp.1–10.

- Michaelis, B.M. et al., 2007. In-flight thermal control of molten metal droplet streams. *International Journal of Heat and Mass Transfer*, 50(23-24), pp.4554–4558.
- Ming, L.W. & Gibson, I., 1999. Possibility of colouring SLS prototypes using the ink-jet method. *Rapid Prototyping Journal*, 5(4), pp.152–154.
- Molesa, S. et al., 2003. High-quality inkjet-printed multilevel interconnects and inductive components on plastic for ultra-low-cost RFID applications. *MRS Proceedings*, 769, p.H8.3.
- Montgomery, D.C. & Runger, G.C., 2011. *Applied Statistics and Probability for Engineers* 5th ed., Wiley.
- Moon, K.-S. et al., 2005. Thermal behavior of silver nanoparticles for low-temperature interconnect applications. *Journal of Electronic Materials*, 34(2), pp.168–175.
- Morita, N., 2012. Thermal Inkjet. In D.-Y. S. Jan G. Korvink, Patrick J. Smith, ed. *Inkjet-based Micromanufacturing*. Weinheim, Germany: Wiley-Vch, pp. 41–56.
- Morley, N.B. et al., 2008. GaInSn usage in the research laboratory. *The Review of scientific instruments*, 79(5), p.056107.
- Mothé, C.G. & Rao, M.A., 2000. Thermal behavior of gum arabic in comparison with cashew gum. *Thermochimica Acta*, 357-358, pp.9–13.
- Mun, R.P., Byars, J. a & Boger, D. V, 1998. The effects of polymer concentration and molecular weight on the breakup of laminar capillary jets. *Journal of Non-Newtonian Fluid Mechanics*, 74(1-3), pp.285–297.
- Mundo, C., Sommerfeld, M. & Tropea, C., 1995. Droplet-wall collisions: Experimental studies of the deformation and breakup process. *International Journal of Multiphase Flow*, 21(2), pp.151–173.
- Munson et al., 2009. *Fundamentals of Fluid Mechanics* 6th ed., Wiley.
- Muth, J.T. et al., 2014. Embedded 3D printing of strain sensors within highly stretchable elastomers. *Advanced Materials*, pp.6307–6312.
- Navarrete, M. et al., 2007. Integrated Layered Manufacturing of a Novel Wireless Motion Sensor System With Gps. In *SFF Symposium*. pp. 575–585.
- Nguon, B. & Jouaneh, M., 2004. Design and characterization of a precision fluid dispensing valve. *International Journal of Advanced Manufacturing Technology*, 24(3-4), pp.251–260.
- Nguyen, Q.H. et al., 2008. Design of a new mechanism for jetting dispenser featuring piezoactuator. *Proceedings of the Institution of Mechanical Engineers, Part C: Journal of Mechanical Engineering Science*, 222(4), pp.711–722.
- Nguyen, Q.H. et al., 2008. Dynamic characteristics of a new jetting dispenser driven by piezostack actuator. *IEEE Transactions on Electronics Packaging Manufacturing*, 31(3), pp.248–259.
- Nguyen, Q.-H., Choi, S.-B. & Kim, J.-D., 2008. The design and control of a jetting dispenser for semiconductor electronic packaging driven by a piezostack and a flexible beam. *Smart Materials & Structures*, 17(6).
- Nordson EFD, 2013. *PICO x MOD Valve Operating Manual* 1st ed.,

- Ober, T.J. et al., 2013. Microfluidic extensional rheometry using a hyperbolic contraction geometry. *Rheologica Acta*, 52(6), pp.529–546.
- Olberding, S., Wessely, M. & Steimle, J., 2014. PrintScreen: fabricating highly customizable thin-film touch-displays. In *Proceedings of the 27th annual ACM symposium on User interface software and technology*. pp. 281 – 290.
- Oosterhuis, G. & Feenstra, F.K., 2008. Pyrolytic printing , the holy grail in metal printing? In *5th European Thermal-Sciences Conference*. The Netherlands.
- Orme, M., Liu, Q. & Smith, R., 2000. Molten aluminum micro-droplet formation and deposition for advanced manufacturing applications. *Aluminum Transactions*.
- Ott, M. & Zaeh, M.F., 2010. Multi-material processing in additive manufacturing. In *21st Solid Freeform Fabrication Symposium (SFF)*. pp. 195–203.
- Pagudala, A.K., 2012. *Roll-to-Roll Embedding of Conductive Sintered Silver Grids*. Royal Institute of Technology.
- Panesar, A. et al., 2015. Design Framework for Multifunctional Additive Manufacturing: Placement and Routing of Three-Dimensional Printed Circuit Volumes. *Journal of Mechanical Design*, 137(11), p.111414.
- Parekh, D.P., Cormier, D. & Dickey, M.D., 2015. Multifunctional Printing: Incorporating Electronics into 3D Parts Made by Additive Manufacturing. In A. Bandyopadhyay & S. Bose, eds. *Additive Manufacturing*. CRC Press, pp. 215–258.
- Park, B.K. et al., 2007. Direct writing of copper conductive patterns by ink-jet printing. *Thin Solid Films*, 515(19), pp.7706–7711.
- Park, J.-U. et al., 2007. High-resolution electrohydrodynamic jet printing. *Nature materials*, 6(10), pp.782–9.
- Park, J.-U. et al., 2008. Nanoscale patterns of oligonucleotides formed by electrohydrodynamic jet printing with applications in biosensing and nanomaterials assembly. *Nano letters*, 8(12), pp.4210–6.
- Paulsen, J.A. et al., 2012. Printing conformal electronics on 3D structures with aerosol jet technology. In *FIIW 2012 - 2012 Future of Instrumentation International Workshop Proceedings*. pp. 47–50.
- Perelaer, B.J. et al., 2008. Inkjet-printed silver tracks: low temperature curing and thermal stability investigation. *Journal of Materials Chemistry*, 18(27), p.3209.
- Perelaer, J. et al., 2009. Microwave flash sintering of inkjet-printed silver tracks on polymer substrates. *Advanced materials (Deerfield Beach, Fla.)*, 21(47), pp.4830–4.
- Perelaer, J., 2012. Postprinting Processes for Inorganic Inks for Plastic Electronics Applications. In D.-Y. S. Jan G. Korvink, Patrick J. Smith, ed. *Inkjet-based Micromanufacturing*. Weinheim, Germany: Wiley-Vch, pp. 111–126.
- Perelaer, J. et al., 2010. Printed electronics: the challenges involved in printing devices, interconnects, and contacts based on inorganic materials. *Journal of Materials Chemistry*, 20(39), p.8446.
- Perelaer, J., de Gans, B.-J. & Schubert, U.S., 2006. Ink-jet Printing and Microwave Sintering of

- Conductive Silver Tracks. *Advanced Materials*, 18(16), pp.2101–2104.
- Périard, D., Malone, E. & Lipson, H., 2007. Printing embedded circuits. *Proceedings of the 18th Solid Freeform Fabrication Symposium*, pp.502–512.
- Petrie, C.J.S., 2006. Extensional viscosity: A critical discussion. *Journal of Non-Newtonian Fluid Mechanics*, 137(1-3), pp.15–23.
- Phoseon Technology, 2013. *FireFly™ 25x10 Product Specifications Rev 2.0*,
- Pilditch, R.L. et al., 2009. Skin-safe conductive ink and method for application on the body.
- Pilkington North America, I., 2013. *Properties of Soda-Lime Silica Float Glass ATS-129*,
- Pipe, C.J., Majmudar, T.S. & McKinley, G.H., 2008. High shear rate viscometry. *Rheologica Acta*, 47(5-6), pp.621–642.
- PiXDRO B.V., 2011. *Documentation PiXDRO LP50 Inkjet printer 3.0 ed.*,
- Priest, J., Smith, C. & DuBois, P., 1997. Liquid metal jetting for printing metal parts. In *Solid Freeform Fabrication Symposium*. Austin, TX.
- Prübe, U. et al., 2002. Practical aspects of encapsulation technologies. *Landbauforschung Völkenrode*, 241, pp.1–10.
- Quinones, H., Babiarz, A. & Fang, L., 2002. Fluid Dispensing Processes for Next Generation Electronics. In *Proceedings of Packaging Technology*. pp. 1–8.
- Quintero, A.V. et al., 2016. Smart RFID label with a printed multisensor platform for environmental monitoring. *Flexible and Printed Electronics*, 1(2), p.025003.
- Redinger, D. et al., 2004. An ink-jet-deposited passive component process for RFID. *IEEE Transactions on Electron Devices*, 51(12), pp.1978–1983.
- Reis, N. & Derby, B., 2000. Inkjet deposition of ceramic suspensions: modelling and experiments of droplet formation. In *Mat. Res. Soc. Symp. Proc. 624*. pp. 65–70.
- Renn, M.J., 2006. Direct Write™ System US 7108894 B2.
- Rijfers, A., Houben, R.J. & Brouwers, L.A.M., 2009. Droplet break-up device WO 2009061202 A1.
- Rioboo, R., Marengo, M. & Tropea, C., 2002. Time evolution of liquid drop impact onto solid, dry surfaces. *Experiments in Fluids*, 33, pp.112–124.
- Rodd, L.E. et al., 2005. Capillary break-up rheometry of low-viscosity elastic fluids. *Applied Rheology*, 15(1), pp.12–27.
- Rosen, D.W., Margolin, L. & Vohra, S., 2008. Printing High Viscosity Fluids Using Ultrasonic Droplet Generation. In *International Solid Freeform Fabrication Symposium – An Additive Manufacturing Conference*. pp. 239–253.
- Roth Elektronik GmbH, *Roth Elektronik® FR4 Boards – Safety Information*,
- Rózanska, S. et al., 2014. Extensional viscosity measurements of concentrated emulsions with the use of the opposed nozzles device. *Brazilian Journal of Chemical Engineering*, 31(1), pp.47–55.
- Rozhkov, A.N., 2005. Dynamics and breakup of viscoelastic liquids (a review). *Fluid Dynamics*,

- 40(6), pp.835–853.
- Ruffo, M. & Hague, R., 2007. Cost estimation for rapid manufacturing — simultaneous production of mixed components using laser sintering. *Proceedings of the Institution of Mechanical Engineers, Part B: Journal of Engineering Manufacture*, 221(11), pp.1585–1591.
- Ryer, A., 1997. *The light Measurement Handbook*, International Light Technologies.
- Salmoria, G. V. et al., 2008. Investigations on cure kinetics and thermal degradation of stereolithography Renshape 5260 photosensitive resin. *Polymer Testing*, 27(6), pp.698–704.
- Salmoria, G. V. et al., 2005. Stereolithography Somos 7110 photosensitive resin: Study of curing kinetic and thermal degradation. *Journal of Materials Processing Technology*, 168(1), pp.164–171.
- Sanchez-Romaguera, V., Madec, M.B. & Yeates, S.G., 2008. Inkjet printing of 3D metal-insulator-metal crossovers. *Reactive and Functional Polymers*, 68(6), pp.1052–1058.
- Sandler, J. et al., 1999. Development of a dispersion process for carbon nanotubes in an epoxy matrix and the resulting electrical properties. *Polymer*, 40(21), pp.5967–5971.
- Sangermano, M. et al., 2013. UV-Cured Acrylic Conductive Inks for Microelectronic Devices. *Macromolecular Materials and Engineering*, 298(6), pp.607–611.
- Sarik, J. et al., 2012. Combining 3D printing and printable electronics. In *Proceedings of TEI 2012 Works in Progress*. pp. 1–5.
- Schiaffino, S. & Sonin, A.A., 1997. Molten droplet deposition and solidification at low Weber numbers Transport and solidification phenomena in molten microdroplet pileup Molten droplet deposition and solidification at low Weber numbers. *Physics of Fluids Appl. Phys. Lett. J. Vac. Sci. Technol. B Fluids J. Appl. Phys. Phys. Fluids*, 9(9), pp.3172–161609.
- Seerden, K. et al., 2001. Ink-jet printing of wax-based alumina suspensions. *Journal of American Ceramic Society*, 84(11), pp.2514–2520.
- Sekitani, T. et al., 2008. Organic transistors manufactured using inkjet technology with subfemtoliter accuracy. *Proceedings of the National Academy of Sciences of the United States of America*, 105(13), pp.4976–80.
- Shemelya, C. et al., 2013. 3D Printed Capacitive Sensors. , (3), pp.0–3.
- Shim, J. et al., 2012. Bioprinting of a mechanically enhanced three-dimensional dual cell-laden construct for osteochondral tissue engineering using a multi-head tissue/organ building. *Journal of Micromechanics and Microengineering*, 22(8), p.085014.
- Shin, D.Y., Lee, Y. & Kim, C.H., 2009. Performance characterization of screen printed radio frequency identification antennas with silver nanopaste. *Thin Solid Films*, 517(21), pp.6112–6118.
- Shon, P.K. et al., 2012. Enhanced luminescence related to transparent conductive oxide in ZnS-based EL device fabricated by screen printing method. *Journal of Luminescence*, 132(7), pp.1764–1767.
- Shu, X. et al., 2010. Experimental study on high viscosity fluid micro-droplet jetting system. *Science in China Series E: Technological Sciences*, 53(1), pp.182–187.
- Singh, M. et al., 2010. Inkjet printing-process and its applications. *Advanced Materials*, 22(6),

pp.673–685.

- Sisko, A.W., 1958. The Flow of Lubricating Greases. *Industrial and Engineering Chemistry*, 50(12), pp.1789–1792.
- Sitthi-Amorn, P. et al., 2015. MultiFab: a machine vision assisted platform for multi-material 3D printing. *ACM Transactions on Graphics*, 34(4), pp.129:1–129:11.
- Small, W.R. & in het Panhuis, M., 2007. Inkjet printing of transparent, electrically conducting single-walled carbon-nanotube composites. *Small (Weinheim an der Bergstrasse, Germany)*, 3(9), pp.1500–3.
- Smet, P.F. et al., 2010. Luminescence in Sulfides: A Rich History and a Bright Future. *Materials*, 3(4), pp.2834–2883.
- Smith, P.J. et al., 2006. Direct ink-jet printing and low temperature conversion of conductive silver patterns. *Journal of Materials Science*, 41(13), pp.4153–4158.
- Soltman, D. & Subramanian, V., 2008. Inkjet-printed line morphologies and temperature control of the coffee ring effect. *Langmuir : the ACS journal of surfaces and colloids*, 24(5), pp.2224–31.
- Song, B. & Springer, J., 1996. Determination of Interfacial Tension from the Profile of a Pendant Drop Using Computer-Aided Image Processing. *Journal of Colloid and Interface Science*, 184, pp.77–91.
- Sowade, E. et al., 2015. Roll-to-roll infrared (IR) drying and sintering of an inkjet-printed silver nanoparticle ink within 1 second. *Journal of Materials Chemistry C*, 3(45), pp.11815–11826.
- Sridhar, A., 2010. *An inkjet printing-based process chain for conductive structures on printed circuit board materials*. Enschede, The Netherlands: University of Twente.
- Stejskal, J., 2013. Conducting polymer-silver composites. *Chemical Papers*, 67(8), pp.814–848.
- Stow, C.D. & Hadfield, M.G., 1981. An Experimental Investigation of Fluid Flow Resulting from the Impact of a Water Drop with an Unyielding Dry Surface. *Proceedings of the Royal Society A: Mathematical, Physical and Engineering Sciences*, 373(1755), pp.419–441.
- Stringer, J. & Derby, B., 2009. Limits to feature size and resolution in ink jet printing. *Journal of the European Ceramic Society*, 29(5), pp.913–918.
- Strutt, J.W. & Rayleigh, Lord, 1879. On the instability of jets. In *Proc. R. Soc. London A*. pp. 4–13.
- Subramanian, V. et al., 2005. Progress Toward Development of All-Printed RFID Tags: Materials, Processes, and Devices. *Proceedings of the IEEE*, 93(7), pp.1330–1338.
- Suganuma, K., 2014. *Introduction to Printed Electronics*, Springer.
- Suter, M., Weingärtner, E. & Wegener, K., 2012. MHD printhead for additive manufacturing of metals. *Procedia CIRP*, 2, pp.102–106.
- Sutter, T., 2012. Inkjet Fabrication of Printed Circuit Boards. In D.-Y. S. Jan G. Korvink, Patrick J. Smith, ed. *Inkjet-based Micromanufacturing*. Weinheim, Germany: Wiley-Vch, pp. 257–278.
- Tabatabai, A. et al., 2013. Liquid-phase gallium-indium alloy electronics with microcontact printing. *Langmuir : the ACS journal of surfaces and colloids*, 29(20), pp.6194–200.
- Tang, Y. et al., 2012. A new approach causing the patterns fabricated by silver nanoparticles to be

- conductive without sintering. *Nanotechnology*, 23(35), p.355304.
- Tanvir, S. & Qiao, L., 2012. Surface tension of Nanofluid-type fuels containing suspended nanomaterials. *Nanoscale research letters*, 7(1), p.226.
- Taubert, P., 2012. *Continuously-variable material properties in RepRap 3D printing*. University of Bath.
- Tekin, E., Smith, P.J. & Schubert, U.S., 2008. Inkjet printing as a deposition and patterning tool for polymers and inorganic particles. *Soft Matter*, 4, pp.703–713.
- Tobjörk, D. et al., 2012. IR-sintering of ink-jet printed metal-nanoparticles on paper. *Thin Solid Films*, 520(7), pp.2949–2955.
- Toyama, T. et al., 2009. An electroluminescence device for printable electronics using coprecipitated ZnS:Mn nanocrystal ink. *Nanotechnology*, 20(5), p.055203.
- Tropmann, A. et al., 2011. Pneumatic dispensing of nano- to picoliter droplets of liquid metal with the StarJet method for rapid prototyping of metal microstructures. *Microfluidics and Nanofluidics*, 12(1-4), pp.75–84.
- Tuck, C., Hague, R. & Ruffo, M., 2008. Rapid manufacturing facilitated customization. *International Journal of Computer Integrated Manufacturing*, 21(3).
- Vafaei, S. et al., 2009. The effect of nanoparticles on the liquid-gas surface tension of Bi<sub>2</sub>Te<sub>3</sub> nanofluids. *Nanotechnology*, 20(18), p.185702.
- Vidim, K., Wang, S. & Ragan-kelley, J., 2013. OpenFab: A Programmable Pipeline for Multi-Material Fabrication. *ACM Transactions on Graphics*, 32(4), pp.1–11.
- Wakuda, D., Kim, K. & Suganuma, K., 2010. Ag nanoparticle paste synthesis for room temperature bonding. *Components and Packaging ...*, 33(2), pp.437–442.
- Wakuda, D., Kim, K. & Suganuma, K., 2008. Room temperature sintering of Ag nanoparticles by drying solvent. *Scripta Materialia*, 59(6), pp.649–652.
- Wakuda, D. & Suganuma, K., 2009. Room-Temperature Sintering Process of Ag Nanoparticle Paste. *IEEE Transactions on Components and Packaging Technologies*, 32(3), pp.627–632.
- Wallace, D., 2012. Overview of Inkjet-Based Micromanufacturing. In D.-Y. S. Jan G. Korvink, Patrick J. Smith, ed. *Inkjet-based Micromanufacturing*. Weinheim, Germany: Wiley-Vch, pp. 1–17.
- Wang, L. et al., 2013. Design and experiment of a jetting dispenser driven by piezostack actuator. *IEEE Transactions on Components, Packaging and Manufacturing Technology*, 3(1), pp.147–156.
- Weng, B. et al., 2010. Printing conducting polymers. *The Analyst (RSC)*, 135(11), pp.2779–89.
- Wijshoff, H., 2010. The dynamics of the piezo inkjet printhead operation. *Physics Reports*, 491(4-5), pp.77–177.
- Winscom, C.J., Harris, P.G. & Silver, J., 2014. Towards a complete understanding of the electronic characteristics of powder ACEL lamps. *Digest of Technical Papers - SID International Symposium*, 45, pp.1301–1304.
- Winston, R., 1962. Method of and apparatus for transferring ink US 3060429 A.
- Withnall, R. et al., 2011. AC powder electroluminescent displays: A state-of-the-art review. *Journal*

- of the Society for Information Display*, 19(11), pp.798–810.
- Withnall, R. et al., 2008. Low cost, flexible electroluminescent displays with a novel electrode architecture printed by offset lithography. , pp.1491–1494.
- Withnall, R., Harris, P. & Silver, J., 2010. Novel, Bright, Inorganic Electroluminescent Flexible Displays Comprising Ink Jet Printed Silver Back Electrodes. In *SID Symposium Digest of Technical Papers*. pp. 397–400.
- Wohlers, T., 2008. *Wohlers Report 2008: State of the industry*,
- Wünscher, S. et al., 2014. Progress of alternative sintering approaches of inkjet-printed metal inks and their application for manufacturing of flexible electronic devices. *J. Mater. Chem. C*, 2, pp.10232–10261.
- Xie, D. et al., 2010. Multi-materials drop-on-demand inkjet technology based on pneumatic diaphragm actuator. *Science China Technological Sciences*, 53(6), pp.1605–1611.
- Yang, C., Wong, C.P. & Yuen, M.M.F., 2013. Printed electrically conductive composites: conductive filler designs and surface engineering. *Journal of Materials Chemistry C*, 1(26), p.4052.
- Yang, H. et al., 2013. High viscosity jetting system for 3D reactive inkjet printing. In *Twenty Forth Annual International Solid Freeform Fabrication Symposium – An Additive Manufacturing Conference*. Austin, Texas, USA: Additive Manufacturing and 3D printing group, pp. 505–513.
- Yao, Y. et al., 2016. Three-Dimensional Printable High-Temperature and High-Rate Heaters. *ACS Nano*, 10(5), pp.5272–5279.
- Yoshioka, Y., Calvert, P.D. & Jabbour, G.E., 2005. Simple Modification of Sheet Resistivity of Conducting Polymeric Anodes via Combinatorial Ink-Jet Printing Techniques. *Macromolecular Rapid Communications*, 26(4), pp.238–246.
- Yung, K.C. et al., 2010. Ink-jet printing and camera flash sintering of silver tracks on different substrates. *Journal of Materials Processing Technology*, 210(15), pp.2268–2272.
- Zhang, R. et al., 2013. Growth of half-meter long carbon nanotubes based on Schulz-Flory distribution. *ACS nano*, 7(7), pp.6156–61.
- Zhang, Z.X., Chen, X.Y. & Xiao, F., 2011. The Sintering Behavior of Electrically Conductive Adhesives Filled with Surface Modified Silver Nanowires. *Journal of Adhesion Science and Technology*, 25(13), pp.1465–1480.
- Zheng, Y. et al., 2014. Personal electronics printing via tapping mode composite liquid metal ink delivery and adhesion mechanism. *Scientific reports*, 4, p.4588.
- Zohuriaan, M.J. & Shokrolahi, F., 2004. Thermal studies on natural and modified gums. *Polymer Testing*, 23(5), pp.575–579.
- Zoltan, S.I., 1972. US3683212 A.